Tampere University

SANTERI LAMPINEN

Increasing the Automation Level of Hydraulic Secondary Breaker Systems

An End-to-End Concept

Tampere University Dissertations 477

Tampere University Dissertations 477

SANTERI LAMPINEN

Increasing the Automation Level of Hydraulic Secondary Breaker Systems

An End-to-End Concept

ACADEMIC DISSERTATION
To be presented, with the permission of
the Faculty of Engineering and Natural Sciences
of Tampere University,
for public discussion in the auditorium K1702
of the Konetalo building, Korkeakoulunkatu 6, Tampere,
on 8 October 2021, at 12 o'clock.

ACADEMIC DISSERTATION
Tampere University, Faculty of Engineering and Natural Sciences
Finland

Responsible supervisor and Custos	Professor Jouni Mattila Tampere University Finland	
Pre-examiners	Professor Keyvan Hashtrudi-Zaad Queen’s University Canada	Professor Guangjun Liu Ryerson University Canada
Opponent	Professor Heikki Handroos Lappeenranta University of Technology Finland	

The originality of this thesis has been checked using the Turnitin OriginalityCheck service.

Cover design: Roihu Inc.

ISBN 978-952-03-2112-3 (print)
ISBN 978-952-03-2113-0 (pdf)
ISSN 2489-9860 (print)
ISSN 2490-0028 (pdf)
http://urn.fi/URN:ISBN:978-952-03-2113-0

PunaMusta Oy – Yliopistopaino
Joensuu 2021

PREFACE

This study was carried out from 2018 to 2021 at the unit of Automation Technology and Mechanical Engineering at Tampere university (TAU) in cooperation with RamBooms Oy.

I would like to express my deepest gratitude to my supervisor, Prof. Jouni Mattila, for his guidance and advice during this project, and for providing the opportunity to work on this dissertation. I wish to thank the preliminary examiners Prof. Keyvan Hastrudi-Zaad and Prof. Guangjun Liu for the evaluation of this thesis and their constructive feedback and encouraging comments. I am grateful for Dr. Wen-Hong Zhu for the invaluable help and guidance with the writing of my first journal article and during its long publication process. It was a great privilege to work with you.

Special thanks go to Dr. Janne Koivumäki for his motivation, patient guidance and assistance from the beginning. Thanks are also due to researchers Lionel Hulttinen, Pauli Mustalahti, and Petri Mäkinen for the good working atmosphere, constructive feedback and valuable discussions over the years.

I would like to express my gratitude to RamBooms Oy for providing the research topic and the platform for this work. Special thanks go to Jouni Niemi and Vesa Marttila for their comments and all the valuable discussions.

This work was mutually funded by Tampere University and RamBooms Oy. Special thanks to Prof. Pauli Kuosmanen for supporting this cooperation. Partial funding was also received from the Finnish Foundation for Technology Promotion.

I wish to thank my parents Aki and Liisa, and my siblings Pyry, Aurora, and Pilvi for their continued support throughout the years. Finally, the greatest thanks go to my beloved Heidi for her support, understanding and motivation during this work.

Santeri Lampinen
Tampere, August 2021.

ABSTRACT

Crushing blasted ore is an essential phase in the extraction of valuable minerals in the mining industry. The first stage in crushing is to process the raw blasted material, which typically contains a broad size distribution. To prevent oversized material from entering into the primary crusher, a metal grate is often used to separate large fragments. A secondary breaker, that is, a hydraulic manipulator with an impact-hammer, is then used for controlled size reduction of the oversized boulders. This is an essential task for ensuring continuous material flow and preventing blockages.

The mining industry, as many other industries, is currently expanding, moving toward increased automation with huge investments being made in research and development. Driven by safety and economic incentives, the demand for autonomous secondary breaking—which is almost exclusively performed manually with line-of-sight teleoperation—is expected to significantly increase in the near future.

This thesis aims to develop an end-to-end concept for an autonomous secondary breaker system. To accomplish this task, this thesis addresses three research problems (RPs) directly related to the automation of the secondary breaking task, that is, manipulator control, machine vision, and high-level autonomous operation coordination, along with one RP related to the force-reflective teleoperation of hydraulic manipulators. The latter was considered for a backup control method of the secondary breaker boom.

Six publications have been generated, addressing the RPs. The work culminates in the concept autonomous breaker system realized on top of a commercial breaker boom. The focus in development of the autonomous concept was to maintain the original functionality of the breaker boom system. In terms of the last RP concerning teleoperation, the work has resulted in significant advances toward effective teleoperation control of dissimilar leader–follower systems. The experimentally verified control theory foundation can be used as a basis for the teleoperation of a wide class of manipulators.

CONTENTS

1 Introduction 15
1.1 Motivation 15
1.2 Research Problems (RPs) 18
1.3 Constraints and Scope of the Research 20
1.4 Thesis Contributions 21
1.5 The Author's Contribution to the Publications 23
1.6 Outline of the Thesis 24

2 State of the Art 25
2.1 State-of-the-Art Control of Hydraulic Serial Manipulators 25
2.2 Control of Real-World Hydraulic Serial Manipulators 27
2.3 Teleoperation 28
2.4 Autonomous Secondary Breaking 30

3 Proposed Solutions 33
3.1 High-Precision Control of the Hydraulic Secondary Breaker Boom . 33
3.2 Teleoperation 36
3.2.1 Experimental System 36
3.2.2 Application to the Secondary Breaker Use Case 40
3.3 Autonomous Secondary Breaker Concept 41
3.3.1 Visual Perception 42
3.3.2 Autonomous Operation Toolbox 44

4 Discussion 47
4.1 High-precision control (RP-I) 47

4.2 Robust boulder detection (RP-II) 48
4.3 High-level control for autonomous operation (RP-III) 48
4.4 Teleoperation (RP-IV) 49
4.5 Levels of Autonomy and Safety Considerations 49
4.6 General Applicability 51

5 Conclusions 53

6 Summary of Publications 55
6.1 Summary of P-I: Model-based Control of a Pressure-compensated Directional Valve with Significant Dead-Zone 55
6.2 Summary of P-II: Flow-Bounded Trajectory-Scaling Algorithm for Hydraulic Robotic Manipulators 56
6.3 Summary of P-III: Autonomous Robotic Rock Breaking Using a Real-time 3D Visual Perception System 57
6.4 Summary of P-IV: Robust Rock Detection and Clustering with Surface Analysis for Robotic Rock Breaking Systems 58
6.5 Summary of P-V: Bilateral Teleoperation of a Hydraulic Robotic Manipulator in Contact with Physical and Virtual Constraints 59
6.6 Summary of P-VI: Force-Sensor-Less Bilateral Teleoperation Control of Dissimilar Master-Slave System with Arbitrary Scaling 59

References 61

Publication I 77

Publication II 89

Publication III 97

Publication IV 127

Publication V 137

Publication VI 149

List of Figures

1.1 RamBooms X88-540r rock breaker at the field test site at TAU. 21
1.2 Outline of the thesis. 24

3.1 Overview of the modular control architecture. 35
3.2 The experimental implementation of the bilateral teleoperation system. 37
3.3 Conceptual illustration of the modular teleoperation system's architecture. 38
3.4 High-level control diagram of the bilateral teleoperation system. . . . 39
3.5 Modular deployment of the autonomous secondary breaker system's architecture and included subcomponents. 43
3.6 Boulder detection using the segmentation approach proposed in P-IV. Individual boulders are drawn in various colors, and bounding volumes are drawn around each boulder. The break locations proposed by the VPS are marked with red dots. 44
3.7 Operation pipeline for the concept of an autonomous breaker system. 45

4.1 Hydraulic impact hammer mounted on an excavator in an open-pit mine. 52

ABBREVIATIONS

ARC	adaptive robust control
CNN	convolutional neural network
DoF	degrees of freedom
IoT	internet of things
IoU	intersection over union
LfD	learning from demonstrations
LHD	load haul dump
LoA	levels of automation
NMB	nonlinear model based
OEM	original equipment manufacturer
PCL	point cloud library
PD	proportional derivative
RoM	run of mine
RP	research problem
TAU	Tampere university
TCP	tool center point
ToF	time of flight
VDC	virtual decomposition control
VPS	visual perception system
YOLOv3	"you only look once" version 3

ORIGINAL PUBLICATIONS

Publication I	S. Lampinen, J. Koivumäki, J. Mattila and J. Niemi. Model-based control of a pressure-compensated directional valve with significant dead-zone. *ASME/BATH 2019 Symposium on Fluid Power and Motion Control*. ASME, Oct. 2019. ISBN: 9780791859339. DOI: `10.1115/fpmc2019-1664`.
Publication II	S. Lampinen, J. Niemi and J. Mattila. Flow-Bounded Trajectory-Scaling Algorithm for Hydraulic Robotic Manipulators. *2020 IEEE/ASME International Conference on Advanced Intelligent Mechatronics (AIM)*. July 2020, 619–624. DOI: `10.1109/AIM43001.2020.9158851`.
Publication III	S. Lampinen, L. Niu, L. Hulttinen, J. Niemi and J. Mattila. Autonomous robotic rock breaking using a real-time 3D visual perception system. *Journal of Field Robotics* 38.7 (2021), 980–1006. DOI: `10.1002/rob.22022`.
Publication IV	S. Lampinen and J. Mattila. Robust Rock Detection and Clustering with Surface Analysis for Robotic Rock Breaking Systems. *2021 IEEE/ASME International Conference on Advanced Intelligent Mechatronics (AIM)*. 2021, 140–147. DOI: `10.1109/AIM46487.2021.9517695`.
Publication V	S. Lampinen, J. Koivumäki and J. Mattila. Bilateral teleoperation of a hydraulic robotic manipulator in contact with physical and virtual constraints. *BATH/ASME 2018 Symposium on Fluid Power and Motion Control*. ASME, Sept. 2018. DOI: `10.1115/FPMC2018-8842`.

Publication VI	S. Lampinen, J. Koivumäki, W.-H. Zhu and J. Mattila. Force-Sensor-Less Bilateral Teleoperation Control of Dissimilar Master-Slave System with Arbitrary Scaling. *IEEE Transactions on Control Systems Technology* (2021). DOI: `10.1109/TCST.2021.3091314`.

1 INTRODUCTION

Increased automation and autonomous systems have become a big trend in both consumer applications and industrial systems. Autonomous vacuum cleaners, lawn mowers, and self-driving cars are just a few examples of how many consumers may already utilize these technological advancements. In addition, numerous applications in the forestry, agriculture, mining, and construction industries are also being automated, and autonomous or semi-autonomous systems are becoming increasingly common [54]. In the scope of the current thesis, a system is considered autonomous when it does not require constant supervision from an operator (either remote or local). Instead, the system uses its sensory data to assess its operating environment and further uses that knowledge for decision making and operation. However, the need for a skilled machine operator still exists, but instead of constantly operating a single machine, the operator's role involves managing a fleet of machines, with only occasional manual control of a single machine during challenging conditions when the autonomous system is unable to execute its task successfully.

The main focus of the present thesis is to extend the state of the art in breaker boom automation by identifying the requirements for such a system, evaluating the necessary technology required, and developing advanced methods to meet these requirements.

1.1 Motivation

Constant improvement, innovations and technical advancements are continuously shaping the industry. Since the original Industrial Revolution, which was led by the mechanization of manual labor together with steam and water power, massive leaps in productivity, performance, efficiency, and connectivity have led to the ongoing Fourth Industrial Revolution, *Industrie 4.0* [44], which is characterized by high-impact topics, such as increased automation, autonomous systems, digitalization, connectivity (internet of things (IoT)), big data, and so forth.

Increased automation and autonomy is a driving force reshaping the mining industry, providing businesses with the opportunities for value creation, enabling profitable operation in new areas [109]. Digitalization also has the potential to improve health, safety, and the environmental impact. The Fourth Industrial Revolution is proceeding at a different pace among industries, and the most advanced solutions are first adopted in more structured environments, for example, mass production factories, where interactions between the production equipment and products are well defined and organized. Increasing automation and designing autonomous processes is much more challenging in semi-/unstructured and dynamic environments, where interactions with the environment rely heavily on sensory perception and independent decision making rather than predefined policies. For example, autonomous container trucks in ports and automated guided vehicles (AGVs) in factories are already widely utilized, whereas self-driving passenger cars are only now starting to emerge, and their technology still requires constant human supervision (only partly because of legal issues) [51].

The benefits of increased automation are attractive in the risk-intensive mining industry. Increased safety and productivity, along with reduced operational costs and more predictable maintenance needs are just a few benefits that can be expected from increased automation. On the other hand, local employment creation and the resulting local benefits of mining, especially in low-income countries, may be affected by the inevitably increasing automation level [76]. Yet even autonomous and more automatic systems require labor in, for example, supervision and maintenance. As a result of increased automation and teleoperation, machine operation can be performed remotely from a safe environment, for example, an air-conditioned office.

For these reasons, it is not surprising that automation has already gained a foothold on various process phases in the mining industry. Material handling such as blasted ore haulage by load haul dump (LHD) trucks has already been widely transformed by automation [15, 61]. Other tasks, such as drilling, bolting, dozing, digging, and loading, are also being automated at an increasing pace [21, 62, 77]. Indeed, the world's first self-proclaimed fully autonomous mine began its operation in 2019 in Mali [66].

Despite the numerous benefits of automation, many process phases still involve unautomatized manual work requiring constant human presence. Secondary breaking, in which the aim is controlled size reduction of oversized boulders that are physically too large for a primary crusher, is one such task.

The blasting process is controlled to obtain a very specific size distribution of the blasted ore to enable efficient transportation from the blasting site and efficient crushing [112]. However, occasionally blasting results in non-ideal-sized boulders that may be too large for the primary crusher. To prevent the primary crusher from jamming and ensure continuous material flow from the primary crusher, a secondary breaker is required.

The secondary breaker is a hydraulic series manipulator equipped with a hydraulic impact hammer. Breaker booms are specifically designed to withstand the large impact forces from the breaking process. Decades of development has resulted in an excavator-like boom geometry with typically three to four rigid boom segments, depending on the reach requirements of the individual applications. The boom-mounted impact hammers come in a wide variety, with the smallest weighing just 100 kg, while heavy-duty hammers reach almost 5000 kg. The control of these booms is achieved with robust proportional control valves, with significant dead zones ensuring safe operation. Because of being intended for manual operation, pressure-compensated valves are preferred for their ability to provide constant cylinder velocity despite varying loading conditions. The typical operation of the secondary breaker is performed using line-of-sight teleoperation. The secondary breaker itself is typically located in the immediate neighborhood of the primary crusher. Depending on the type of primary crusher, the setup has characteristic differences; two of the most typical applications are described here.

In the grizzly application, a common setup is that a secondary breaker is located immediately adjacent to a run of mine (RoM) bin that is fitted with a static metal screening structure, which is called a grizzly, that prevents oversized material from entering the RoM bin. The size of the openings of the screening structure are designed in such a manner that rocks that are small enough for the primary crusher may pass through the grizzly openings. Oversized material is broken against the grizzly using the secondary breaker.

Another typical application for secondary breaking is to ensure continuous material flow at a gyratory crusher facility. In this application, a typical arrangement is that LHD-trucks dump their load directly into the crushing chamber. Oversized material and blockages can be dealt with directly by the secondary breaker, either by attempting to move stuck and/or oversized material into the mouth of the crusher or by breaking the oversized material into smaller pieces.

Currently, this process requires constant operator presence and manual operation to ensure continuous material flow. When oversized material is detected, an operator manually controls the secondary breaker to reduce the size of the oversized boulders, typically by line-of-sight teleoperation or remotely from a specific control room via video feedback. Controlling the secondary breaker is typically performed primitively with an open-loop control, where each actuator of the manipulator is controlled individually.

A larger mine may have several crushing stations, with each having its own secondary breaker. Moreover, in the case of underground mining, these stations are located at the bottom, where the operation environment can be challenging and transportation from the surface a time-consuming process. The transportation of crushed material is more efficient than unprocessed blasted ore because more consistently sized ore fragments are packed into a smaller volume. Therefore, the economic justification to automate the secondary breaking task with a reliable teleoperation method is notable.

Secondary breakers play an important role in assisting the primary crushing process by preventing blockages and reducing the size of oversized material [10]. In a study assessing the operation of an underground mine, it was found that blockages in the secondary ore pass, a minor breakdown of a the rock breaker, and a major breakdown of an LHD truck were identified as having the greatest impact on the production of a mine [20]. The first two issues stress the importance and impact of secondary breaking to the operation of a mine, hence encouraging development in this regard.

1.2 Research Problems (RPs)

The current thesis analyzes and defines the requirements for an autonomous secondary breaker boom system built on the foundation of an existing commercial breaker boom from a Finnish original equipment manufacturer (OEM) RamBooms Oy. The work culminates in an end-to-end autonomous breaker boom concept proposal. The research problems (RPs) seek to address distinct critical issues that require elaborate solutions to realize the end-to-end autonomous breaker system. Importantly, the RPs are formulated, keeping reliability as a priority. The extra functionality developed in the present thesis is built on top of the existing system while maintaining the original functionality and hardware. This is important in view of a mine's operation, which is highly optimized for 24/7 production, where unplanned downtime can lead to tremendous costs.

RP-I **High-precision control:** Can the secondary breaker boom be retrofitted (with minimal modifications) for high-precision robotic control using the existing control valves?

RP-II **Robust boulder detection:** Can time of flight (ToF) cameras be used to achieve robust boulder detection in harsh conditions?

RP-III **High-level control for autonomous operation:** What are the most critical components for realizing a conditionally autonomous breaker system in a grizzly application, and how should those components be managed at a high-level. What are the most critical operations that need to be addressed by the tactical operation toolbox?

RP-IV **Teleoperation:** Is stability-guaranteed force-reflective bilateral teleoperation feasible for hydraulic multi-degrees of freedom (DoF) manipulators? Could such a system be leveraged for controlling industrial manipulators, for example, as a backup method? Unavoidably, an autonomous system may require that a human operator take control of the system occasionally. Can the same teleoperation interface be augmented with artificially rendered constraints and forces to assist and guide the operator?

These research problems are discussed within the publications included in this thesis. **RP-I** was addressed in Publications P-I–P-II, while Publication P-III addressed **RP-III**. Publication P-IV addressed **RP-II** and was conducted based on the insights gained from P-III. Publication P-III did not use the boulder detection method proposed in P-IV but instead utilized the one designed by Niu et al. in [71]. The method proposed in P-IV was developed only later. Publications P-V and P-VI addressed **RP-IV** and both utilized the control system of [48] for the control of the follower manipulator with slight modifications.

1.3 Constraints and Scope of the Research

The aim of the current thesis is to study the feasibility of autonomous robotic secondary breaking and develop methods required to realize an autonomous system. The developed methods are built on top of commercial systems, here with specific attention to the generic applicability and possibility for further development toward the commercialization of the technology. These constraints limit the available methods in the development process. For instance, the secondary breaker boom studied in the current thesis comes equipped with slow proportional control valves with significant dead zones that were primarily developed for manual operation. Instead of retrofitting vastly more expensive high-bandwidth servo valves, methods that can take advantage and utilize the current valves are investigated. Retrofitting extra instrumentation is kept minimal in view of the harsh target application, in which robust operation requires a simplistic approach that is tolerant to disturbances and has minimal possible points of failure in terms of components and instrumentation. Moreover, the existing functionality of the boom is kept intact to enable the possibility to revert back to the original control scheme in case of the failure of some system component. The evaluation of the feasibility of the autonomous robotic secondary breaking concept is performed at the field test site built at the outdoor area of the research laboratory of Tampere university (TAU) (see Figure 1.1). The development is performed using a RamBooms X88-540r secondary breaker, that is, a nine-ton manipulator with a 1700 kg Rammer impact breaker and horizontal reach of 5.4 m with the breaker vertical [80].

The constraints affecting the development and evaluation of the autonomous secondary breaker are listed as follows:

- Reusability and generalizable methods
- Minimal extra instrumentation
- Suitable for harsh mining environments
- Experimental setup built at the field test site in TAU

Figure 1.1 RamBooms X88-540r rock breaker at the field test site at TAU.

1.4 Thesis Contributions

As a compendium thesis, the main contributions are directly related to the associated publications. The scientific contributions of the individual publications are as follows:

P-I This publication proposes a method to address the dead zone of a pressure-compensated directional valve and to establish an nonlinear model based (NMB) control approach for it. The main contributions of the publication are as follows: 1) dead zone compensation was established with respect to hydraulic valve control laws that were originally proposed for high-bandwidth (servo-) valve control, and 2) the proposed method is experimentally verified as being capable of accurate motion (position and velocity) and force tracking despite the use of a slow-response pressure-compensated directional valve with bandwidth of only 4 Hz.

P-II This publication proposes dynamic scaling of the tool center point (TCP) velocity, which is based on the available pump capacity to allow operation at the absolute maximum achievable TCP velocity by considering the mechanical and hydraulic limitations of the manipulator. The main contributuion is the introduction of trajectory scaling into the scope of hydraulic manipulators. The proposed approach solves the problem of bounded volumetric flow from the supply unit, enabling higher utilization of the manipulator's capabilities.

P-III This publication presents the novel autonomous robotic secondary breaking system concept. The paper presents complete measures to automate the secondary breaking task, verifying the feasibility of the concept while identifying several challenges that need to be addressed for further improvement of the system before commercialization. The outcome of this paper culminates in field experiments acting as a technological proof of concept in a simplified environment.

P-IV This publication investigates an alternative method to detect boulders using a ToF camera, here in lieu of the stereo camera utilized in P-III. The main contribution of this study is the clustering algorithm that achieves similar performance as the deep-learning-based approach but without any training dataset. The second contribution of this publication is the proposed method for break point selection and break difficulty estimation.

P-V This publication presents the preliminary design and results on the teleoperation of a hydraulic heavy-duty manipulator. The publication proposes artificial constraints in the scope of the teleoperation structure. The information about the virtual fixtures in the workspace of the teleoperated hydraulic manipulator is transmitted to the operator via haptic feedback on the leader manipulator. The proposed approach enables the operator to intuitively feel the physical and virtual constraints in the workspace. The artificial constraints in the workspace can be used to limit the movement of the follower manipulator and to, for example, avoid fragile objects or provide guidance to the operator.

P-VI For the first time, this publication proposes a theoretically sound NMB control approach for bilateral teleoperation of dissimilar leader–follower systems with a hydraulic follower manipulator. The publication presents the following distinguishable contributions: 1) We propose a leader manipulator contact force estimation by using joint control torques and estimated manipulator dynamics. A solution to a computational algebraic loop formed around the actuation and force estimation is proposed. 2) We propose a novel method for estimating the exogenous force of the human operator. 3) The stability of the overall control design is rigorously guaranteed with robustness against an arbitrary time delay.

1.5 The Author's Contribution to the Publications

This section clarifies the author's contribution to the publications presented in this thesis.

P-I The author wrote the paper, developed the approach to compensate valve dead zones in pressure-compensated directional control valves within the NMB control laws of the virtual decomposition control (VDC), and implemented the control system on the experimental setup. Dr. Janne Koivumäki helped with the mathematical derivations and aided in writing the paper. Mr. Jouni Niemi, the industrial supervisor, reviewed the paper and gave an industrial view. Professor Jouni Mattila, the academic supervisor, reviewed the paper and suggested improvements.

P-II The author wrote the paper and developed the online trajectory scaling method for the flow-bounded control of hydraulic systems. Mr. Jouni Niemi and Professor Jouni Mattila reviewed the paper and proposed improvements.

P-III The author and Dr. Longchuan Niu contributed equally to the paper. The author developed the control system, the operation strategy and the break instance detection, and managed the implementation. Dr. Longchuan Niu developed the visual perception system (VPS) and managed it during the experiments. M.Sc. Lionel Hulttinen calibrated the manipulator's forward kinematics model and wrote the corresponding part of the paper. Mr. Jouni Niemi provided industrial insights and views regarding rock breaking, including system evaluation. Professor Jouni Mattila reviewed the paper and made corrections.

P-IV The author wrote the paper, gathered the experimental data set, and developed the boulder detection and clustering algorithm, break point selection method, and break difficulty estimation. Professor Jouni Mattila reviewed the paper and proposed improvements.

P-V The author wrote the paper and expanded the teleoperation scheme with virtual obstacles. Dr. Janne Koivumäki aided in the writing process and assisted with the experimental setup. Professor Jouni Mattila reviewed the paper and suggested improvements.

P-VI The author wrote the paper and expanded the teleoperation scheme with a completely force-sensor-less design and novel force estimation strategy. Dr. Janne

Koivumäki aided in the writing process and assisted with the experimental setup. Dr. Wen-Hong Zhu provided support with the mathematical foundation of the paper, reviewed the paper, and suggested corrections. Professor Jouni Mattila reviewed the paper and suggested improvements.

1.6 Outline of the Thesis

The introductory part of the present thesis is divided into five chapters. This chapter has introduced the topics of the thesis and research problems. The structure of the remaining chapters is as follows: Chapter 2 introduces the state of the art related to manipulator control, teleoperation, and breaker boom automation. Chapter 3 presents the proposed solutions for the development of an autonomous secondary breaker system. Chapter 4 discusses the research problems and their fulfillment, levels of automation (LoA), and general applicability of the results of the conducted research. Chapter 5 concludes the introductory part. Chapter 6 summarizes the publications included in this thesis. The outline of the thesis and the relations between the publications are summarized in Figure 1.2.

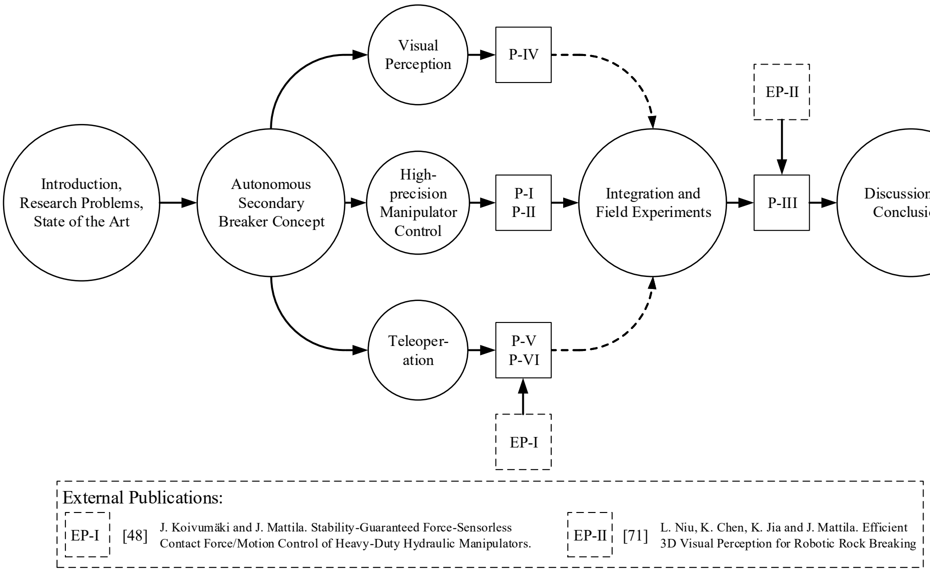

Figure 1.2 Outline of the thesis.

2 STATE OF THE ART

This chapter reviews the state of the art in the fields related to the topics of the current thesis. In the thesis, the control problems of hydraulic manipulators have a strong emphasis on practical implementations. This may restrict the use of high-performance hardware (e.g., high-bandwidth servo-valves, pressure sensors, and a high-speed, real-time control system). However, the teleoperation research has been conducted on high-end hardware components.

2.1 State-of-the-Art Control of Hydraulic Serial Manipulators

A fundamental difference in the control of hydraulic systems against their electrical counterparts is caused by the characteristic and highly nonlinear dynamic behavior of hydraulics. Instead of directly controlling the torque of an actuator, the control of a hydraulic actuator is performed indirectly by controlling the flow rate and pressure of the hydraulic oil going into the actuator by an electro-hydraulic valve. Because of this indirect approach, the control laws for hydraulic actuators are typically much more complex so that they can rigorously address the system's dynamics. Because of the involved complex and nonlinear dynamics, it can be argued that linear control theory alone is insufficient for high-precision control of hydraulic systems. Bech et al. provided evidence supporting this claim, showing how various linear and nonlinear controls methods were evaluated for the control of hydraulic robotic manipulators [8]. The study concluded that all the nonlinear controllers outperformed the best linear counterpart. Bonchis et al. observed similar results in an earlier study [11].

A recent review of the state-of-the-art methods for the control of hydraulic systems by Mattila et al. has provided a good summary on the topic by separately reviewing methods for free space motion control and contact control approaches [63]. The study suggested that the best results in the high-precision control have been achieved using various stability-guaranteed NMB approaches. In terms of research on free space control, high-precision motion control, i.e., velocity and position tracking, is considered as the main objective. Conrad evaluated linear perturbation adaptive control and adaptive model-based actuator control [19]. Mattila et al. proposed a model-based computed force controller [64]. Bu and Yao proposed an observer based adaptive robust control (ARC) [12]. Chang and Lee applied time delay control for a hydraulic excavator [16]. Kalmari proposed model-predictive control [45]. Zhu and Piedboeuf proposed an adaptive model based control [116] that is further based on a broader subsystem's dynamics based control approach, VDC [113, 114, 118]. Koivumäki and Mattila further demonstrated the capability of the VDC approach for free-space control in [50]. The control performance of various control schemes can be compared using, for example, a normalizing performance indicator, such as that used by Zhu and Piedboeuf in [116], defined as

$$\rho = \frac{\max\ ||\mathbf{e}||}{\max\ ||\dot{\mathbf{x}}||} \tag{2.1}$$

where $\mathbf{e}$ and $\dot{\mathbf{x}}$ denote the position tracking error and velocity vectors of the TCP, respectively. The lower the value of the indicator is, the better the control performance. Large maximum velocity and small maximum position tracking error are required for good performance values. This promotes rigorous control methods, as high velocities typically require large accelerations, under which an insufficient controller may induce large position tracking errors. The rationale for this performance indicator is given in more detail in [115].

Despite numerous studies on the free space motion control of hydraulic manipulators, force control has received less attention in the literature. Generally, the force control of robotic manipulators is a challenging task that requires rigorous handling of the underlying dynamics of the manipulator [106]. In addition, interaction dynamics with the environment affect the overall control results; thus, the dynamics of the environment should be considered [2, 3]. Most force control methods in hydraulics are derived either from the impedance control scheme proposed by Hogan [37] or the hybrid position/force control scheme proposed by Craig and Raibert [23]. The hybrid position/force control was applied to hydraulic manipulators [27], complemented with adaptive control [56], and with self-tuning position and force control [18]. Impedance control of a hydraulic excavator was proposed in [96] and an active impedance control of a hydraulic legged robot in [9]. Stability-guaranteed impedance control for compliant contact control with the VDC framework was proposed in [48], and more generally with both free-space and contact control covered in [49].

2.2 Control of Real-World Hydraulic Serial Manipulators

High-precision control of real-world hydraulic serial manipulators has received little attention in the literature. A distinct feature separating manipulators used in state-of-the-art research from those used in industrial applications is the type of hydraulic control valves responsible of controlling the actuators. Although state-of-the-art research is often conducted on hardware utilizing expensive high-bandwidth servo valves, industrial hydraulic manipulators almost exclusively rely on proportional control valves, which are characterized by slow spool dynamics and significant dead zones caused by positive spool overlaps. The design choice is endorsed by a lower price and more robust performance, as well as efficiency. The first two benefits are caused by vastly lower manufacturing tolerances, while the third benefit is because of the positive spool overlap enabling passive load holding.

Performance increases in real-world hydraulic manipulators require methods that can address the dynamics and nonlinearities of these kind of electro-hydraulic valves. Early attempts at the high-precision control of real-world hydraulic manipulators were reported in [85, 96], where a hydraulic excavator was controlled using position-based proportional derivative (PD) control complemented with dead zone compensation with satisfactory tracking performance. Pressure-compensated proportional valves are selected for closer inspection in this thesis. An early study on the modeling of pressure-compensated valves with nonlinear and linearized models was proposed by Wu et al. in [110]. Bak and Hansen proposed modeling and parameter identification of Danfoss PVG32 control valves [7]. Aranovskiy et al. proposed static nonlinearity inversion and velocity feedforward for the control of a forestry crane with pressure-compensated valves [5].

The theoretical background for dead-zone compensation and identification is discussed generally in [53, 91, 99]. Kivelä and Mattila proposed an adaptive method for valve dead-zone compensation [47]. Nurmi et al. proposed automatic feed-forward mapping of pressure compensated valves with significant dead zones using a Lyapunov stable nonlinear adaptive control in [74] and using a convolutional neural network (CNN) in [73]. Li et al. proposed a backstepping-based ARC method for dead zone compensation in [59].

Besides component-wise hard nonlinearities like valve dead-zone, hydraulic systems are constrained by the saturation of available hydraulic flow. The saturation of the flow can be considered analogous to saturation of torque, that is, electrical current, in electric manipulators. Dahl and Nielsen proposed torque-bounded control methods for electrical systems [24, 25] using a time-scaling approach for trajectory-following tasks. Wanner and Sawodny and Tremblay et al. proposed an optimization method using quadratic programming to satisfy the flow limitations in [105, 107, 108].

2.3 Teleoperation

Teleoperation has been studied extensively since the mid-1940s, when first mechanical pantograph mechanisms were developed for radioactive material handling. The mechanical design was soon replaced by electrical servomechanisms that enabled teleoperation over further distance away [88]. A wide range of applications from space applications to terrestrial systems [38, 89] has kept researchers interested in this subject for decades, even though teleoperation research has since polarized between space teleoperation with arbitrary and time-varying delays and terrestrial applications with more or less constant transmission times and low latencies. Especially now, in the advent of 5G cellular networks, time delays can be alternatively addressed for terrestrial applications [1]. For more comprehensive understanding of the various teleoperation control schemes and their respective histories, the readers are referred with the following reviews [38, 70, 86, 88, 89].

From the control theory perspective, teleoperation provides an interesting platform that requires sophisticated methods and a deep understanding to maintain the stability of the human–machine–environment interconnected closed-loop control system. Early teleoperation approaches modeled this system using a two port network scheme, for which readily available analysis tools from electrical systems could be applied [32, 79]. This approach addresses the control architecture without dealing with the actual controller design. To address the stability issues induced by a time delay, scattering operators were proposed for teleoperation systems with passive operator and environment [4]. The scattering operators enforced the passivity of the teleoperation system, combining this with a passive environment and operator that resulted in the passivity and, consequently, stability of the entire system. Similarly, wave variables were proposed to ensure passivity under a time delay [69]. Hannaford and Ryu proposed an energy based time-domain passivity control method for passivating the communication channel under time delay using a "passivity observer"–"passivity controller" pair [33].

In contrast to the passivity-based approaches following the two-port analogy, Lawrence suggested four-channel communication and cancellation of the dynamics of both the leader and follower subsystems through the controllers designed in the teleoperation channels [57]. Moreover, the trade-off between stability and transparency was explicitly shown. Yokohji and Yoshikawa pointed out that the four-channel approach enables perfect transparency, here given that the dynamics of both plants are known and that acceleration measurements are available [111]. Hastrudi-Zaad and Salcudean proposed local force-feedback loops to increase the stability and robustness against time delays [35]. In addition, the stability of four-channel approaches and the maximum achievable transmitted impedance were investigated from a passivity point of view [34]. The applicability of hydraulic systems was also considered. Zhu and Salcudean proposed independent adaptive control of both leader and follower subsystems [117], which fundamentally differed from the four-channel approach with respect to the communication channel design. Instead of performing inverse dynamics control within the communication channels, both the leader and follower subsystems were treated individually. The four communication channels were left to transmit the states (motion/force) of the opposing manipulators as motion/force tracking commands rather than direct control actions.

Teleoperation based on other approaches, such as $\mathscr{H}_\infty$ and μ synthesis [46, 58], sliding mode control [14], and adaptive/robust control [87] have also been proposed. Recent state-of-the-art research in teleoperation has been focusing on electrical manipulators in symmetrical 1:1 scale configurations, including multi-leader or multi-follower setups [60, 87, 90], shared control [92], or dealing with time delays [17, 30]. The methods for the teleoperation of hydraulic manipulators have mainly relied on linear control theory and system linearization [68, 75, 85, 96]. However, these methods have limitations in the teleoperation of complex, highly nonlinear, and asymmetric systems.

Learning from demonstrations (LfD) applications using teleoperation for the demonstrations has recently gained attention. LfD is an established technique in robotics, where a robot is taught to perform tasks by demonstrations given by a human teacher. The goal of the method is that the robot can perform the same tasks independently afterwards [6]. Teleoperated demonstrations have been successfully used for LfD applications, with promising results using 1:800 force scaling in [93] and 1:1 scaling in [36, 78].

2.4 Autonomous Secondary Breaking

Previous works concerning the further development and automation of secondary rock breaking systems are few, despite the numerous benefits and demand for such systems, as discussed in Chapter 1.1. Autonomous secondary breaking systems were first proposed in 1998 by two independent studies [22, 98]. Takahashi and Sano proposed boulder detection by using an image processing approach, while the localization of the boulders was performed using an assistive articulated laser [98]. Takahashi and Monden proposed a strain-gauge-based approach for automatic break instance detection [97]. Corke et al. proposed a nodding laser scanner that produced point clouds of the target scene and discussed the important features and requirements for an autonomous rock breaking system [22]. The following requirements were identified: closed-loop controlled breaker boom, a 3D sensing system, an autonomous decision-making system, and a teleoperation system for backup control. The study implied that with only limited human intervention required, one operator could monitor several booms at the same time. However, it was concluded that the technology for such system is “many decades from reality.”

The first teleoperated rock breaker was reported in [39]. A communication system was designed to control the manipulators from a surface control room, but the machine operation was kept in an open-loop manner. This approach is still widely used today. Duff et al. took a critical step toward creating a robotic rock breaker by introducing robotic functions, such as Cartesian control mode, automatic deployment and park, collision avoidance, and teleoperation over the internet [26]. Moreover, a mixed reality interface was developed to provide rich information to the boom operator. Boeing et al. presented a commercial system that is very similar to that proposed by Duff et al., with the exception of not having a machine-vision system to provide a mixed reality display to the operator [10]. Instead, teleoperation was performed using a live video feed. Integration with a higher-level mine automation system was also incorporated. Autonomous raking operations were studied in [42, 43, 94], where a small-scale mock-up was built to evaluate strategies for automatic boulder reorientation. More recently, autonomous breaker operation was reported in [52, 119] with field experiments in the Polkowice-Sieroszowice mine. The proposed system used a nodding laser scanner for visual perception of the environment and localization of boulders on the grizzly. The tactical procedures included both size reduction of oversizes material and raking operations. A reported success rate of 38% was achieved, with a successful attempt referring to a situation when the autonomous system was able to clean the grizzly after a load was dumped on it.

As a critical and necessary component for autonomous breaker operation, it is fitting to evaluate the recent developments of vision-based boulder detection. Takahashi and Sano proposed an early image-processing approach to detect boulders from a mono-camera imagery [98]. Corke et al. used a nodding laser scanner to generate point clouds in [22]. Fox et al. proposed the use of stereo cameras for boulder detection in [29], where an algorithm for an onboard rock shape analysis system was built for planetary rovers. Thurley and Ng proposed a watershed segmentation method for boulder segmentation from 3D data in [102], here with aim to estimate the fragmentation size distribution of blasted ore piles, expanding the concept to point clouds obtained with laser scanners in [101, 103]. McKinnon and Marshall studied the use of a ToF camera for automatic identification of large fragments in a pile of broken rocks [65]. Niu et al. proposed ToF cameras for boulder detection in a rock breaking application [72], but the selected camera had serious limitations in terms of resolution. Because of the observed limitations, Niu et al. proposed the use of stereo camera for the same application [71]. The proposed method incorporated the functionality of a state-of-the-art object detector "you only look once" version 3 (YOLOv3) [81] into a 3D detection pipeline for automatic boulder detection.

3 PROPOSED SOLUTIONS

This section reviews the contributions proposed in the publications from the perspective of solving the RPs. First, subsolutions for the individual RPs are discussed, eventually culminating in the discussion on the autonomous secondary breaking concept that involves the integration of these subsolutions.

3.1 High-Precision Control of the Hydraulic Secondary Breaker Boom

As reviewed in Chapter 2.2, high-precision control, here considered as high-precision trajectory tracking, and pursuit of state-of-the art control performance has relied on the performance of expensive high-bandwidth servo valves. Unarguably, the control laws become more manageable when complicated valve dynamics can be ignored and the valves are only considered by a set of fixed or adapted gains in the control design. However, arguments against servo valves can be made, and without a doubt, the necessity of proportional valves cannot be denied.

Practical applications, such as the breaker boom case studied in the current thesis, require robust and reliable components. The price of the components is also an important factor affecting component selection. Because of the much stricter manufacturing tolerances of servo valves, they tend to cost significantly more than their proportional valve counterparts. In addition to these expense concerns, spool lapping plays an important role within heavy duty manipulators, where the lifting of heavy loads is a common task. Critically lapped servo valves cannot be used to hold the loads in central spool position because of high leakage flows. For safety reasons, positive spool overlap is required to limit this leakage to a much slower pace. Besides safer operation, positive spool overlap may result in improved energy efficiency because no energy is required while the manipulator is stationary.

High-precision control using proportional valves requires more consideration because of the slow response of the main spool, hence causing additional nonlinearities. Moreover, hard nonlinearities, such as dead zone and output saturation, are often an issue. To properly address these issues, model-based methods incorporating the valve dynamics need to be developed in more accurate ways. Alternatively, some of the valve nonlinearities may be addressed by the valve design itself. Load-sensing systems and pressure compensators may be used to linearize and compensate for the response of control valves, despite varying loading conditions. A pressure-compensated valve may be regarded (approximately) as an ideal velocity source. However, some non-ideal variations in the flow rate may be observed due to rapid changes in loading conditions or changes in the oil viscosity that changes proportional to the oil temperature. With an accurately identified velocity feed-forward model, high-precision trajectory tracking of the valve-actuator pair can be achieved at a fraction of the computational burden of state-of-the-art model-based approaches [74]. However, these approaches are limited to trajectory tracking only and, therefore, are not suitable for force control applications.

Realizing high-precision control for the hydraulic breaker boom generally begins by evaluating the requirements for the control system, available instrumentation, robustness to uncertainties, and computational capabilities of the control computer. The requirement for closed-loop contact control is a major deciding factor that, if required, imposes strict prerequisites for the control system. In terms of stability, force control requires a rigorous design process that may extend to the modeling of the environment to achieve stable contact control [2, 3]. Publication I suggested an NMB control approach built on the VDC framework, here with specific attention paid to the dead zone cancellation and extending of the framework to cover pressure-compensated valves. The results suggest good trajectory and force-tracking performance, despite the low-bandwidth proportional valve. At cylinder space, maximum of 25 mm position error was observed while the cylinder was driven as fast as physically possible (0.2 m/s). This result is not exceptional, but during the making of P-III, an error in the joint measurement was identified, that caused non-existent dead-zone in the joint angle measurement, that affected the results of both P-I and P-II. If force control is not a necessity, a more practical control structure using a strong feed-forward and a complementary linear PD controller may achieve sufficient performance. Automatic velocity feed-forward identification was investigated in

[74], and this approach was utilized in P-II and P-III. With an accurately identified feed-forward mapping, a practical PD control can be used to correct uncertainties and improve tracking performance.

Regardless of the used control approach, the physical limitations of the controlled system need consideration, even before considering any control approach. In this regard, P-II proposed an approach to dynamically scale the trajectories to maintain velocity at an achievable level. This approach can greatly improve tracking performance, as evidenced by the results in P-II and P-III. Figure 3.1 illustrates a modular control architecture that includes the trajectory-scaling algorithm. The low-level manipulator controller is visualized as the next logical component, and its design may be altered based on the control objective. In P-I, an NMB controller was used, while P-II and P-III relied on PD control and velocity feed-forward mapping.

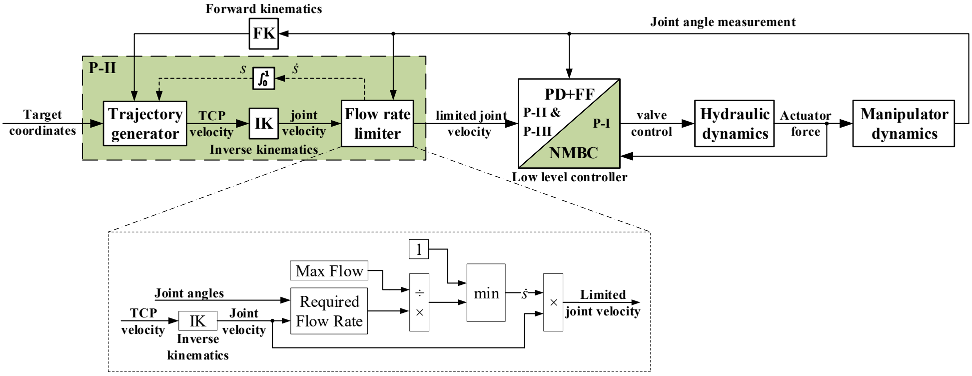

Figure 3.1 Overview of the modular control architecture.

To bring NMB control closer to practical applications with pressure-compensated proportional valves, an approach to address the pressure compensation and valve dead zones was discussed in P-I. However, the proposed approach does not address the complete model of the hydraulic valve; for example, the dynamics of the main spool and the pressure compensator are omitted. These simplifications may affect performance under rapid variations of loading conditions and control signals. Further development and inclusion of these nonlinearities in model-based feed-forward compensation terms are likely to yield more advanced performance.

3.2 Teleoperation

Teleoperation can be used to enable manipulation on a remote site, where direct operation may be uncomfortable, impossible to reach, or hazardous for a human operator. These kinds of environments may have high levels of radiation, be extraterrestrial, or be otherwise dangerous for human health. In addition, teleoperated systems may be used to scale human operations to micro- and macro-environments for accurate and nonfatiguing operations (e.g., teleoperated surgery or heavy material handling). In view of the secondary breaking application, the rationale for an intuitive teleoperation system is evident. Despite achieving a high level of autonomy in the secondary breaking, occasional situations when a human operator is required to take control of the system are unavoidable (e.g., during manipulator service, system/component malfunction, or a failure of the autonomous system). Some of these situations may require the actual presence of the operator, that is, line-of-sight teleoperation (e.g., service/malfunction), while others (e.g., manual breaking of a challenging boulder) may be safely performed remotely.

Bilateral teleoperation refers to an arrangement where motion and/or force information are transmitted both ways between the leader and follower manipulators. This system has the advantage that an operator can perceive the forces from the other side of the teleoperation system and use that information to assist in operation and decision-making processes. As reviewed in Chapter 2.3, bilateral teleoperation has been mainly studied from a control theoretical perspective with time delays and symmetrical systems, while asymmetric teleoperation of heavy-duty machinery has received little attention. Publications P-V and P-VI proposed transparent bilateral teleoperation of a hydraulic heavy-duty manipulator using an electric leader manipulator with arbitrary motion and force scaling; these studies can be used to evaluate the feasibility of this teleoperation approach on the control of the hydraulic secondary breaker system. Figure 3.2 displays the teleoperation system realized in Publications P-V and P-VI.

3.2.1 Experimental System

The control system for the teleoperation system is built on the foundation of the teleoperation scheme proposed by Zhu and Salcudean [117]; the study of Zhu and

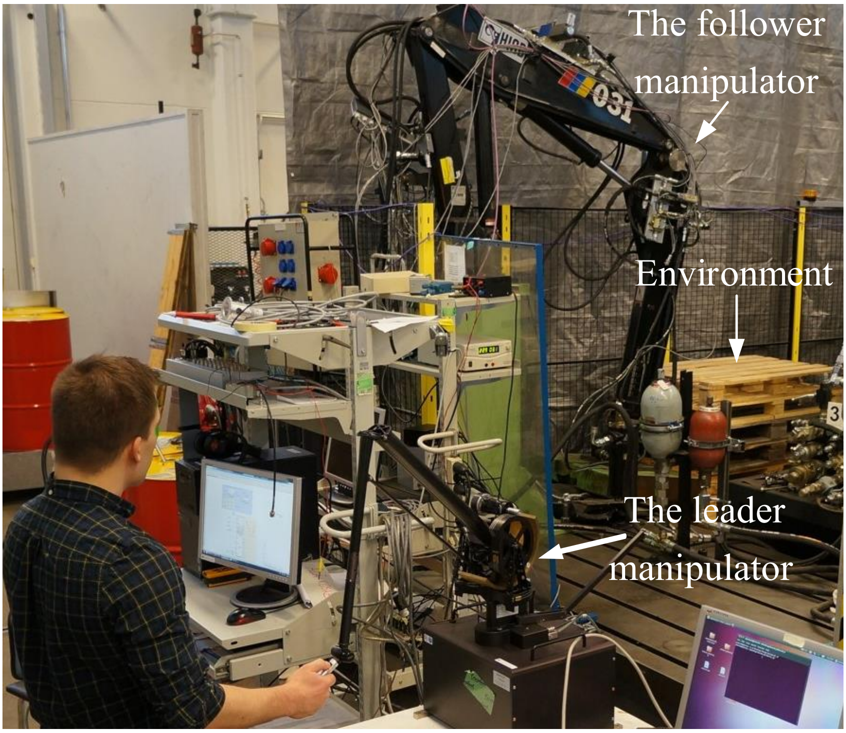

Figure 3.2 The experimental implementation of the bilateral teleoperation system.

Salcudean proposed a notorious change in the design against the state of the art of its time by addressing the teleoperation system as two independently controlled systems subject to independent parameter adaptation and local force-feedback, effectively enabling a modular design of the teleoperation system and teleoperation of notably dissimilar manipulators.

Figure 3.3 displays the system used in P-V and P-VI with the control structure arranged into the modular components of leader side and follower side, here in accordance with the scheme in [117]. The leader-side system includes the full-model-based adaptive control of the leader manipulator together with a dynamics model of the human operator, while the follower-side controller includes the dynamics of the environment. Communication between the manipulators consist of the position, velocity, and force signals of each manipulator, respectively. The controllers for both sides of the teleoperation system are designed and handled independently, even though in the publications, the control computations for these systems were performed under the same dSPACE real-time controller. In terms of modularity, the control system for the follower subsystem is based on the approach presented in [48] but with minor

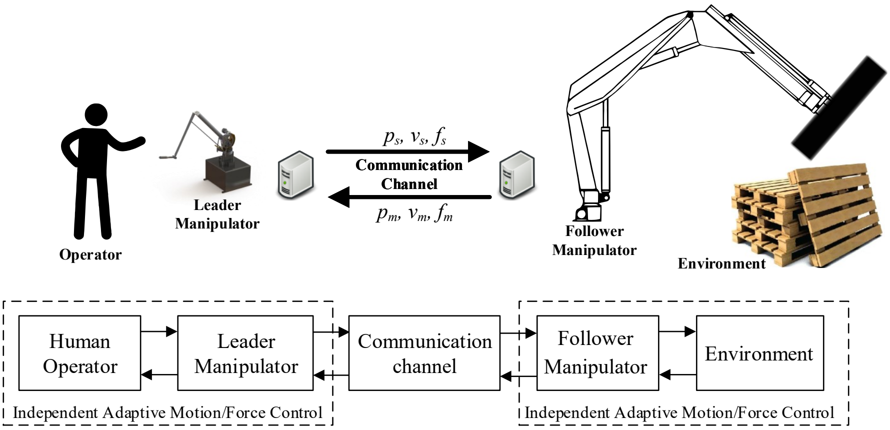

Figure 3.3 Conceptual illustration of the modular teleoperation system's architecture.

modifications.

The availability of force measurements is typically a fundamental requirement for a teleoperation system with force-reflection capabilities. However, in the scope of heavy-duty machinery, fragile force/torque sensors are typically avoided because of their poor robustness against impacts and overloading. Moreover, commercial haptic manipulators, which are typically used for teleoperation research, often lack these as well. Therefore, indirect force-estimation strategies are required to alternatively address the requirement for force measurement. A comprehensive survey of alternative force-estimation methods is presented in [31], and two distinct approaches are implemented for the controllers in P-V and P-VI.

The controller for the leader and follower systems include the following distinct subcomponents:

Leader side

- NMB control of the manipulator
- Including the model of the operator
- Exogenous force adaptation
- Force-sensor-less force estimation
- High-gain feedback control to compensate for parametric uncertainties

Follower side

- NMB control of the manipulator
- Parameter adaptation of the rigid body parameters
- Parameter adaptation of the fluid power parameters
- High-gain feedback control to compensate for parametric uncertainties

A more detailed visualization of the control scheme is presented in Figure 3.4. The diagram has the NMB controllers for both manipulators highlighted in blue, while the physical systems being controlled are highlighted in red. The difference between force-estimation strategies of the leader and follower manipulators is also visible in the diagram. Local processing of the teleoperation signals is performed in the immediate neighborhood of the communication channel on both sides.

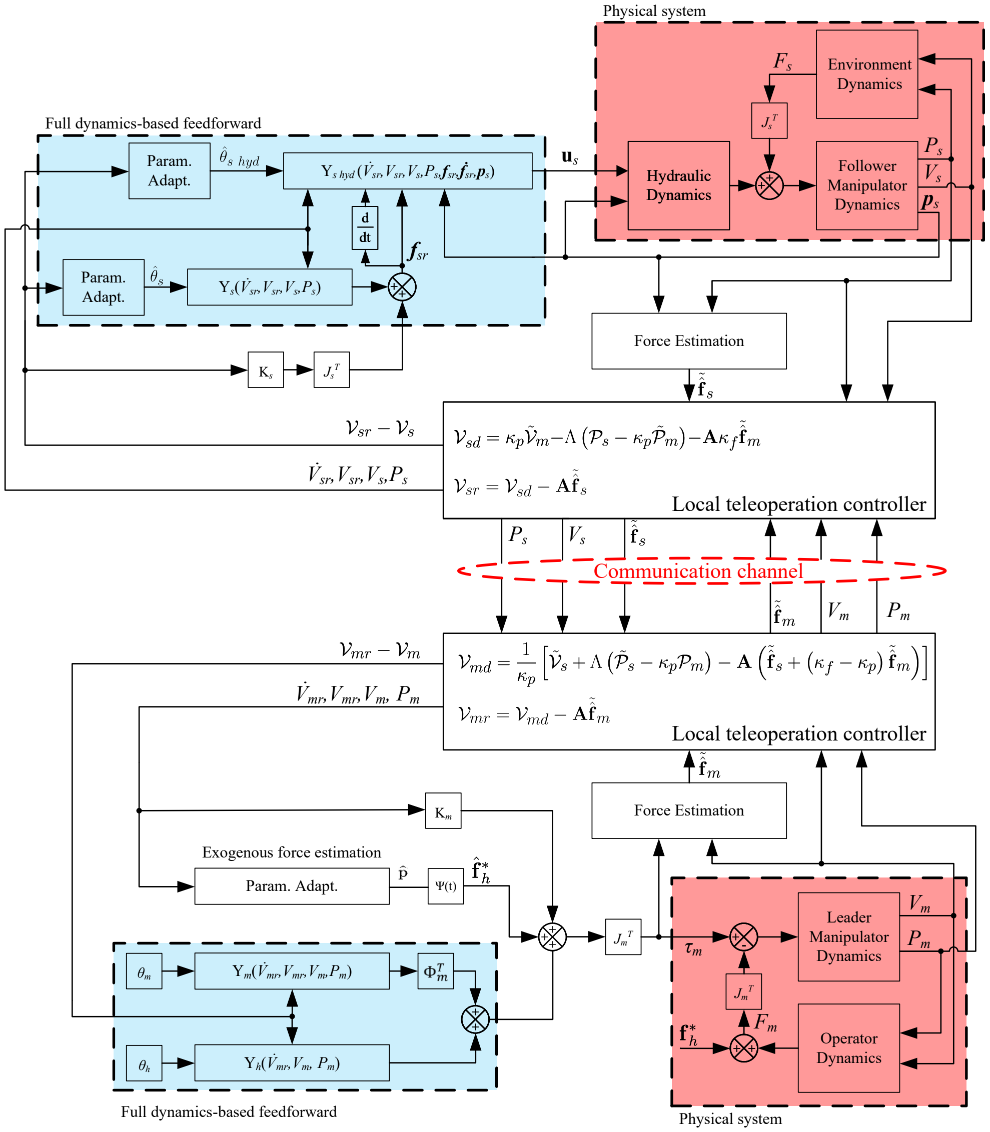

Figure 3.4 High-level control diagram of the bilateral teleoperation system.

3.2.2 Application to the Secondary Breaker Use Case

The discussed teleoperation method has great potential as a supplementary control method for use in the secondary breaker boom. As mentioned in the beginning of this section, autonomously operated systems require some kind of backup control method for occasional and unavoidable situations. If we consider a situation where the manipulator is unable to break a specific rock autonomously, manual control by a human operator is required to complete this task. For such situations, force-reflective teleoperation can be used to provide an intuitive means to operate the boom. The force-reflective scheme allows the operator to feel the surface of the oversized boulder and apply sufficient force against it to for successful breaking.

The proposed teleoperation approach imposes additional technical challenges and hardware requirements compared with the more traditional unilateral open-loop mannered teleoperation, where an operator only controls the velocity of individual actuators or–in the more advanced case–the tip of the manipulator. In addition to the hardware components required for the autonomous secondary breaker system, the force-reflective teleoperation scheme requires pressure measurements from all hydraulic pressure lines, as well as measurement of the supply pressure. Moreover, precise modeling of the manipulator (in the case of an OEM, all supplied manipulators) is required to obtain good estimates of the rigid body parameters although parameter adaptation should still be implemented to address unavoidable parametric uncertainties. Alternatively, parameter identification methods could be further explored (see [40, 41, 84, 95]). Besides modeling the manipulator, modeling the environment is also required to increase the performance of the teleoperation system. However, modeling rigid boulders in a cluttered scene with little prior knowledge of the environment and the interaction dynamics between the boulders and grizzly is a challenging task. Fortunately, the hydraulic impact hammer has a compliant structure that can be readily modeled and has a stabilizing effect on the contact dynamics with the rigid boulders by rendering the environment flexible to some extent.

To simplify the design process, the environment may be considered rigid, and compliance in the interaction with the environment is caused by mechanical compliance in the axial direction of the hydraulic impact hammer. The fact that this compliance is only present in the axial direction only makes this assumption valid when the manipulator is pushed against the boulders in the axial direction of the impact hammer. Modeling the environment when it comes to, for example, raking tasks, is more challenging. In a practical application, the teleoperation could be most efficiently used in the force-reflecting mode for realizing good contact against an oversized boulder. For stability reasons, the actual breaking process should be performed using a different controller due to the force spiking during hammer operation, that may induce instability.

Integration with the flow-bounded control scheme presented in Section 3.1 can be designed using the virtual constraints presented in Publication P-V. Artificially rendered virtual constraints for teleoperation have also been proposed in [13] in a three-channel teleoperation architecture. Virtual forces against the direction of motion can be applied linearly near the saturation of the hydraulic flow rate to prevent the operator from requesting motions that the manipulator cannot track. In addition, virtual forces can be used similarly as in P-V to limit the workspace of the secondary breaker and prevent collisions with fixed structures in the workspace.

In terms of time delay and the issues it may raise, Publication P-VI demonstrated the robustness of the proposed teleoperation method against time delay both in theoretical level and in practice by demonstrations. One-way time delay of up to 80 ms were used without significant loss of performance. If we consider teleoperation in an underground mine from a control room located at the surface to the crushing station at the bottom, such delay are not expected. Instead, in the private network of a mine, the delays are expected to be near constant within a couple milliseconds. However, if we were to consider teleoperation over longer distances over public internet, the delays are expected to grow and vary more. In such situations the delays between the operation site and control site need to be evaluated in advance and more development may be required. Moreover, safety concerns in such situations differ and safety systems for connection monitoring become more critical.

3.3 Autonomous Secondary Breaker Concept

This section presents the concept for an autonomous rock breaker system for grizzly applications. Development and testing have been conducted by keeping more general applicability in mind, but because of the limitations imposed by our testing facility, the full development and testing of other features was not feasible. The test breaker boom–RamBooms X88-540r–at the field test site at TAU is depicted in Figure 1.1.

The solution aims to address the following requirements identified for an autonomous rock breaker system:

1. High precision closed-loop manipulator control
2. Autonomous path planner and trajectory generator
3. Collision avoidance system
4. Backup control method
5. VPS

Besides these elements, more development is necessary for the commercialization of the technology. Communication and cooperation with the mine's automation system, for instance, is an essential feature that greatly enhances the capabilities of an autonomous breaker system. For instance, task scheduling and automatic retraction and deployment of the breaker boom on an approaching LHD-truck enhances the flow of material handling and can affect the productivity of other mine systems. In addition, the breaker system must have the capability to give a notification about blockages to prevent loaders from dumping into a full/blocked ore pass. Rigorous safety features, risk assessments, and protective measures for commercial product are also required but omitted in the scope of the current thesis.

The concept system that was built to evaluate the feasibility of the autonomous secondary breaker system is depicted in Figure 3.5, and it is discussed in greater detail in P-III. The individual components are only briefly discussed here. Motion control was already discussed in Chapter 3.1, and the teleoperation as a backup control method is discussed in Chapter 3.2. The remaining subsystems are presented in the next sections.

3.3.1 Visual Perception

The objective of the VPS is to identify, localize, and classify oversized boulders on the grizzly. The design of the VPS is constrained by several requirements imposed by the intended application. First, the application environment is very hash–dust and water mist are routinely present, and the system might be subject to wide temperature variations, depending on the mine's location. Moreover, inherent to rock breaking, fragments of rocks may fly in the air, occasionally hitting the perception device. For these reasons, the selected perception device, be it a camera, scanner,

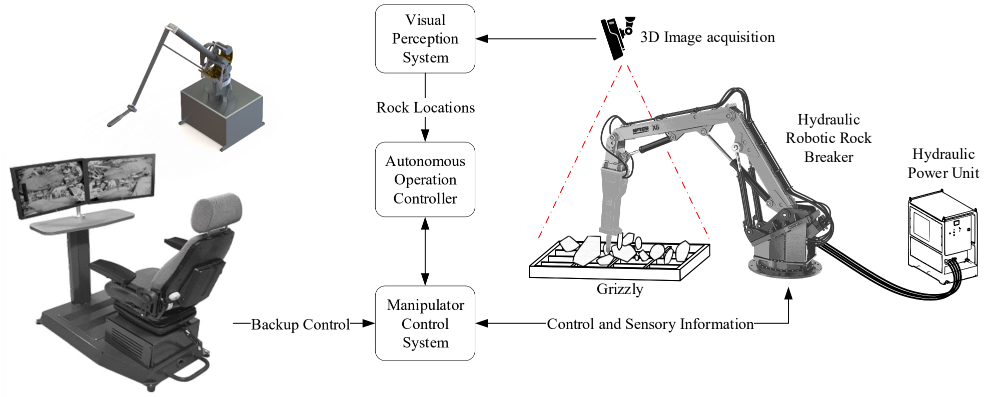

Figure 3.5 Modular deployment of the autonomous secondary breaker system's architecture and included subcomponents.

or something else, must be durable and robust against the elements and, to some extent, to external shocks. In addition, this is seen as a component that may require occasional replacement; therefore, inexpensive solutions are preferable.

Laser scanners [22, 52], stereo cameras [22, 43, 71], and ToF cameras [65, 72] have been proposed for boulder detection, and arguments between these methods have also been discussed in P-III and P-IV. VPS, utilizing a stereo camera and a deep-learning object detector, was proposed by Niu et al. [71], and that approach was utilized in P-III. The approach was successful at detecting and localizing boulders from the grizzly but had several practical limitations. The object detection from mono images was performed using a single-shot object detection algorithm called YOLOv3 [81]. An average precision of 97.5% at a intersection over union (IoU) threshold of 0.75 was reported for boulder detection with the trained network. However, the data gathering took over several weeks (not to mention the time required for manually labeling the data), and yet, the system could only operate within specific environmental illumination conditions because of the limited training data.

Publication P-IV explored the use of a modern, relatively high-resolution ToF camera for boulder detection. The Blaze 101 ToF camera from Basler AG was selected for the study because of its relatively low price (approximately 1,500€), good protection against the elements (IP67), connectivity (GigE Vision), and resolution (640x480). For these reasons, it is an attractive choice for the rock breaker application. A clustering algorithm was developed in P-IV that requires no time-intensive training or data gathering but that can reach the same accuracy as reported in [71]. The clustering algorithm can be described as a seeded watershed algorithm, which is an established method in image processing applications but one that has not been applied to point clouds. The boulder detection results are demonstrated in Figure 3.6.

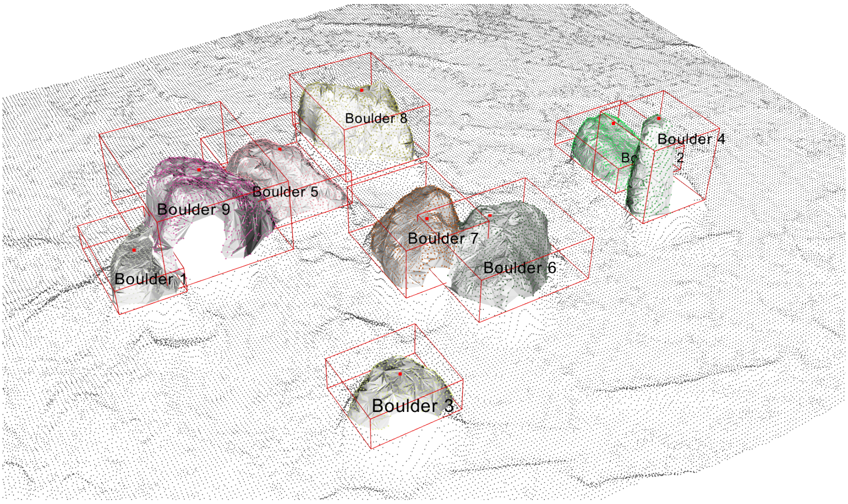

Figure 3.6 Boulder detection using the segmentation approach proposed in P-IV. Individual boulders are drawn in various colors, and bounding volumes are drawn around each boulder. The break locations proposed by the VPS are marked with red dots.

The VPS can be used to provide an estimation of the difficulty of break attempts for each identified boulder by analyzing the size and shape of the boulders. Publications P-III and P-IV discussed the break difficulty issue, and several features were suggested for difficulty estimation. The relative flatness around the proposed break position, the height of the boulder compared with its cross-sectional area, and the horizontal distance between the perceived centroid of the boulder and break position were identified as features that could be used for the difficulty estimation. Based on the estimated difficulty, the autonomous system may either attempt to break the boulder or reorient it to a better position for breaking.

3.3.2 Autonomous Operation Toolbox

A key to the successful deployment and operation of any autonomous system is a rigorous operational toolbox comprising operation strategies for the different situations the system may encounter. In the case of the autonomous rock breaker system, the following operational strategies are identified as essential features that need to be implemented for the autonomous system:

1. Autonomous breaking strategy, including break instance detection
2. Individual boulder reorientation
3. Automatic deployment and retraction of the boom
4. Raking and grizzly cleanup
5. Alert and request manual operation when unable to proceed autonomously

In addition, recovery strategies, safety features, and condition monitoring systems are important features for any reliable commercial systems, but these are not discussed in the scope of this thesis. The operational pipeline for the autonomous breaker system is depicted in Figure 3.7.

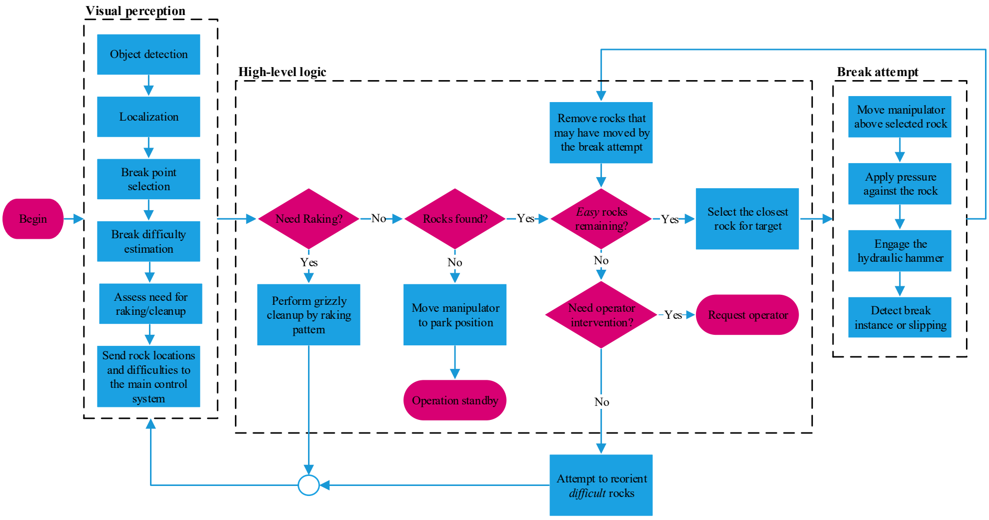

Figure 3.7 Operation pipeline for the concept of an autonomous breaker system.

The autonomous break strategy includes a determination of the break order for the detected boulders, manipulator control during a break attempt, and detection of either the break instance or loss of contact with the boulder. The manipulator control during a break attempt is an interesting topic, and the solution provided in the current thesis has room for improvement. The operation of the hydraulic impact hammer causes pressure spiking and vibrations in the joints, which may induce instability under high-gain closed-loop control. Therefore, the manipulator control during break attempts is switched to feed-forward control only, while the sensory data are still used for monitoring the state of the manipulator and deducing external events, such as loss of contact and the break instance. The control mode is switched right before the hydraulic impact hammer is engaged, and the closed-loop control is engaged again, after a break instance is detected or the manipulator's TCP has descended below a set threshold level. Force-estimation using inverse dynamics and pressure monitoring was considered in P-III, but a more simplistic approach using only acceleration measurement was found capable of providing accurate break instance detection.

For difficult boulders, for example, boulders without sufficiently large flat surfaces, a strategy for boulder reorientation may be required for successful operation. Graspless manipulation using the chisel of the breaker tool has been studied [42, 43, 94]. The contact point with respect to the center of the mass of the target boulder is a critical factor that affects the manipulation outcome. Contact above the center of mass results in tumbling when the boulder is pushed, here given sufficient friction with the grizzly.

Grizzly cleanup by raking may occasionally be a useful approach when smaller boulders are stuck on the grizzly [52, 119]. Such situations may occur immediately after an LHD-truck has dumped boulders on the grizzly. Smaller boulders can be assisted through the grizzly by raking them through the fragmented rock mass with the chisel. After smaller rocks are cleaned from the grizzly, the system can proceed with autonomous breaking of the oversized boulders. The need for raking can be estimated using the VPS, but such an approach has not been discussed in P-III nor in P-IV.

Unavoidably, the system will encounter situations where it is unable to break all boulders from the grizzly within the time frame between load dumps. For these situations, different approaches need to be designed, and this may require cooperation with the mine's automation system. In addition, varying procedures may exist between mines. In these situations, the rock breaker may, for instance, request manual operation, attempt to clear the remaining boulder to the side to allow dumping of a new load, or request the incoming loader to wait until the operation is finished.

4 DISCUSSION

This chapter discusses the research problems defined at the beginning of the doctoral work and summarizes how these problems have been dealt with. After discussing the RPs, conclusions are drawn for the summary part of this thesis.

4.1 High-precision control (RP-I)

> *Can the secondary breaker boom be retrofitted (with minimal modifications) for high-precision control using the existing control valves?*

The first research problem involves the high-precision control of the commercial RamBooms breaker boom. In the scope of the current dissertation, two approaches are considered. First, publication P-I explored the extension of a state-of-the-art NMB control method–an established method for laboratory condition manipulators–into an industrial manipulator with pressure-compensated proportional valves. Accurate motion and force tracking of the controlled system were reported in the study. However, the advanced control approach has its drawbacks. First, it requires pressure measurement of all the line pressures in the system. Second, the velocity and acceleration of each rigid link must be known, and in practice, this often involves differentiation from position measurement, which induces delay and noise to these signals. Third, precise modeling of the boom is required to obtain accurate dynamic parameters for the model-based controller. The third issue may be addressed with adaptation and parameter identification.

Reasonable control performance may also be obtained with alternative approaches, as evidenced by publication P-II. A critical issue affecting control performance with hydraulic manipulators is limiting the actuator velocities based on the available flow rate. The algorithm proposed in publication P-II proved capable of addressing this issue with significantly improved motion-tracking performance. Moreover, the results of P-II successfully demonstrate that when the capabilities of the pressure compensated valves are harnessed using a strong velocity feed-forward control complemented with the PD feedback, a relatively high-precision control of the hydraulic manipulator can be achieved with a relatively simple control strategy.

4.2 Robust boulder detection (RP-II)

> *Can time-of-flight cameras be used to achieve robust boulder detection in harsh conditions?*

As evidenced by publication P-III, the robustness and reliability of the boulder detection system could be further improved. Changing weather and illumination was a serious issue with the deep-learning-based approach, which would have required more data from different scenarios to perform more robustly, despite the already huge data set that had required several weeks to be gathered and then manually labeled.

For a more robust method for use in the visual perception task, publication P-IV explored a ToF camera for the application. The proposed camera was robust against the environments and provided sufficiently high spatial resolution and low noise output. A clustering method proposed in the publication for the boulder detection task achieved similar performance as the deep-learning-based approach, but it does not require any training and is immune to changes in ambient lighting.

4.3 High-level control for autonomous operation (RP-III)

> *What are the most critical components for realizing a conditionally autonomous breaker system in a grizzly application, and how should those components be managed at a high level? What are the most critical operations that need to be addressed by the tactical operation toolbox?*

Publication P-III described an end-to-end solution for an autonomous secondary breaker capable of fully autonomous operation under certain circumstances. The achieved break pace of 3.3 break attempts per minute and an average success rate of 33% indicate feasibility of the concept. The publication described step by step each subsystem, its calibration, and the integration into the final concept system. Moreover, suggestions for future work and improvements are provided based on the observed shortcomings during the experiments. The designed system was capable of breaking random multi-layered rock piles in the experiments at a pace comparable to an actual operator, although the achieved success rate fell short of our more ambitious goals. Yet the built concept system can be regarded as a successful experiment, verifying the research question.

4.4 Teleoperation (RP-IV)

> *Is stability-guaranteed force-reflective bilateral teleoperation feasible for hydraulic multi-DoF manipulators? Could such a system be leveraged for controlling industrial manipulators, for example, as a backup method? Unavoidably, an autonomous system may require a human operator to occasionally take control of the system. Can the same teleoperation interface be augmented with artificially rendered constraints and forces to assist and guide the operator?*

The objective of designing a bilateral force-reflective teleoperation system was met successfully in publications P-V and P-VI on a laboratory condition hydraulic manipulator and commercial haptic device. Given an accurate model of both manipulators, the human operator and the environment, a teleoperation system can be realized. As a backup control method, it is highly advanced technology, and commercial adaptations will likely seek more traditional and elementary approaches. However, technological readiness exists, and it has been shown capable in laboratory conditions.

The use of virtual fixtures as a method for limiting the workspace of the follower manipulator was investigated in publication P-V. It was found capable of providing intuitive feedback to the operator via the force-reflective teleoperation interface, and the experimental results proved it can be successfully applied along with physical constraints.

4.5 Levels of Autonomy and Safety Considerations

The LoA for on-road motor vehicles has been defined into a six-level scale in [100]; no driving automation (level 0), driver assistance (level 1), partial driving automation (level 2), conditional driving automation (level 3), high driving automation (level 4), and full driving automation (level 5). From these levels, all but the last two require human supervision and an alert operator ready to take control if the autonomous driving system encounters problems. A level 3 autonomous system is able to perform autonomously under most driving tasks, and the machine has the capability to monitor the driving environment comprehensively. A level 2 autonomous system may have similar capabilities as a level 3 system, but the responsibility of monitoring the environment is left predominantly to the driver. Tesla's full self-driving autopilot is an example of a level 2 autonomous system [67]. A vehicle with, for example, a cruise control qualifies as a level 1 autonomous system.

On-road vehicles intended for personal transportation are subject to significantly dissimilar intended use compared with off-road heavy machinery, for which requirements and safety considerations vary greatly. With automation rapidly proceeding, machine safety requirements and standards have been revised to support and manage these rapid changes [104]. Safety requirements and the machine system safety of autonomous and semi-autonomous earth-moving and mining machinery is discussed in ISO 17757 [28]. However, its focus is strongly on mobile work machines, while stationary machinery, for example, the rock breaker boom, remains a niche application. More suitable requirements for the proposed application can be sought from the field of robotics, which already has established practices in terms of autonomy. Relevant standards for the machine safety of industrial robots that may partly be applied in the case of breaker booms are ISO 10218-1 and ISO 10218-2 [82, 83].

The current industry standard of secondary rock breaker systems remains mainly at level 0 autonomy, but rapid advancement is foreseen. The current doctoral work, which was conducted over the last three years, began with an ambitious goal of producing a highly autonomous secondary breaker concept. The robotic rock breaking application itself is ripe for automation, and the technological readiness has been clearly demonstrated in this thesis and its accompanying publications. Key to successful implementation lies in the system's ability to perform independently, minimizing the amount of required operator intervention. The added benefit of system automation can be seen in the reduced wear and tear of the equipment. Machine operators may occasionally abuse the machine by using it in ways that cause excessive wear to the joints and the hammer (e.g., use of the hydraulic hammer with non-axial loads, having a hydraulic cylinder at its mechanical stop while hammering, using the manipulator's momentum to push rocks sideways, etc.). Through smooth trajectories, precise pose control, and high-precision motion control, reduced wear can be expected, thus increasing availability and the machine's economic value proposition.

4.6 General Applicability

The significance of the developed methods extends beyond the secondary breaking application. The methods developed in P-I and P-II can be utilized widely in a class of industrial hydraulic manipulators in, for example, forestry, mining and construction, agriculture, and material handling industries. The flow-bounded velocity scaling approach is especially useful now, a time when many traditionally manually operated serial manipulators are being redesigned or retrofitted for robotic control. The possibility to scale either velocity along a trajectory or during resolved rate control is an inherent feature of the scaling algorithm.

The concept design of P-III has applications besides stationary applications in, for example, mobile breaker systems. The hydraulic impact hammer is often attached to an excavator for size reduction of oversized material that cannot be transported in its current state. In addition, boulders may occasionally spontaneously detach from the walls of tunnels or open-pit mines. Again, if these boulders are too large for transportation, they need to be broken on-site (see Figure 4.1). In this application, the results of P-III can be used as a foundation to extend the concept for mobile manipulators. Using an excavator-mounted perception system, boulders can be localized relative to the mobile manipulator. The VPS developed in P-IV could be directly applied to this application. Moreover, the setup could be extended for an eye-in-hand setup, where the camera is mounted on some point of the boom.

The teleoperation system developed in P-V and P-VI represents significant advancement toward effective teleoperation control of dissimilar leader–follower systems by enabling the use of LfD (or supervised learning) approaches on heavy-duty manipulators. Teleoperation is seen as a key enabling technology for the safe use of LfD-type methods on larger scale manipulators that cannot be taught by kinesthetic teaching. The author's vision is that in the future, large manipulators can be taught to perform various tasks with the same ease as programming light weight arms using LfD methods with their built-in force/torque feedback-enabled kinesthetic teaching. In addition to applications toward LfD-methods, publications P-V and P-VI laid down

Figure 4.1 Hydraulic impact hammer mounted on an excavator in an open-pit mine.

an experimentally verified control theoretic foundation that can be applied in a wide variety of industrial applications of teleoperation of arbitrary sized manipulators intuitively and safely over large distances.

5 CONCLUSIONS

This thesis has developed significant new methods for increasing the automation level of the current secondary breaker systems in mines. The conducted work toward autonomous secondary breaking culminates in a concept system that has been evaluated with real-world field experiments in a relevant mock-up environment. As summarized in Chapter 4, the RPs were successfully answered by the accompanying publications. Publications P-I–P-III addressed **RP-I** by implementing high-precision control systems for the studied hydraulic breaker system. Publication P-IV successfully implemented a ToF camera for the boulder detection task, verifying **RP-II**. Publication P-III demonstrated the autonomous secondary breaker concept and developed the required operation strategies considered in **RP-III**. A teleoperation system is seen as a crucial feature to complement the autonomous breaker system because unavoidably, occasional situations when a human operator is required will arise. Publications P-V and P-VI developed a stability guaranteed full-dynamics-based teleoperation system capable of controlling hydraulic heavy-duty manipulators, thus providing a solution to **RP-IV**.

In view of the future commercialization of the developed technology, several challenges remain. Sub-component calibration and system integration, a focused topic in P-III, was performed rigorously and with extreme caution to achieve the highest possible accuracy. However, performing such rigorous calibration on-site for each production machine would require several skilled technicians and impose great costs. In addition, the extrinsic calibration of the VPS is a delicate process that needs repeating after the slightest movement of the camera system. Because the camera is seen as a part that might require occasional replacement, this is an important issue.

To address these identified shortcomings, future research should focus on developing automatic methods for calibration and system integration. Automatic calibration methods should be investigated while also acknowledging a compromise between accuracy and less time-consuming calibration methods. In addition, the inevitable manipulator wear should be taken into consideration (although reduced wear is expected from using the autonomous system). Metrics and methods to accurately estimate and evaluate the wear should be designed to determine safe operation limits in terms of the wear level. Automatic perception system calibration and registration with the manipulator's coordinate system should be investigated. This type of method could be used occasionally to verify the accuracy and correctness of the VPS. For instance, using point cloud registration methods, extrinsic calibration could be achieved automatically after camera replacement.

In addition, future research should focus on extending the operational toolbox to cover raking and boulder reorientation operations. Multi-camera setups for more comprehensive visual perceptions are also seen as a promising way to improve the performance of the VPS and avoid situations where the manipulator occludes the view. Importantly, future experimental research in an actual operating environment, preferably in an operational mine, is crucial for enabling rapid prototyping and evaluation of alternative approaches for increased performance, in terms of success rate, breaking pace, and the handling of challenging situations that require, for example, the raking or reorientation of challenging boulders.

The conducted research on the teleoperation of a completely force-sensorless dissimilar leader–follower system is a significant contribution toward the practical teleoperation of heavy-duty machinery. This research can be seen as a key enabler when it comes to, for example, LfD approaches on industrial heavy-duty machines, where common kinesthetic teaching is not an option because of physical limitations and safety concerns. The technical feasibility of the control scheme has been clearly shown in publications P-V and P-VI. It is also worth noting that terrestrial applications, which are typically overlooked by teleoperation researchers, far outnumber the possible applications of space teleoperation (in terms of the number of applications, not price per setup). Now, in the era of 5G for wireless transmission and fast optical networks for wired communication, time delays, which have been a strongly focused on topic among teleoperation researchers, can be alternatively addressed for most terrestrial applications.

6 SUMMARY OF PUBLICATIONS

This chapter summarizes each publication of the current thesis and clarifies how each publication addresses the research problems, along with how they each build up to form the theoretical background for the concept of an autonomous secondary breaker. The high-precision control of the retrofitted commercial breaker boom was discussed in P-I and P-II, with special attention given to the applicability of real-world hydraulic manipulators with proportional control valves. Visual perception and detection of the boulders using a ToF camera were discussed in P-IV, while integration and testing of the first concept autonomous breaker were discussed in P-III. The field experiments were performed using the VPS designed in [71], and the method in P-IV was designed later. Force-reflective bilateral teleoperation was considered in P-V and P-VI, with an advanced state-of-the-art control system and laboratory condition manipulators. The modular teleoperation system utilized an existing manipulator control design proposed in [48] for the follower manipulator.

6.1 Summary of P-I: Model-based Control of a Pressure-compensated Directional Valve with Significant Dead-Zone

This publication discussed applying the glsvdc approach for hydraulic manipulators equipped with pressure-compensated electro-hydraulic control valves with a static output dead zone. The aim was to explore the applicability of state-of-the-art control methods for non-laboratory equipment, thus enabling wider acceptance and use in industry. The special challenges addressed in this publication are related to the NMB control of the proportional control valve. The pressure compensator was modeled as an ideal compensator, with a constant pressure over the valve control edge, until the load pressure starts to reach the supply pressure. The dead zone was identified manually for both directions.

The results indicate accurate motion and force tracking at a sinusoidal trajectory, without chattering of the control signal around the dead zone. Maximum position error of approximately 20 mm was observed on a sinusoidal trajectory driven at the manipulator's maximum velocity. This result is promising in view of the RP-I and validates the feasibility of the used NMB control method with nonlaboratory equipment.

6.2 Summary of P-II: Flow-Bounded Trajectory-Scaling Algorithm for Hydraulic Robotic Manipulators

This publication discussed a flow-bounded trajectory-scaling algorithm that considers the limited capacity of the hydraulic supply unit. The constrained maximum volumetric flow rate of the supply unit is a much-overlooked issue in the control of hydraulic machinery. A simple solution for the problem is to globally limit the actuator velocities to a relatively low velocity to avoid too fast motions that would require more flow than what the supply can produce. To better utilize the system capabilities, a method that scales trajectories and motion inputs was designed. The approach was inspired by research on torque-bounded minimum time trajectory designs and has similarities to them. The proposed algorithm can be used either to scale trajectories or manually control the inputs in the resolved rate control mode.

The design was validated with simulations and experiments on the rock breaker boom using a square trajectory. The experimental results indicate significant improvement regarding the motion tracking performance when using the algorithm. The motion control system was designed using automatically identified velocity feed-forward mappings for each valve-actuator pairs using the adaptive approach proposed by Nurmi and Mattila [74]. The feed-forward control was complemented with linear PD-feedback control on the cylinder space. The maximum error on a Cartesian square trajectory was reduced from about 461 mm to 71 mm with the trajectory-scaling algorithm. The results indicate that accurate motion tracking of the rock breaker boom can be achieved using a practical control approach together with the identified feed-forward mappings; thus, these results speak for **RP-I**. The proposed algorithm can be also applied to more advanced control systems, such as that proposed in P-I.

6.3 Summary of P-III: Autonomous Robotic Rock Breaking Using a Real-time 3D Visual Perception System

This publication realized the concept autonomous rock breaker system that was the end goal of the work undertaken for this thesis. The paper discussed in detail the original problem and use case we aimed to perform autonomously, described the design of each subcomponent of the concept system, and presented experimental results with the built system. The concept included the design of the manipulator control system, the VPS, and the decision-making framework for autonomous operation. In addition, comprehensive calibration of each subsystem was performed prior to the experiments. The experimental system was built outdoors in a field test environment at the mobile hydraulics laboratory at TAU.

The developed system was evaluated with experiments on autonomous rock breaking operation lasting over 45 minutes in total. The results indicate feasibility of the concept with a 34% success rate of break attempts and a pace of 3.3 break attempts per minute, answering **RP-III**. Control performance of the manipulator was improved from the results in P-II, and a maximum position error of about 58 mm was reported on a 3D trajectory, which is more complex than that in P-II. The width of the manipulator's blunt tool is approximately 130 mm, thus rendering the achieved accuracy more than sufficient. After the experiments, a reflection on identified shortcomings of the first concept system were reported, including a discussion on the need for a more sophisticated tactical layer for the autonomous operation that could react and cover more of the most typical situations, along with having the skills to proceed with them.

6.4 Summary of P-IV: Robust Rock Detection and Clustering with Surface Analysis for Robotic Rock Breaking Systems

This publication aimed to solve some of the problems identified in P-III regarding the robustness of the deep-learning-based VPS. Instead of the stereo camera used in P-III, a ToF camera was used to record a data set of boulders in various configurations on the ground. Then, segmentation of the resulting point clouds was performed using various readily available methods of the point cloud library (PCL) to detect and localize each individual boulder in the captured scene. The available segmentation algorithms were used as benchmark methods for a novel segmentation method specifically designed for the boulder detection application. The proposed algorithm outperformed the benchmark methods in our 20-scene data set recorded for this study, and its performance (97.4%) was on par with the deep-learning-based approach previously used. However, this approach does not require any time-consuming data gathering and labeling for training the detector, only some fine-tuning of a few control parameters. Environmental illumination does not affect the performance of the ToF camera, and it is tolerant to a wide range of ambient temperatures, dust, and rain.

In addition to the segmentation algorithm, this paper proposed a novel approach to determine suitable break location for each of the detected boulders based on their geometric conditions. Moreover, a method to estimate the break difficulty for each boulder was proposed. This information can be used to determine whether a boulder should be reoriented to a better position before a break attempt. The paper addressed the issues identified during experiments of P-III and answers to **RP-II** and in part to **RP-III**.

6.5 Summary of P-V: Bilateral Teleoperation of a Hydraulic Robotic Manipulator in Contact with Physical and Virtual Constraints

This publication acted as a preliminary study for the bilateral teleoperation of an asymmetric leader–follower system. The teleoperation control was designed between a commercial Phantom Premium 3.0/6DOF–haptic manipulator and a heavily retrofitted Hiab-031 hydraulic serial manipulator. The control system was built on the VDC framework, but a stability analysis was not provided. A special focus in this publication was the inclusion of artificially rendered virtual constraints on the workspace of the follower manipulator. Their use was investigated as a method to guide the operator and limit specific areas of the workspace. The results indicated the feasibility of the method and verified its usefulness. This publication is directly related to **RP-IV**.

6.6 Summary of P-VI: Force-Sensor-Less Bilateral Teleoperation Control of Dissimilar Master-Slave System with Arbitrary Scaling

This publication presented a bilateral teleoperation system comprising of a hydraulic follower manipulator and an electric leader manipulator. The control design was built using the modular VDC framework for the leader and follower manipulators, and the control system for the follower manipulator was repurposed from [48] with only minor modifications. The work described in this publication was continuum of the authors' preliminary study in [55]. The major work in this paper was related to the interconnected control design of the leader manipulator and human operator. The control design included force-sensorless force estimation of the leader manipulator through a direct inverse dynamics approach, with a solution to address the algebraic loop formed around the actuation and the force estimation. The exogenous intention force of the human operator was adapted, and a framework for a more comprehensive design of the intention force estimation was discussed using, for example, muscle activation measured using electromyography. The stability of the entire control system can be guaranteed under arbitrary motion/force scaling and a time delay. The experimental results verify the effectiveness of the proposed teleoperation scheme with good motion and force tracking between the teleoperation system. Force scaling up to a factor of 800 and position scaling up to a factor of 4 between the manipulators were used in the experiments. The results verify the feasibility of high-precision bilateral teleoperation of hydraulic manipulators using state-of-the-art control methods and equipment, thus answering **RP-IV**.

REFERENCES

[1] A. Aijaz, M. Dohler, A. H. Aghvami, V. Friderikos and M. Frodigh. Realizing the Tactile Internet: Haptic Communications over Next Generation 5G Cellular Networks. *IEEE Wireless Communications* 24.2 (2017), 82–89. ISSN: 1536-1284. DOI: `10.1109/MWC.2016.1500157RP`.

[2] C. H. An and J. M. Hollerbach. Dynamic Stability Issues in Force Control of Manipulators. *1987 American Control Conference*. 1987, 821–827. DOI: `10.23919/ACC.1987.4789427`.

[3] C. H. An and J. M. Hollerbach. The Role of Dynamic Models in Cartesian Force Control of Manipulators. *The International Journal of Robotics Research* 8.4 (1989), 51–72. DOI: `10.1177/027836498900800403`.

[4] R. Anderson and M. Spong. Bilateral control of teleoperators with time delay. *IEEE Transactions on Automatic Control* 34.5 (1989), 494–501. DOI: `10.1109/9.24201`.

[5] S. Aranovskiy, A. Losenkov and C. Vázquez. Position control of an industrial hydraulic system with a pressure compensator. *22nd Mediterranean Conference on Control and Automation*. 2014, 1329–1334. DOI: `10.1109/MED.2014.6961560`.

[6] B. D. Argall, S. Chernova, M. Veloso and B. Browning. A survey of robot learning from demonstration. *Robotics and Autonomous Systems* 57.5 (2009), 469–483. ISSN: 0921-8890. DOI: `10.1016/j.robot.2008.10.024`.

[7] M. K. Bak and M. R. Hansen. Modeling, performance testing and parameter identification of pressure compensated proportional directional control valves. *Proc. of the 7th FPNI PhD Symposium on Fluid Power, June 27-30, 2012, Reggio Emilia, Italy*. 2012, 889–908. ISBN: 978-88-7559-069-7.

[8] M. M. Bech, T. O. Andersen, H. C. Pedersen and L. Schmidt. Experimental evaluation of control strategies for hydraulic servo robot. *2013 IEEE International Conference on Mechatronics and Automation*. 2013, 342–347. DOI: `10.1109/ICMA.2013.6617942`.

[9] T. Boaventura, G. A. Medrano-Cerda, C. Semini, J. Buchli and D. G. Caldwell. Stability and performance of the compliance controller of the quadruped robot HyQ. *2013 IEEE/RSJ International Conference on Intelligent Robots and Systems*. 2013, 1458–1464. DOI: `10.1109/IROS.2013.6696541`.

[10] A. Boeing. A Remotely Operated Robotic Rock Breaker with Collision Avoidance for the Mining Industry. *30th International Symposium of Automation and Robotics in Construction and Mining (ISARC 2013) Proceedings*. IAARC, Aug. 2013, 875–884. ISBN: 9781926872162. DOI: `10.22260/ISARC2013/0095`.

[11] A. Bonchis, P. Corke and D. Rye. Experimental evaluation of position control methods for hydraulic systems. *IEEE Transactions on Control Systems Technology* 10.6 (2002), 876–882. DOI: `10.1109/TCST.2002.804128`.

[12] F. Bu and B. Yao. Observer based coordinated adaptive robust control of robot manipulators driven by single-rod hydraulic actuators. *Proceedings 2000 ICRA. Millennium Conference. IEEE International Conference on Robotics and Automation. Symposia Proceedings (Cat. No.00CH37065)*. Vol. 3. 2000, 3034–3039 vol.3. DOI: `10.1109/ROBOT.2000.846488`.

[13] W. Bu, G. Liu and C. Liu. Online generation of virtual fixture for bilateral teleoperation based on intention recognition. *2016 International Conference on Advanced Robotics and Mechatronics (ICARM)*. 2016, 122–126. DOI: `10.1109/ICARM.2016.7606906`.

[14] P. Buttolo, P. Braathen and B. Hannaford. Sliding Control of Force Reflecting Teleoperation:Preliminary Studies. *Presence: Teleoperators and Virtual Environments* 3.2 (May 1994), 158–172. DOI: `10.1162/pres.1994.3.2.158`.

[15] K. Casteel. Underground Haulage Equipment Trends. *Engineering and Mining Journal* 209.3 (Apr. 2008), 58–60. ISSN: `0095-8948`.

[16] P. H. Chang and S.-J. Lee. A straight-line motion tracking control of hydraulic excavator system. *Mechatronics* 12.1 (2002), 119–138. ISSN: 0957-4158. DOI: `10.1016/S0957-4158(01)00014-9`.

[17] Z. Chen, F. Huang, C. Yang and B. Yao. Adaptive Fuzzy Backstepping Control for Stable Nonlinear Bilateral Teleoperation Manipulators With Enhanced Transparency Performance. *IEEE Transactions on Industrial Electronics* 67.1 (2020), 746–756. DOI: `10.1109/TIE.2019.2898587`.

[18] A. Clegg, M. Dunnigan and D. Lane. Self-tuning position and force control of an underwater hydraulic manipulator. *Proceedings 2001 ICRA. IEEE International Conference on Robotics and Automation (Cat. No.01CH37164).* Vol. 4. 2001, 3226–3231 vol.4. DOI: `10.1109/ROBOT.2001.933115`.

[19] F. Conrad. Transputer control of hydraulic actuators and robots. *IEEE Transactions on Industrial Electronics* 43.1 (1996), 38–47. DOI: `10.1109/41.481406`.

[20] F. Córdova, L. Cañete, L. Quezada and F. Yanine. An Intelligent Supervising System for the Operation of an Underground Mine. *International Journal of Computers Communications & Control* III (Sept. 2008), 259–269. DOI: `10.15837/ijccc.2008.3.2394`.

[21] P. Corke, J. Roberts, J. Cunningham and D. Hainsworth. Mining Robotics. *Springer Handbook of Robotics*. Ed. by B. Siciliano and O. Khatib. Berlin, Heidelberg: Springer Berlin Heidelberg, 2008, 1127–1150. ISBN: 978-3-540-30301-5. DOI: `10.1007/978-3-540-30301-5_50`.

[22] P. I. Corke, J. M. Roberts and G. J. Winstanley. Robotics for the mining industry. *Autonomous Robotic Systems*. Ed. by A. T. de Almeida and O. Khatib. London: Springer London, 1998, 163–181. ISBN: 978-1-84628-530-1.

[23] J. Craig and M. Raibert. A systematic method of hybrid position/force control of a manipulator. *COMPSAC 79. Proceedings. Computer Software and The IEEE Computer Society's Third International Applications Conference, 1979.* 1979, 446–451. DOI: `10.1109/CMPSAC.1979.762539`.

[24] O. Dahl. Path-constrained robot control with limited torques-experimental evaluation. *IEEE Transactions on Robotics and Automation* 10.5 (Oct. 1994), 658–669. ISSN: 1042-296X. DOI: `10.1109/70.326570`.

[25] O. Dahl and L. Nielsen. Torque-limited path following by online trajectory time scaling. *IEEE Transactions on Robotics and Automation* 6.5 (Oct. 1990), 554–561. ISSN: 1042-296X. DOI: `10.1109/70.62044`.

[26] E. Duff, C. Caris, A. Bonchis, K. Taylor, C. Gunn and M. Adcock. The Development of a Telerobotic Rock Breaker. *Field and Service Robotics*. Ed. by A. Howard, K. Iagnemma and A. Kelly. Berlin, Heidelberg: Springer Berlin Heidelberg, 2010, 411–420. ISBN: 978-3-642-13408-1. DOI: `10.1007/978-3-642-13408-1_37`.

[27] M. Dunnigan, D. Lane, A. Clegg and I. Edwards. Hybrid position/force control of a hydraulic underwater manipulator. *IEE Proceedings-Control Theory and Applications* 143.2 (1996), 145–151. DOI: `10.1049/ip-cta:19960274`.

[28] *Earth-moving machinery and mining – Autonomous and semi-autonomous machine system safety*. ISO 17757:2019(en), Standard. Geneva, Switzerland: International Organization for Standardization, July 2019.

[29] J. Fox, R. Castano and R. C. Anderson. Onboard autonomous rock shape analysis for Mars rovers. *Proceedings, IEEE Aerospace Conference*. Vol. 5. Mar. 2002, 5–2052 vol.5. DOI: `10.1109/AERO.2002.1035371`.

[30] J. Guo, C. Liu and P. Poignet. A Scaled Bilateral Teleoperation System for Robotic-Assisted Surgery with Time Delay. *Journal of Intelligent & Robotic Systems* (Aug. 2018). ISSN: 1573-0409. DOI: `10.1007/s10846-018-0918-1`.

[31] S. Haddadin, A. De Luca and A. Albu-Schäffer. Robot Collisions: A Survey on Detection, Isolation, and Identification. *IEEE Transactions on Robotics* 33.6 (Dec. 2017), 1292–1312. ISSN: 1941-0468. DOI: `10.1109/TRO.2017.2723903`.

[32] B. Hannaford. A design framework for teleoperators with kinesthetic feedback. *IEEE Transactions on Robotics and Automation* 5.4 (Aug. 1989), 426–434. ISSN: 1042-296X. DOI: `10.1109/70.88057`.

[33] B. Hannaford and Jee-Hwan Ryu. Time-domain passivity control of haptic interfaces. *IEEE Transactions on Robotics and Automation* 18.1 (2002), 1–10. DOI: `10.1109/70.988969`.

[34] K. Hashtrudi-Zaad and S. E. Salcudean. Analysis of Control Architectures for Teleoperation Systems with Impedance/Admittance Master and Slave Manipulators. *The International Journal of Robotics Research* 20.6 (2001), 419–445. DOI: `10.1177/02783640122067471`.

[35] K. Hastrudi-Zaad and S. E. Salcudean. On the use of local force feedback for transparent teleoperation. *Proceedings 1999 IEEE International Conference on Robotics and Automation (Cat. No.99CH36288C).* Vol. 3. 1999, 1863–1869 vol.3. DOI: `10.1109/ROBOT.1999.770380`.

[36] I. Havoutis and S. Calinon. Learning from demonstration for semi-autonomous teleoperation. *Autonomous Robots* 43.3 (2019), 713–726. ISSN: 1573-7527. DOI: `10.1007/s10514-018-9745-2`.

[37] N. Hogan. Impedance Control: An Approach to Manipulation. *1984 American Control Conference.* 1984, 304–313. DOI: `10.23919/ACC.1984.4788393`.

[38] P. F. Hokayem and M. W. Spong. Bilateral teleoperation: An historical survey. *Automatica* 42.12 (2006), 2035–2057. ISSN: 0005-1098. DOI: `10.1016/j.automatica.2006.06.027`.

[39] G. Hubert, S. Dirdjosuwondo, R. Plaisance and L. Thomas. Tele-operation at Freeport to reduce wet muck Hazards. *MassMin 2000* (2000), 173–179.

[40] L. Hulttinen, J. Koivumäki and J. Mattila. Parameter identification for improved performance of model-based control of hydraulic manipulators. *Proceedings of the IEEE 2019 9th International Conference on Cybernetics and Intelligent Systems (CIS) and IEEE Conference on Robotics, Automation and Mechatronics (RAM).* IEEE, 2019, 124–129. ISBN: 978-1-7281-3459-8. DOI: `10.1109/CIS-RAM47153.2019.9095831`.

[41] L. Hulttinen, J. Koivumäki and J. Mattila. Parameter identification for model-based control of hydraulically actuated open-chain manipulators. *ASME/BATH 2019 Symposium on Fluid Power and Motion Control (FPMC).* ASME, 2019. DOI: `10.1115/FPMC2019-1656`.

[42] A. Iamrurksiri, T. Tsubouchi and S. Sarata. Rock Moving Operation Using a Rod-Shaped Manipulator. *Journal of Robotics and Mechatronics* 25.1 (2013), 232–239. DOI: `10.20965/jrm.2013.p0232`.

[43] A. Iamrurksiri, T. Tsubouchi and S. Sarata. Rock Recognition Using Stereo Vision for Large Rock Breaking Operation. *Field and Service Robotics: Results of the 8th International Conference.* Ed. by K. Yoshida and S. Tadokoro. Berlin, Heidelberg: Springer Berlin Heidelberg, 2014, 383–397. ISBN: 978-3-642-40686-7. DOI: `10.1007/978-3-642-40686-7_26`.

[44] H. Kagermann, W.-D. Lukas and W. Wahlster. Industrie 4.0: Mit dem Internet der Dinge auf dem Weg zur 4. industriellen Revolution. *VDI nachrichten* 13.1 (2011), 2–3.

[45] J. Kalmari. *Nonlinear Model Predictive Control of a Hydraulic Forestry Crane*. G5 Compendium Thesis. 2015. URL: `http://urn.fi/URN:ISBN:978-952-60-6325-6`.

[46] H. Kazerooni, T. Tsay and K. Hollerbach. A controller design framework for telerobotic systems. *IEEE Transactions on Control Systems Technology* 1.1 (1993), 50–62. DOI: `10.1109/87.221351`.

[47] T. Kivelä and J. Mattila. Adaptive dead zone compensation of proportional mobile valve. *The Twelfth Scandinavian International Conference on Fluid Power, SICFP'11, May 18-20, 2011, Tampere, Finland*. Ed. by H. Sairala and K. Koskinen. Scandinavian International Conference on Fluid Power SICFP 3. Scandinavian International Conference on Fluid Power, 2011, 411–422. ISBN: 978-952-15-2520-9.

[48] J. Koivumäki and J. Mattila. Stability-Guaranteed Force-Sensorless Contact Force/Motion Control of Heavy-Duty Hydraulic Manipulators. *IEEE Transactions on Robotics* 31.4 (Aug. 2015), 918–935. ISSN: 1552-3098. DOI: `10.1109/TRO.2015.2441492`.

[49] J. Koivumäki and J. Mattila. Stability-Guaranteed Impedance Control of Hydraulic Robotic Manipulators. *IEEE/ASME Transactions on Mechatronics* 22.2 (2017), 601–612. DOI: `10.1109/TMECH.2016.2618912`.

[50] J. Koivumäki and J. Mattila. High Performance Non-Linear Motion/Force Controller Design for Redundant Hydraulic Construction Crane Automation. *Automation in Construction* 51 (2015), 59–77. ISSN: 0926-5805. DOI: `10.1016/j.autcon.2014.12.014`.

[51] Konecranes. *Our self-driving future is being shaped in ports*. Available at: `https://www.konecranes.com/resources/our-self-driving-future-is-being-shaped-in-ports` (accessed 20.5.2021). 2020.

[52] K. Krauze, W. Rączka, M. Sibielak, J. Konieczny, D. Kubiak, H. Culer and D. Bajus. Automated transfer point URB/ZS-3. *Mining - Informatics, Automation and Electrical Engineering* 2 (530).2 (2017), 80–. ISSN: 2449-6421. DOI: `10.7494/miag.2017.2.530.80`.

[53] M. Krstić, I. Kanellakopoulos and P. V. Kokotović. *Nonlinear and Adaptive Control Design*. 1st. USA: John Wiley & Sons, Inc., 1995. ISBN: 0471127329.

[54] A. Krug, P. Seidel and T. Knoblinger. *Autonomous machines in the fast lane?* Available at: `https://www.adlittle.com/en/insights/viewpoints/autonomous-machines-fast-lane` (accessed 15.4.2021). Arthur D Little, 2019.

[55] S. Lampinen, J. Koivumäki and J. Mattila. Full-Dynamics-Based Bilateral Teleoperation of Hydraulic Robotic Manipulators. *2018 IEEE 14th International Conference on Automation Science and Engineering (CASE)*. 2018, 1343–1350. DOI: `10.1109/COASE.2018.8560444`.

[56] D. Lane, M. Dunnigan, A. Clegg, P. Dauchez and L. Cellier. A comparison between robust and adaptive hybrid position/force control schemes for hydraulic underwater manipulators. *Transactions of the Institute of Measurement and Control* 19.2 (1997), 107–116. DOI: `10.1177/014233129701900205`.

[57] D. Lawrence. Stability and transparency in bilateral teleoperation. *IEEE Transactions on Robotics and Automation* 9.5 (1993), 624–637. ISSN: 1042-296X. DOI: `10.1109/70.258054`.

[58] G. M. H. Leung, B. A. Francis and J. Apkarian. Bilateral controller for teleoperators with time delay via μ-synthesis. *IEEE Transactions on Robotics and Automation* 11.1 (1995), 105–116. DOI: `10.1109/70.345941`.

[59] L. Li, Z. Lin, Y. Jiang, C. Yu and J. Yao. Valve Deadzone/Backlash Compensation for Lifting Motion Control of Hydraulic Manipulators. *Machines* 9.3 (2021). ISSN: 2075-1702. DOI: `10.3390/machines9030057`.

[60] P. Malysz and S. Sirouspour. A Kinematic Control Framework for Single-Slave Asymmetric Teleoperation Systems. *IEEE Transactions on Robotics* 27.5 (Oct. 2011), 901–917. ISSN: 1552-3098. DOI: `10.1109/TRO.2011.2152950`.

[61] J. Marshall, T. Barfoot and J. Larsson. Autonomous underground tramming for center-articulated vehicles. *Journal of Field Robotics* 25.6–7 (2008), 400–421. DOI: `10.1002/rob.20242`.

[62] J. A. Marshall, A. Bonchis, E. Nebot and S. Scheding. Robotics in Mining. *Springer Handbook of Robotics*. Ed. by B. Siciliano and O. Khatib. Cham:

Springer International Publishing, 2016, 1549–1576. ISBN: 978-3-319-32552-1. DOI: `10.1007/978-3-319-32552-1_59`.

[63] J. Mattila, J. Koivumäki, D. G. Caldwell and C. Semini. A Survey on Control of Hydraulic Robotic Manipulators With Projection to Future Trends. *IEEE/ASME Transactions on Mechatronics* 22.2 (2017), 669–680. ISSN: 1083-4435. DOI: `10.1109/TMECH.2017.2668604`.

[64] J. Mattila and T. Virvalo. Energy-efficient motion control of a hydraulic manipulator. *Proceedings 2000 ICRA. Millennium Conference. IEEE International Conference on Robotics and Automation. Symposia Proceedings (Cat. No.00CH37065).* Vol. 3. 2000, 3000–3006 vol.3. DOI: `10.1109/ROBOT.2000.846483`.

[65] C. McKinnon and J. A. Marshall. Automatic Identification of Large Fragments in a Pile of Broken Rock Using a Time-of-Flight Camera. *IEEE Transactions on Automation Science and Engineering* 11.3 (July 2014), 935–942. ISSN: 1558-3783.

[66] Mining-Technology. *Sizing up Syama: the world's first fully automated mine*. Available at: `https://www.mining-technology.com/features/sizing-syama-worlds-first-fully-automated-mine/` (accessed 23.2.2021). Oct. 2018.

[67] J. Morris. *Why Is Tesla's Full Self-Driving Only Level 2 Autonomous?* Available at: `https://www.forbes.com/sites/jamesmorris/2021/03/13/why-is-teslas-full-self-driving-only-level-2-autonomous/` (accessed 17.5.2021). Forbes, Mar. 2021.

[68] A. Muhammad, S. Esque, J. Mattila, M. Tolonen, P. Nieminen, O. Linna, M. Vilenius, M. Siuko, J. Palmer and M. Irving. Development of Water Hydraulic Remote Handling System for Divertor Maintenance of ITER. *2007 IEEE 22nd Symposium on Fusion Engineering*. 2007, 1–4. DOI: `10.1109/FUSION.2007.4337865`.

[69] G. Niemeyer and J. J. E. Slotine. Stable adaptive teleoperation. *IEEE Journal of Oceanic Engineering* 16.1 (1991), 152–162. DOI: `10.1109/48.64895`.

[70] G. Niemeyer, S. Preusche Carsten and Stramigioli and D. Lee. Telerobotics. *Springer Handbook of Robotics*. Ed. by B. Siciliano and O. Khatib. Cham: Springer International Publishing, 2016, 1085–1108. ISBN: 978-3-319-32552-1. DOI: `10.1007/978-3-319-32552-1_43`.

[71] L. Niu, K. Chen, K. Jia and J. Mattila. Efficient 3D Visual Perception for Robotic Rock Breaking. *2019 IEEE 15th International Conference on Automation Science and Engineering (CASE)*. 2019, 1124–1130. DOI: `10.1109/COASE.2019.8842859`.

[72] L. Niu, M. Aref and J. Mattila. Clustering Analysis for Secondary Breaking Using a Low-Cost Time-of-Flight Camera. *2018 Ninth International Conference on Intelligent Control and Information Processing (ICICIP)*. IEEE, Nov. 2018, 318–324. ISBN: 978-1-5386-5861-1. DOI: `10.1109/ICICIP.2018.8606682`.

[73] J. Nurmi, M. Aref and J. Mattila. A neural network strategy for learning of nonlinearities toward feed-forward control of pressure-compensated hydraulic valves with a significant dead zone. *BATH/ASME 2018 Symposium on Fluid Power and Motion Control, FPMC 2018*. ASME, 2018. DOI: `10.1115/FPMC2018-8847`.

[74] J. Nurmi and J. Mattila. Automated Feed-Forward Learning for Pressure-Compensated Mobile Hydraulic Valves With Significant Dead-Zone. *Proc. of ASME/BATH Symp. on Fluid Power and Motion Control (FPMC2017), Oct. 16-19, 2017, Sarasota, Florida*. 2017. DOI: `10.1115/FPMC2017-4258`.

[75] M. Ostoja-Starzewski and M. Skibniewski. A master-slave manipulator for excavation and construction tasks. *Robotics and Autonomous Systems* 4.4 (1989), 333–337. ISSN: 0921-8890. DOI: `10.1016/0921-8890(89)90032-8`.

[76] D. Paredes and D. Fleming-Muñoz. Automation and robotics in mining: Jobs, income and inequality implications. *The Extractive Industries and Society* 8.1 (2021), 189–193. ISSN: 2214-790X. DOI: `10.1016/j.exis.2021.01.004`.

[77] T. Peinsitt, H. Haubmann, H. Kargl and C. Kary. Recent developments towards autonomous tunneling and mining machinery. *Tunnels and Underground Cities: Engineering and Innovation meet Archaeology, Architecture and Art*. Ed. by T. C. Daniele Peila Giulia Viggiani. 1st ed. Routledge, 2019, 2849–2858. ISBN: 1138388653.

[78] A. Pervez, A. Ali, J. Ryu and D. Lee. Novel learning from demonstration approach for repetitive teleoperation tasks. *2017 IEEE World Haptics Conference (WHC)*. June 2017, 60–65. DOI: `10.1109/WHC.2017.7989877`.

[79] G. J. Raju, G. C. Verghese and T. B. Sheridan. Design issues in 2-port network models of bilateral remote manipulation. *Proceedings, 1989 International Conference on Robotics and Automation*. 1989, 1316–1321 vol.3. DOI: `10.1109/ROBOT.1989.100162`.

[80] RamBooms. *RamBooms X88-540R rock breaker boom*. Available at: `https://mrbbooms.com/x-series/x8/x88-540r/` (accessed 3.4.2021).

[81] J. Redmon and A. Farhadi. *YOLOv3: An Incremental Improvement*. 2018. arXiv: `1804.02767 [cs.CV]`.

[82] *Robots and robotic devices — Safety requirements for industrial robots — Part 1: Robots*. ISO 10218-1:2011, Standard. Geneva, Switzerland: International Organization for Standardization, July 2011.

[83] *Robots and robotic devices — Safety requirements for industrial robots — Part 2: Robot systems and integration*. ISO 10218-2:2011, Standard. Geneva, Switzerland: International Organization for Standardization, July 2011.

[84] S. Sakai and Y. Maeshima. A new method for parameter identification for N-DOF hydraulic robots. *2014 IEEE International Conference on Robotics and Automation (ICRA)*. 2014, 5983–5989. DOI: `10.1109/ICRA.2014.6907741`.

[85] S. E. Salcudean, K. Hashtrudi-Zaad, S. Tafazoli, S. P. DiMaio and C. Reboulet. Bilateral matched impedance teleoperation with application to excavator control. *IEEE Control Systems Magazine* 19.6 (1999), 29–37. DOI: `10.1109/37.806913`.

[86] M. Shahbazi, S. F. Atashzar and R. V. Patel. A Systematic Review of Multilateral Teleoperation Systems. *IEEE Transactions on Haptics* 11.3 (2018), 338–356. DOI: `10.1109/TOH.2018.2818134`.

[87] A. Shahdi and S. Sirouspour. Adaptive/Robust Control for Time-Delay Teleoperation. *IEEE Transactions on Robotics* 25.1 (2009), 196–205. DOI: `10.1109/TRO.2008.2010963`.

[88] T. B. Sheridan. Telerobotics. *Automatica* 25.4 (1989), 487–507. ISSN: 0005-1098. DOI: `10.1016/0005-1098(89)90093-9`.

[89] T. B. Sheridan. Space teleoperation through time delay: review and prognosis. *IEEE Transactions on Robotics and Automation* 9.5 (Oct. 1993), 592–606. ISSN: 1042-296X. DOI: `10.1109/70.258052`.

[90] S. Sirouspour. Modeling and control of cooperative teleoperation systems. *IEEE Transactions on Robotics* 21.6 (Dec. 2005), 1220–1225. ISSN: 1552-3098. DOI: `10.1109/TRO.2005.852254`.

[91] J. Slotine and W. Li. *Applied Nonlinear Control*. Prentice Hall, 1991. ISBN: 9780130408907.

[92] D. Sun and Q. Liao. Asymmetric Bilateral Telerobotic System With Shared Autonomy Control. *IEEE Transactions on Control Systems Technology* (2020), 1–14. DOI: `10.1109/TCST.2020.3018426`.

[93] M. Suomalainen, J. Koivumäki, S. Lampinen, V. Kyrki and J. Mattila. Learning from Demonstration for Hydraulic Manipulators. *2018 IEEE/RSJ International Conference on Intelligent Robots and Systems (IROS)*. Oct. 2018, 3579–3586. DOI: `10.1109/IROS.2018.8594285`.

[94] K. Tadano, T. Tsubouchi, M. Kurisu and S. Sarata. Massive Rock Handling by a Breaker-Graspless Manipulation and Object Recognition. *23rd Int. Symposium on Automation and Robotics in Construction*. 2006, 487–492.

[95] S. Tafazoli, P. D. Lawrence and S. E. Salcudean. Identification of inertial and friction parameters for excavator arms. *IEEE Transactions on Robotics and Automation* 15.5 (1999), 966–971. DOI: `10.1109/70.795801`.

[96] S. Tafazoli, S. E. Salcudean, K. Hashtrudi-Zaad and P. D. Lawrence. Impedance control of a teleoperated excavator. *IEEE Transactions on Control Systems Technology* 10.3 (May 2002), 355–367. ISSN: 1063-6536. DOI: `10.1109/87.998021`.

[97] H. Takahashi and T. Monden. Automatic system for boulder breakage using force sensors. *Fragblast* 3.3 (1999), 267–277.

[98] H. Takahashi and K. Sano. Automatic detection and breaking system for boulders by use of CCD camera and laser pointer. *Fragblast* 2.4 (1998), 397–414. DOI: `10.1080/13855149809408785`.

[99] G. Tao and M. Tian. Discrete-time adaptive control of systems with multisegment piecewise-linear nonlinearities. *IEEE Transactions on Automatic Control* 43.5 (1998), 719–723. DOI: `10.1109/9.668844`.

[100] *Taxonomy and Definitions for Terms Related to Driving Automation Systems for On-Road Motor Vehicles*. SAE J3016_202104, Standard. SAE International, Apr. 2021. DOI: `10.4271/J3016_202104`.

[101] M. J. Thurley. Automated Image Segmentation and Analysis of Rock Piles in an Open-Pit Mine. *2013 International Conference on Digital Image Computing: Techniques and Applications (DICTA)*. 2013, 1–8. DOI: `10.1109/DICTA.2013.6691484`.

[102] M. J. Thurley and K. C. Ng. Identifying, visualizing, and comparing regions in irregularly spaced 3D surface data. *Computer Vision and Image Understanding* 98.2 (2005), 239–270. ISSN: 1077-3142. DOI: `10.1016/j.cviu.2003.12.002`.

[103] M. J. Thurley and K. C. Ng. Identification and sizing of the entirely visible rocks from a 3D surface data segmentation of laboratory rock piles. *Computer Vision and Image Understanding* 111.2 (2008), 170–178. ISSN: 1077-3142. DOI: `10.1016/j.cviu.2007.09.009`.

[104] R. Tiusanen, T. Malm and A. Ronkainen. An overview of current safety requirements for autonomous machines – review of standards. *Open Engineering* 10.1 (2020), 665–673. DOI: `10.1515/eng-2020-0074`.

[105] L.-F. Y. Tremblay, M. Arsenault and M. Zeinali. Development of a trajectory planning algorithm for a 4-DoF rockbreaker based on hydraulic flow rate limits. *Transactions of the Canadian Society for Mechanical Engineering* 44.4 (2020), 501–510. DOI: `10.1139/tcsme-2019-0173`.

[106] M. Vukobratovic, D. Surdilovic, Y. Ekalo and D. Katic. *Dynamics and Robust Control of Robot-Environment Interaction*. World Scientific, Mar. 2009. ISBN: 978-981-283-475-1. DOI: `10.1142/7017`.

[107] J. Wanner and O. Sawodny. Tool-center-point control of a flexible link concrete pump with hydraulic limitations using quadratic programming. *2019 IEEE 15th International Conference on Automation Science and Engineering (CASE)*. Aug. 2019, 561–566. DOI: `10.1109/COASE.2019.8842831`.

[108] J. Wanner and O. Sawodny. Tool-Center-Point Control of a Concrete Pump Using Constrained Quadratic Optimization. *IEEE Transactions on Automation Science and Engineering* 18.1 (2021), 382–396. DOI: `10.1109/TASE.2020.3031691`.

[109] World Economic Forum. *Digital transformation initiative: Mining and metals industry*. Available at: `http://reports.weforum.org/digital-trans\formation/wp-content/blogs.dir/94/mp/files/pages/files/wef-dti-mining-and-metals-white-paper.pdf` (accessed 20.4.2021). 2017.

[110] D. Wu, R. Burton, G. Schoenau and D. Bitner. Analysis of a Pressure-Compensated Flow Control Valve. *Journal of Dynamic Systems, Measurement, and Control* 129.2 (Mar. 2004), 203–211. ISSN: 0022-0434. DOI: `10.1115/1.1870037`.

[111] Y. Yokokohji and T. Yoshikawa. Bilateral control of master-slave manipulators for ideal kinesthetic coupling-formulation and experiment. *IEEE Transactions on Robotics and Automation* 10.5 (Oct. 1994), 605–620. ISSN: 1042-296X. DOI: `10.1109/70.326566`.

[112] Z.-X. Zhang. Chapter 21 - Optimum Fragmentation. *Rock Fracture and Blasting*. Ed. by Z.-X. Zhang. Butterworth-Heinemann, 2016, 411–423. ISBN: 978-0-12-802688-5. DOI: `10.1016/B978-0-12-802688-5.00021-X`.

[113] W.-H. Zhu. Dynamics of general constrained robots derived from rigid bodies. *Journal of Applied Mechanics* 75.3 (2008), 031005-031005–11. DOI: `10.1115/1.2839633`.

[114] W.-H. Zhu. *Virtual decomposition control: toward hyper degrees of freedom robots*. Vol. 60. Springer Science & Business Media, 2010. DOI: `10.1007/978-3-642-10724-5`.

[115] W.-H. Zhu, T. Lamarche, E. Dupuis, D. Jameux, P. Barnard and G. Liu. Precision Control of Modular Robot Manipulators: The VDC Approach With Embedded FPGA. *IEEE Transactions on Robotics* 29.5 (2013), 1162–1179. DOI: `10.1109/TRO.2013.2265631`.

[116] W.-H. Zhu and J.-C. Piedboeuf. Adaptive Output Force Tracking Control of Hydraulic Cylinders With Applications to Robot Manipulators. *Journal of Dynamic Systems, Measurement, and Control* 127.2 (June 2004), 206–217. ISSN: 0022-0434. DOI: `10.1115/1.1898237`.

[117] W.-H. Zhu and S. E. Salcudean. Stability guaranteed teleoperation: an adaptive motion/force control approach. *IEEE Transactions on Automatic Control* 45.11 (Nov. 2000), 1951–1969. ISSN: 0018-9286. DOI: `10.1109/9.887620`.

[118] W.-H. Zhu, Y.-G. Xi, Z.-J. Zhang, Z. Bien and J. D. Schutter. Virtual decomposition based control for generalized high dimensional robotic systems with complicated structure. *IEEE Transactions on Robotics and Automation* 13.3 (June 1997), 411–436. ISSN: 1042-296X. DOI: `10.1109/70.585903`.

[119] L. Ziętkowski, J. Młynarczyk and W. Sobolewski. Optimization test of operation of URB/ZS-3 automatic machine for breaking oversized lumps under conditions of Polkowice-Sieroszowice mine. *Mining - Informatics, Automation and Electrical Engineering* 4 (536).1 (2018), 83–. ISSN: 2449-6421. DOI: `10.7494/miag.2018.4.536.83`.

PUBLICATIONS

PUBLICATION

I

Model-based control of a pressure-compensated directional valve with significant dead-zone

S. Lampinen, J. Koivumäki, J. Mattila and J. Niemi

ASME/BATH 2019 Symposium on Fluid Power and Motion Control. 2019
DOI: `10.1115/fpmc2019-1664`

PUBLICATION

II

Flow-Bounded Trajectory-Scaling Algorithm for Hydraulic Robotic Manipulators

S. Lampinen, J. Niemi and J. Mattila

2020 IEEE/ASME International Conference on Advanced Intelligent Mechatronics (AIM). 2020, 619–624

DOI: `10.1109/AIM43001.2020.9158851`

Flow-Bounded Trajectory-Scaling Algorithm for Hydraulic Robotic Manipulators

Santeri Lampinen, Jouni Niemi and Jouni Mattila

***Abstract*— On-line methods for trajectory scaling have focused on torque or acceleration bounded minimum time trajectories, while other system constraints have received little attention. For hydraulic systems, volumetric flow rate of the supply unit establishes a critical constraint, that has been neglected in control design. Consequently, commercial solutions for robotic control of hydraulic manipulators are typically limited to a compromise of a slower constant endpoint velocity, that can be achieved in any operating point without violating the constrained flow rate. However, with real-time analysis of the required volumetric flow rate, the desired trajectories can be executed much faster without violating the flow rate constraint or losing control accuracy. This study proposes an on-line method for trajectory scaling to perform predetermined trajectories in minimum time. Essentially, the method scales velocity along the trajectory to maintain achievable velocity at all times. The proposed method is capable of enforcing a global volumetric flow limit, whether it is constant or time-varying. The method is validated with simulations and experiments with a real hydraulic robotic manipulator. Experimental results show a very significant improvement in the trajectory tracking control, where the tracking error is reduced from 461 mm to 73 mm on a square trajectory.**

I. INTRODUCTION

Hydraulic heavy-duty machinery is undergoing a revolution as these traditionally manually operated machines are being retrofitted with more advanced control systems or completely redesigned with robotic control in mind. Commercial solutions for retrofitting coordinated control for hydraulic manipulators are emerging [1], and manufacturers like Hiab, John Deere, Ramboooms, etc. are beginning to implement advanced control in their products [2], [3]. These heavy-duty manipulators were designed first for manual operation, where the operator controls each hydraulic actuator separately. A skilled operator can drive multiple actuators simultaneously, and is able to automatically adjust the control in order to respect the limitation on the available flow rate. If the limitations are not considered, the least loaded actuator would receive the highest flow rate, and the most loaded actuators could not track the desired trajectory. This results in undesired motions, despite having fancy load sensing valves.

Limitations on the available flow rate, and consequently the obtainable tool center point (TCP) velocity is not something the current robotic control methods have taken into consideration. Traditional inverse kinematics solutions, such as those reviewed in [4], are not designed with limitations of the manipulators in mind, and thus, are not sufficient alone for applications with hydraulic machinery with limited volumetric flow.

At this point, it is worth considering a fundamental difference between electrical and hydraulic actuators. Electrical actuators can be viewed as torque sources, where the output torque is proportional to the control current. However, hydraulic actuators can be considered as velocity sources, with actuator velocity approximately proportional to the valve control. Due to this fundamental difference, a natural path of research with electric manipulators was to take the actuator limitations, namely the maximum obtainable torque, into consideration. Minimum-time control of robotic manipulators with torque-bounded trajectory generation was proposed in [5] to perform desired motions as fast as possible within the physical limitations of the controlled manipulator. Further studies [6]–[8] have carried this idea, and evolved the theory around torque-bounded time scaling on-line. In these studies, the trajectory is scaled in real-time, based on constraints on individual joint accelerations and joint velocity limits. However, the focus has been on individual limits for different actuators, without consideration of global limitations.

In view of the nature of hydraulic actuators, a natural approach with these actuators is velocity-bounded. With hydraulic manipulators, the maximum velocity of the manipulator is dictated by the available hydraulic flow from the supply unit. Moreover, while multiple actuators are driven simultaneously, the flow is divided among the actuators, and thus, joint velocity bounds change dynamically. Last, hydraulic systems contain nonlinearities from the closed chain mechanical structure, which may even be combined with a four-bar link to achieve a wider operation range.

In *closed-loop resolved rate control*, the typical solution is to limit the maximum velocity of the TCP to a level that can be achieved within the whole operating range. However, the manipulability (see [9, chapter 4]) can vary significantly in different manipulator configurations, and with hydraulic systems, this is even more notable than with electric manipulators. In hydraulic systems, cylinder velocities are used to define manipulability ellipsoids. The ellipsoids describe how well a manipulator can move its TCP in an arbitrary direction. A hydraulic manipulator can move much faster in some operating points and directions, where the manipulability is greater. Thus, this typical solution of choosing a constant maximum velocity is a mere compromise, and it leaves a huge potential of the manipulator unused. An experienced operator may complain in such case about sluggish movement and decreased efficiency, when compared to a manually operated machine.

To allow operation of the manipulator at its mechanical limits, we propose dynamic scaling of the TCP velocity, based on the available pump capacity. This allows the absolute

S. Lampinen, and J. Mattila are with the faculty of Engineering and Natural Sciences, Tampere University, Finland. `name.surname@tuni.fi`

J. Niemi is with Rambooms Oy, Lahti, Finland.

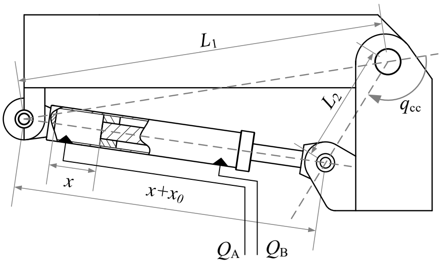

Fig. 1. Closed chain angles and dimensions.

maximum achievable TCP velocity with the mechanical and hydraulic limitations of the manipulator in the resolved rate control mode. A very similar idea was proposed in [10], where the inverse kinematics control problem was turned into an optimization problem by the means of quadratic programming. There, the method is not extended for trajectory scaling, however. Here, the proposed method can be applied to on-line time-scaling higher-level path planners to reduce too fast trajectories and can be implemented to act with torque-limiting controllers as proposed in [6]–[8]. The main result of this study is the introduction of trajectory scaling into the scope of hydraulic manipulators. In many cases, although not desired by design, the hydraulic flow of the supply unit is not sufficient in resolved rate control. The proposed approach solves the described problem and allows higher utilization of the manipulator's capabilities. Moreover, it is expandable to on-line time-scaling of the planned trajectory.

The remainder of this paper is organized as follows. Section II introduces the algorithm for flow-bounded trajectory scaling. Section III introduces the experimental system. Section IV provides results for the proposed control method in simulations and experiments. Section V concludes the paper.

II. CONSTRAINT BOUNDED COORDINATED CONTROL

Let $\mathbf{v} \in \mathbb{R}^3$ denote the desired velocity of the manipulator in world coordinates. For a redundant n-joint manipulator, the required joint velocities can be identified by using a pseudo-inverse of the Jacobian matrix as

$$\dot{\mathbf{q}} = \mathbf{W}^{-1}\mathbf{J}^T\left(\mathbf{J}\mathbf{W}^{-1}\mathbf{J}^T\right)^{-1}\mathbf{v}, \tag{1}$$

where $\dot{\mathbf{q}} \in \mathbb{R}^n$ is the required joint velocities, $\mathbf{W} \in \mathbb{R}^{n\times n}$ is a symmetric positive definite weighing matrix, and $\mathbf{J} \in \mathbb{R}^{n\times n}$ is the non-invertible Jacobian matrix [11].

Consider the kinematic closed chain structure of Fig. 1, that is part of the manipulator. To calculate the flow rates Q_A and Q_B, the cylinder velocity must be solved from the joint velocity $\dot{q}_{cc}$ as

$$x = \sqrt{L_1^2 + L_2^2 + 2L_1L_2\cos\left(q_{cc}\right)} - x_0 \tag{2}$$

$$\dot{x} = -\frac{L_1L_2\sin\left(q_{cc}\right)}{x + x_0}\dot{q}_{cc}, \tag{3}$$

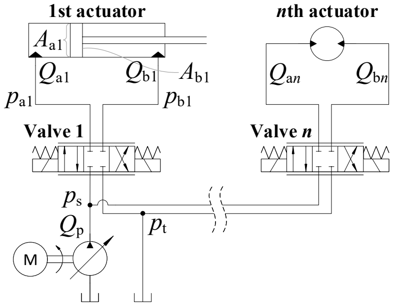

Fig. 2. A hydraulic system of *n* actuators.

where L_1 and L_2 are the structural lengths of the closed chain, x_0 is the minimum length of the hydraulic cylinder, x is the displacement of the piston, and q_cc is the joint angle transformed into the closed chain space.

Then the flow rate into the cylinder can be written as

$$Q_{in} = \begin{cases} A_A\dot{x}, & \text{when } \dot{x} \geq 0 \\ -A_B\dot{x}, & \text{when } \dot{x} < 0, \end{cases} \tag{4}$$

where A_A and A_B are the areas on the A- and B-sides of the hydraulic cylinder, respectively.

In the case of a rotational joint actuated by a hydraulic motor, the flow into the actuator is calculated using

$$Q_{\text{motor}} = \frac{\dot{q}D_m}{2\pi R_t \eta_{vol}}, \tag{5}$$

where D_m is the volumetric displacement of the motor, R_t is the gear ratio of the transmission, and η_{vol} is the volumetric efficiency of the motor. Due to the high internal leakage of the hydraulic motor, volumetric efficiency of the hydraulic motor is needed for better accuracy.

In addition to the maximum flow constraint defined by the supply unit, the flow into the actuator can be saturated in the control valve. Moreover, the movement of the main spool of the control valve may be tuned independently for both directions to have similar behavior of the actuator for both directions, despite the asymmetric surface areas of the cylinder. In this case, the maximum flow rate to each direction is unique.

Consider a hydraulic system of n actuators and a hydraulic pump that outputs Q_p flow. The system is illustrated in Fig. 2. Algorithm 1 is defined to reduce the required joint velocities to satisfy constraints on individual and total flow limits, defined by the system capabilities. The algorithm can be used to output the scaling factor as well as the limited joint velocities. The scaling factor $\dot{s}$ can be used with high-level path planners for time-scaling. Using the algorithm, the path planner can limit trajectories to physical limitations of the controlled manipulator, without the need for experimentally or arbitrarily set constant limits on joint or TCP velocity. Q_r in the algorithm denotes the volumetric flow required for joint velocities $\dot{\mathbf{q}}$. $Q_{A\,\text{limit}}$ and $Q_{B\,\text{limit}}$ denote the individual flow limits defined by the control valve for the A- and B-sides, respectively.

Algorithm 1 Satisfying flow constraints

```
Input: joint velocities $\dot{\mathbf{q}}$, joint angles $\mathbf{q}$
Output: limited joint velocities $\dot{\mathbf{q}}_{\mathrm{lim}}$
  $Q_r \leftarrow 0$
  $\dot{s} \leftarrow 1$
  for each $q \in \mathbf{q}$ do
    determine the required flow into the actuator using (2)–(5)
    $Q_i \leftarrow$ required flow into actuator
    if $\dot{x} > 0$ then
      $\dot{s} \leftarrow \min\left(\dot{s}, \frac{Q_{A\,\mathrm{limit}}}{Q_i}\right)$
    else if $\dot{x} < 0$ then
      $\dot{s} \leftarrow \min\left(\dot{s}, \frac{Q_{B\,\mathrm{limit}}}{Q_i}\right)$
    end if
    $Q_r \leftarrow Q_r + Q_i$
  end for
  $\dot{s} \leftarrow \min\left(\dot{s}, \frac{Q_p}{\dot{s} Q_r}, 1\right)$
  $\dot{\mathbf{q}}_{\mathrm{lim}} \leftarrow \dot{s}\,\dot{\mathbf{q}}$
```

A. Application to Velocity Bounded Trajectory Control

Let $f(s) \in \mathbb{R}^n$ be a continuous function defined in the interval $[s_i,\ s_f]$ of the scalar path parameter s. The starting point of the path is defined as $f(s_i)$, while the end point is defined as $f(s_f)$. The individual joint positions and velocities of the manipulator, along the path, are obtained as

$$\mathbf{q} = f(s) \quad \dot{\mathbf{q}} = f'(s)\dot{s}. \tag{6}$$

Note that here it is assumed that the derivative of the path exists. However, this should not be a problem, as smooth trajectories should be self-evident in trajectory generation.

Without scaling, the path parameter s is typically time dependent and expressed as

$$s = at + b, \tag{7}$$

where $a \in \mathbb{R}$ and $b \in \mathbb{R}$ are constants (e.g., used to normalize s between 0 and 1).

In order to enforce the bound on the available volumetric flow from the pump, the derivative of the path parameter is obtained using Algorithm 1. Then s is obtained by integrating $\dot{s}$ with s_i as the initial value.

III. THE SYSTEM

The proposed algorithm is verified with simulations and experiments with a commercial rock breaking boom from a Finnish original equipment manufacturer, RamBooms. The rock breaking boom is from their commercial x8 lineup. Breaker booms are used in the mining industry for secondary breaking of blasted ores that are still too large for a crusher or feeder. Secondary crushing is performed using a hydraulic hammer attached to the tip of the breaker boom. Fig. 4 illustrates the hydraulic manipulator. The whole system weighs roughly 9400 kg while the hydraulic hammer alone weighs 1700 kg. The boom has a reach of 7-meters [12].

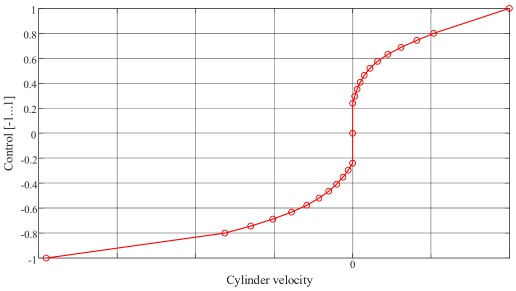

Fig. 3. Identified velocity feed-forward model for dual cylinder lift function.

The hydraulic supply unit of the manipulator produces a near constant hydraulic flow of $180\frac{l}{min}$ regardless of the loading conditions. Each actuator alone can draw almost all the flow from the supply, and thus, advanced control is needed for high-precision motion control.

The manipulator (see Fig. 4) is equipped with Siko WV58MR 14-bit absolute rotary encoders, with a resolution of 21.97×10^{-3} degrees, and Trafac 8270 pressure transducers. Control of the manipulator was achieved using dSPACE MicroAutoBox 2.

The motion control system used in the experiments is a simple P-controller combined with velocity feed-forward using an automatically learned velocity feed-forward model for each cylinder. The feed-forward model identification is based on the algorithm proposed in [13]. The algorithm identifies 24 distinct segments of the feed-forward model yielding good accuracy with reasonable converging time. The identified feed-forward model for the lift joint is presented in Fig. 3.

In the velocity feed-forward identification process in [13], an input-to-state stabilizable controller was designed with respect to an unknown disturbance input (parametric uncertainty). Then, an adaptive law was designed for estimation of the uncertain parameters of the feed-forward model. The adaptation law was designed using z-swapping [14] on the error system, to allow the use of standard adaptation methods. Then, a gradient update law was designed to estimate the uncertain parameters.

The manipulator is equipped with Danfoss PVG-120 mobile proportional control valves that have a significant (approximately 30 % per direction) dead-zone, thus making dead-zone inversion necessary in the control design. Moreover, it significantly improves the control accuracy. For more accurate control of the manipulator, model-based control methods seem the most promising option. In [15], a model-based controller was designed for the same manipulator. A very similar method has also been applied to a complete manipulator with fast servo valves, showing state-of-the-art performance in [16].

IV. THE EXPERIMENTS

Consider a quintic rest-to-rest trajectory created between two points using

$$x(t) = a_0 + a_1 t + a_2 t^2 + a_3 t^3 + a_4 t^4 + a_5 t^5 \tag{8}$$

where coefficients $a_i \in \mathbb{R}$ are obtained from

$$\begin{bmatrix} 1 & t_0 & t_0^2 & t_0^3 & t_0^4 & t_0^5 \\ 0 & 1 & 2t_0 & 3t_0^2 & 4t_0^3 & 5t_0^4 \\ 0 & 0 & 2 & 6t_0^2 & 4t_0^3 & 20t_0^3 \\ 1 & t_f & t_f^2 & t_f^3 & t_f^4 & t_f^5 \\ 0 & 1 & 2t_f & 3t_f^2 & 4t_f^3 & 5t_f^4 \\ 0 & 0 & 2 & 6t_f & 12t_f^2 & 20t_f^3 \end{bmatrix} \begin{bmatrix} a_0 \\ a_1 \\ a_2 \\ a_3 \\ a_4 \\ a_5 \end{bmatrix} = \begin{bmatrix} x_0 \\ \dot{x}_0 \\ \ddot{x}_0 \\ x_f \\ \dot{x}_f \\ \ddot{x}_f \end{bmatrix} \tag{9}$$

where t_0 is the time at the beginning, and t_f is the time at the end; x_0, $\dot{x}_0$, and $\ddot{x}_0$ denote the initial position, velocity, and acceleration, respectively; while x_f, $\dot{x}_f$, and $\ddot{x}_f$ define the final position, velocity, and acceleration, respectively [17].

The trajectory used in the experiments is created with the method above, and the time for each segment is set to 4 s. In the experiments, time t is replaced with s, which is obtained by integrating $\dot{s}$, as suggested by theory.

Due to the limited operation space of the manipulator and the authors' desire for a relatively large trajectory in the experiments, the pseudo-inverse of the manipulator brought problems with joint limits. To solve this issue, the weight matrix W in (1) was redesigned to address this issue. Our solution was to model the individual weights as a function of the joint angle. The weights for each joint were calculated by using two sigmoid functions as

$$W_i = 1 + \frac{w}{1 + e^{\lambda(q_{i\,\min} - q_i)}} + \frac{w}{1 + e^{\lambda(q_i - q_{i\,\max})}}, \tag{10}$$

where $w \in \mathbb{R}$ denotes the maximum weight near joint bounds, $\lambda \in \mathbb{R}$ defines the slope of the weight function, and q_i, $q_{i\,\min}$, and $q_{i\,\max}$ denote the current value, lower bound and the upper bound of the ith joint, respectively. The values W_i represent diagonal elements of W in (1).

The use of these weight functions alone to penalize joint usage near the ends is not enough, however. When a joint is driven near its end, the weight begins to restrict the joint's movement even when trying to drive it away from the end. To address this issue, the restrictive weights are applied only to a joint that is moving toward the limit the joint is closer to. If a joint is moving away from its closer bound, the weight is set to equal 1. Consequently, only movement toward the cylinder ends is penalized.

Another approach for enforcing joint limits in the inverse kinematics problem is to form the inverse kinematics control problem into a constraint optimization problem, such as a quadratic programming problem. This approach was used in [10]. Moreover, the redundancy resolution could be exploited using null space control as discussed in [11, Chapter 3.5.1] to avoid the joint limits.

A. Simulation Study

The proposed method to limit the velocity of the tip in coordinated control was first validated with simulations. The simulation was based on kinematic modeling of the boom and the dynamics of the manipulator were neglected. The required flow and the actual flow from the supply unit were calculated based on the required and limited joint velocities, respectively.

In the simulations, the manipulator was driven in a square path in four segments, with 4 s travel time between segments. Each segment began from one corner and ended in another. Between the segments, there was a 0.5 s rest time. In the experiments, the flow constraint was set to 120 $\frac{l}{min}$. The trajectory used in the simulation study and the actual experiment is presented in Fig. 5.

Results from the simulations are shown in Fig. 6. The trajectory is shown in Fig. 7, where the y-axis points away from the base of the manipulator and the z-axis points directly up (see Fig. 5). In the first simulation, the limiting algorithm was disabled, and the maximum flow required during the trajectory was almost 300 $\frac{l}{min}$, and the time to complete the trajectory was approximately 18 s. In the second simulation, the proposed algorithm was enabled, and

Fig. 4. Rambooms X88-540R. [12]

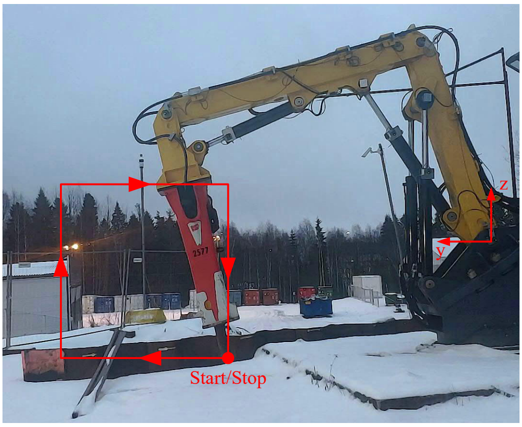

Fig. 5. Trajectory of the experiments.

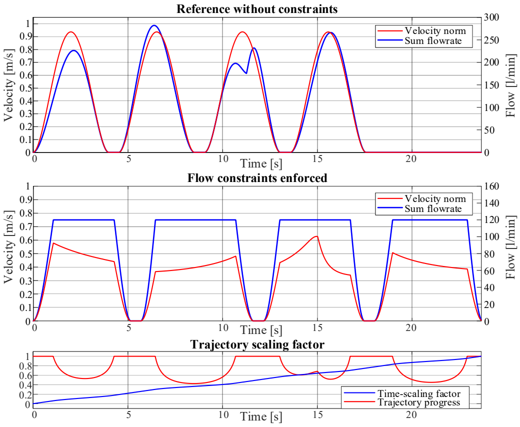

Fig. 6. Simulation results with the proposed algorithm.

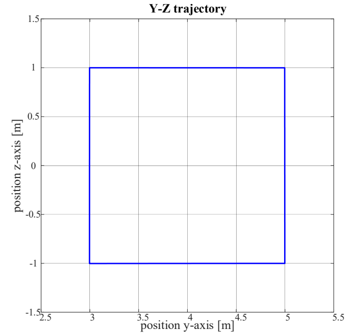

Fig. 7. Simulation trajectory.

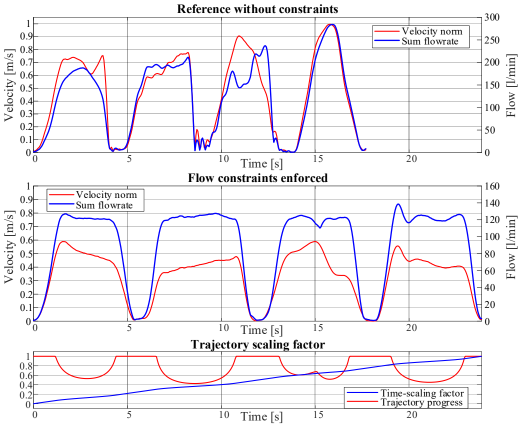

Fig. 8. Experimental results with the proposed algorithm.

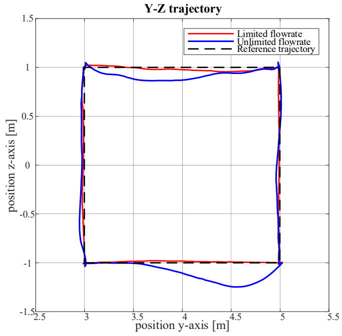

Fig. 9. Experimental trajectory tracking.

the maximum observed flow rate remained at 120 $\frac{l}{min}$. The manipulator completed the set trajectory in 24 s with the algorithm. Moreover, it can be seen that the velocity was limited most on the second segment of the trajectory. This result was expected, as in the second segment of the trajectory, the boom is in such a configuration that most of the movement is done with the first joint of the manipulator, which has two parallel cylinders (see Fig. 4).

B. Experiments with a Real Machine

In the experiment with the real manipulator, the driven trajectory was identical to the one used in the simulation study. Again, the experiment was repeated twice, once with the algorithm in use and once without any trajectory scaling. The maximum flow of 120 $\frac{l}{min}$ was selected for the experiments mainly to highlight the operation of the scaling algorithm and the benefits it brings.

Results from the experiment with the actual manipulator are shown in Figs. 8 and 9. The velocity norm of the TCP and the volumetric flow rate from the reference measurement without trajectory scaling is shown at the top of Fig. 8, while the same data from the measurement with the algorithm in use is shown in the middle. The trajectory scaling factor, $\dot{s}$, is shown at the bottom of the same figure along with the normalized trajectory parameter, s. The measured TCP positions of both experiments are shown in Fig. 9.

Figure 10 presents the Cartesian trajectory tracking error from both experiments. From the figure, it can easily be seen that without the algorithm, errors in trajectory tracking grow notably, as the demanded flow rate exceeds the available capacity. As a result, the manipulator deviates almost half a meter from the desired trajectory. In contrast, results with the algorithm in use reveal greatly improved tracking although no other parameters of the control system were changed. The manipulator still deviates a little from the trajectory, but this can be expected from such a simple controller. The maximum tracking error was reduced from 461 mm of the measurement without the algorithm to 73 mm with the algorithm. The calculated flow rate going to the actuators is clearly limited compared to the reference measurement, and comparable to the respective plot from the simulation study. The small deviations from the desired velocities of the actuators cause the disturbances in the flow rate.

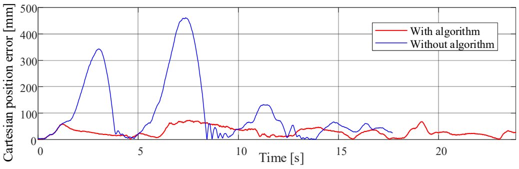

Fig. 10. Trajectory tracking error.

V. CONCLUSIONS

In this study, we designed and demonstrated an algorithm for trajectory and motion scaling for hydraulic systems. Although this paper is formed around hydraulic manipulators, the algorithm is general and can be implemented on different kinds of hydraulic systems as well (e.g., the drive transmission of a hydraulic platform). The algorithm is compatible with motion scaling when the manipulator is operated manually in the resolved rate control mode. More importantly, the algorithm can also be used for trajectory scaling. In this application, a predetermined trajectory can be slowed down when necessary, to satisfy constraints on the available pump flow. Moreover, this approach is compatible with the torque-bounded control methods proposed in [6].

The proposed method was demonstrated with simulations and experiments on a hydraulic breaker boom system with promising results. The simulation study shows clearly the working principle of the algorithm in ideal conditions and shows the effectiveness of the method. The experiments with the actual machine show that the algorithm can effectively scale a trajectory on-line to a level achievable with the manipulator and greatly improve the tracking performance of the manipulator. The maximum tracking error during the experiments was reduced from 461 mm to 73 mm when the proposed algorithm was in use.

It should be noted that the controller in the experiment relied heavily on learned feed-forward mapping that is complemented only with a proportional controller. With a more sophisticated control design, like those proposed in [15], [16], the experimental results would converge closer to the simulation results, and the tracking error could be even further reduced. For comparison, experiments without the algorithm were performed as well, and the results showed the results of insufficient available volumetric flow. When all of the provided flow is being used, the least loaded actuators receive most of the flow, leaving the other actuators unable to track their respective trajectories. The division of flow is analogous to Kirchhoff's law in electronics.

The proposed method can be applied to a wide range of hydraulic systems to improve their performance. With the proposed algorithm, hydraulic systems can be utilized at higher capacity, as the maximum velocity for movements does not need to be such that can be achieved at any configuration.

ACKNOWLEDGMENT

The authors wish to acknowledge support from the Finnish Foundation for Technology Promotion.

REFERENCES

[1] Technion, "Technion xcrane crane control system." Available at: `https://technion.fi/wp-content/uploads/xcrane-brochure-en.pdf` (accessed 3.6.2019).

[2] Hiab, "Ctc – crane tip control." Available at: `http://www.podshop.se/content/12/opensearchresult.aspx?file=PF-CTC-EN-EU_L.pdf` (accessed 3.6.2019).

[3] J. Deere, "Intelligent boom control ibc." Available at: `https://www.deere.co.uk/en/forestry/ibc/` (accessed 13.6.2019).

[4] D. N. Nenchev, "Redundancy resolution through local optimization: A review," *Journal of Robotic Systems*, vol. 6, no. 6, pp. 769–798, 1989.

[5] Kang Shin and N. McKay, "Minimum-time control of robotic manipulators with geometric path constraints," *IEEE Transactions on Automatic Control*, vol. 30, pp. 531–541, June 1985.

[6] O. Dahl and L. Nielsen, "Torque-limited path following by online trajectory time scaling," *IEEE Transactions on Robotics and Automation*, vol. 6, pp. 554–561, Oct 1990.

[7] O. Dahl, "Path-constrained robot control with limited torques-experimental evaluation," *IEEE Transactions on Robotics and Automation*, vol. 10, pp. 658–669, Oct 1994.

[8] L. Zlajpah, "On time optimal path control of manipulators with bounded joint velocities and torques," in *Proceedings of IEEE International Conference on Robotics and Automation*, vol. 2, pp. 1572–1577 vol.2, April 1996.

[9] T. Yoshikawa, *Foundations of Robotics : Analysis and Control.* The MIT Press, 1990.

[10] J. Wanner and O. Sawodny, "Tool-center-point control of a flexible link concrete pump with hydraulic limitations using quadratic programming," in *2019 IEEE 15th International Conference on Automation Science and Engineering (CASE)*, pp. 561–566, Aug 2019.

[11] L. Sciavicco and B. Siciliano, *Modelling and Control of Robot Manipulators*. Advanced Textbooks in Control and Signal Processing, Springer-Verlag London, 2 ed., 2012.

[12] RamBooms, "Rambooms X88-540R rock breaker boom." Available at: `https://mrbbooms.com/x-series/x8/x88-540r/` (accessed 3.4.2019).

[13] J. Nurmi and J. Mattila, "Automated feed-forward learning for pressure-compensated mobile hydraulic valves with significant dead-zone," in *Proc. of ASME/BATH Symp. on Fluid Power and Motion Control (FPMC2017), Oct. 16-19, 2017, Sarasota, Florida*, 2017.

[14] M. Krstić, I. Kanellakopoulos, and P. Kokotović, *Nonlinear and Adaptive Control Design*. John Wiley & Sons, Inc., 1995.

[15] S. Lampinen, J. Koivumäki, J. Mattila, and J. Niemi, "Model-based control of a pressure-compensated directional valve with significant dead-zone," in *ASME/BATH 2019 Symposium on Fluid Power and Motion Control*, American Society of Mechanical Engineers Digital Collection, 2019.

[16] J. Koivumäki and J. Mattila, "Stability-guaranteed force-sensorless contact force/motion control of heavy-duty hydraulic manipulators," *IEEE Trans. Robot.*, vol. 31, pp. 918–935, Aug 2015.

[17] R. N. Jazar, *Theory of Applied Robotics: Kinematics, Dynamics, and Control*. Springer Publishing Company, 2nd ed., 2010.

PUBLICATION

III

Autonomous robotic rock breaking using a real-time 3D visual perception system

S. Lampinen, L. Niu, L. Hulttinen, J. Niemi and J. Mattila

Journal of Field Robotics 38.7 (2021), 980–1006
DOI: `10.1002/rob.22022`

Received: 10 September 2020 | Revised: 17 March 2021 | Accepted: 30 April 2021
DOI: 10.1002/rob.22022

RESEARCH ARTICLE

WILEY

Autonomous robotic rock breaking using a real-time 3D visual perception system

Santeri Lampinen[1] | **Longchuan Niu**[1] | **Lionel Hulttinen**[1] | **Jouni Niemi**[2] | **Jouni Mattila**[1]

[1]Faculty of Engineering and Natural Sciences, Unit of Automation Technology and Mechanical Engineering, Tampere University, Tampere, Finland

[2]Rambooms Oy, Lahti, Finland

Correspondence
Santeri Lampinen, Faculty of Engineering and Natural Sciences, Unit of Automation Technology and Mechanical Engineering, Tampere University, Tampere, Finland.
Email: santeri.lampinen@tuni.fi

Abstract

Crushing of blasted ore is an essential phase in extraction of valuable minerals in mining industry. It is typically performed in multiple stages with each stage producing finer fragmentation. Performance and throughput of the first stage of crushing is highly dependent on the size distribution of the blasted ore. In the crushing plant, a metal grate prevents oversized boulders from getting into the crusher jaws, and a human-controlled hydraulic manipulator equipped with a rock hammer is required to break oversized boulders and ensure continuous material flow. This secondary breaking task is event-based in the sense that ore trucks deliver boulders at irregular intervals, thus requiring constant human supervision to ensure continuous material flow and prevent blockages. To automatize such breaking tasks, an intelligent robotic control system along with a visual perception system (VPS) is essential. In this manuscript, we propose an autonomous breaker system that includes a VPS capable of detecting multiple irregularly shaped rocks, a robotic control system featuring a decision-making mechanism for determining the breaking order when dealing with multiple rocks, and a comprehensive manipulator control system. We present a proof of concept for an autonomous robotic boulder breaking system, which consists of a stereo-camera-based VPS and an industrial rock-breaking manipulator robotized with our retrofitted system design. The experiments in this study were conducted in a real-world setup, and the results were evaluated based on the success rates of breaking. The experiments yielded an average success rate of 34% and a break pace of 3.3 attempts per minute.

KEYWORDS
computer vision, control, manipulators, mining, perception

Santeri Lampinen and Longchuan Niu should be considered as joint first authors.

1 | INTRODUCTION

Driven by safety and operational cost concerns, mining and construction automation systems have recently acquired foothold in various process phases of the mineral industry. However, many mineral processing tasks still involve unautomatized manual work that requires constant human supervision and intervention, which can act as a critical bottleneck for the process throughput.

One such task is secondary breaking, where controlled size reduction of mineral ore is achieved with heavy-duty manipulators equipped with hydraulic impact hammers. The mining industry extensively uses these types of rock breaker booms for size reduction of oversized boulders, which we will refer to as “rocks” in this paper. The economic justification for using such booms is to reduce process delays and ensure a steady flow of material, leading to minimal process downtime, maximized throughput, and increased productivity.

Rock breaker booms can be roughly divided into two categories based on their application. Small-scale breaker booms are used in mobile jaw crushers (see Figure 1a) to resolve material blockages, for example, for breaking oversized rocks entering the crusher cavity. In contrast, large-scale pedestal-mounted breaker booms (see Figure 1b,c) are mainly used in stationary grizzly applications, for example, in underground and surface mines, to process run-of-mine ore delivered by trucks. In grizzly applications, a steel grate is used as a screening medium to control the coarseness of the material entering an ore pass. In the event of buildup caused by oversized rocks that cannot pass through the openings of the grate structure, the rocks must be demolished into smaller particles using the hydraulic impact hammer.

Rock breaking systems require skilled and alert operators, since the interaction between the hammer and the rocks must be controlled with appropriate levels of force. Presently, rock breaking systems are largely operated via manual open-loop control of each individual joint, making their use inergonomic and unintuitive from the operator's point of view, thus increasing accident-proneness. Much of an operator's cognitive effort is dedicated to avoiding potentially dangerous and/or harmful situations, such as sudden loss of contact between the hammer and the rock, which might cause idle strokes of the hammer in the air–or worse, an unintended collision with the environment, which could deteriorate the hammer and shorten its lifespan (Sandvik Mining and Construction, 2016). Impact on the grizzly itself must also be avoided, as breaking it can lead into prolonged downtime in production. It has also been reported that nearly three out of four crane accidents are operator-induced (Lovgren, 2004), which is a strong argument for developing semiautonomous solutions for rock breaking systems. With this in mind, it is worth noting that even human operators cannot achieve a 100% success rate in the breaking process, but will experience many failed attempts resulting from rocks being moved under the hammer during break attempts. Another strong argument for semiautonomous and autonomous systems is the fact that labor represents a major share of costs in underground mining operations (Hustrulid & Bullock, 2001). The fact that a large-scale underground mine can contain several crusher units further highlights the significance of automating this phase of the mining process.

To automate such breaking tasks in a harsh environment, the need for an intelligent robotic system with visual perception is evident. Human operators can easily distinguish between individual rocks on the grizzly and choose an ideal spot on the rock's surface to break it efficiently. However, real-time three-dimensional (3D) rock detection is challenging, as rocks come in arbitrary shapes, sizes, colors, and surface textures and do not follow any specific patterns. The high-precision control of the breaker boom presents another challenge, as the manipulators have been designed with manual operation in mind, and are thus typically equipped with slow control valves with highly nonlinear characteristics. In addition, a successful breaking process involves accurate pose estimation of the rock (the 3D position and 3D orientation of its major surface plane), precise calibration of the intrinsic and extrinsic camera parameters as well as the robotic manipulator itself, and a reliable decision-making mechanism that takes action autonomously after an oversized rock has been detected.

In this manuscript, we propose an autonomous robotic rock breaking system that utilizes the 3D object detection pipeline

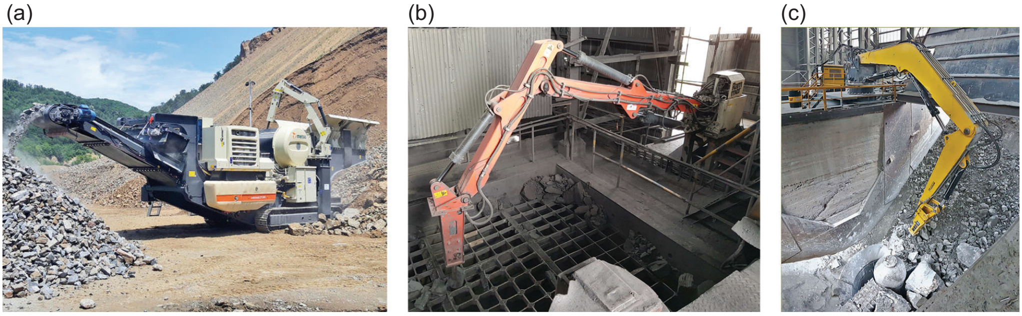

FIGURE 1 (a) A rock breaker boom on a Metso Locotrack mobile crusher, (b) a pedestal breaker boom in a grizzly application, and (c) a breaker boom at a gyratory crusher facility [Color figure can be viewed at wileyonlinelibrary.com]

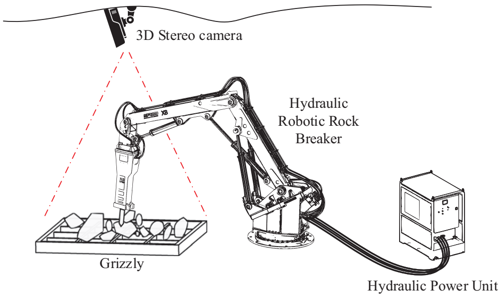

FIGURE 2 Conceptual illustration of the proposed autonomous rock breaker system [Color figure can be viewed at wileyonlinelibrary.com]

proposed in Niu et al. (2019) to automatically detect and localize rocks on the grizzly using a low-cost stereo camera. The rock positions are utilized by our real-time control system for which we have designed a robust decision-making mechanism along with a comprehensive manipulator controller, trajectory generator, and rock breaking control algorithm. Figure 2 illustrates the proposed system on a practical level. We present the measures conducted to precisely calibrate each subsystem, first separately and then together as a complete system. The outcome of this manuscript culminates on a field experiment of the system that acts as a technological proof of concept in a simplified environment.

1.1 | Literature review

Previous works concerning the automatization or modernization of rock breaking systems are few. The first reported attempts at autonomous vision-based rock breaking originates from 1998. Takahashi and Sano (1998) proposed an early image processing approach to detect rocks on the grizzly. The position of the rocks was obtained by complementing image data with a laser pointer mounted on the manipulator. Corke et al. (1998) proposed an actuated scanning laser rangefinder to identify and localize rocks. However, it was evaluated insufficient based on a concluded field test. In the field test, the rangefinder was positioned only slightly above the grizzly, and thus larger rocks on the grizzly blocked the view easily. The study discussed different visual sensing approaches as well, such as stereo vision, and proposed a concept of a semiautomated rock breaker. They identified several key requirements for an automated rock breaker system, such as a closed-loop controlled breaking boom, a 3D sensing system, an autonomous decision-making system, and a teleoperation system as a backup control method. They proposed a system that attempts to autonomously break rocks on the grizzly; if unable to complete the operation, it signals an operator to finish the job. With limited human intervention required, one operator could monitor several booms at the same time. The study was concluded, however, with a statement that the technology for such system is “many decades from reality.”

The first teleoperated rock breaker was reported in Hubert et al. (2000). Designing a teleoperation system for the rock breakers was motivated by safety concerns. An underground mine in Indonesia was suffering from wet muck spills that placed the machine operators in danger. A communication system was designed to control the manipulators from a surface control room, but the machine operation was kept in open-loop manner. More recently, teleoperated rock breakers have been proposed by Duff et al. (2010), who demonstrated teleoperation over a distance of 1000 km over the internet. The breaker boom was also under closed-loop control, and the operator used resolved rate control to affect the velocity of the manipulator tip directly. Automatic deployment and parking of the manipulator was incorporated into the system with a mixed reality interface that combined computer-generated scene of the environment with reconstructed rocks on the grizzly. The 3D view from the grizzly was obtained using two stereo cameras. A more recent approach was reported in Boeing (2013) which discusses a system reportedly similar to the one presented by Duff, but it is accompanied by a collision avoidance system to prevent collisions with the environment.

Space exploration has also advanced the sophistication of vision based rock detection. In Fox et al. (2002), 2D camera images were combined with range data to detect larger rocks autonomously. A more recent study of the automatic detection of large rocks using a time-of-flight (TOF) camera, which is commonly used in the industry, was presented in McKinnon and Marshall (2014). The intended application was evaluating rock piles for excavation purposes. In Niu et al. (2018), a TOF camera was employed for rock detection on the grizzly, but the TOF camera's low resolution made it insufficient for the task. In Niu et al. (2019), a deep learning approach was presented in which the functionality of “you only look once” version 3 (YOLOv3), a state-of-the-art real-time object detection algorithm (Redmon & Farhadi, 2018), was extended from using 2D images to 3D point clouds for rock detection.

The notable lack of more recent reported automated rock breaking applications indicate that there is further room for improvement and plenty of opportunities to apply visual perception and robotic control in rock breaking tasks, with the aim of making rock breaking systems safer, faster, and more efficient.

1.2 | Organization of the manuscript

The rest of this paper is organized as follow: Section 2 states the problem this manuscript aims to solve, along with the identified challenges and research objective. Section 3 presents the design of each subsystem of the proposed system. The section describes first the architecture on a high level, then in more detail about the visual perception and the control system design. Section 4 discusses the calibration of the manipulator and camera, as well as their integration into the same coordinate system. Section 5 presents the experiments with the proposed system and discusses about the obtained results. Section 6 discusses identified shortcomings of the proposed system and suggests improvements to address these issues. Section 7 concludes the paper with a projection on future research potential in this area of study.

2 | PROBLEM STATEMENT

2.1 | Rock breaking—use case

Size reduction of blasted ore is an integral part of mineral extraction in mining. It is an essential process in the sense, that smaller ore pieces can be transferred more easily and also chemical/mechanical extraction methods can be applied to them. Size reduction of the vast majority of material is performed using a primary breaker (e.g., gyratory- or jaw-crusher), while oversized rocks, too big for the primary breaker, need to be broken with a secondary breaker.

Secondary breaking processes utilizing impact breaking can occur in multiple contexts, for example, directly at the blasting site using an excavator-mounted hydraulic hammer or with a special breaker boom at a gyratory crusher against the wall of the gyrator cone. In this study, our focus is on grizzly applications (see Figure 3), where a steel grating plate is used to prevent oversized rocks from getting into the primary crusher. The primary crushers are designed for a specific size reduction of the material flow, and overly coarse material can lead to material buildups or even material flow blockage, thus halting the entire operation.

The need for secondary breaking varies between mines and construction sites and depends on the material being processed. Even so, the need for secondary breaking is a symptom of imperfect blasting and problems in the blasting process. In ideal conditions, the blasting cycle is controlled to obtain material of a desired size (Zhang, 2016). When the process is well controlled, the need for secondary breaking is minimal.

Whenever oversized rocks are caught on the grizzly structure, the rock hammer is used to reduce their size. This temporarily halts material flow; for example, an ore truck must stop feeding material to a silo until the breaker boom operator breaks the oversized rocks into smaller pieces that can pass through the grizzly. If the boom cannot execute its task in a limited time frame, the rock is pushed away from the grizzly for later processing and the arm returns to its resting position. The material that cannot pass through the openings of the screening medium should be broken with a hydraulic hammer. This process is referred to as screening, which is an essential step in crushing unprocessed run-of-mine ore and turning it into a finer substance suitable for further treatment (Metso Mining and Construction, 2015).

The actual use case studied here can be described as the process of breaking an oversized rock caught in the grizzly. Additional use cases in grizzly applications are raking with the boom to break and prevent blockages, and reorienting hard-to-break rocks for easier breaking. The current study is limited to the breaking process. The studied use case can be described on a high-level with the following steps:

(1) The boom is driven from a rest position to a standby position beside the grizzly, with its hammer kept at a 90-degree angle relative to the grizzly.
(2) A 3D visual perception system (VPS) detects and localizes oversized rocks on the grizzly and passes the information on to the main control system.
(3) The main control system determines the shortest rock-to-rock trajectory from the information provided by the VPS, employing a lower level control system to break each rock.
(4) The path planner receives the target rock coordinates from the high-level controller and generates a trajectory from the manipulator's current position to a position above the target rock.
(5) An approach motion toward the target rock is performed while maintaining the desired tool orientation.
(6) When target coordinates are reached, the boom maintains pressure against the rock and switches the rock hammer on.
(7) After the rock has been broken, the boom shall rise up to a safe transition height and wait for the next target from the high-level control system.

FIGURE 3 Rambooms X88-540R breaker boom at the field test site at Tampere University [Color figure can be viewed at wileyonlinelibrary.com]

(8) After clearing the rocks, the boom returns to the standby position to wait while the VPS inspects the work and identifies remaining rocks on the grizzly.

A critical issue in rock breaking is to make contact with the rock in a controlled manner and with sufficient force against the rock. In the case of grizzly applications, tool alignment is an important issue, as the supportive force from the grizzly points upward and there is not necessarily anything holding the rock in place in the horizontal plane. In these scenarios, roughly a 90-degree angle relative to the grizzly is the most suitable (see Figure 3). An incorrect breaking angle may cause excess wear and stress to the manipulator or the rock can slip away under the hammer. Situations in which a hydraulic cylinder is at its mechanical stroke limit during hammer operation must be avoided. Given all these concerns, significant attention and effort is necessary to avoid dangerous situations and achieve a good contact with the rock.

2.2 | Challenges

To implement an autonomous system for the rock breaking process, we have identified four distinct main challenges we will need to consider and solve. The challenges are related to: (1) The visual perception, (2) the autonomous operation strategies, (3) the high-precision manipulator control and stable contact control, and (4) system calibration and integration.

To achieve autonomy in the rock breaking process, it is crucial for the robot to properly understand the scene. However, detecting each individual rock in a cluttered and dynamic scene is a highly complex activity, as rocks cannot be characterized by any particular feature. They may possess a variety of colors, unique surface textures and arbitrary shapes and sizes. Despite these challenges, the VPS should operate robustly under dynamic outdoor weather conditions being able to accurately detect all rocks in the grizzly. The detection must also include rocks partially occluded by overlapping rocks or the manipulator arm. The VPS should propose a suitable breaking position based on the surface of each rock.

Next, we need a robust and efficient strategy for autonomous operation. The decision-making process should consider the shortest trajectories between rocks and have the ability to govern manipulator movement sequences. To properly make decisions, perception information from the vision system must be assessed and cataloged. In addition, the system should discern valid rock positions and discard any invalid positions received from the perception system. Locations may be considered invalid for rocks below the grizzly and rocks outside the grizzly.

Building the control system for the robotic manipulator is another challenge that requires sophisticated and rigorous solutions. As the manipulator is not retrofitted with fast servo valves and has a slow natural frequency, its precise control requires thorough consideration. Other constraints, such as tool orientation and flow rate limitations need consideration as well.

For contact control, we assume the accuracy of the manipulator's tool center point (TCP), which is the tip of the hammer, to stay at all times within the initial requirement of 150 mm from the target position. As rocks are typically much larger than this and the mesh size in our testing grizzly is 400 × 400 mm, this accuracy requirement is reasonable. Based on our preliminary experiments, the most challenging task is making contact with rock surfaces so that they do not slide under the hammer or tip over. Since blasted boulders come in arbitrary shapes and sizes with sharp edges, they end up laying on the grizzly randomly. As a consequence, the following two main challenges apply to rock breaking: first, a boulder or multiple piled boulders may be poorly balanced on the grizzly and thus cannot support the required hammer tip loading force without rotating into new orientations, slipping away from the applied contact force and thus failing to break. Second, if a boulder has inadequate flat surface area for firm hammer contact force, the hammer tip may slide along the rock without breaking it.

Uncertainty about subsystem-level accuracies is also a challenge in estimating the final system performance and accuracy. Individual subsystem calibration for the robotic manipulator and stereo camera is required to estimate the accuracy of the final autonomous system. Causes of uncertainty about the accuracy of the final system can be the precision of rock detection model, the accuracy of the intrinsic and extrinsic camera calibration, kinematic parameters of the manipulator used to calculate TCP position, and control system accuracy.

The most important challenge, however, is integrating all the distinct subsystems together with their respective safety functions. Responsibilities and communication between subsystems can be vague and multifaceted, and managing their complexity is critical.

2.3 | Research objective

The primary objective of this manuscript is to demonstrate a proof of concept for an autonomous hydraulic breaker boom system. The aim of this manuscript is not to showcase a finished product, but rather to demonstrate the feasibility of the concept. This should be noted when evaluating the experimental results and required hardware.

The major function of the robotic VPS is twofold: first, achieving a fast and robust 3D rock detection mechanism regardless of rock shapes and sizes in overlapping scenarios, and second, providing reliable positions for the manipulator to break rocks. The objective of studying visual perception systems is to assess their effectiveness in detecting objects with unpredictable features for heavy duty manipulator applications.

From the control system point of view, the objectives can be categorized as the desired control accuracy of the manipulator and the desired behavior of the autonomous functions and safety features. Given the size of the rocks being broken, the absolute accuracy of the control system should be within 150 mm, which an interview with a domain expert substantiated. Manipulator limitations, such as the size of the control valves, that define maximum velocity for each actuator, maximum volumetric flow rate of the hydraulic supply unit that limits maximum endpoint velocity, and the reachable workspace, must be taken in account when designing the control system.

Our goal is to make the manipulator independently decide an intelligent rock breaking order based on the data provided by the VPS, generate trajectory between each rock, execute the trajectory in the breaking process. While the chance of successful breaks will not be high initially, we will also endeavor to make the system detect rocks from the grizzly during operation and adjust its plan in real time. Safety functions built into the control system prevent impact to the grizzly during the breaking process to avoid damage to the hammer and premature component failure.

3 | SYSTEM DESIGN

3.1 | High-level architecture

The proposed system comprises of three distinct parts: the instrumented hydraulic breaker boom and its hydraulic power unit, the VPS and the real-time control system that governs decision-making, the manipulator control system, and all measurement data. The complete system is depicted in the high-level architecture diagram in Figure 4.

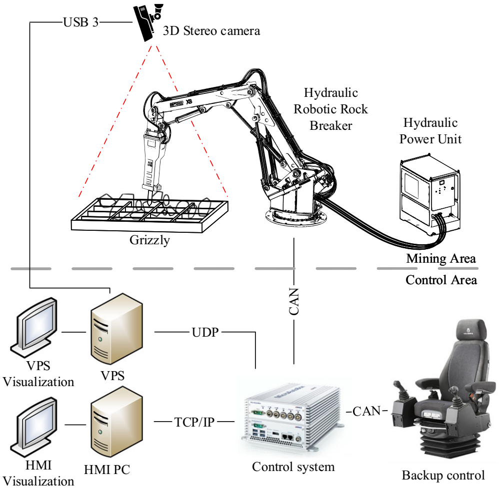

FIGURE 4 High-level architecture of the proposed system. For clarity, the site cameras surrounding the crushing site and their visualization computer has been left out. HMI, human machine interface; TCP, tool center point; UDP, user datagram protocol; VPS, visual perception system [Color figure can be viewed at wileyonlinelibrary.com]

3.1.1 | Hardware architecture

The hydraulic breaker boom used in this study was the commercial Rambooms X88-540R manipulator equipped with a Rammer 2577 hydraulic impact hammer. The breaker boom weighs in total over 10,000 kg and has a horizontal reach of 5.4 m with the breaker in vertical orientation. The coordinate frame assignment of the manipulator along with the joint naming convention is shown in Figure 5. The link lengths a_2, a_3, and a_4 in Figure 5 are all roughly 3 m. The size of the grizzly (see Figure 3) is 2.6 m × 4.0 m. The manipulator was retrofitted with Siko WV58MR 14-bit absolute rotary encoders for joint angle measurements. The sensor data and the valve controls were transmitted to and from the real-time control system via CAN-bus interfaces.

The 3D VPS consists of a ZED stereo camera and a Linux PC. The stereo camera is mounted on a pole approximately 5 m above the workspace such that the grizzly is centered in the camera's field of view. The 3D VPS is connected to the real-time control system through a user datagram protocol (UDP) interface.

The real-time control system was run on a dSpace MicroAutoBox 2 real-time controller, where all control computations and decision-making logic were performed. The interface for the real-time controller was created using the dSpace ControlDesk software on a separate human machine interface (HMI) PC.

3.1.2 | Software architecture

The software architecture is divided into two parts based on the hardware architecture; The VPS running on a linux PC and the control system running on the dSpace real-time controller. The VPS is responsible for perceiving rocks on the grizzly, using the data from the stereo camera to detect and localize rocks and estimate the pose of the major surface plane near the highest point of the rocks. The

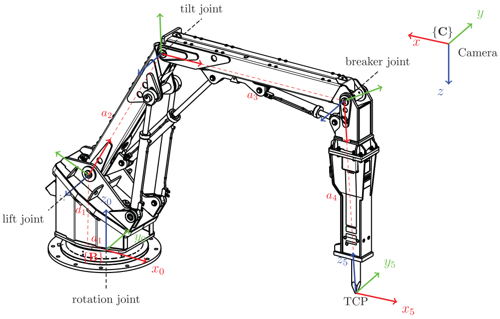

FIGURE 5 Coordinate frame assignment for the breaker boom. Frame {B} denotes the base coordinate frame of the manipulator, while frame {C} denotes the coordinate frame of the stereo camera. Joint naming convention is also depicted on the figure and the TCP is marked. TCP, tool center point [Color figure can be viewed at wileyonlinelibrary.com]

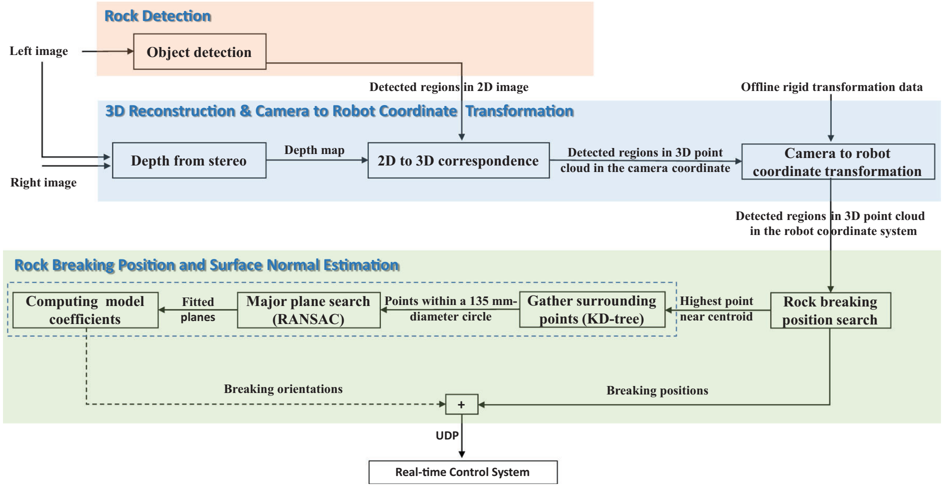

FIGURE 6 Workflow architecture of the 3D visual perception system [Color figure can be viewed at wileyonlinelibrary.com]

operation of the VPS is described in detail in Section 3.2. The real-time control system is responsible for decision-making related to break order logic, controlling the movements of the manipulator, and managing the safety functions. The operation of the control system is described in Section 3.3.

3.2 | Visual perception system

A high-level architecture for the workflow of the 3D VPS is illustrated in Figure 6, which consists of three stages: rock detection, 3D reconstruction and camera to robot coordinate transformation, and position and orientation estimation for rock breaking. At the first stage, the object detection module processes the left images of the ZED stereo camera and extracts the detected rocks as 2D regions. At the second stage, the detected 2D regions are reconstructed into 3D point clouds in the camera coordinate system with the aid of calibrated intrinsic camera parameters and the depth map. Then, the detected rock regions in 3D point clouds are transformed into the manipulator's coordinate system. At the last stage, the positions required to break each rock are determined by searching the highest point near the centroid of each region. The surface normals of each rock are estimated (in the dashed area in Figure 6) using KD-tree and RANSAC.

3.2.1 | 3D sensing modalities

Common 3D visual perception sensors are Lidar sensors, TOF cameras, and stereo cameras. The 3D sensor selected for visual perception must account for the aforementioned design challenges. At the boundary distance of 5 m to the grizzly, the mesh (400 × 400 mm) and rocks of similar size may appear small in the field of view. The empirical study with a TOF sensor (Niu et al., 2018) implies that spatial resolution and the amount of available information from a scene are decisive factors in accurate rock detection.

Lidar is gaining popularity across industries. However, compared to high-resolution images, Lidar point clouds are unstructured; as such, generic convolutional neural network (CNN) are not well suited to process them directly (Qi et al., 2019). In addition, relatively sparse Lidar point clouds can be inadequate in assessing the details of a scene where a pile of small irregularly shaped rocks are overlapping each other. In fact, current 3D object detection methods in Lidar applications have been targeted for use with spatially independent objects (Al Hakim, 2018; He et al., 2020; Ku et al., 2018; Liang et al., 2019, 2018; Qi et al., 2018; Yang et al., 2018; Zhao et al., 2019; Zhou & Tuzel, 2018). In contrast, an industry-ready stereo camera provides both high resolution images and dense point clouds. Its images contain rich texture information which is a useful cue for discriminating objects from the background. Therefore, we adopted a stereo camera in this study.

A camera setup can be classified as eye-in-hand or eye-to-hand. The eye-in-hand configuration is known as a close-range camera, which is rigidly attached to a robot's end effector. For rock breaking, this setup requires sustainable solutions to the following challenges: (1) involvement of robot and eye-in-hand calibration errors, (2) susceptibility to heavy vibrations, and (3) fragile lenses in close proximity to hazardous rock breaking operations. In light of these challenges, we considered eye-to-hand configuration, in which a compact ZED stereo camera is mounted on a pole 5 m above the workspace.

3.2.2 | Object detection

Three-dimensional object detection is one of the most prominent research areas of visual perception that serves as base for autonomous robotic tasks. As one of the main challenges in autonomous rock breaking, rock detection requires a deep understanding of the contexts of a scene. Background removal with semantic segmentation is inefficient, as this task requires every rock to be made visually distinct from one another in a cluttered and dynamic scene.

In recent years, deep learning frameworks have been available to computer vision applications to assist learning of deep and high-level features. The substantial improvements to object detection have mostly been applied to 2D images rather than 3D point clouds. Generally, 2D convolution-based detection approaches are more sophisticated than 3D ones in industrial deployment. Among a number of 2D object detection architectures, region-based methods like region-based convolutional neural networks (R-CNN) (Girshick et al., 2014), Fast R-CNN (Girshick, 2015), and Faster R-CNN (Ren et al., 2015) are accurate for detecting multiple objects in an image. However, their rather complex architectures and relatively low detection speeds are not sufficient for our purposes. In addition, the potential source of errors is high due to their complexity.

Mentioned briefly in the literature review, the object detection algorithm YOLOv3 prioritizes both recognition and speed. It is an improved version of the initial release of YOLO (Redmon et al., 2016), that used a new approach to object detection. Instead of repurposing classifiers to perform detection, YOLO uses a single neural network to predict bounding boxes and class probabilities from a full image. The third version, YOLOv3, is the result of incremental updates (Redmon & Farhadi, 2017, 2018), and it achieves high precision and high speeds on benchmark data sets; as such, the infrastructure of our deep learning network for object detection is based on YOLOv3.

The next step in deep learning is gathering data, the quality and quantity of which will determine the performance of the model. Our rock image data set initially contained 4733 distinct images[1] collected from the field test site (see Figure 3), where the amount of rocks varied between 1 and 15. These images were taken in September and October of 2018. The image data set contains images taken under sunny daylight condition. Images exhibiting other seasonal and weather-based conditions, such as rain, snow, and fog, are missing.

To emulate these missing weather conditions, synthetic data via data augmentation can be used to bridge the experiment-reality gap. Generating realistic environmental variant data can be achieved using OpenCV and NumPy in Python. Besides different weather conditions, also dynamic lighting can cause challenges for the stereo camera and the model. For example, rock edges may become indistinguishable under bright lighting conditions. With this in mind, our data augmentation process involves generating portions of brighter images for labeling. This way the original data set was expanded to a total of 23,850 images. More training data from situations the model cannot cope with might be used to further improve it. Such conditions may include for example, low and bright lighting, and partly shaded rocks.

Our image data set contains only one class: the “rock” class. The data set was split into three parts: 70% images for training the model, 20% images for validation, and 10% images for testing. The training was conducted on YOLOv3's darknet-53 architecture (Redmon, 2018) on an Ubuntu 16.04 Linux PC with a NVIDIA Quadro P5000 graphics card. The training step used our training set to incrementally improve the model's ability to make inferences, while each epoch updated the weights of the model. The training converged at an average loss of 0.12 with a batch size of 64 and a learning rate of 0.001. An evaluation experiment given in Figure 7 illustrates the results of the model inference after training. It also points to the improvement gained through data augmentation.

To further evaluate the performance of our model, we used the average precision (AP) metric to compute precision and recall by Equation (1), where TP denotes the number of true positives, FP the number of false positives, and FN the number of false negatives.

$$\text{Precision} = \frac{TP}{TP + FP}, \quad \text{Recall} = \frac{TP}{TP + FN}. \tag{1}$$

Table 1 shows the test with the AP metric, where AP_{50} and AP_{75} denote the average precision computed at an intersection over union (IOU) threshold of 0.5 and 0.75, respectively. An average detection speed of 85 ms per frame was achieved during testing.

3.2.3 | Establishing 2D to 3D correspondence

Estimating scene geometry from a pair of pinhole cameras is often referred to as depth-from-stereo. For ease of setup, we employed a ZED stereo camera. From the left and right images of a stereo camera, its depth map can be generated with a rectification-based stereo-matching method (Scharstein & Szeliski, 2002) or plane-sweeping method (Smirnov et al., 2015). A depth map is an image representing the depth information of the scene associated with the corresponding left and right images of the stereo camera.

With the left image and associated depth map, a 3D point cloud of the scene can be reconstructed with the camera's intrinsic parameters. As illustrated in Figure 8, this 3D reconstruction process is known as triangulation, which can be applied to detected regions in an image to generate detected regions in a 3D point cloud. Processing a 3D point cloud of only the detected regions instead of the whole image decreases the associated computational burden.

3.2.4 | Determining the breaking position for each rock

The detected rocks are represented as rectangular regions in a 2D image. The position of the geometrical center of each detected rectangular region is used to describe each rock position in the image

---

[1] https://github.com/epoc88/SecondaryBreakingDataset

TABLE 1 Average detection rates of our model

	AP_{50} (%)	AP_{75} (%)
Proposed method	99.00	97.61

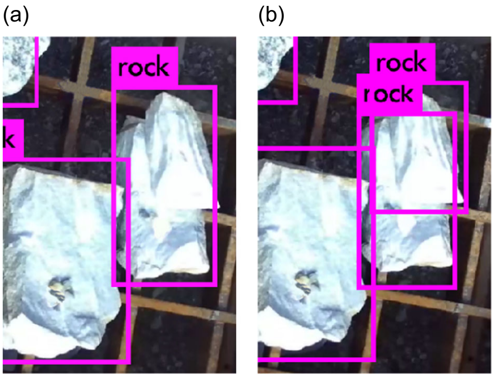

FIGURE 7 Compared detection results following data augmentation. The scenario depicts a smaller rock on top of a bigger rock under overexposed lighting conditions. (a) Original model (Niu et al., 2019) and (b) improved model [Color figure can be viewed at wileyonlinelibrary.com]

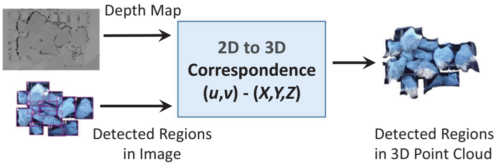

FIGURE 8 This figure illustrates the process of obtaining 3D point cloud of detected regions from stereoscopic imagery. To each pixel (*u*,*v*) in a detected region, there is corresponding depth information in the depth map. Combining these two sources for each detected region, we acquire a 3D point cloud representation of the detected objects in the camera's coordinate system [Color figure can be viewed at wileyonlinelibrary.com]

coordinate system, which can be transformed into the robot coordinate system by using the calibrated intrinsic and extrinsic camera parameters, see Figure 17.

The geometrical centroid of the identified rectangle itself is not necessarily an ideal breaking position due to fact that the detection algorithm does not take the shape of the rock into account. A better alternative for the breaking position can be obtained instead by searching for the highest point near the identified centroid. An examplatory case is depicted in Figure 9. The centroid position as it appears to the camera is not an ideal breaking position, and the attempt would fail with a high likelihood due to a probable rock movement.

Based on our preliminary field tests, the highest point near the centroid of a rock typically yields the highest likelihood for successful breaking. Thus, we limit the search area to a concentric rectangle quarter the size of the detected region. Breaking positions outside of the search area are discarded, in view of the fact that the likelihood of the manipulator slipping or the rock moving increases when the breaking position is located near the edges of the rock.

3.2.5 | Estimating the rock surface normal

At the time of breaking, the tip of the manipulator's blunt tool is in contact with the rock's breaking position. The contacted area must be within roughly 70 mm of the highest point, as the diameter of the manipulator's blunt tool is 135 mm. To transfer the energy of the impact hammer to the rocks most efficiently, the orientation of the hammer must be perpendicular to the surface of the rocks. To achieve this, the orientation of the rock surface must be estimated. This process is divided into three steps:

(a) *Gather surrounding points*: A KD-Tree algorithm (Bentley, 1975) is used to search for points contained within a sphere with the same diameter as of the blunt tool and centroid at the breaking position. The search yields a cluster of points in the form of circular areas at each rock surface. For a visualization, see the points colored in blue in Figure 10.

(b) *Major plane search*: This step analyzes every cluster of points and carries out plane fitting with a RANSAC algorithm (Fischler &

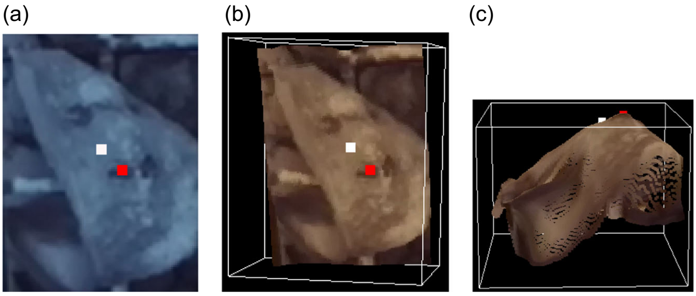

FIGURE 9 A detected rock region in a 2D image and a 3D point cloud. The white and red dots in the figure indicate the centroid of the detected region and the highest point within a quarter of the size of the detected region, respectively. (a) The rock in 2D image, (b) a point cloud from above, and (c) a point cloud from the side [Color figure can be viewed at wileyonlinelibrary.com]

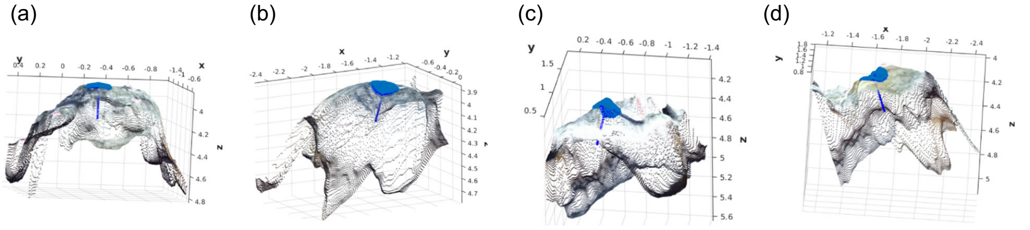

FIGURE 10 Some examples of estimated surface normals. The blue clusters are the rock surface points nearby each breaking position, and the blue arrows indicate the estimated surface normals. (a) Rock 1, (b) rock 2, (c) rock 3, and (d) rock 4 [Color figure can be viewed at wileyonlinelibrary.com]

Bolles, 1981). The algorithm randomly takes three points in the cluster to establish a plane. Points lying close to the plane are considered the consensus set for the plane. This process repeats until all the planes in the cluster are found; the plane with the largest consensus set is accepted as the fitted plane.

(c) *Computing model coefficients*: Finally, the model coefficients of each plane are computed to obtain the corresponding normal vectors of the plane. An example of the results of this process are shown in Figure 10.

In the conducted experiments, the 90 degree orientation of the hammer to the surface at the point of contact was not applied. Instead 90 degrees relatively to the grizzly was used.

3.3 | Control system

The control system design is depicted at a general level in Figure 11. The control system can be divided into four distinct subsystems with specific tasks. The breaking order logic and path optimization initializes the pipeline, working at a high level to determine rock breaking order. The second highest level subsystem is the high-level manipulator controller, a state machine that dictates the operation of the manipulator. The third level consists of the trajectory generator and is closely interconnected with the inverse kinematics controller and the flow rate limitation algorithm. The lowest level controller is used for the actual manipulator control, which uses desired joint angles and velocities as well as the operational state of the hydraulic hammer.

3.3.1 | Break order logic

The break order logic subsystem is devised around the idea that the manipulator might be blocking the camera's view, making it inevitable that the logic would store previous rock locations sent by the VPS. The path optimization should minimize movement between rocks. The optimal trajectory for breaking each rock in a sequence could be obtained by finding a solution to the classical traveling salesman problem, in which a traveling salesman seeks to find the shortest path that visits each city exactly once and return to the origin. To limit the complexity of our solution, we opted for a simple heuristic nearest neighbor approach with some additional constraints. The developed approach is showcased in the high-level

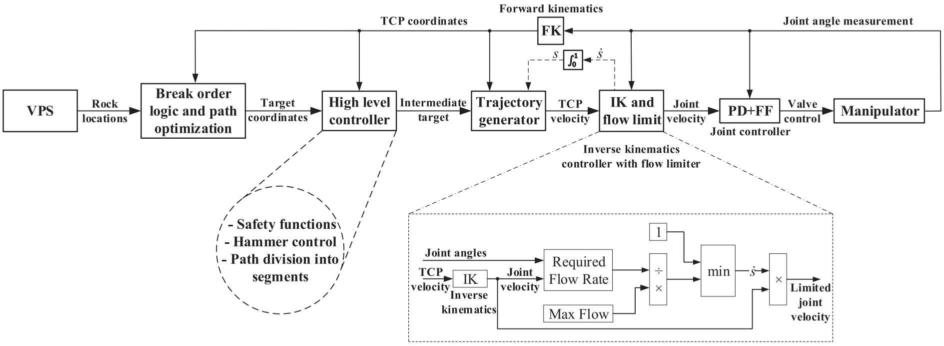

FIGURE 11 General block diagram of the proposed control system for autonomous operation. The VPS in the first block on the left is described in more detail in Figure 6

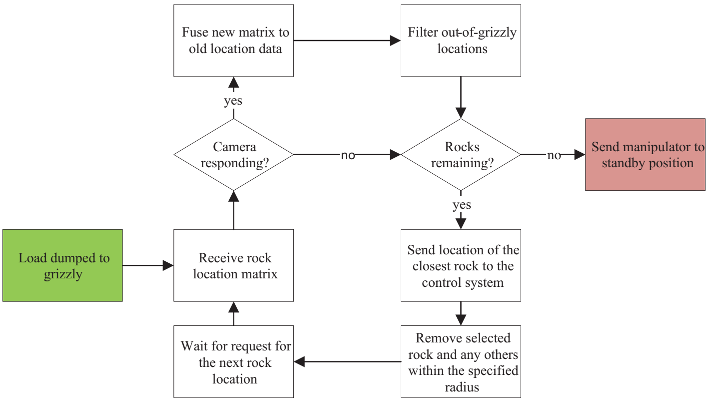

FIGURE 12 Breaking order logic pipeline. The start of the process is marked with green color and the end with red. The loop in the middle is continued until no rock are remaining on the grizzly [Color figure can be viewed at wileyonlinelibrary.com]

diagram in Figure 12. The pipeline can be described by the following steps:

(1) The cycle starts when a load of rocks is dumped on the grizzly, and the system receives command to begin operation. In our experiments, the cycle was started manually.
(2) First, rock positions from the VPS are obtained via UDP messages. If the vision system does not respond within a specific time frame (e.g., camera view is blocked by manipulator), the next target is determined using existing data. At the first round, the manipulator is at its standby position and not blocking the view.
(3) The received data is then fused into the existing location data. This step is omitted in the first round. The data fusion is performed by calculating the Euclidean norm between each rock from the old and the new data set. If the norm between a rock from the old and the new data set is less than or equal to 0.1 m, the rocks are assumed to be the same, and the old position for that particular rock is updated to correspond to the newly obtained information. If the norm is greater for all rocks in the old data set, the rock is assumed to be new, and it is added to the data set. The algorithm is described using pseudo code in Algorithm 1.
(4) Rocks that are out of the grizzly area and possible misidentified points, for example, due to a manipulator blocking the view, are filtered out from the data set.
(5) After filtering, the rock closest to the TCP is selected as the next target to be broken.
(6) The data set cleanup is followed then. The rock selected for breaking is removed first. Then, based on Remark 1, rocks that are within 0.5 m of the selected rock are also removed, as they may be shifted by the break attempt. Aging of data could also be utilized for more robust operation (e.g., rocks that have not been detected by the vision system for a set number of rounds can be assumed invalid).
(7) The system is then suspended until a request for a new target is received, that is, the manipulator has finished the break attempt of the last target.
(8) After receiving request for the next target, the systems resumes operation from Step 2.
(9) After no more rocks are found by the VPS nor any are remaining in the data set, the system informs the high-level manipulator controller and the boom is driven to its standby position.

Algorithm 1 Data fusion algorithm

```
Input: Stored position matrix $\mathbf{P}_{memory}$, New position matrix $\mathbf{P}_{camera}$
Output: Data sets fused into $\mathbf{P}_{memory}$
for each $p_{new} \in \mathbf{P}_{camera}$ do
    newRock ← True
    for each $p \in \mathbf{P}_{memory}$ do
        if $\| p_{new} - p \|_2 \leq 0.1$ then
            newRock ← False
            $p \leftarrow p_{new}$
        end if
    end for
    if newRock then
        $\mathbf{P}_{memory} \leftarrow \begin{matrix} \mathbf{P}_{memory} \\ p_{new} \end{matrix}$
    end if
end for
```

Remark 1. Based on our observations from preliminary experiments, an attempt to break a specific rock will not affect rocks that are not in the immediate proximity of the rock being broken. A 0.5 m radius is sufficient margin beyond which rocks will not be shifted by the broken rock. Due to the vibrations during the hydraulic hammer operation, rocks might move slightly farther away than expected, but the total movement of the rocks remains minor. However, any rocks inside the set radius are likely to move considerably. This has been tested only in situations, where the rocks are resting on the grizzly in a single layer, and may not be valid in other situations.

3.3.2 | High-level manipulator controller

The high-level manipulator controller is an event-triggered state-machine that defines different operating modes of the test manipulator. In this application, three operational states are defined as follows: automatic unfolding, automatic folding, and autonomous rock breaking. In its nonoperational state, the main motion controller of the manipulator is disabled for safety reasons. The nonoperational state is defined as the default initialization state.

The automatic motion states move the manipulator from its current position to specific predetermined positions within the workspace of the manipulator. These positions are called standby position and resting position, respectively. The boom is driven to these positions through the following steps: first, the TCP is driven to a specified transition height. Then, the target is set to the *XY* coordinates of the prespecified position. Finally, the TCP is driven to the final target position. Note that the last movement of the TCP is only vertical.

The autonomous operation pipeline follows a specific pattern. First, the system requests target position from the break order logic subsystem. After a new target is obtained, the manipulator is raised to the transition height, if not already at that height, after which it is driven above the target rock. The approach move is triggered next, and this phase is linked to the breaking sequence. The approach move is executed so that the manipulator is set to drive 50 mm below the rock's surface to load the internal spring of the hydraulic hammer. After reaching the rock surface, all joints but the lift joint are locked to prevent the TCP from slipping away from the rock. The lift joint is used to maintain pressure against the rock. The hydraulic impact hammer is then engaged and kept on for 5 s or until the tip of the manipulator has entered a virtual safety zone, which is set 50 mm above the grizzly as a collision-avoidance measure. After the break attempt, the manipulator is driven back up to the transition height. The sequence is then repeated from the first step.

Remark 2. After the first experiments, the autonomous breaking sequence was revised so that after every third attempt, the manipulator moves aside to the standby position to give the stereo camera a clear view of the grizzly.

Remark 3. The modular system design allows for rapid testing of different approaches for breaking rocks. Contact and external force estimation are particularly interesting research topics, here omitted, that may notably increase the success rate of the break attempts. Impedance control has been proposed as one possible solution to achieve the required compliant behavior (Hulttinen, 2017; Koivumäki & Mattila, 2017; Tafazoli et al., 2002). At this stage, a strategy for approaching the rocks without them slipping and moving away could be devised. Learning from demonstrations is another interesting and seemingly promising approach for instructing robots on contact control with teleoperated demonstrations from a human operator (Havoutis & Calinon, 2019; Suomalainen et al., 2018).

3.3.3 | Trajectory generation and inverse kinematics

The trajectory generator for the manipulator is designed to generate trajectories from the current position of the manipulator's TCP to the target coordinates. Trajectories are created in a cylindrical coordinate system to minimize unnecessary actuator movements. The trajectory generator first converts the start and end coordinates to the cylindrical coordinate system, respectively. Then, quintic rest-to-rest trajectories are created between the two points using

$$x(t) = a_0 + a_1 t + a_2 t^2 + a_3 t^3 + a_4 t^4 + a_5 t^5, \tag{2}$$

where x contains an individual point-to-point trajectory, and coefficients $a_i \in \mathbb{R}$ are obtained using

$$\begin{bmatrix} 1 & t_0 & t_0^2 & t_0^3 & t_0^4 & t_0^5 \\ 0 & 1 & 2t_0 & 3t_0^2 & 4t_0^3 & 5t_0^4 \\ 0 & 0 & 2 & 6t_0^2 & 4t_0^3 & 20t_0^3 \\ 1 & t_f & t_f^2 & t_f^3 & t_f^4 & t_f^5 \\ 0 & 1 & 2t_f & 3t_f^2 & 4t_f^3 & 5t_f^4 \\ 0 & 0 & 2 & 6t_f & 12t_f^2 & 20t_f^3 \end{bmatrix} \begin{bmatrix} a_0 \\ a_1 \\ a_2 \\ a_3 \\ a_4 \\ a_5 \end{bmatrix} = \begin{bmatrix} x_0 \\ \dot{x}_0 \\ \ddot{x}_0 \\ x_f \\ \dot{x}_f \\ \ddot{x}_f \end{bmatrix}, \tag{3}$$

where t_0 is time at the beginning and t_f is time at the end. x_0, $\dot{x}_0$, and $\ddot{x}_0$ denote the initial position, velocity and acceleration, respectively, whereas $x_f, \dot{x}_f$, and $\ddot{x}_f$ define the final position, velocity and acceleration, respectively (Jazar, 2010).

The trajectory generator provides the position and velocity along the path in Cartesian coordinates, but those must be transformed into joint space for the joint controller. Let $\mathbf{v} \in \mathbb{R}^3$ denote the desired velocity of the manipulator in robot coordinates. For a redundant four-joint manipulator, the required joint velocities can be identified using a pseudo-inverse of the Jacobian matrix, which is defined as

$$\mathbf{J}^{\dagger} = \mathbf{W}^{-1}\mathbf{J}^{T}(\mathbf{J}\mathbf{W}^{-1}\mathbf{J}^{T})^{-1}, \tag{4}$$

where $\mathbf{J}^{\dagger} \in \mathbb{R}^{4\times4}$ is the Jacobian pseudo-inverse, $\mathbf{W} \in \mathbb{R}^{4\times4}$ is a symmetric positive definite weighing matrix, and $\mathbf{J} \in \mathbb{R}^{3\times4}$ is the non-invertible Jacobian matrix (Sciavicco et al., 2000). The weight matrix W is updated dynamically based on the joint configuration and the direction the joints are moving to prevent any actuator from reaching its mechanical stroke limits. Near the mechanical stroke limits, the weight of the corresponding actuator increase and thus prevent it from reaching mechanical limits. For more detailed description see (Lampinen et al., 2020).

The redundancy of the manipulator is utilized to control the angle of the hammer with respect to the ground. To change the pose of the manipulator without moving the TCP, we use the null space of the Jacobian matrix. The null space $\mathcal{N}(\mathbf{J})$ is obtained using

$$\mathcal{N}(\mathbf{J}) = I - \mathbf{J}^{\dagger}\mathbf{J}. \tag{5}$$

The joint velocities with null space control are finally calculated as

$$\dot{\mathbf{q}} = \mathbf{J}^{\dagger}\mathbf{v} + \mathcal{N}(\mathbf{J})\,\dot{\mathbf{q}}_0, \tag{6}$$

where $\dot{\mathbf{q}}_0 \in \mathbb{R}^4$ is the joint control term that changes the pose of the manipulator without affecting the position or velocity of the end-effector, while $\dot{\mathbf{q}} \in \mathbb{R}^4$ denotes the joint velocities corresponding to the Cartesian velocity $\mathbf{v} \in \mathbb{R}^3$.

3.3.4 | Flow-rate limitation

Hydraulic systems are characterized by many nonlinearities and constraints specific to hydraulics. An important restriction for hydraulic systems is the flow restriction from the hydraulic supply unit, that limits the achievable TCP velocity, especially when driving multiple actuators simultaneously. To address this constraint, a flow-bounded control strategy is utilized. This approach is presented in detail in Lampinen et al. (2020). The selected approach is inspired by torque-bounded trajectories presented in Dahl and Nielsen (1990) and Dahl (1994), and is similar to an online method proposed recently to limit velocity in manual coordinated control (Wanner & Sawodny, 2019).

The main function of the algorithm is to dynamically scale trajectories to a velocity that is attainable for the manipulator's configuration. Due to the nonlinear nature of hydraulic systems, the attainable velocity can vary significantly depending on the manipulator configuration. To ensure that the manipulator can reach the desired velocity of the trajectory generator, the required volumetric flow rate for the hydraulic actuators must not exceed the flow rate generated by the hydraulic supply unit.

Let $\mathbf{J}_x \in \mathbb{R}^{4\times4}$ be an actuator space mapping matrix that translates joint velocities into actuator space as

$$\begin{bmatrix} \dot{q}_{\text{motor}} \\ \dot{x}_{\text{lift}} \\ \dot{x}_{\text{tilt}} \\ \dot{x}_{\text{breaker}} \end{bmatrix} = \mathbf{J}_x\dot{\mathbf{q}}. \tag{7}$$

In the case of the hydraulic motor, the velocity is simply the angular velocity of the base of the manipulator divided by the gear ratio of the ring gear and the planetary gear.

The required flow rate of each cylinder can be obtained by using

$$Q_{cylinder} = \begin{cases} A_A\dot{x}_i, & \text{when} \quad \dot{x}_i \geq 0 \\ -A_B\dot{x}_i, & \text{when} \quad \dot{x}_i < 0,' \end{cases} \tag{8}$$

where $\dot{x}_i \in \{\dot{x}_{\text{lift}}, \dot{x}_{\text{tilt}}, \dot{x}_{\text{breaker}}\}$, A_A and A_B are the areas on the A- and B-sides of the hydraulic cylinder, respectively, and for the hydraulic motor by using

$$Q_{\text{motor}} = \frac{|\dot{q}_{\text{motor}}|D_m}{2\pi\eta_{vol}}, \tag{9}$$

where D_m is the volumetric displacement of the motor, and η_{vol} is the volumetric efficiency of the motor. Summing the required flow of each actuator yields the total required flow from the supply, Q_r. The scaling factor is then obtained using

$$\dot{s} = \min\left(1, \frac{Q_p}{Q_r}\right), \tag{10}$$

where Q_p is the maximum flow from the supply pump.

The algorithm is employed by the control system via a connection to the trajectory generator. In equation (2), the trajectory is a function of time. However, if we define $\dot{t} = \dot{s}$, where $\dot{s}$ is the trajectory scaling factor, we can make (2) a function of scaled time that effectively limits the trajectory to an attainable velocity. This connection is visible in Figure 11.

3.3.5 | Motion control

The motion control system used in the experiments relies heavily on learned velocity feed-forward mapping complemented by a proportional controller. The manipulator is equipped with Danfoss PVG-120 mobile proportional control valves with a significant dead-zone (approximately 30% per direction), thus making dead-zone inversion obligatory in the control design (Bak & Hansen, 2012). Moreover, it significantly improves control accuracy. For more accurate control of the manipulator, stability guaranteed model-based control methods have been shown to achieve state-of-the-art performance (Mattila et al., 2017). In Lampinen et al. (2019), such a model-based controller was proposed. Its use was demonstrated on the last link of the manipulator with a novel method of handling the nonlinearities of the pressure-compensated valves with dead zones.

In this study, velocity feed-forward learning for each valve-actuator pair was performed using the algorithm proposed in Nurmi and Mattila (2017). The algorithm identifies a feed-forward model of the valve-actuator pair by driving the actuator in a sinusoidal trajectory, while at the same time using adaptive control methods to map valve control and actuator velocity. The feed-forward model is identified in 24 distinct segments of the whole control region to accurately represent the valve characteristics.

3.3.6 | Control system verification

To demonstrate the control system's performance with dynamic trajectory tracking, a 3-DOF test trajectory was designed. This trajectory is shown in Figure 13. It consisted of five piecewise smooth segments of quintic paths generated using Equation (2), with the design time of each segment set to 8 s. However, due to the scaling of the trajectory, the timing was not absolute. The total time required to complete the trajectory was 42.4 s. The Cartesian tracking error during the trajectory was shown in Figure 14. The maximum tracking error during the trajectory was approximately 58 mm, while the mean error was 17.8 mm. Individual trajectories of each joint are shown in Figure 15, which highlights that each joint can track their respective trajectories with high precision.

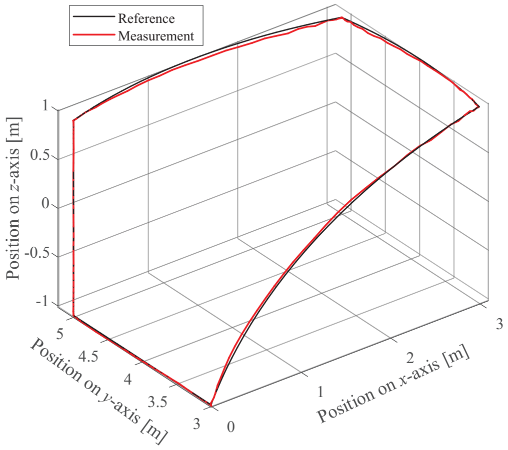

FIGURE 13 Cartesian trajectory used for control system verification [Color figure can be viewed at wileyonlinelibrary.com]

3.3.7 | Short discussion on implementing force control with force estimation

This section continues the discussion of Remark 3 on the topic of force estimation and force control. Force control of hydraulic series manipulators is not a novel concept, but due to the highly nonlinear dynamic behavior of hydraulic systems, it has remained mainly a curiosity in industrial applications, and the documented implementations limit to technical demonstrations in laboratory environment (Mattila et al., 2017). Contact identification and classification methods on the other hand have been well surveyed in (Haddadin et al., 2017).

Within the scope of this study, our aim was to create a system that requires minimal modifications to the original system and thus has less possible points of failure. With the aid of pressure sensors, similar model based control approach as proposed by Lampinen et al. (2019) could be extended to the whole manipulator. Force estimation could then be implemented using the measurable cylinder piston forces and estimated dynamics of the manipulator as proposed by Koivumäki and Mattila (2015). The more advanced model based control method could be utilized with impedance control scheme as shown in Koivumäki and Mattila (2017) to achieve the compliant and force aware contact control for a stable rock contact. A different route of utilizing force estimation could be to leave the control system untouched and use the force estimation only for contact detection and classification as well as external event detection, for example, tool slipping, rock slipping, or detection of a break instance.

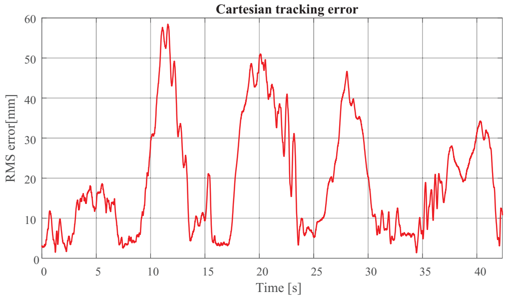

FIGURE 14 Cartesian tracking error during the experiment [Color figure can be viewed at wileyonlinelibrary.com]

4 | MANIPULATOR AND CAMERA CALIBRATION

4.1 | Manipulator calibration

An accurate forward kinematic model of the manipulator is a prerequisite for vision-based operations using absolute coordinates. Therefore, before anything else, the manipulator's internal link coordinate system, from its base to the TCP, must be calibrated using accurate external measurements, to compensate for errors in nominal link lengths and uncalibrated encoder offsets. Alternatively, the uncertainty related to the kinematic parameters could be mitigated by using eye-in-hand tracking of the TCP and relative positions (i.e., the vision system gives rock positions relative to the perceived TCP location). However, such an application could prove to be very harsh for the camera, due to the high-frequency vibrations of the impact hammer. Therefore, we opted for the kinematic calibration process instead.

All four joint axes of the manipulator are equipped with 14-bit SIKO WV58MR absolute rotary encoders, with an angular resolution of 0.022°. The external measurement device used was a SOKKIA NET05 total station laser theodolite, which provides 3D position data with sub-millimeter accuracy. A spherically mounted retroreflector was attached to the hammer tip, and its laser-indicated position together with joint encoder readings were recorded in 28 joint configurations when the boom was static.

Figure 5 illustrates the coordinate frame assignment for the boom, which was done following the Denavit–Hartenberg (DH) convention. First, the homogenous transformation from the theodolite measurement frame to the mechanical base frame of the manipulator (which is found at the intersection of its first two joints) was estimated with a circle fitting procedure (Bernard & Albright, 1994). Then, using the nominal dimensions of the boom as an initial guess, an estimate of the actual DH parameters was determined by applying the Levenberg–Marquardt algorithm to iteratively find a numerical solution that best described the boom geometry.

The resulting position residuals between the calibrated forward kinematic model and the values indicated by the external measurement device are visualized in Figure 16. The top of the figure visualizes *X*, *Y*, *Z*, and Cartesian position residuals from each individual measurement, while the bottom presents the distributions of these respective errors as a histogram. The kinematic calibration resulted in a spatial mean error of less than 10 mm and maximum errors of less

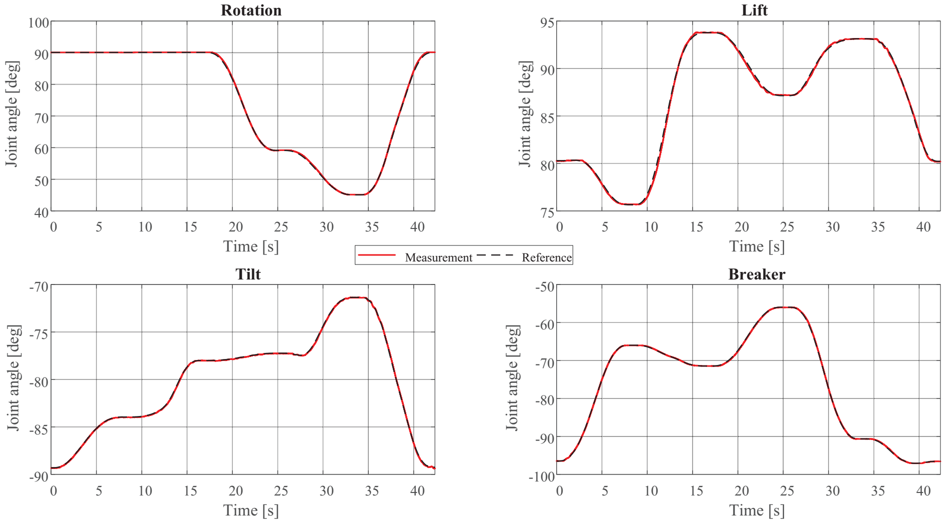

FIGURE 15 Individual joint tracking during control system verification experiment [Color figure can be viewed at wileyonlinelibrary.com]

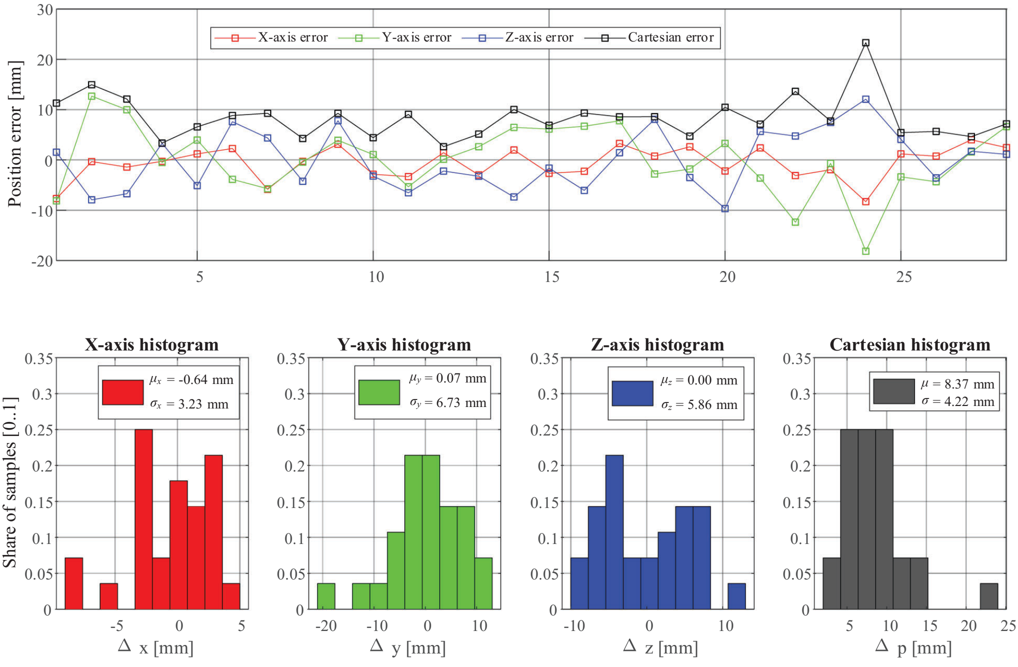

FIGURE 16 Position residuals after kinematic calibration [Color figure can be viewed at wileyonlinelibrary.com]

than 25 mm. By comparison, the diameter of the blunt tool that comes into contact with rocks is 135 mm. For a 9-ton manipulator with a reach of 7 m, this degree of accuracy can be considered impressive, and higher accuracy is likely impossible due to structural flexibilities.

As a remark, the accuracy reported here was achieved with a less than 4 year old breaker boom that has seen only light work-cycles (acting mainly as motion control platform without significant amounts of rock breaking activity) and can thus be considered relatively intact. In an actual breaker boom plant subject to continuous stress and impacts, the repeatability of the manipulator might deteriorate over time due to wear. Consequently, the achievable absolute accuracy of the manipulator might decrease during its lifespan, despite including regular recalibration as a part of maintenance operations.

4.2 | Camera calibration

Stereo cameras have been extensively used in real-time robotic vision applications, such as detecting and measuring objects, and estimating objects' poses in a scene. The accuracy of such stereoscopic visual system relies entirely on calibration, which determines the overall performance of the system.

A stereo camera is typically composed of a pair of pinhole cameras. The camera calibration process estimates the geometric properties of the camera, as well as its pose in robot coordinate system (Forsyth & Ponce, 2002). The camera calibration parameters include intrinsic and extrinsic parameters and distortion coefficients, as illustrated in Figure 17.

Given a 3D point (X, Y, Z) in the robot coordinate system, its corresponding point (x, y, z) in the camera coordinate system and (u, v) in the 2D image plane, the extrinsic calibration parameters follow a rigid transformation between camera and robot coordinates:

$$\begin{bmatrix} x \\ y \\ z \\ 1 \end{bmatrix} = \begin{bmatrix} R_{3\times 3} & t_{3\times 1} \\ 0_{1\times 3} & 1 \end{bmatrix} \begin{bmatrix} X \\ Y \\ Z \\ 1 \end{bmatrix}. \tag{11}$$

The intrinsic calibration parameters represent the projective transformation between the 2D image coordinates and 3D camera coordinates:

$$z \begin{bmatrix} u \\ v \\ 1 \end{bmatrix} = \begin{bmatrix} f_x & 0 & c_x & 0 \\ 0 & f_y & c_y & 0 \\ 0 & 0 & 1 & 0 \end{bmatrix} \begin{bmatrix} x \\ y \\ z \\ 1 \end{bmatrix}, \tag{12}$$

where z is the depth at the image coordinate (u, v). Combining the above two equations, a general perspective transformation can be written as

$$\begin{bmatrix} u \\ v \\ 1 \end{bmatrix} = \frac{1}{z} \begin{bmatrix} f_x & 0 & c_x \\ 0 & f_y & c_y \\ 0 & 0 & 1 \end{bmatrix} \begin{bmatrix} R \mid t \end{bmatrix}_{3\times 4} \begin{bmatrix} X \\ Y \\ Z \\ 1 \end{bmatrix}, \tag{13}$$

where (f_x, f_y) is the focal length in pixels, (c_x, c_y) is the optical center in pixels, $R \in \mathbb{R}^{3\times 3}$ is a rotation matrix, and $t \in \mathbb{R}^3$ is a translation vector.

4.2.1 | Intrinsic calibration

Real lenses always exhibit some radial distortion and slight tangential distortion. Camera calibration helps correct radial lens distortions and measurement errors. The Stereolabs ZED stereo camera in our system is an integrated parallel stereoscopic camera with a known baseline. Even though it comes with factory calibration, its accuracy can still be improved with recalibration. The calibration process follows a multi-plane calibration approach (Zhang, 2000), which only requires a planar pattern. Without knowing positions and orientations, calibration was performed by moving the camera with respect to the planar calibration pattern on a 27-inch 2560 × 1440 display. The ZED camera calibration parameters for a resolution of 1280 × 720 pixcel were recorded in Table 2, which contains the intrinsic parameters, focal lengths f_x, f_y, principal points c_x, c_y, and the lens distortion of both the left and right eye of the camera $[k_1, k_2, p_1, p_2, k_3]$, as well as the extrinsic parameters of the right eye with respect to the left eye of the camera, R_0 and t_0. Here, the common lens distortion can be corrected with Brown-Conrady model (Brown, 1966), which takes into account both radial distortion and tangential distortion:

$$\begin{aligned} u_d &= u_n(1 + k_1 r^2 + k_2 r^4) + \left(2p_1 u_n v_n + p_2(r^2 + 2u_n^2)\right), \\ v_d &= v_n(1 + k_1 r^2 + k_2 r^4) + \left(2p_2 u_n v_n + p_1(r^2 + 2v_n^2)\right), \end{aligned} \tag{14}$$

where $r^2 = (u_n - u_c)^2 + (v_n - v_c)^2$, u_d, v_d are coordinates in the distorted image, u_n and v_n are coordinates in the undistorted image, u_c and v_c are coordinates of the distortion center, k_1 and k_2 are radial distortion coefficients, and p_1 and p_2 are tangential distortion coefficients.

4.2.2 | Extrinsic calibration

The extrinsic parameters are determined by how the camera is positioned in the robot coordinates. A point in the camera coordinate frame depicts its position with respect to the optical center of the left eye of the camera. For the robot manipulator, it is more useful to know where this point is relative to the robot base in the robot coordinate frame, which coincides with the world coordinate frame. Both the camera and the robot coordinate frame follow the right hand rule, as shown in Figure 5.

For a stationary camera and robot base, any objects in the camera coordinates should retain the same geometry and scale after transformation into robot coordinates. This geometric transformation aligns every corresponding point of two-point cloud sets; this is referred to as rigid transformation, which is expressed by Equation (11). The approaches to find rotation R and translation t can be categorized as singular value decomposition (SVD)-based (Arun et al., 1987; Ho, 2013) and quaternion-based (Horn, 1987; Horn et al., 1988; Walker et al., 1991). The SVD-based method was adopted to obtain the highest possible level of accuracy and stability.

Let the points in camera coordinate be $C = \{c_i\}$, and $c_i = [x_i, y_i, z_i]^T$ in 3D, where $i = 1, 2, \ldots N$ and N is the number of points and corresponding

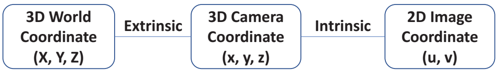

FIGURE 17 Camera calibration process [Color figure can be viewed at wileyonlinelibrary.com]

TABLE 2 Stereo camera parameters

ZED	f_x	f_y	c_x	c_y	Distortion coefficient $[k_1, k_2, p_1, p_2, k_3]$
Left	700.79	700.79	634.822	356.993	[−0.176, 0.029, 0.00196, −0.00044, 0.00]
Right	700.71	700.71	626.699	356.066	[−0.172, 0.027, 0.00164, 0.00016, 0.00]
R_0	[−0.00659, 0.01328, −0.00013]				
t_0 [mm]	[−120.002, 0.00, 0.00]				
R	[−0.019, −0.003, −0.024]				
t [m]	[−0.480, −4.491, −3.209]				

points. Then let the corresponding points in the robot coordinates be $W = \{w_i\}$, and $w_i = [X_i, Y_i, Z_i]^T$ in 3D, which can be expressed as

$$\begin{bmatrix} X_i \\ Y_i \\ Z_i \end{bmatrix} = R_{3\times3}^{-1}\left(\begin{bmatrix} x_i \\ y_i \\ z_i \end{bmatrix} - t_{3\times1}\right). \tag{15}$$

According to the SVD approach,

$$[U, S, V] = SVD(CW^T), \tag{16}$$

where C and W are the $3 \times N$ matrices that have $c_i - \frac{1}{N}\sum_{i=1}^{N} c^i$ and $w_i - \frac{1}{N}\sum_{i=1}^{N} w^i$ as their columns, respectively, and U and V are orthonormal matrices from which we obtain

$$R = VU^T. \tag{17}$$

Subsequently, the translation vector t can be computed as

$$t = \frac{1}{N}\sum_{i=1}^{N} c^i - R\left(\frac{1}{N}\sum_{i=1}^{N} w^i\right). \tag{18}$$

Unlike intrinsic calibration, which was performed indoors, the actual extrinsic calibration was conducted outdoors at a rock breaking field. The calibration workspace in the field consisted of measurement equipment, the grizzly, markers, the overhead ZED camera, and the Rambooms manipulator. For successful extrinsic calibration, the following conditions were fulfilled:

- The intrinsic calibration of the ZED camera was completed;
- The manipulator's forward kinematics model was calibrated;
- The marker positions in camera coordinates were accurately measured;
- The corresponding marker positions in robot coordinates were accurately measured.

Extrinsic calibration was initiated by distributing markers into the workspace in such a way that flat red markers appeared around the middle of the camera's field of view. To achieve the best possible contrast between the markers and the background, lower exposure for image acquisition was set. An example of the acquired image (at 1280 × 720 resolution) is shown in Figure 18, where there are six markers in the scene. Next, the process for marker segmentation was performed to the corresponding point cloud in the camera coordinates using a color mask to filter all objects except the markers. After filtering, what remained of the scene were the markers, presented in the form of clusters of points, as shown in Figure 19. A k-means clustering algorithm was used to locate all markers' centroid positions and thus obtain their positions in the camera's coordinates.

For measuring marker positions in robot coordinates, multiple approaches were available. A quick and effective approach was to take advantage of the calibrated Rambooms manipulator to manually align the centroid position of each marker with the manipulator's TCP, so the manipulator could convert each marker position to robot coordinates. For this method, robot accuracy must be taken into account. Once all corresponding camera and robot coordinate positions were measured, measurement data was validated and represented in homogeneous coordinates. Finally, the extrinsic parameter rotation matrix R and translation vector t were calculated according to Equation (17) and (18), respectively. These numerical values are presented in Table 2, together with the camera intrinsic parameters.

4.2.3 | Verification of vision system accuracy

The accuracy of the vision system was determined with the ZED camera's inherent accuracy, intrinsic and extrinsic camera calibration methods, and measurement errors during camera calibration. The

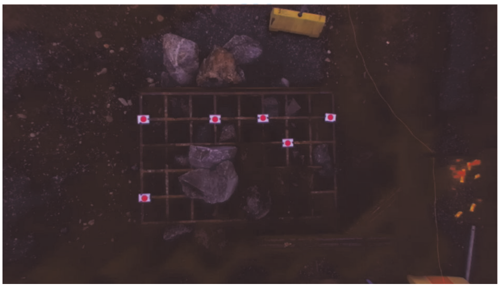

FIGURE 18 A view of red markers acquired at low exposure [Color figure can be viewed at wileyonlinelibrary.com]

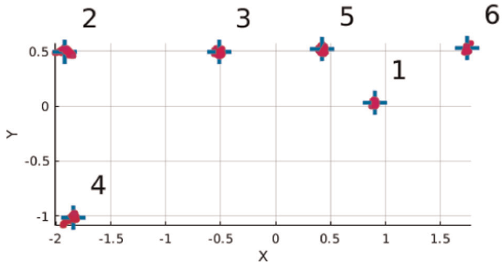

FIGURE 19 An example of red markers in a point cloud in the camera coordinates. The blue crosses denote the markers' centroid positions [Color figure can be viewed at wileyonlinelibrary.com]

ZED camera is a binocular pinhole camera with an operating range of up to 20 m, but its depth accuracy decreases when the distance between the camera and the target increases. The accuracy test was conducted with four to five meters between the grizzly and the ZED camera. The target objects were the red markers used for calibration. The calibrated intrinsic and extrinsic parameters of the ZED camera were used to obtain the estimated target object positions in robot coordinates. These estimated marker positions were then compared to corresponding data given by the manipulator. In total, 24 measurements were performed. Figure 20 illustrates position residuals, where the maximum deviations are 18.4, 22.4, 67.5, and 67.19 mm along *X*, *Y*, *Z* axes and Cartesian, respectively. SDs in the *X*, *Y*, *Z* axes and Cartesian are 10.0, 10.5, 27.9, and 15.14 mm, respectively. Considering the 135 mm diameter of the manipulator's blunt tool, as well as the grizzly's grid size of 400 × 400 mm, the position errors are acceptable.

5 | EXPERIMENTS AND RESULTS

5.1 | Rock detection

Rock detection and localization is a crucial step in autonomous breaking. During the data collection phase, we collected a total of 4733 images of the breaking scene with the grizzly and rocks visible. Ninty percent of them were used for training and validation data, while the remaining 10% were used for model and system-level testing, which ensured the final experiments could be carried out seamlessly.

The maximum amount of rocks the grizzly can hold depends on the size of rocks. During the final rock breaking experiments, the amount of rocks in each experiment varied from 6 to 12. An example of a scene with 12 rocks is presented in Figure 21, where the detection speed was 85 ms. Once a rock was detected, it was numbered and enclosed in a purple bounding box. The total sum of detected rocks is shown in the upper left corner of the image.

To further enhance the robustness of the rock detection process, we set a region of interest (ROI) indicated with white rectangles in the image coordinate frame. Rocks detected outside the ROI were ignored. Whether a rock lay inside or outside the ROI was determined by the centroid position of its bounding box. In addition, we ignored rocks smaller than the grid openings of the grizzly, as well as rocks laying beneath the grizzly's upper surface.

5.2 | Position for rock breaking

The positions and orientations for rock breaking presented in Figure 21 were estimated based on the reconstructed 3D surface point cloud of each rock. As the software architecture in Figure 6 depicts, this was a long process that began with 3D reconstruction of the environment using the detected 2D images. Within each region, every pixel was reprojected onto a corresponding point in the camera coordinates with position values (*X*, *Y*, *Z*) and RGB color codes. We could thus obtain detected rocks in the form of 3D regions in a dense point cloud. This process is detailed in Section 3.2.3. Next, the reconstructed 3D regions were transformed from camera coordinates to robot coordinates. This result is shown in Figure 22. Finally, the process for estimating the position and orientation required for rock breaking could be initiated. A more detailed description of each of these processes is provided in Section 3.2.4 and 3.2.5, respectively.

To validate the results, the breaking positions for the aforementioned 12 rocks are visualized in Figure 23, which verifies the correctness and effectiveness of the position values online in Figure 21. The positions for guiding the manipulator's blunt tool are marked as red spots on the surface of each rock (including partially occluded ones). A 3D viewer was implemented for live monitoring purposes using the Point Cloud Library (PCL) in C++.

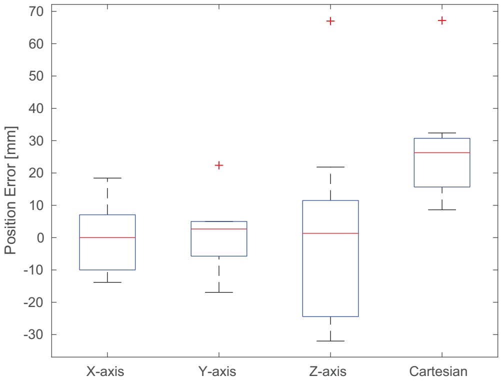

FIGURE 20 Box plot of position residuals in the *X*, *Y*, *Z* axes and Cartesian. The boxes show the 25th and 75th percentiles of residuals, while red lines represent medians, whiskers represent the minimum and maximum values, and the red “+” symbols signify large residuals regarded as outliers [Color figure can be viewed at wileyonlinelibrary.com]

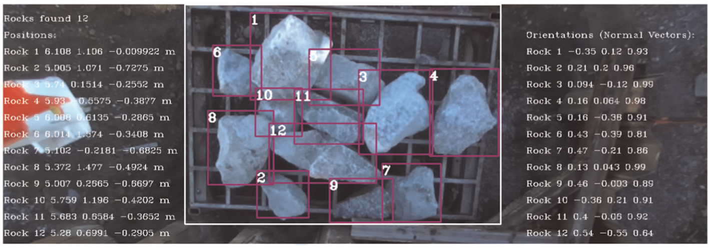

```
Rocks found 12
Positions:
Rock 1 6.108 1.106 −0.009922 m
Rock 2 5.005 1.071 −0.7275 m
Rock 3 5.74 0.1514 −0.2552 m
Rock 4 5.93 0.5575 −0.3877 m
Rock 5 6.008 0.6135 −0.2865 m
Rock 6 6.014 1.574 −0.3408 m
Rock 7 5.102 −0.2181 −0.6825 m
Rock 8 5.372 1.477 −0.4924 m
Rock 9 5.007 0.2665 −0.6697 m
Rock 10 5.759 1.196 −0.4202 m
Rock 11 5.683 0.6584 −0.3652 m
Rock 12 5.28 0.6991 −0.2905 m
```

```
Orientations (Normal Vectors):
Rock 1 −0.35 0.12 0.93
Rock 2 0.21 0.2 0.96
Rock 3 0.094 −0.12 0.99
Rock 4 0.16 0.064 0.98
Rock 5 0.16 −0.38 0.91
Rock 6 0.43 −0.39 0.81
Rock 7 0.47 −0.21 0.86
Rock 8 0.13 0.043 0.99
Rock 9 0.46 −0.003 0.89
Rock 10 −0.36 0.21 0.91
Rock 11 0.4 −0.08 0.92
Rock 12 0.54 −0.55 0.64
```

FIGURE 21 Real-time view of the rock detection scene. The positions and orientations for rock breaking are aligned to the left and right side accordingly [Color figure can be viewed at wileyonlinelibrary.com]

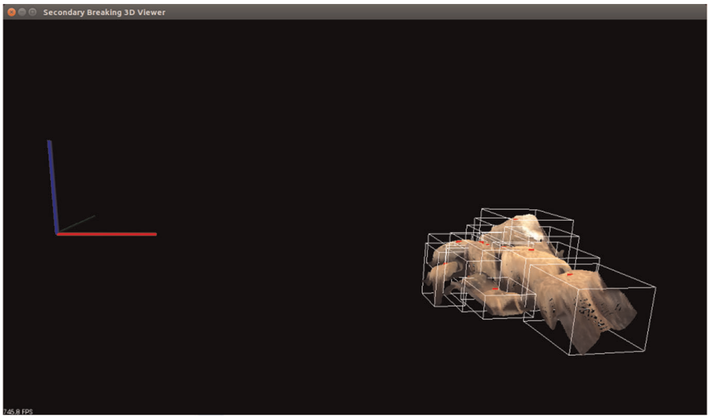

FIGURE 22 Real-time view of the detected rocks in a 3D point cloud in robot coordinates (the *X*, *Y*, and *Z* axes are marked in red, green, and blue, respectively) [Color figure can be viewed at wileyonlinelibrary.com]

5.3 | Description of the autonomous operation evaluation

The experiments reported in this manuscript serve as a technical demo. The experiments herein represent real use cases of the manipulator and demonstrate the potential for increased automation of such systems. The experiments consisted of autonomous rock breaking ranging from 1 to 10 min long, during which there was no human intervention with the autonomous operation. Before each experiment, 5–10 rocks of various sizes and shapes were laid on the grizzly. During the experiment each break attempt were recorded. After the experiment, success rates and break pace were calculated.

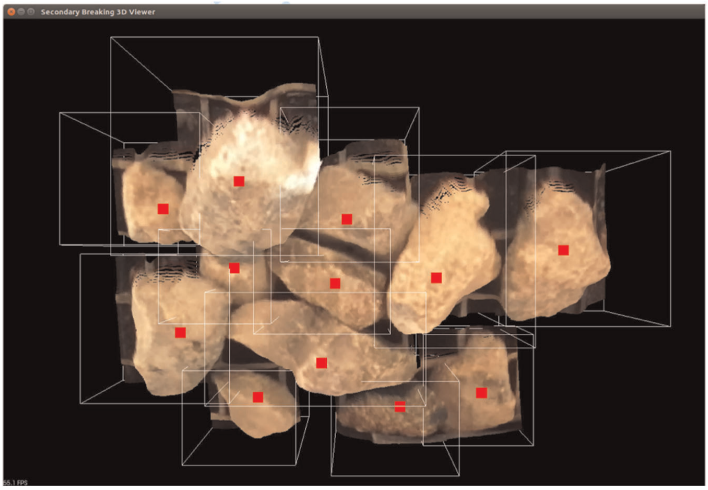

FIGURE 23 Real-time view of the detected rocks with breaking positions indicated in red dots [Color figure can be viewed at wileyonlinelibrary.com]

The break pace describes how many break attempts were performed within a 1-min span.

Each of the experiments were performed without any human intervention during the process. The system was equipped with additional safety features, such as a dead man's switch for the breaker operation and an emergency stop for the entire manipulator to ensure safety during the experiments. Fortunately, there was no need for either of these features during the experiments. The safety features included in the control system already prevented direct hits against the grizzly, and the manipulator was operated in a limited area above the grizzly. The logic of the autonomous operations during the experiments follows what is described in Section 3.3.1 and in Figure 12. The process was repeated until no rocks remained on the grizzly or the operation was halted by the operator.

Remark 4. The rocks used in the experiment were granite from a nearby construction site. This is not a typical material in this application, which should be considered when analyzing the results. Granite can have compressive strength values of over 200 MPa, which makes it very difficult to break. This might lead to lower overall success rates than what could be achievable in an actual environment with more brittle material.

5.4 | Results from the autonomous breaking experiment

The autonomous breaking experiment consisted of approximately 47 min of autonomous operation with varying numbers of differently sized rocks laid on the grizzly. The breaking was considered successful if the rock broke into two or more pieces that were at least 25% of the original volume of the rock being broken, or if the hammer pushed the rock through the grizzly. Break success rates were evaluated visually from recorded videos. The average break success rate was 34.2%, while the break pace was approximately 3.30 attempts per minute. The experiments were conducted during a very bright weather and objects in the scene suffered from over exposure and shadows which notably differed from the conditions in our data set, which resulted in degraded performance of the VPS. The average Recall of the VPS during the experiments was approximately 75%. Results from each individual experiment are gathered in Table 3. All the experiments presented here were conducted without using the rock surface normals as breaking guides; instead, the hammer was kept at a 90-degree angle with respect to the ground at all times.

During Experiment 6, we implemented a change to the autonomous operation so that after every third attempt, the manipulator moved aside to allow a better view of the grizzly for the stereo camera. Despite the addition of this extra step, the break pace remained almost identical as the manipulator's movements were also sped up. In Experiment 6, a sharp angled rock was very close to the area where the manipulator was moved after every third attempt; consequently the system attempted to break that specific rock always first. Due to the difficulty caused by the shape of the rock, the success rate of Experiment 6 was lower compared to other experiments.

As seen in Table 3, the success rate between experiments varied considerably. This was caused mainly by the fact that the rocks on the grizzly in each experiment were dissimilar in shape and size. Sharp edges were identified as causing the most problems for the system, which is owed to the relatively low stiffness of the manipulator. An especially problematic feature of the manipulator was the backlash of the rotation joint. The rotation of the manipulator is controlled with a hydraulic motor attached to a planetary gear and a ring gear, which together contribute as a significant source of backlash. Because of this, the manipulator slipped on inclined surfaces easily.

The reference and measured positions of the manipulator's TCP during Experiment 8 are visualized in Figure 24, where the red lines indicate the measured trajectory while black dashed lines represent the reference trajectory. Accurate path following can be observed in this figure. A closer look at the first 100 s of the experiment at the

TABLE 3 Results from autonomous breaking experiments

	Duration	Break attempts	Successful breaks	Success rate (%)	Break pace (attempts/min)
Experiment 1	3 min 50 s	13	7	53.8	3.39
Experiment 2	4 min 15 s	14	5	35.7	3.29
Experiment 3	7 min 30 s	26	8	30.8	3.47
Experiment 4	1 min 10 s	4	1	25.0	3.43
Experiment 5	4 min	12	5	41.7	3.39
Experiment 6	5 min 30 s	19	2	10.5	3.84
Experiment 7	5 min 30 s	16	7	43.8	3.15
Experiment 8	5 min	18	5	27.8	3.70
Experiment 9	10 min	33	13	39.4	3.42
Total	47 min	155	53	34.2	3.30

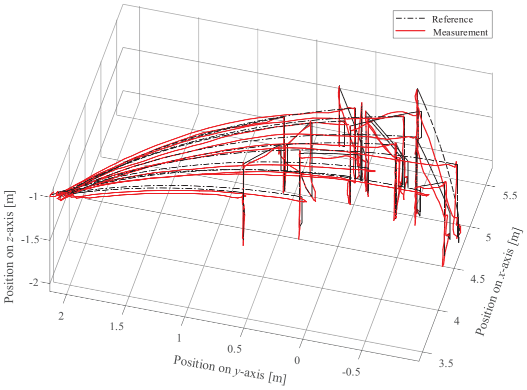

FIGURE 24 Trajectory during 5 min of autonomous operation in Experiment 8. Continuous visits at the left corner represent the manipulator moving aside to allow better view for the stereo camera over the grizzly [Color figure can be viewed at wileyonlinelibrary.com]

individual joint tracking level is shown in Figure 25 while RMS tracking errors over the same time frame are shown in Figure 26. The figures indicate the accurate tracking of each joint and demonstrate that the average Cartesian RMS tracking error over the whole experiment was only 57.9 mm. The RMS error was the largest when the controller detected broken rock and began to raise the TCP, preventing it from hitting the grizzly due to the inertia of the manipulator. The interaction with the rocks before the break attempt also caused tracking error due to the trajectory being set below the rock's surface to achieve pressure against the rock.

A close-up of an individual break attempt is shown in Figure 27 in which TCP height and lift valve control are shown in parallel to give better understanding of the actual breaking process. In the beginning, the manipulator moved to the rock. Then, control was continued in an open-loop manner, mimicking manual operation. Pressure against the rock was first built up using the dual cylinders of the lift joint of the manipulator. After pressure against the rock was ensured, the hydraulic hammer was activated. At this point, the manipulator began slowly moving downward until the rock was broken, which can be observed as a sudden loss of opposing force from the rock. In turn, this caused the manipulator's quick acceleration. When the manipulator descended below a threshold height, the rock was considered broken and the manipulator was raised back up. Due to the large inertia of the 2700 kg hydraulic hammer, the manipulator kept descending below the threshold height despite the fact that the control valve had been changed to the opposite opening. Therefore, for safety reasons, the threshold height must be set higher than the actual grizzly height to avoid impact with it. In our experiments, this height was set 50 mm above the grizzly. Due to the large inertia of the manipulator, the TCP could occasionally hit the grizzly after a rock was broken, but the hammer operation was halted automatically in advance so that no damage to the grizzly or the boom could happen.

In this study, we limited our focus on the use of only joint angle encoders for the sake of applicability to industrial applications with minimal need of retrofitting the system. However, if we consider the break attempt shown in Figure 27, it is evident that the use of pressure sensors would prove beneficial in detecting the instance a rock is broken; during this time, the pressure inside the lift cylinders collapse due to the loss of opposing force from the rock, thus making the break detectable via pressure sensors. The impacts from the

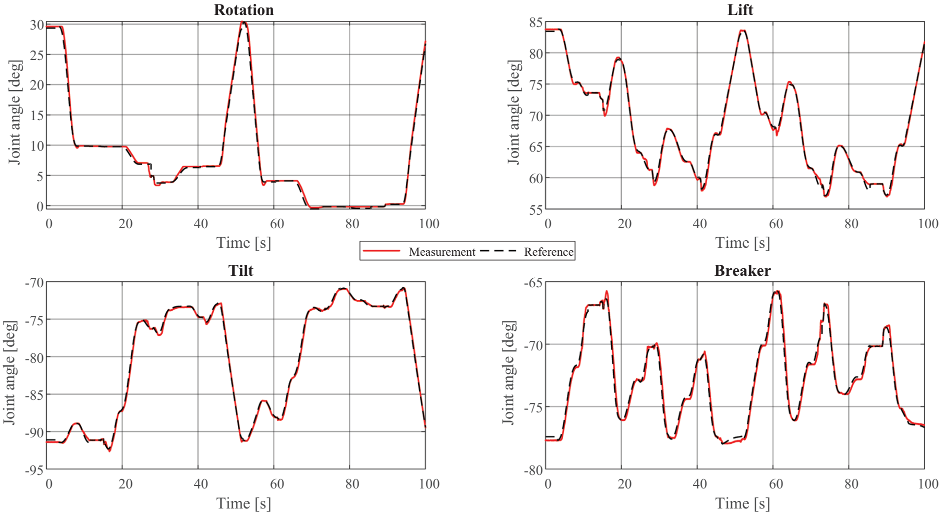

FIGURE 25 A snippet of individual joint angle tracking during break Experiment 8 [Color figure can be viewed at wileyonlinelibrary.com]

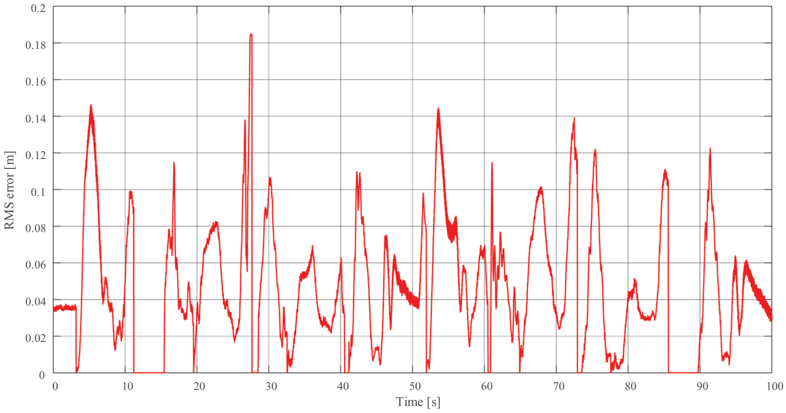

FIGURE 26 Cartesian tracking errors during Experiment 8. The mean error over the whole experiment was 57.9 mm, while the maximum error was 202 mm. The maximum error occurred during a breaking process, immediately after a rock was broken and the controller was attempting to stop the movement of the TCP toward the grizzly due to the sudden loss of opposing force from the rock. RMS, root mean square [Color figure can be viewed at wileyonlinelibrary.com]

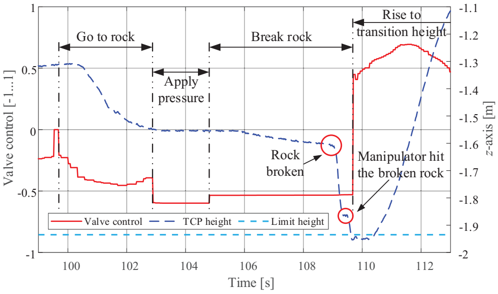

FIGURE 27 Individual break attempt from Experiment 9. The left y-axis shows the valve control of the lift valve used to maintain pressure against rock during the breaking process. The right y-axis (labeled Z-axis) shows the TCP's height. When the breaking begins, valve control is lowered slightly to limit the jerk of the manipulator upon the sudden loss of opposing force when the rock is broken. After approximately 0.5 s after the rock was broken the manipulator hit one half of the broken rock that is seen as a pause in the descent of the TCP in the plot. TCP, tool center point [Color figure can be viewed at wileyonlinelibrary.com]

hydraulic hammer can also be detected from pressure spikes. Using such data, the breaking process can be controlled more precisely.

6 | SUGGESTED IMPROVEMENTS

The performed experiments in our simplified field test environment served as a feasibility study providing valuable insight on the automation of the secondary breaking tasks in grizzly applications. However, the setup also limited the number of experiments practically possible to perform, due to a large number of auxiliary tasks required for each experiment. Yet, the simplified field test environment served us well and helped at identifying several key challenges and shortcomings of the proposed system. Further improvement of the proposed system would benefit from testing environment with continuous ore flow which would mean preferably an operational mine. However, these are continuously running highly optimized production facilities, where production downtime can lead to large costs. Arranging an experimental setup in such conditions without affecting the mine operation is a challenging task that requires a lot of planning, coordination, and development to achieve a mature enough research platform that can be used in cooperation with the mine operation. Such environment would prove fruitful for gathering data for performance analysis between an autonomous system and a human operator. Similar study comparing forwarder operators with boom tip control versus traditional control were conducted in Manner et al. (2019).

This section presents improvements to the proposed system based on the insight gained from the experiments. The major improvements to the rock breaking system are aimed to improve the robustness and effectiveness of the system under more complex and realistic environments. The herein proposed changes enhance the tactical layer of the rock breaking system, bringing it one-step-closer to practical implementations. These improvements are seen as way to overcome the following shortcomings of the proposed system identified during the experiments: (1) the break position selection was able to select a break position on inclined surfaces under specific conditions. (2) the system was unable to distinguish the difficulty of a break attempt beforehand in any way. (3) reorientation of difficult rocks was not considered as a strategy for more difficult rocks. (4) detection of the break instance relied only on position measurements, which yielded slow reaction to the dynamically fast break instance.

6.1 | Break point selection

A few flaws in the proposed method for break position selection were identified in the experiments, that should be addressed in future research. First, the constraint that the break position must locate within a rectangular region quarter the size of the bounding box enclosing the boulder does not always yield the best break position. For instance, if the boulder has its centroid of mass near one of its edges and is shaped like an off center pyramid, the highest point within the search area would yield a break position on a slanted surface. Based on the experiments, those conditions result with a high likelihood in an unsuccessful break attempt. Second, due to the physical constraints of the manipulator, aligning of the rock hammer is not possible in most cases. Therefore, finding the surface normal based on the break point may not be the best approach. Instead, an alternative method could be investigated in the future. Rather than selecting the angle for impact based on the break point, the break point should be selected based on the surface properties of the rock to minimize the possibility of slipping and also avoid having to align the manipulator for each rock separately.

To fulfill these conditions, suitable break locations may be obtained by first calculating normal vectors for each point of a point cloud representing a single rock. Then, the point cloud is filtered based on the normal vectors, to remove points belonging to inclined surfaces. After filtering, the point cloud is left with points belonging to flat surfaces. Then, a suitable break position can be obtained by finding a point with most points in its local neighborhood, i.e., within a specific radius around the point. Figure 28a,b illustrate the results of this method. The radius is here set to 65 mm, which is the same as the radius of the blunt tool of the hydraulic hammer.

6.2 | Per rock difficulty estimation

The inability to make any difference between rocks on the grizzly was identified as an adverse property of the evaluated VPS. Without any information regarding the difficulty of break attempts, the autonomous system was selecting it's targets only based on the Euclidean distance metric. However, this was identified as overly simplified approach, as the strategy for difficult rocks often involves manipulating the rocks into different poses.

The above described method for the break location identification can be leveraged for estimating the difficulty of a break attempt at the same time. By analyzing the surface properties of the local neighborhood of the break location its flatness can be estimated and used as a quality metric. Break points with more points in its local neighborhood in the filtered cloud indicate flatter surfaces, while low number of points in the local neighborhood indicate sharp-edged surface, as point belonging to inclined surfaces are removed. As observed in the experiments sharp-edged and inclined surfaces are much harder to break.

Other criteria related to the per rock difficulty include, for example, the height of the rock in relation to its cross-sectional area and the horizontal distance of the break point and the centroid of the rock. Other criteria may exist as well, such as the overlapping percentage, but the fine-tuning and finding correct relations between each criteria becomes more complex with more criteria. The main goal of the difficulty estimation is after all determining whether a rock may be broken as such or it should be manipulated into a different pose first. Figure 28c has the difficulties estimated for each break location based on the three first-mentioned criteria. Difficulty scores below 10 indicate a typical difficulty, while scores above 10 indicate a challenging rock, that may need to be manipulated into a different pose before a break attempt. Defining a meaningful metrics for the difficulty estimation requires further testing to obtain a balanced relation between different difficulty criteria, and to validate the results.

6.3 | Break instance detection

Another shortcoming of the experimental setup was the naive approach for detecting break instances, or more specifically, the lack of such system. Therefore, we acknowledge the necessity to describe a few approaches that could be leveraged to detect the break instances. To detect the shattering of the target rock, an intuitive

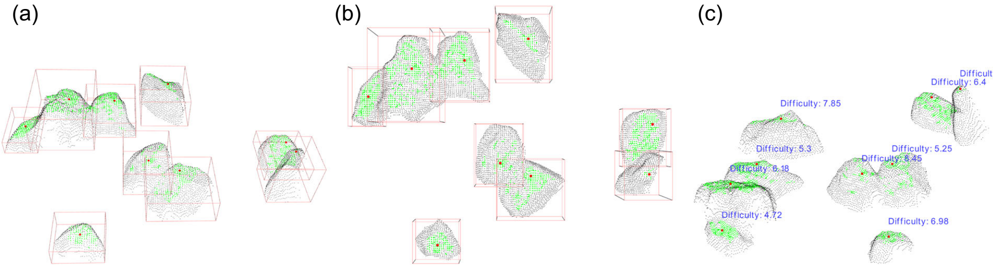

FIGURE 28 Visualization of the results of the second break location selection method. The suitable areas with normal vector pointing up are drawn with green, while the selected break points are marked with red points. (a) Break locations from side, (b) break locations from above, and (c) break difficulty estimation [Color figure can be viewed at wileyonlinelibrary.com]

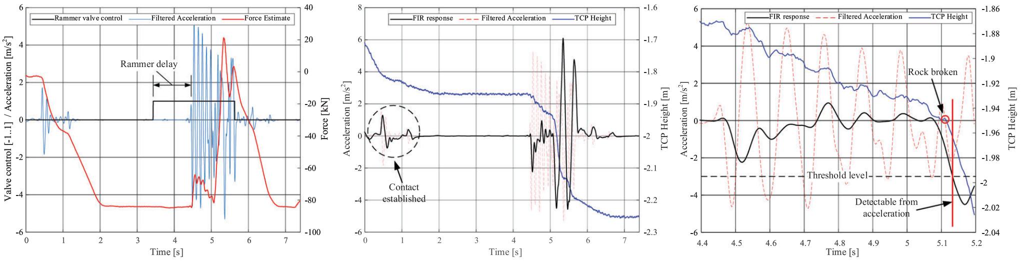

FIGURE 29 Demonstration of the break instance detection using external force estimation and acceleration measurements [Color figure can be viewed at wileyonlinelibrary.com]

method is to observe the forces of the manipulator and detect a sudden loss of external opposing force at the TCP. However direct contact force measurement is not practical due to the harsh application, that is typically of of question for fragile force/torque sensors. Instead, indirect approaches are required to estimate the external force. Takahashi and Monden (1999) proposed strain gauges at the chisel of the hammer to detect the external force and ultimately the break instance. However, the chisel is subject to such harsh use that the longevity of the strain gauges is susceptible at best. In Section 3.3.7, force estimation based on model based dynamics compensation and pressure signals was discussed. Such approach is an effective way to obtain a force estimate for the break instance detection, but it requires sophisticated modeling of the dynamics of the manipulator as well as multiple pressure sensors (in this case six), both typically avoided in commercial applications. A simpler approach could be to monitor the pressure of only one side of one cylinder and detect rapid changes to identify the break instance. Alternatively, accelerometer could be utilized for the same purpose.

Figure 29 visualizes measurements from a successful break attempt performed manually. The break instance is here detectable by two methods. First, we have implemented the force estimation within the manipulator controls, and second, we utilize acceleration measurements gathered using a Novatron G2 IMU. The acceleration in the direction of the hammer is first filtered using a high-pass filter to remove the effect of gravity. Then, a FIR filter with a window length of 120 ms is used to detect the break instance. The frequency of the hydraulic hammer is roughly 8 Hz, which yields a near zero response from the FIR filter at the hammer operating frequency. However, when the rock is broken, the response will show a large negative value, due to one half of the acceleration spike being lost. This method enables us to detect a successful break within approximately 60–90 ms.

6.4 | Improved autonomous operation pipeline

The suggested improvements lead to an improved operational pipeline for the autonomous system that has tactical tools to handle more versatile and realistic situations and environment. The improved break point selection is foreseen to improve the success rate of breaking as the break points are selected more carefully on locations that inherently minimize the possibility of manipulator slipping on the rock surface, or the rock moving away. Moreover, the ability to distinguish challenging rocks from the grizzly further enhances the success rate as the system can first focus on easier rocks and then attempt the harder cases after it has attempted to reorient

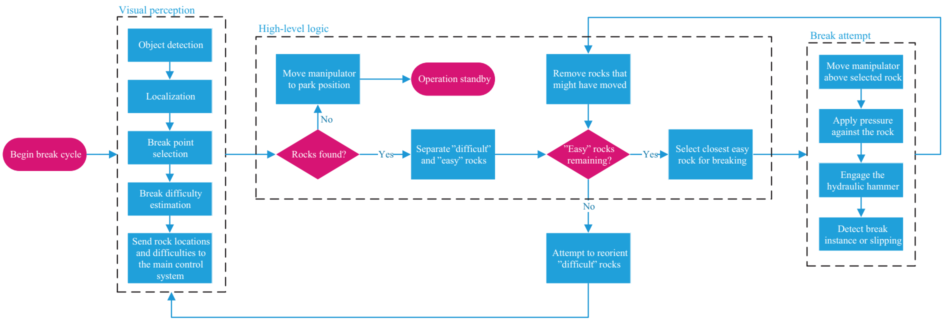

FIGURE 30 An improved autonomous operation pipeline based on the tactical layer improvements [Color figure can be viewed at wileyonlinelibrary.com]

them first. To manipulate difficult rocks into better poses, we propose that the manipulator is driven through a trajectory that goes trough the centroid of each difficult rock. Other manipulation tactics can be applied here as well, for example, the rock may be moved toward the largest unoccupied area near it, or as a last resort just to the side of the grizzly for later manual treatment by a human operator.

The break instance detection can be seen as a feature that increases safety of the operation and at the same time reduces time between break attempts. The reduced time between the detection of a break instance is very critical for stopping the manipulator's downward movement after a sudden loss of opposing force from the rock being broken. Similar methodology can be applied to detect other relevant information about the break attempt, for example, number of impacts from the hydraulic hammer, or the slipping of the manipulator.

Figure 30 illustrates a simplified operational pipeline possible with the improvements suggested in this section. The pipeline is simplified in a sense that it only covers the operations in a high level leaving smaller details out to just give clear visualization.

7 | CONCLUSIONS AND FUTURE WORK

In this paper, we presented a novel autonomous robotic rock breaking system that was verified in a full-scale real-world environment. The proposed system is built on two developments: (1) a commercially available rock breaker boom that is instrumented with high-precision joint angle encoders used for our robotic control system deployed on a dSpace MicroAutoBox 2 real-time system, and (2) a 3D VPS incorporating YOLOv3 infrastructure. Recent leaps in the performance of deep learning models enabled us to design a 3D vision system for resolving real-world object detection problems. The proposed integral system enables completely autonomous rock breaking, which serves to increase automation in the mining industry.

The main contribution of this paper is the full-scale demonstration and integration of an autonomous system for breaker boom operation in grizzly applications. Such a system has been proposed as early as the 1990s, but to the authors' knowledge, it has not been demonstrated before this study. The vision system can achieve rock detection with an average precision of 97.61%. The manipulator control system has dynamic accuracy of 60 mm in free space operation, which is sufficient for the intended application. Based on the data gathered by the vision system, the autonomous control system finds the best rock to break and can sequence the rock breaking, even in a cluttered and dynamic scene.

The proposed system was shown to be capable of autonomous operation without any need for human intervention. In the experiments, the system was able to both recognize and localize oversized rocks on the grizzly, move the manipulator in contact with the rocks, and engage the hydraulic hammer to reduce the size of oversized rocks. The shape of the rocks was identified as a crucial factor in successful breaking, especially with rocks slanted perpendicular to the rotation of the manipulator, which would slip away from the rock during the breaking process when pressure was applied against the slanted rock. The main reason for this is the backlash in the rotation joint of the manipulator. In the authors' opinions, the break success rate could be substantially increased even in manual operation if this problem is addressed and considered in the manipulator's design. Despite these challenges, our proof-of-concept system was able to achieve a success rate of 34%, which can be considered an adequate result for a system that can operate continuously without interruption at a pace of over 3 break attempts per minute. It is also worth noting that even a human operator will not achieve a 100% success rate, as the same challenges of rocks or the manipulator slipping away will persist regardless of the operator. However, a human operator can most likely react and adapt to these challenges more rapidly by attempting to break different spots on the rock based on observing to which side the rock is rolling or moving. Teaching the manipulator control system how to make such observations may be explored in future research to enhance the performance of the proposed system.

The results from the preliminary study of autonomous rock breaker operation presented in this paper are promising and highlight the system's technological readiness. The road from technical demo to commercial product is long and requires a lot more testing, but the main challenges of employing such a system can be overcome, as shown in this paper. In the experiments, no operator interference was required and no unexpected behavior was encountered. The system had a good success rate in breaking large and sturdy rocks, while smaller rocks with sharp shapes caused difficulty for the system. Nevertheless, the benefit from an autonomous rock breaker is seen in the more consistent and tireless nonstop operation that is only achievable with robotic operations. The occasional situations when the system requires human intervention for aid in the breaking is seen negligible, as operators are foreseen to be able to simultaneously monitor multiple booms.

Future work on this system should focus on further developing the individual components of the system, as well as aim for wider and more practical testing. More comprehensive experiments in a relevant environment are required to obtain quantitative information to analyze and compare the performance of the autonomous system to experienced operators. An interesting path for further research is to implement skills that mimic and exploit operating strategies that experienced operators use to achieve higher success rates, for example, manipulating difficult rocks into different poses for easier breaking. It is worth noting that in different breaker boom applications, especially with gyratory crushers, the raking and manipulation of rocks to prevent and remove blockages is almost as widely used of a strategy as the actual breaking. Different operating strategies for these applications should also be considered in future research. In an ideal scenario, the system could be deployed in a real mine as a secondary system for testing and prototyping purposes. On the subsystem level, the VPS requires more training data on different situations to cover a broader range of environmental conditions, for example, snowfall, rainfall, fog, dust, and artificial lighting. In addition, the currently used stereo camera is unsuitable for the intended harsh outdoor conditions of the target application. As such, alternatives should be considered and designed from scratch, if necessary. Another interesting path for future research lies in the control of the breaker boom—more specifically, contact control with the rocks. To control the force applied to the rocks, the use of more sophisticated control methods must be investigated. A promising way to achieve higher precision control lies in nonlinear model-based control.

DATA AVAILABILITY STATEMENT

The data that support the findings of this study are openly available in Github at https://github.com/epoc88/SecondaryBreakingDataset.

ORCID

Santeri Lampinen http://orcid.org/0000-0003-1201-9027
Longchuan Niu https://orcid.org/0000-0003-4996-5519
Jouni Mattila https://orcid.org/0000-0003-1799-4323

REFERENCES

Al Hakim, E. (2018). *3d yolo: End-to-end 3d object detection using point clouds* (Master's thesis). KTH, School of Electrical Engineering and Computer Science (EECS).

Arun, K. S., Huang, T. S., & Blostein, S. D. (1987). Least-squares fitting of two 3-d point sets. In *IEEE Transactions on pattern analysis and machine intelligence*, PAMI-9 (Vol. 5, pp. 698–700).

Bak, M. K., & Hansen, M. R. (2012). Modeling, performance testing and parameter identification of pressure compensated proportional directional control valves. In *Proceedings of the 7th FPNI PhD Symposium on Fluid Power*, June 27–30, 2012, Reggio Emilia, Italy (pp. 889–908).

Bentley, J. L. (1975). Multidimensional binary search trees used for associative searching. *Communications of the ACM*, *18*(9), 509–517.

Bernard, R., & Albright, S. (1994). *Robot calibration*. Springer.

Boeing, A. (2013). A remotely operated robotic rock breaker with collision avoidance for the mining industry. In *30th International Symposium of Automation and Robotics in Construction and Mining (ISARC 2013) Proceedings*, IAARC, (pp. 875–884).

Brown, D. C. (1966). Decentering distortion of lenses. *Photogrammetric Engineering and Remote Sensing*, *32*(3), 444–462.

Corke, P. I., Roberts, J. M., & Winstanley, G. J. (1998). Robotics for the mining industry. In A. T. de Almeida, & O. Khatib (Eds.), *Autonomous robotic systems* (pp. 163–181). Springer.

Dahl, O. (1994). Path-constrained robot control with limited torques-experimental evaluation. *IEEE Transactions on Robotics and Automation*, *10*(5), 658–669.

Dahl, O., & Nielsen, L. (1990). Torque-limited path following by online trajectory time scaling. *IEEE Transactions on Robotics and Automation*, *6*(5), 554–561.

Duff, E., Caris, C., Bonchis, A., Taylor, K., Gunn, C., & Adcock, M. (2010). The development of a telerobotic rock breaker. In A. Howard, K. Iagnemma, & A. Kelly (Eds.), *Field and service robotics*. –. : Springer.

Fischler, M. A., & Bolles, R. C. (1981). Random sample consensus: a paradigm for model fitting with applications to image analysis and automated cartography. *Communications of the ACM*, *24*(6), 381–395.

Forsyth, D. A., & Ponce, J. (2002). *Computer vision: a modern approach*. Prentice Hall Professional Technical Reference.

Fox, J., Castano, R., & Anderson, R. C. (2002). Onboard autonomous rock shape analysis for mars rovers. In *Proceedings, IEEE Aerospace Conference* (Vol. 5, pp. 5–2052).

Girshick, R. (2015). Fast R-CNN. In *Proceedings of the IEEE International Conference on Computer Vision* (pp. 1440–1448).

Girshick, R., Donahue, J., Darrell, T., & Malik, J. (2014). Rich feature hierarchies for accurate object detection and semantic segmentation. In *Proceedings of the IEEE Conference on Computer Vision and Pattern Recognition* (pp. 580–587).

Haddadin, S., De Luca, A., & Albu-Schäffer, A. (2017). Robot collisions: A survey on detection, isolation, and identification. *IEEE Transactions on Robotics*, *33*(6), 1292–1312.

Havoutis, I., & Calinon, S. (2019). Learning from demonstration for semi-autonomous teleoperation. *Autonomous Robots*, *43*(3), 713–726.

He, Q., Wang, Z., Zeng, H., Zeng, Y., Liu, S., & Zeng, B. (2020). SVGA-Net: Sparse voxel-graph attention network for 3D object detection from point clouds. *arXiv*, 2006.04043.

Ho, N. (2013). Finding optimal rotation and translation between corresponding 3D points. http://nghiaho.com/?page_id=671. Accessed May 16, 2021.

Horn, B. K. (1987). Closed-form solution of absolute orientation using unit quaternions. *JOSA A*, *4*(4), 629–642.

Horn, B. K., Hilden, H. M., & Negahdaripour, S. (1988). Closed-form solution of absolute orientation using orthonormal matrices. *JOSA A*, *5*(7), 1127–1135.

Hubert, G., Dirdjosuwondo, S., Plaisance, R., & Thomas, L. (2000). Tele-operation at freeport to reduce wet muck hazards. *MassMin 2000*, 173–179.

Hulttinen, L. (2017). *Position-based impedance control of a hydraulic rock breaker boom* (Master's thesis). Tampere University of Technology.

Hustrulid, W. A., & Bullock, R. L. (2001). *Underground mining methods: Engineering fundamentals and international case studies*. Society for Mining, Metallurgy, and Exploration (SME).

Jazar, R. N. (2010). *Theory of applied robotics: kinematics, dynamics, and control* (2nd ed.). Springer Publishing Company.

Koivumäki, J., & Mattila, J. (2015). Stability-guaranteed force-sensorless contact force/motion control of heavy-duty hydraulic manipulators. *IEEE Transactions on Robotics*. *31*(4), 918–935.

Koivumäki, J., & Mattila, J. (2017). Stability-guaranteed impedance control of hydraulic robotic manipulators. *IEEE/ASME Transactions on Mechatronics*, *22*(2), 601–612.

Ku, J., Mozifian, M., Lee, J., Harakeh, A., & Waslander, S. L. (2018). Joint 3d proposal generation and object detection from view aggregation. In *2018 IEEE/RSJ International Conference on Intelligent Robots and Systems (IROS)*. IEEE (pp. 1–8).

Lampinen, S., Koivumäki, J., Mattila, J., & Niemi, J. (2019). Model-based control of a pressure-compensated directional valve with significant dead-zone. In *ASME/BATH 2019 Symposium on Fluid Power and Motion Control*. American Society of Mechanical Engineers Digital Collection.

Lampinen, S., Niemi, J., & Mattila, J. (2020). Flow-bounded trajectory-scaling algorithm for hydraulic robotic manipulators. In *2020 IEEE/ASME International Conference on Advanced Intelligent Mechatronics (AIM)*.

Liang, M., Yang, B., Chen, Y., Hu, R., & Urtasun, R. (2019). Multi-task multi-sensor fusion for 3d object detection. In *Proceedings of the IEEE/CVF Conference on Computer Vision and Pattern Recognition (CVPR)*.

Liang, M., Yang, B., Wang, S., & Urtasun, R. (2018). Deep continuous fusion for multi-sensor 3d object detection. In *Proceedings of the European Conference on Computer Vision (ECCV)* (pp. 641–656).

Lovgren, R. (2004). Radical improvements in crane safety. *ISO Focus*, *1*(7), 21–93.

Manner, J., Mörk, A., & Englund, M. (2019). Comparing forwarder boom-control systems based on an automatically recorded follow-up dataset. *Silva Fenn*, *53*, 10161.

Mattila, J., Koivumäki, J., Caldwell, D. G., & Semini, C. (2017). A survey on control of hydraulic robotic manipulators with projection to future trends. *IEEE/ASME Transactions on Mechatronics*, *22*(2), 669–680.

McKinnon, C., & Marshall, J. A. (2014). Automatic identification of large fragments in a pile of broken rock using a time-of-flight camera. *IEEE Transactions on Automation Science and Engineering*, *11*(3), 935–942.

Metso Mining and Construction. (2015). Basics in Minerals Processing Handbook.

Niu, L., Aref, M. M., & Mattila, J. (2018). Clustering analysis for secondary breaking using a low-cost time-of-flight camera. In *2018 Ninth International Conference on Intelligent Control and Information Processing (ICICIP)*. IEEE (pp. 318–324).

Niu, L., Chen, K., Jia, K., & Mattila, J. (2019). Efficient 3d visual perception for robotic rock breaking. In *2019 IEEE 15th International Conference on Automation Science and Engineering (CASE)*. IEEE (pp. 1124–1130).

Nurmi, J., & Mattila, J. (2017). Automated feed-forward learning for pressure-compensated mobile hydraulic valves with significant dead-zone. In *Proceedings of ASME/BATH Symposium on Fluid Power and Motion Control (FPMC2017)*, Oct. 16–19, 2017, Sarasota, FL.

Qi, C. R., Litany, O., He, K., & Guibas, L. J. (2019). Deep hough voting for 3d object detection in point clouds. In *Proceedings of the IEEE International Conference on Computer Vision* (pp. 9277–9286).

Qi, C. R., Liu, W., Wu, C., Su, H., & Guibas, L. J. (2018). Frustum pointnets for 3d object detection from rgb-d data. In *Proceedings of the IEEE Conference on Computer Vision and Pattern Recognition*, (pp. 918–927).

Redmon, J. (2018). Darknet: Open source neural networks in c. Pjreddie.com.

Redmon, J., Divvala, S., Girshick, R., & Farhadi, A. (2016). You only look once: Unified, real-time object detection. In *2016 IEEE Conference on Computer Vision and Pattern Recognition (CVPR)*, (pp. 779–788).

Redmon, J., & Farhadi, A. (2017). Yolo9000: better, faster, stronger. In *Proceedings of the IEEE conference on computer vision and pattern recognition* (pp. 7263–7271).

Redmon, J., & Farhadi, A. (2018). YOLOv3: An incremental improvement. *arXiv*, 1804.02767.

Ren, S., He, K., Girshick, R., & Sun, J. (2015). Faster r-cnn: Towards real-time object detection with region proposal networks. In *Advances in neural information processing systems* (pp. 91–99).

Sandvik Mining and Construction. (2016). *Hydraulic Hammer Rammer 2577, Operator's Manual*. Available at https://www.rammer.com/en/products/hydraulic-hammers/excellence-line/medium-range/2577/

Scharstein, D., & Szeliski, R. (2002). A taxonomy and evaluation of dense two-frame stereo correspondence algorithms. *International Journal of Computer Vision*, *47*(1-3), 7–42.

Sciavicco, L., Siciliano, B., & Sciavicco, B. (2000). *Modelling and control of robot manipulators* (2nd ed.). Springer-Verlag.

Smirnov, S., Georgiev, M., & Gotchev, A. (2015). Comparison of cost aggregation techniques for free-viewpoint image interpolation based on plane sweeping. In *Ninth International Workshop on Video Processing and Quality Metrics for Consumer Electronics.*

Suomalainen, M., Koivumäki, J., Lampinen, S., Mattila, J., & Kyrki, V. (2018). Learning from demonstration for hydraulic manipulators. In *IEEE/RSJ International Conference on Intelligent Robots and System (IROS).*

Tafazoli, S., Salcudean, S. E., Hashtrudi-Zaad, K., & Lawrence, P. D. (2002). Impedance control of a teleoperated excavator. *IEEE Transactions on Control Systems Technology. 10*(3), 355–367.

Takahashi, H., & Monden, T. (1999). Automatic system for boulder breakage using force sensors. *Fragblast*, *3*(3), 267–277.

Takahashi, H., & Sano, K. (1998). Automatic detection and breaking system for boulders by use of ccd camera and laser pointer. *Fragblast*, *2*(4), 397–414.

Walker, M. W., Shao, L., & Volz, R. A. (1991). Estimating 3-d location parameters using dual number quaternions. *CVGIP: Image understanding*, *54*(3), 358–367.

Wanner, J., & Sawodny, O. (2019). Tool-center-point control of a flexible link concrete pump with hydraulic limitations using quadratic programming. In *2019 IEEE 15th International Conference on Automation Science and Engineering (CASE)*, (pp. 561–566).

Yang, B., Luo, W., & Urtasun, R. (2018). Pixor: Real-time 3d object detection from point clouds. In *Proceedings of the IEEE Conference on Computer Vision and Pattern Recognition (CVPR).*

Zhang, Z. (2000). A flexible new technique for camera calibration. *IEEE Transactions on Pattern Analysis and Machine Intelligence*, *22*(11), 1330–1334.

Zhang, Z. -X. (2016). Chapter 21- optimum fragmentation, *Rock Fracture and Blasting* (pp. 411–423). Butterworth-Heinemann.

Zhao, X., Liu, Z., Hu, R., & Huang, K. (2019). 3d object detection using scale invariant and feature reweighting networks. In *Proceedings of the AAAI Conference on Artificial Intelligence* (Vol. 33, pp. 9267–9274).

Zhou, Y., & Tuzel, O. (2018). Voxelnet: End-to-end learning for point cloud based 3d object detection. In *Proceedings of the IEEE Conference on Computer Vision and Pattern Recognition* (pp. 4490–4499).

How to cite this article: Lampinen, S., Niu, L., Hulttinen, L., Niemi, J., & Mattila, J. (2021). Autonomous robotic rock breaking using a real-time 3D visual perception system. *Journal of Field Robotics*, 1–27. https://doi.org/10.1002/rob.22022

PUBLICATION
IV

Robust Rock Detection and Clustering with Surface Analysis for Robotic Rock Breaking Systems

S. Lampinen and J. Mattila

2021 IEEE/ASME International Conference on Advanced Intelligent Mechatronics (AIM). 2021, 140–147
DOI: `10.1109/AIM46487.2021.9517695`

Robust Rock Detection and Clustering with Surface Analysis for Robotic Rock Breaking Systems

Santeri Lampinen and Jouni Mattila

***Abstract*—A reliable and robust visual perception system is often a key-enabler for autonomous robotic systems working in at least partially unknown environment. For autonomous robotic rock breaking system, boulder detection and localization system is an essential part that must be able to operate under challenging environments. The problem can be summarized as detecting unstructured objects in a structured environment. A key to robust boulder detection is an effective clustering algorithm, that can segment a point cloud, captured by e.g., a Time-of-Flight (TOF) camera, into clusters of individual boulders. This information is crucial for an autonomous robotic secondary breaking system, that uses it to break each individual boulder by a hydraulic impact hammer. This study proposes a novel algorithm for point cloud segmentation that can be used for the boulder detection application. The method is designed using features of the Point Cloud Library (PCL), and it is benchmarked against other readily available algorithms in the PCL. The results indicate robust performance with an impressive 97.4% accuracy on our dataset.**

***Index Terms*—Point cloud, clustering, segmentation, time-of-flight camera, secondary breaking, mining automation**

I. INTRODUCTION

Increasing the automation level is a highly considered aim of the risk-intensive mining and construction industries. As various process-phases, such as loading, tramming, haulage, dumping and blasthole drilling [1]–[3] are being automated for increased safety and productivity [4], visual perception systems are needed to provide the autonomous machines vital information from the environment they are operating in.

Secondary breaking of blasted ore is a task, that aims at a controlled size reduction of the oversized material that is too coarse for the primary crusher (e.g., a jaw crusher). To ensure a continuous material flow the oversized ore pieces are broken using a secondary breaker, i.e., a hydraulic heavy-duty manipulator equipped with a hydraulic impact hammer; see Fig. 1 for reference. This process-phase is still human-operated due to the challenges posed by the rough environment and the high-precision control of the hydraulic manipulator. As a mine can contain multiple such secondary breaking stations, the automation of the process phase is highly desirable. Alone the transportation of the personnel from the surface to an underground breaking station may take over an hour.

Automation of this process-phase has been first proposed in 1998 [5] and [6], where rock detection was performed from 2D images and the localization was achieved using actuated laser assisted measurements. Later Fox et al. proposed fusion of 2D imagery and range data for autonomous rock detection for a planetary rover [7]. Laser scanners have been proposed for blasted ore pile size distribution estimation in [8]–[10], with a specific segmentation method. Similarly, Time-of-Flight (TOF) cameras were proposed for large boulder detection from a pile of broken rocks in [11]. TOF cameras for rock detection were later revisited by Niu et al., where a low-cost low resolution TOF camera was used for boulder detection on a metal grizzly [12]. The use of a stereo camera combined with a deep learning-based object detector was proposed in [13], where rock detection and localization were achieved at an impressive accuracy under a very specific conditions.

Fig. 1. RamBooms X88-540R breaker boom at the field test site at Tampere University.

The deep learning-based method achieved an impressive accuracy at the rock detection and localization, but it was found to be very prone to varying environmental conditions. One observed shortcoming of the method was the poor dynamics of the used stereo camera. Under lower lighting conditions the image quality decreased significantly and under a very bright weather the contrast ratio was also poor. Moreover, the camera didn't have any protection from the elements. This is a strong argument against stereo cameras, as robust IP rated cameras can be very expensive. The second notable challenge with the deep learning approach was the gathering and labelling of the training data. The approach in [13] required over 4000 unique and hand labelled images of the target scene. That number may even be considered quite low, despite that alone the gathering of the training data took several weeks, not to mention the labelling efforts.

For these reasons, this study investigates the use of a high

S. Lampinen, and J. Mattila are with the faculty of Engineering and Natural Sciences, Tampere University, Finland. `name.surname@tuni.fi`

resolution TOF camera for the boulder detection to achieve a robust system that can be utilized under the harsh conditions of the target application. The study utilizes a Blaze 101 TOF camera from Basler AG [14], that can acquire 3D point clouds at a resolution of 640x480 in lieu of the 1280x720 in [13]. Despite the lower resolution compared to the stereo camera, it is still a huge leap from the camera used in [12] with a resolution of 64x16. The camera outputs low noise point clouds using a Sony IMX556PLR sensor combined with 940 nm VCSEL illumination, that is more robust against ambient illumination than traditional 850 nm illumination. Moreover, the new TOF camera is rated IP67, i.e., dust-tight enclosure protected against temporary immersion in water, and it uses a robust GigE interface for the data transmission, both essential features considering the harsh target application. Compared to stereo cameras, the point cloud has lower noise level, as the stereo matching algorithms often introduce noise to the depth perception, especially with relatively small baseline stereo cameras.

The breaker boom in Fig. 1 is a commercial boom from a Finnish OEM RamBooms, and it is heavily retrofitted to facilitate the robotic rock breaking study. The high-precision control of the boom is already realized in [15], and the remaining notable challenges for the fully autonomous breaker lie in the designing of a tactical layer for the autonomous operation and a robust boulder detection and break location identification system. The current study focuses on the latter. To achieve robust boulder detection, this study compares different clustering algorithms for point clouds and proposes an improved algorithm for efficient automatic clustering of the obtained point clouds. Moreover, this study propose a method for selecting a suitable position for a break attempt and classify an estimate of the difficulty for break attempts based on the geometric conditions of the identified boulders.

The remainder of this paper is organized as follows. Section II provides theoretical background into clustering and presents the benchmark methods shortly. Section III introduces the proposed algorithm for the rock detection. Section IV discusses the proposed method for selecting suitable break positions and estimating difficulty for the breaking. Section V presents the results from the different clustering algorithms and discusses their suitability for the task. Section VI concludes the paper.

II. POINT CLOUD CLUSTERING

Detecting points of data belonging to the same underlying object or a group is an essential part of unsupervised learning, called clustering [16]. In this study, we focus specifically on clustering of 3D point cloud data. Numerous clustering methods for point clouds have been defined for different tasks and a wide variety of algorithms are already implemented and readily available using the open source Point Cloud Library (PCL) [17]. Commonly used point cloud clustering algorithms can be divided into following categories; edge-, region-, attribute-, model- and graph-based methods [18]. Selecting the most appropriate approach is not a simple task, but is affected by multiple factors, such as data quality, viewpoint, noise and prior knowledge of the target scene.

Prior knowledge of the scene can be used to make assumptions about the objects of interest. In the case of rock detection, model-based approaches are not very attractive, as boulders cannot be characterized by any particular feature. Instead, vague assumptions about the size of the boulders are reasonable. The mesh size of the grizzly defines the minimum size for the boulders and that can be very useful for the clustering algorithm. Based on the minimum size, smaller clusters can either be discarded or considered part of some neighbor cluster.

The segmentation of a point cloud is typically started by separating the data in the region of interest (ROI) from the ground plane. In the case of a fixed camera setup, this process is a trivial process as the point cloud can be filtered using a prior known ROI. In an unknown environment or in a moving camera setup, the ground plane can be removed using e.g., random sample consensus plane fitting method [19]. The remaining point cloud contains the useful information about the objects of interest.

The main challenge of this manuscript is the clustering of the remainder points to form a segmented visualization and insightful understanding of the boulders in the scene. The clustering algorithm needs to be able to cope with not only boulders far away from each other but also with ones partially occluded and overlapping. The possibility of partially overlapping and occluded rocks imposes constraints on the suitable algorithms. Algorithms that rely only on e.g., the proximity of neighboring points would detect such cases simply as one large cluster. Therefore, more advanced methods are required.

Several readily available segmentation methods can be applied for the above mentioned problem of boulder detection and in this manuscript we will be using Euclidean clustering [20], region growing segmentation, difference of normals based segmentation [21] and conditional Euclidean clustering methods as benchmark and comparison points for the proposed method.

A. *Euclidean clustering*

Spatial clustering based on Euclidean distance between neighboring points can be considered one of the simplest algorithms for point cloud segmentation. The algorithm is an unseeded method that iterates through the whole point cloud once and merges points that form a cluster with minimum distance between neighbor points smaller than a set threshold distance.

B. *Conditional Euclidean clustering*

Conditional Euclidean clustering method is essentially identical to Euclidean clustering, except for a custom condition used along the Euclidean distance to determine if a candidate point should be merged to the processed cluster. The algorithm is unseeded, and by default iterates the point cloud through in an unspecified order. In this study, we used this method for the comparative experiments, with a merge condition that returns true if the angle between the seed point normal and the candidate point normal is smaller than a set threshold value.

C. Region growing segmentation

Local connectivity alone as is the case with Euclidean clustering, is typically insufficient condition for clustering of point clouds. Instead, surface properties can be further leveraged for higher precision. Region growing segmentation enforces surface smoothness besides the local connectivity for clustering point clouds [22]. The segmentation begins from a point with the lowest local curvature value (curvature value describes here how well a plane can be fitted to the neighborhood of the point). Then adjacent points are merged based on an Euclidean distance enforcing local connectivity and difference between surface normal angles. The points that are merged to the processed cluster are selected as new seed points only if their curvature value is lower than a set smoothness threshold.

D. Difference of normals based segmentation

Image processing algorithms have been giving inspiration for point cloud segmentation, and so is the case with Difference of Normals (DoN) based segmentation [21]. The algorithm is inspired by Difference of Gaussians (DoG) based filtering, that is used e.g., for edge detection in digital images. The DoN is a multi-scale algorithm that uses Euclidean distance and the difference of normals calculated by two different scales. The idea behind the method is that local neighborhood of an edge will have greater variation in the normal vectors calculated by different number of neighbor points.

III. ALGORITHM

This section presents the proposed algorithm for the point cloud processing and clustering. Figure 2 presents an overview of the data processing pipeline. The segmentation process is divided into three distinct phases; preprocessing, clustering, and post-processing. The preprocessing consists of filtering points outside of the region of interest (ROI) and down sampling of the original point cloud. Then, the actual clustering is commenced on the filtered point cloud, and finally in the post-processing phase, close clusters are merged together and small clusters are removed.

A. Preprocessing and filtering

After obtaining the cloud from the ToF Camera, the data must be preprocessed to filter irrelevant points and outliers. As we are working with a fixed camera setup, a simple ROI based filtering can be used for the ground removal. Outliers and noise can be filtered from the cloud using a simple constant radius outlier removal algorithm to detect points standing out from the large clusters. Due to the fact that the ToF camera produces point clouds that are organized, that is, the point cloud can be considered as a 2.5D image with each pixel containing depth information, we can leverage the known structure for an efficient normal estimation based on integral images as shown in [23]. The normal vectors contain useful information of the point cloud that can be utilized by many clustering algorithms. The preprocessing of the point cloud is visualized in Fig. 3, where the filtered cloud is shown with larger point that are colored based on the z-component of the normal vectors. Brighter red colors represent normals pointing up, while darked colors represent more inclined surfaces.

B. Clustering

The proposed clustering method can be considered as a seeded flood fill algorithm. In a sense, it is analogous to pouring water over the seed points and clustering together all the points that are covered by the water. This method is similar to watershed segmentation, an established method in image processing [24], and a similar approach has been proposed in [8]–[10]. The approach proposed by Thurley et. al involved a three-part seed region generation based on distance transforms from detected edges, local maxima and seed merging. Here we propose a local maxima based seed forming. For the seed points we want to use the local maxima of the point cloud, as those represent the highest points of each individual boulder with a high likelihood. For the algorithm to work most effectively, we start the clustering from the lowest local maximum and proceed in order from the lowest local maximum to the highest one.

The actual algorithm is built on top of the conditional Euclidean clustering framework of the PCL. The algorithm uses a list of point cloud indices to determine the order it goest the cloud through. By providing the list in a specific order, the seed points can be specified according to our needs. In addition, the merge condition of proximal points can be custom defined. The seeding of the algorithm is done by finding all the local maxima of the point cloud with a specific radius. For this, the PCL has a method we can leverage as long as we filter the point cloud in advance based on the normal vectors of the cloud. Due to the possibility of partly overlapping boulders, local maximum of partly overlapping boulders might be missed, if the local maximum of a rock is very close to the edge of an overlapping rock that is also higher. This issue can be seen in Fig. 4(a), where one of the boulders does not have its highest point identified. To address this issue, we filter inclined surfaces from the cloud before the search for local maxima. Figures 4(b) and 4(c) demonstrate this method. After filtering, the local maxima of the remaining point cloud are extracted using a readily available filter implementation of the PCL called LocalMaximum.

After obtaining the seed points for clustering, we need to sort them from the lowest to the highest. Doing so increases separation between clusters as we will avoid merging higher boulders to lower ones. After preparing the seed points, the actual clustering can be performed using Algorithm 1. For practical implementations, PCL provides a class called pcl::ConditionalEuclideanClustering, that is a powerful and customizable class for point cloud segmentation. To leverage the provided class implementation, we need to provide the class with indices of all the points in the point cloud as the seed points. To perform the clustering in the specified order, the sorted local maxima are placed at the beginning of the indices vector, while the rest of the indices are located after the seed points. The rest of the cloud indices are sorted from highest to lowest to further improve the clustering results.

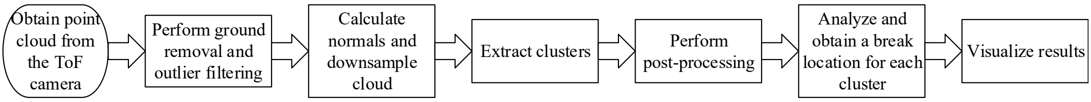

Fig. 2. A coarse overview of the point cloud processing structure for the proposed application.

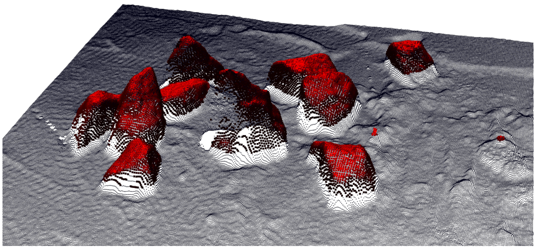

Fig. 3. Preprocessing of the point cloud. Filtered point cloud is represented with larger points that are colored based on the z-component of the normal vector. Red points have normal vector pointing up.

The clustering algorithm takes advantage of the identified normal vectors of the point cloud in two ways. First, the normals of the seed point and candidate point need to point roughly at the same direction. Enforcing the similarity of normal vectors improves separation of boulders and reduces oversegmentation of overlapping bouders, as the normal vectors typically vary significantly between boulders. Second, the requirement for the height difference between the seed point and the candidate point is determined based on the z-component of the normal vector. If the seed point is located on an inclined surface, the height difference must be greater. The condition to merge the candidate point to the current cluster is presented in Algorithm 2. The additional constraints in the merge condition greatly improve separation between partly overlapping boulders and prevent oversegmentation.

C. *Post-processing clusters*

Due to the possibility of multiple local maxima per boulder, a simple post-processing is required to obtain more uniform clusters as a result of the segmentation. Based on the assumption of the minimum size of the boulders, we opted to merge close clusters together. The condition for merging close clusters was designed to minimize oversegmentation, while merging all points belonging to the same underlying boulder together. The proposed condition is twofold; first, we check if the bounding volumes of two clusters overlap. Then, if the intersection volume divided by the smaller cluster's bounding volume is larger than a set threshold, the clusters are merged. If the intersection percentage is smaller than that, but the clusters have some intersection and the centroids are closer than a set proximity threshold, the clusters are still merged. Finally, the obtained clusters are filtered based on their size so that only

Algorithm 1 Geometric clustering

```
Input: Point cloud $\{P\}$, Neighbor finding function $\Omega(.)$, List of point indices sorted with priority seed points at the beginning $\{P_i\}$
Output: list of identified clusters $\{C\}$
initialize an empty list of clusters $\{C\}$.
initialize a list of processed points $\{P_{processed}\} \leftarrow (\text{Length}(P_i), \textbf{false})$
for each $p_i \in \{P_i\}$ do
    if $\{P_{processed}\{p_i\}\}$ then
        continue
    end if
    Start growing a new cluster from the seed point $p_i$
    Initialize a new empty cluster $\{C_{tmp}\}$
    $\{P_{processed}\{p_i\}\} \leftarrow$ true
    $\{C_{tmp}\} = \{C_{tmp}\} \cup p_i$
    for each $c_i \in \{C_{tmp}\}$ do
        Find nearest neighbor indices of the current seed point $\{P_n\} \leftarrow \Omega(c_i)$
        for each $p_n \in \{P_n\}$ do
            if $\{P_{processed}\{p_i\}\}$ then
                continue
            end if
            check if merge condition is met for the candidate
            if MergeCondition$(p_i, p_n)$ then
                $\{C_{tmp}\} = \{C_{tmp}\} \cup p_n$
                $\{P_{processed}\{p_n\}\} \leftarrow$ true
            end if
        end for
    end for
    Add processed cluster to the list of clusters $\{C\} = \{C\} \cup \{C_{tmp}\}$
end for
```

Algorithm 2 MergeCondition

```
Input: Point cloud $\{P\}$, Point cloud normal vectors $\{N\}$, seed point indice $p_s$, and candidate point indice $p_c$
Output: Boolean indicating if the merge conditions were met.

if $\{N\{p_s\}\} \bullet \{N\{p_c\}\} < \cos(angleThreshold)$ then
    if $\{N\{p_s\}\}.z > normalThreshold$ then
        return $\{P\{p_c\}\}.z < \{P\{p_s\}\}.z$
    else
        return $\{P\{p_c\}\}.z + depthThreshold < \{P\{p_s\}\}.z$
    end if
end if
return false
```

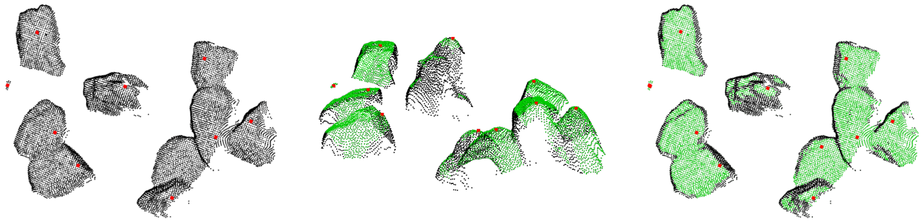

(a) Without normal-based filtering. (b) With normal-based filtering (c) With normal-based filtering

Fig. 4. Identified local maxima with normal-based filtering. Local maxima represented with red dots. Filtered point cloud represented with green color.

clusters containing more points than a size threshold are kept. Results of the postprocessing are depicted in Fig. 5.

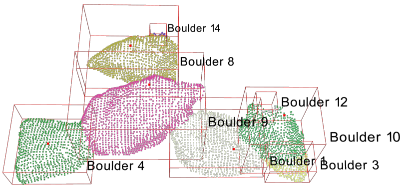

(a) Not post-processed results.

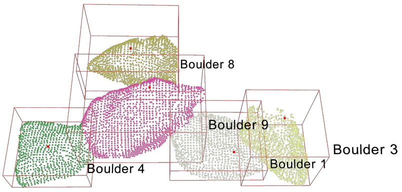

(b) Post-processed segmentated boulders.

Fig. 5. Effect of post-processing on the segmentation results.

IV. FINDING SUITABLE BREAK POSITIONS

The automatic identification and localization of boulders alone is an insufficient solution for the autonomous rock breaking use case. To meet the application requirements, the visual perception system must be able to propose a suitable breaking position for each boulder. In [12], the centroid of each cluster was proposed as the break position, ignoring the surface properties of the boulder. However, the surface properties of the break position have a large impact on the effectiveness of the break attempt. In inclined surfaces, a typical outcome of a break attempt is that either the boulder or the manipulator slips, resulting in an unsuccessful attempt. To address this issue, [13] proposed the use of the normal vectors of the break position as a guide to align the hydraulic hammer to the surface of the boulder. The supportive force from the grizzly however is insufficient to keep the boulders in place if the impact force is not vertical, and moreover, the manipulator is constrained with only 4 degrees of freedom (DOF), leaving only one redundant DOF for aligning of the impact hammer. Thus, the manipulator cannot be aligned properly to inclined surfaces.

To address these challenges, we propose a different approach to determine a suitable break position. Instead of using the centroid of the boulders, suitable break locations are selected based on the surface properties of each boulder. Suitable break positions are obtained by filtering the inclined surfaces from each cluster and then finding the largest uniform cluster. The centroid of this cluster is then selected as the most suitable break position. This approach yields break positions on flat surfaces where the normal vector is pointing roughly upward, thus eliminating the need for changing the orientation of the rock hammer for each attempt. The break position selection is illustrated in Fig. 6, where the filtered surfaces are presented by red points, while the selected break positions are drawn in blue.

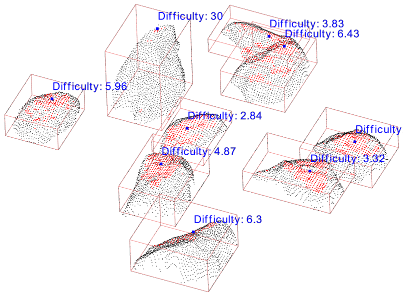

Fig. 6. The break locations are obtained for each cluster by finding the largest uniform cluster of points with normals pointing upward. The filtered points are drawn with red, while the break locations are dawn in blue. Estimated difficulty associated with each break location is shown above each break point.

The proposed method for the break location identification can be leveraged for estimating the difficulty for the break attempt at the same time. By analyzing the size of the cluster defining the break location, we can get a hint about the shape of the boulder. Larger cluster i.e., more points describing it, suggest at larger flat surfaces (requires less accurate positioning of the manipulator), which typically indicates higher probability of a successful break attempt, while less points describing the break location indicate a sharp-edged boulder that is typically more challenging to break. Other criteria that can be used to classify the per rock difficulty are e.g., the height divided by the horizontal cross-section surface area and the horizontal distance of the break location and the centroid of the boulder. These metrics can be used to obtain a simple estimate of the difficulty that can differentiate challenging boulders from the point cloud. Figure 6 has the difficulties estimated for each break location with a numerical dimensionless value. Numerical values below 10 indicate typical difficulty, while values above 10 indicate a challenging boulder, that may need to be manipulated to a different pose before a break attempt.

V. THE EXPERIMENTS

The proposed clustering algorithm was evaluated and benchmarked against four segmentation algorithms implemented in PCL 1.11. The selected comparative methods were Euclidean clustering (EC), conditional Euclidean clustering (CEC), region growing segmentation (ReG) and difference of normals (DoN) based segmentation. The data used for the evaluation was gathered outdoors during winter in a mockup setup. Instead of laying boulders on an actual grizzly, the boulders were kept on the ground for easier manipulation with a municipal tractor. The experimental setup is depicted in Fig. 7. The experimental data was gathered in a $-15°$C ambient temperature with boulders partly covered in snow. Yet, the TOF camera performed remarkably well despite the challenging conditions. A total of 20 unique scenes were recorded for the comparative study between different algorithms. Each scene had between 8 to 10 boulders randomly located in the field of view of the TOF camera. For the most realistic situation, scenes with partly overlapping rocks were preferred as that is a typical situation in the target application.

Fig. 7. Setup for experimental data gathering. The boulders are placed under the aerial work platform that is holding the TOF camera at a height of roughly 5 meters above ground.

TABLE I
RESULTS FROM THE SEGMENTATION EXPERIMENT

	Proposed	ReG	DoN	EC	CEC
Accuracy:	97.4%	85.3%	78.5%	49.7%	86.4%
Parameters:	7	4	5	2	3
Common parameters:			Leaf size [mm^3]:	8000 (20 × 20 × 20)	
			Min cluster size [pts]:	250	
			Bounding volume overlap [%]:	50	
			Merge threshold [mm]:	325	

The evaluation of different methods was done to gain a coarse indication of the fitness of different algorithms for the target application. The experimental data set comprised of 20 unique point clouds, totaling with 191 boulder instances. The different algorithms were evaluated by how many boulders they were able to cluster correctly. Incorrectly clustered boulders, e.g., two or more boulders identified as one, or one boulder identified as two or more, were all considered as failed results. Oversegmentation, i.e., points from another boulder identified as part of the main boulder of an individual cluster, or undersegmentation, i.e., points belonging to a boulder are not identified to the correct cluster, is also not considered in the numerical evaluation. These aspects are discussed only by qualitative terms.

The results from the experiments are gathered into Table I. The pre-processing and the post-processing were conducted using the same parameters with each algorithm. The results indicate great improvement over the classical benchmark methods. Not only does the proposed approach have the highest number of successfully detected boulders, but also, it yields most uniform clustering results with least over- and undersegmentation. Over the dataset, the proposed algorithm failed in only two cases, in which all the other benchmark algorithms failed with the same boulders as well. An example of the algorithm failing is shown in Fig. 8, where only one of the four boulders is correctly detected. Cluster 1 and 9 both shown major oversegmentation. The cluster 9 should be clustered as two boulders, but the point cloud in this case is really hard for all of these algorithms. Comparative figures of the different algorithms are shown for two different scenes in Figs. 9 and 10. The figures are picked from two of a more difficult scenarios, where some of the algorithms were struggling. The other approaches yielded similar results in other scenarios as well. Failed cases almost exclusively were the result of oversegmentation, where multiple boulders were detected as one.

The time spent on tuning parameters for each individual method depends a lot on the number of parameters required. On that aspect, the proposed method is not the most efficient. The proposed method requires 7 parameters: 2 for finding the local maxima, and 5 for the clustering algorithm itself. The search for the seed points requires a radius for local maxima identification (130 mm) and a threshold value for the normal based filtering (0.75). The main algorithm requires *minimum size* of each cluster (10 points), *search radius* for candidate points (45 mm), *maximum angle* between the seed point's

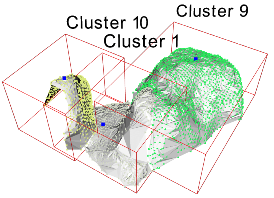

Fig. 8. An example of incorrect clustering. Cluster 10 is correctly identified, but clusters 1 and 9 show major oversegmentation. The cluster 9 comprises of two boulders, while cluster 1 is close to a correct result, but has parts of another boulder incorrectly clustered to the main boulder.

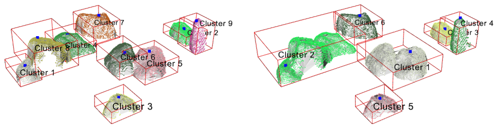

(a) Proposed method. (b) Region growing.

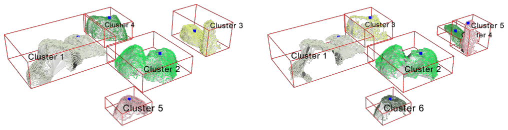

(c) Euclidean clustering. (d) Difference of normals.

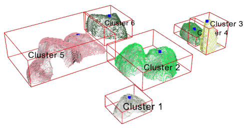

(e) Conditional Euclidean clustering.

Fig. 9. Comparison of segmentation results between different algorithms on a slightly harder scene with overlapping boulders.

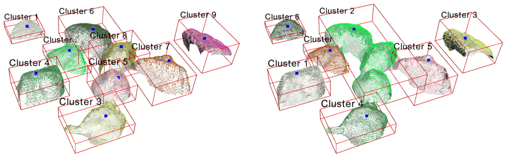

(a) Proposed method. (b) Region growing.

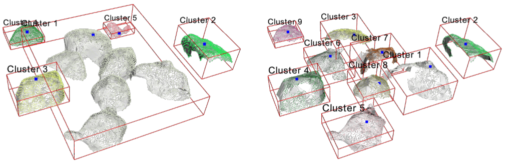

(c) Euclidean clustering. (d) Difference of normals.

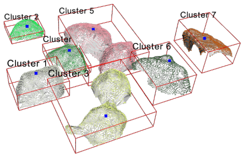

(e) Conditional Euclidean clustering.

Fig. 10. Comparison of segmentation results between different algorithms on a scene with overlapping boulders.

normal and candidate points' normals (40°), and a *threshold value for the z-component of the normal vector* (0.80), beyond which the depth difference between the seed point and the candidate point must be larger than a specified *depth threshold* (20 mm) (see Algorithms 1 and 2). For the *search radius* and the *depth threshold*, the down sampling leaf size was utilized to deduce reasonable values, while the selection of the minimum size of individual clusters can be set to almost any low value, as small clusters will be merged in the post processing phase.

In terms of parametric tuning, the conditional Euclidean clustering yielded relatively high accuracy with only three tunable parameters; minimum cluster size, search radius, and maximum deviation angle between the seed point and the candidate point. With the selected merge condition, the algorithm is very similar to region growing segmentation, and thus, the similar results are also expected. Both of these algorithms fared well with the test data, but occasionally close boulders were clustered as one, as shown in Figs. 9 and 10. Despite the high number of parameters of the proposed algorithm, its tuning process is relatively robust, and many of its parameters can be deduced using prior knowledge of the targer boulders size and the downsampling leafsize. To accommodate the algorithm e.g., for much smaller boulders, only the search radiuses for candidate points and local maxima, and depth thresholds should require tuning, which can be largely deduced from the target boulder size. Depending on density of the original point cloud, minimum cluster size and downsampling leaf size may also require adjusting.

VI. CONCLUSIONS

In this study, we designed and demonstrated a robust clustering algorithm for boulder detection in a robotic rock breaking application. The proposed method takes advantage of the readily available conditional Euclidean clustering method in the PCL using a novel seeding method to deduce suitable seed points, a custom condition for the clustering algorithm, and a post processing strategy to achieve the most uniform and complete results. The study also proposes a novel method for identifying suitable break locations for the hydraulic impact hammer, and a method for estimating difficulty of a break attempt based on geometric features of the target boulder. These features are essential for practical applications in robotic boulder breaking.

The proposed algorithm was evaluated against four common clustering algorithms on a dataset gathered using a commercial Basler Blaze 101 TOF camera under challenging conditions.

The dataset comprised of 20 unique point clouds of scenes with 8 to 11 boulders laying on the ground captured from a height of 5 meters. The proposed algorithm achieved an impressive 97,4% accuracy over the whole dataset with only 5 boulders incorrectly clustered. Yet, none of the boulders were completely missed, but instead, multiple boulders were occasionally clustered as one. Adjacent boulders with a smooth and relatively flat transition between each other are challenging for the proposed clustering method (see Fig. 8). Compared to the deep learning-based approach in [13] the performance is on par, but the proposed method has the added benefit of not having to gather and label a massive dataset for the training purposes.

Future work on this topic lies in implementing a sophisticated tactical layer for the autonomy of the boulder breaking system, that has the capability of performing the actual boulder breaking as well as manipulating difficult boulders into different poses. Successful integration of visual perception, advanced robotic manipulator control and a sophisticated tactical layer is seen as a fundamental requirement for an autonomous secondary breaker system.

REFERENCES

[1] K. Casteel, "Underground haulage equipment trends: Engineering, geology, mineralogy, metallurgy, chemistry, etc," *Engineering and Mining Journal*, vol. 209, pp. 58–60, 04 2008.

[2] J. A. Marshall, A. Bonchis, E. Nebot, and S. Scheding, *Robotics in Mining*, pp. 1549–1576. Springer International Publishing, 2016.

[3] Mining-Technology, "Sizing up syama: the world's first fully automated mine." Available at: https://www.mining-technology.com/features/sizing-syama-worlds-first-fully-automated-mine/ (accessed 23.2.2021), 10 2018.

[4] D. Paredes and D. Fleming-Muñoz, "Automation and robotics in mining: Jobs, income and inequality implications," *The Extractive Industries and Society*, vol. 8, no. 1, pp. 189–193, 2021.

[5] P. I. Corke, J. M. Roberts, and G. J. Winstanley, "Robotics for the mining industry," in *Autonomous Robotic Systems* (A. T. de Almeida and O. Khatib, eds.), (London), pp. 163–181, Springer London, 1998.

[6] H. Takahashi and K. Sano, "Automatic detection and breaking system for boulders by use of ccd camera and laser pointer," *Fragblast*, vol. 2, no. 4, pp. 397–414, 1998.

[7] J. Fox, R. Castano, and R. C. Anderson, "Onboard autonomous rock shape analysis for mars rovers," in *Proceedings, IEEE Aerospace Conference*, vol. 5, pp. 5–2052 vol.5, March 2002.

[8] M. J. Thurley and K. C. Ng, "Identifying, visualizing, and comparing regions in irregularly spaced 3d surface data," *Computer Vision and Image Understanding*, vol. 98, no. 2, pp. 239–270, 2005.

[9] M. J. Thurley and K. C. Ng, "Identification and sizing of the entirely visible rocks from a 3d surface data segmentation of laboratory rock piles," *Computer Vision and Image Understanding*, vol. 111, no. 2, pp. 170–178, 2008.

[10] M. J. Thurley, "Automated image segmentation and analysis of rock piles in an open-pit mine," in *2013 International Conference on Digital Image Computing: Techniques and Applications (DICTA)*, pp. 1–8, 2013.

[11] C. McKinnon and J. A. Marshall, "Automatic identification of large fragments in a pile of broken rock using a time-of-flight camera," *IEEE Transactions on Automation Science and Engineering*, vol. 11, pp. 935–942, July 2014.

[12] L. Niu, M. Aref, and J. Mattila, "Clustering analysis for secondary breaking using a low-cost time-of-flight camera," in *2018 Ninth International Conference on Intelligent Control and Information Processing (ICICIP)*, pp. 318–324, IEEE, 11 2018.

[13] L. Niu, K. Chen, K. Jia, and J. Mattila, "Efficient 3d visual perception for robotic rock breaking," in *2019 IEEE 15th International Conference on Automation Science and Engineering (CASE)*, pp. 1124–1130, IEEE, 2019.

[14] Basler AG, "Basler blaze-101 technical specifications." Available at: https://www.baslerweb.com/en/products/cameras/3d-cameras/basler-blaze/ (accessed 10.02.2021).

[15] S. Lampinen, J. Niemi, and J. Mattila, "Flow-bounded trajectory-scaling algorithm for hydraulic robotic manipulators," in *2020 IEEE/ASME International Conference on Advanced Intelligent Mechatronics (AIM)*, 2020.

[16] G. E. Hinton, T. J. Sejnowski, *et al.*, *Unsupervised learning: foundations of neural computation*. MIT press, 1999.

[17] R. B. Rusu and S. Cousins, "3D is here: Point Cloud Library (PCL)," in *IEEE International Conference on Robotics and Automation (ICRA)*, (Shanghai, China), May 9-13 2011.

[18] A. Nguyen and B. Le, "3d point cloud segmentation: A survey," in *2013 6th IEEE Conference on Robotics, Automation and Mechatronics (RAM)*, pp. 225–230, 2013.

[19] M. A. Fischler and R. C. Bolles, "Random sample consensus: A paradigm for model fitting with applications to image analysis and automated cartography," *Commun. ACM*, vol. 24, p. 381–395, June 1981.

[20] R. B. Rusu, *Semantic 3D Object Maps for Everyday Manipulation in Human Living Environments*. PhD thesis, Computer Science department, Technische Universitaet Muenchen, Germany, October 2009.

[21] Y. Ioannou, B. Taati, R. Harrap, and M. Greenspan, "Difference of normals as a multi-scale operator in unorganized point clouds," in *2012 Second International Conference on 3D Imaging, Modeling, Processing, Visualization Transmission*, pp. 501–508, 2012.

[22] T. Rabbani, F. Van Den Heuvel, and G. Vosselmann, "Segmentation of point clouds using smoothness constraint," *International archives of photogrammetry, remote sensing and spatial information sciences*, vol. 36, no. 5, pp. 248–253, 2006.

[23] S. Holzer, R. B. Rusu, M. Dixon, S. Gedikli, and N. Navab, "Adaptive neighborhood selection for real-time surface normal estimation from organized point cloud data using integral images," in *2012 IEEE/RSJ International Conference on Intelligent Robots and Systems*, pp. 2684–2689, 2012.

[24] J. Goutsias, L. Vincent, and D. S. Bloomberg, *Mathematical morphology and its applications to image and signal processing*, vol. 18. Springer Science & Business Media, 2006.

PUBLICATION

V

Bilateral teleoperation of a hydraulic robotic manipulator in contact with physical and virtual constraints

S. Lampinen, J. Koivumäki and J. Mattila

BATH/ASME 2018 Symposium on Fluid Power and Motion Control. 2018
DOI: `10.1115/FPMC2018-8842`

PUBLICATION

VI

Force-Sensor-Less Bilateral Teleoperation Control of Dissimilar Master-Slave System with Arbitrary Scaling

S. Lampinen, J. Koivumäki, W.-H. Zhu and J. Mattila

IEEE Transactions on Control Systems Technology (2021)
DOI: `10.1109/TCST.2021.3091314`

Force-Sensor-Less Bilateral Teleoperation Control of Dissimilar Master–Slave System With Arbitrary Scaling

Santeri Lampinen, Janne Koivumäki, *Member, IEEE*, Wen-Hong Zhu, *Senior Member, IEEE*,
and Jouni Mattila, *Member, IEEE*

***Abstract*— This study designs a high-precision bilateral teleoperation control for a dissimilar master–slave system. The proposed nonlinear control design takes advantage of a novel subsystem-dynamics-based control method that allows designing of individual (decentralized) model-based controllers for the manipulators locally at the subsystem level. Very importantly, a dynamic model of the human operator is incorporated into the control of the master manipulator. The individual controllers for the dissimilar master and slave manipulators are connected in a specific communication channel for the bilateral teleoperation to function. Stability of the overall control design is rigorously guaranteed with arbitrary time delays. Novel features of this study include the completely force-sensor-less design for the teleoperation system with a solution for a uniquely introduced computational algebraic loop, a method of estimating the exogenous operating force of an operator and the use of a commercial haptic manipulator. Most importantly, we conduct experiments on a dissimilar system in two degrees of freedom (DOFs). As an illustration of the performance of the proposed system, a force scaling factor of up to 800 and position scaling factor of up to 4 was used in the experiments. The experimental results show an exceptional tracking performance, verifying the real-world performance of the proposed concept.**

***Index Terms*— Contact force estimation, motion/force control, nonlinear control, stability, teleoperation, telerobotics.**

NOMENCLATURE

$(\cdot)_\gamma$	Subscript indicating whether the attribute refers to the master ($\gamma = m$) or the slave ($\gamma = s$).
$\Theta_m \in \mathbb{R}^{30\times 2}$	Mapping matrix.
$\dot{\mathbf{q}}_m \in \mathbb{R}^2$	Independent joint velocity coordinates of the master manipulator.
$\mathcal{V}_\gamma \in \mathbb{R}^2$	Velocity of the master/slave manipulator.
$\mathcal{V}_{\gamma r} \in \mathbb{R}^2$	Required counterpart of $\mathcal{V}_\gamma$.
$\mathcal{V}_{\gamma d} \in \mathbb{R}^2$	Desired counterpart of $\mathcal{V}_\gamma$.
$\mathcal{P}_\gamma \in \mathbb{R}^2$	Control point position of the manipulator.
$\mathbf{J}_m \in \mathbb{R}^{2\times 2}$	Jacobian matrix.
$\Phi_m \in \mathbb{R}^{30\times 2}$	Mapping matrix.
$M_m^* \in \mathbb{R}^{30\times 30}$	Equivalent inertial matrix.
$C_m^* \in \mathbb{R}^{30\times 30}$	Skew-symmetric matrix of the centrifugal and Coriolis terms.
$G_m^* \in \mathbb{R}^{30}$	Gravitation vector.
$\boldsymbol{\tau}_m \in \mathbb{R}^2$	Applied torques of the master manipulator.
$\boldsymbol{\tau}_{mm} \in \mathbb{R}^2$	Estimated dynamics of the master manipulator.
$\mathbf{f}_\gamma \in \mathbb{R}^2$	Contact force of the master/slave manipulator.
$\mathbf{A} \in \mathbb{R}^{2\times 2}$	Diagonal positive-definite matrix defining the gain of the force feedback.
$\mathbf{C} \in \mathbb{R}^{2\times 2}$	Diagonal positive-definite matrix defining the time constant of the first-order filter.
$\boldsymbol{\Lambda} \in \mathbb{R}^{2\times 2}$	Diagonal positive-definite matrix defining the gain of the position feedback.
$K_m \in \mathbb{R}^{2\times 2}$	Diagonal positive-definite matrix defining the gain of the internal velocity feedback.
$\kappa_f \in \mathbb{R}$	Force scaling factor.
$\kappa_p \in \mathbb{R}$	Position scaling factor.
$T \in \mathbb{R}$	Length of the one-way time delay.
$\sigma_f \in \{0, 1\}$	Selective factor to detect contact motion.

Tilde (˜) on top of a variable implies that the variable is filtered with a first-order filter, unless explicitly specified otherwise. Hat (ˆ) on top of a variable implies that the variable is an estimate of itself, while wide hat ($\widehat{\ }$) is used to denote adapted parameters.

I. INTRODUCTION

BILATERALLY teleoperated robotic systems can bring the perception and precision of direct manipulation into challenging and risk-intensive tasks in environments that may be hazardous or hostile for humans. In contrast to unilateral teleoperation where the command flow goes only from the master to the slave, bilateral teleoperation provides the operator with information about the slave manipulator in the form of force feedback, to assist in the coordination and decision-making processes. To broaden the application scope of teleoperation,

---

Manuscript received December 2, 2020; revised March 23, 2021; accepted June 4, 2021. Manuscript received in final form June 18, 2021. This work was supported by the Finnish Foundation for Technology Promotion. Recommended by Associate Editor W. He. *(Corresponding author: Santeri Lampinen.)*

This work did not involve human subjects or animals in its research.

Santeri Lampinen, Janne Koivumäki, and Jouni Mattila are with the Faculty of Engineering and Natural Sciences, Tampere University, 33720 Tampere, Finland (e-mail: santeri.lampinen@tuni.fi; janne.koivumäki@tuni.fi; jouni.mattila@tuni.fi).

Wen-Hong Zhu is with the Canadian Space Agency, Longueuil (Saint-Hubert), QC J3Y 8Y9, Canada (e-mail: wenhong.zhu@canada.ca).

Color versions of one or more figures in this article are available at https://doi.org/10.1109/TCST.2021.3091314.

Digital Object Identifier 10.1109/TCST.2021.3091314

arbitrary motion and forces scaling has been pursued by many researchers, but no rigorously stability guaranteed method has been shown to work in a multidegrees of freedom (DOF) system.

Currently, one of the most interesting applications for teleoperation lies in learning from demonstrations (LfD) applications with heavy-duty manipulators. LfD is an established technique in robotics, where a robot is taught to perform tasks by demonstrations from a human teacher. The robot can then repeat these tasks in even slightly varying conditions [1]. The *key enabler* for LfD applications with heavy-duty manipulators is teleoperation of asymmetric systems with *motion* and *force scaling*. Conventional kinesthetic teaching methods, established methods for providing teaching samples, cannot be applied to such manipulators due to the size and force limitations (workspace over 2 m and payload over 500 kg) [2]. Instead, teaching samples can be captured using teleoperation with motion and force scaling between the manipulators. Teleoperation has the advantage of an intuitive and efficient communication and operation strategy between humans and robots. Teleoperated demonstrations have been successfully used for LfD applications with promising results using 1:800 force scaling in [2], and using 1:1 scaling in [3] and [4].

In applications where heavy objects are handled or a great amount of force is required, hydraulic actuation has remained the most attractive solution due to its great power-to-weight ratio. Furthermore, hydraulic actuators have the benefits of simplicity, robustness, and low cost. However, control of such actuators is significantly challenged by their complex nonlinear dynamic behavior. When the actuators are used in articulated systems, the control design is further complicated by the associated nonlinear multibody dynamics, and the overall dynamics can be described by coupled nonlinear third-order differential equations. Consequently, the constrained motion control of multiple degrees-of-freedom (n-DOF) hydraulic robotic manipulators has been a well-recognized challenge [5]. As an additional challenge to the above, direct contact force measurements are usually used in contact control. In conventional applications, a 6-DOF force/torque sensor is often attached to the tip of the manipulator for this purpose. However, these force/torque sensors are expensive and prone to overloading and shocks, a situation frequently occurring with hydraulic heavy-duty manipulators [6]. Therefore, methods avoiding direct contact force measurements have become desirable.

Needless to say, teleoperation of hydraulic manipulators has been an extremely difficult problem due to unresolved challenges in their high-precision control [7]–[10]. However, due to recent state-of-the-art improvements and advances in high-precision control of hydraulic manipulators (see [5], [6], [11], [12]), their advanced teleoperation is suddenly becoming a feasible and interesting field of study again. Moreover, *time delay* (a focused research topic, especially in the teleoperation of extraterrestrial systems [13]) can be alternatively addressed for terrestrial applications in the advent of 5G cellular networks with ultralow latencies [14]. Such terrestrial applications are within the authors' main scope.

In contrast to a dissimilar master–slave configuration in Fig. 1, the current state of the art in teleoperation control has been mainly focusing on electrical manipulators in symmetrical 1:1 scale configurations, including multimaster or multislave setups, shared control, or dealing with time delays [15]–[20]. The existing methods for teleoperation of hydraulic manipulators have mainly relied on linear control theory and system linearization [8]–[10], [21]. However, these methods have limitations in teleoperation of complex, highly nonlinear, and asymmetric systems. In contrast, the adaptive teleoperation scheme proposed by Zhu and Salcudean in [22] was reported to be capable of addressing nonlinear dynamics of asymmetric master and slave manipulators with arbitrary motion and force scaling. However, experiments with only a 1-DOF symmetrical system were presented. Moreover, both manipulators were equipped with force sensors. Very recently, asymmetric teleoperation with motion scaling was discussed in [20], where a shared autonomy control strategy was proposed for handling redundant DOFs of the slave manipulator. Transparency was not considered in this study. Another recent approach for teleoperation of symmetric systems with varying time-delay was proposed in [19], where independent controllers were designed for both manipulators. The study demonstrated good transparency performance in constrained motion despite varying time delay, but lacked the ability to maintain transparency during transitions from free space motion to contact control.

A. Aim and Contribution

In this work, we target an asymmetric bilateral teleoperation system comprised of a commercial haptic master manipulator and a hydraulic slave manipulator. The system has notable asymmetry between the manipulators due to substantial differences between the dynamics of the master and slave manipulators. Due to this asymmetry, handling motion and force scaling in the teleoperation architecture becomes necessary. The studied system is shown in a high level in Fig. 1. The control design takes advantage of a novel subsystem-dynamics-based control method (see Section I-B) that enables individual model-based control designs for the manipulators locally at the subsystem level. Very importantly, a dynamic model of the human operator is incorporated into the control of the master manipulator. The individual controllers for the dissimilar master and slave manipulators are connected in a specific communication channel for the bilateral teleoperation to function.

In this study, the results of [22] and [23] are used as the foundation for designing a theoretically sound high-precision bilateral teleoperation control for significantly asymmetric systems. In [23], preliminary attempts for full-dynamics-based bilateral teleoperation for an asymmetric hydraulic/electric system were demonstrated, while in [24], artificial constraints in the task space were implemented. However, in-depth stability analysis and theoretical discussions were not included in [23] nor in [24].

To improve the preliminary theory and control performance reported in [23], the following *distinguishable contributions* are demonstrated in this study:

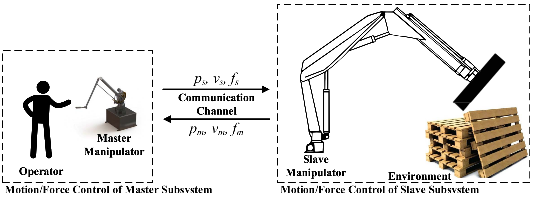

Fig. 1. High-level illustration of the studied dissimilar teleoperation system. A commercial haptic manipulator is used as the master manipulator, while a hydraulic loader crane complemented with a 500-kg dummy load at the TCP is used as the slave manipulator.

1) We propose a master manipulator contact force estimation by using joint control torques and estimated manipulator dynamics. A solution to a computational algebraic loop formed around the actuation and force estimation is proposed.
2) We propose a novel method for estimating the exogenous force of the human operator.
3) Stability of the overall control design is rigorously guaranteed with transparency and robustness against an arbitrary time delay.

With the control theoretical developments described above, the experiments demonstrate significant improvements in relation to our preliminary study [23]. The experiments with a 2-DOF system with a force scaling ratio of up to 800 and a position scaling ratio of up to 4, in lieu of the 1-DOF experiments in [22], serve *a critical step toward practical 6-DOF applications*.

B. Concept of the Virtual Decomposition Control

In modern control systems engineering, *modularity* is considered as a key aspect to address the ever-growing complexity of target applications [25]. To design the intended high-precision teleoperation for complex asymmetric system, the study takes advantage of a novel virtual decomposition control (VDC) approach (see [26], [27]). The method is developed especially for controlling complex robotic systems, with a number of significant state-of-the-art control performance improvements with robotic systems (see [5], [6], [11], [12], [22], [23], [28]). As a key feature, VDC enables to *virtually* break down complexity of the original system to a set of manageable *modular subsystems* [26], [28] such that the control design and stability analysis can be performed *locally at the subsystem level* without imposing additional approximations. This allows, for example, that *changing the control (or dynamics) of a subsystem does not affect the control equations of the rest of the system* [26].

The subsystem-dynamics-based control design philosophy in VDC originates from two unique concepts, namely *virtual stability* and *virtual power flows* (VPFs) (see Appendix B). The VPFs uniquely define the dynamic interactions among the subsystems such that the *virtual stability* of every subsystem ensures that a positive VPF is connected to its corresponding negative VPF in the adjacent subsystem (and vice versa). Thus, when every subsystem qualify as *virtually stable*, all the VPFs cancel each other out, eventually, leading to the stability of the entire system in the sense of Lebesgue integrable functions (see Appendix A). For more detailed information and additional benefits of VDCs, see [5] and [26].

C. Organization of the Article

The rest of this article is organized as follows: Section II presents the mathematical preliminaries. Section III discusses control of the master manipulator, while Section IV discusses control of the slave manipulator. Section V presents the teleoperation scheme and discusses properties of the teleoperation method. Section VI presents the experimental system and results. Finally, conclusions are drawn in Section VII.

II. MATHEMATICAL PRELIMINARIES

Let an orthogonal coordinate system (i.e., a frame) $\{\mathbf{A}\}$ be attached to a rigid body. Then, the linear/angular velocity vector ${}^{\mathbf{A}}V \in \mathbb{R}^6$ and the force/moment vector ${}^{\mathbf{A}}F \in \mathbb{R}^6$ of the rigid body, expressed in frame $\{\mathbf{A}\}$, can be expressed as [26]

$${}^{\mathbf{A}}V = [{}^{\mathbf{A}}\mathbf{v}\ \ {}^{\mathbf{A}}\boldsymbol{\omega}]^T, \quad {}^{\mathbf{A}}F = [{}^{\mathbf{A}}\mathbf{f}\ \ {}^{\mathbf{A}}\mathbf{m}]^T$$

where ${}^{\mathbf{A}}\mathbf{v} \in \mathbb{R}^3$ and ${}^{\mathbf{A}}\boldsymbol{\omega} \in \mathbb{R}^3$ are the linear and angular velocity vectors of frame $\{\mathbf{A}\}$, expressed in frame $\{\mathbf{A}\}$, and ${}^{\mathbf{A}}\mathbf{f} \in \mathbb{R}^3$ and ${}^{\mathbf{A}}\mathbf{m} \in \mathbb{R}^3$ are the force and moment vectors that are being measured and expressed in frame $\{\mathbf{A}\}$, respectively.

Transformation of linear/angular and force/moment vectors between two frames, attached to a common rigid body, namely $\{\mathbf{A}\}$ and $\{\mathbf{B}\}$, can be expressed as [26]

$${}^{\mathbf{B}}V = {}^{\mathbf{A}}\mathbf{U}_{\mathbf{B}}^{T}\,{}^{\mathbf{A}}V \tag{1}$$

$${}^{\mathbf{A}}F = {}^{\mathbf{A}}\mathbf{U}_{\mathbf{B}}\,{}^{\mathbf{B}}F \tag{2}$$

where ${}^{\mathbf{A}}\mathbf{U}_{\mathbf{B}} \in \mathbb{R}^{6\times 6}$ is a force/moment transformation matrix that also transform velocities between frames $\{\mathbf{A}\}$ and $\{\mathbf{B}\}$.

The dynamics of a freely moving rigid body, expressed in the fixed rigid body frame $\{\mathbf{A}\}$, can be defined as

$$\mathbf{M}_{\mathbf{A}}\frac{d}{dt}({}^{\mathbf{A}}\mathbf{V}) + \mathbf{C}_{\mathbf{A}}({}^{\mathbf{A}}\omega){}^{\mathbf{A}}\mathbf{V} + \mathbf{G}_{\mathbf{A}} = {}^{\mathbf{A}}F^{*} \tag{3}$$

where $\mathbf{M}_{\mathbf{A}} \in \mathbb{R}^{6\times 6}$ is the mass matrix, $\mathbf{C}_{\mathbf{A}} \in \mathbb{R}^{6\times 6}$ the Coriolis and centrifugal terms, and $\mathbf{G}_{\mathbf{A}} \in \mathbb{R}^{\mathbf{6}}$ the gravity vector of the rigid body. For a detailed formulation of $\mathbf{M}_{\mathbf{A}}$, $\mathbf{C}_{\mathbf{A}}$, and $\mathbf{G}_{\mathbf{A}}$, readers are referred to [26].

III. MASTER MANIPULATOR

Phantom premium 3.0/6DOF, a commercial haptic manipulator without any modifications to the hardware, has been chosen to act as the master manipulator in this study. It possesses 6-DOF manipulability and force feedback along each individual DOF, with a workspace mimicking human arm motion pivoting from the shoulder. For this study, we developed a new control system for the manipulator to rigorously address the dynamics of the lightweight manipulator. As a challenge to the control design, the manipulator lacks force/torque sensors. Therefore, human operator contact force estimation is required. Without loss of generality, we consider manipulation and force perception only within a specific 2-DOF plane (by

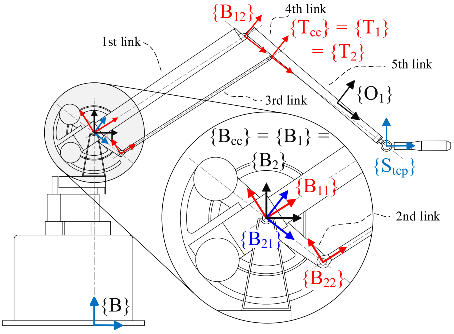

Fig. 2. Frame assignment of the haptic manipulator.

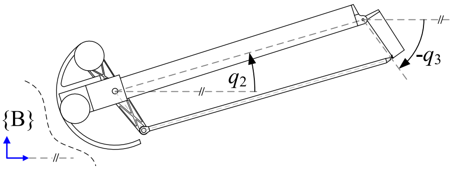

Fig. 3. Illustration of the joint angles of the master manipulator.

using joint 2 and joint 3), while the rest of the DOFs are locked with software. The benefit of using a commercial haptic device as the master manipulator is the ease of implementation for wide range of applications.

Frame $\{\mathbf{S_{tcp}}\}$ is assigned to the tool center point (TCP) of the master manipulator (see Fig. 2), and the external forces resulting from the dynamics of the human operator as well as the exogenous operating hand force are estimated and expressed in this frame. Orientation of frame $\{\mathbf{S_{tcp}}\}$ is aligned with the handle of the master manipulator and the handle is held horizontally as shown in Fig. 2 by position control at the spherical wrist.

A. Kinematics

Relevant coordinate frames in terms of control of the master manipulator are shown in Fig. 2. Notably, frame $\{\mathbf{B}_{11}\}$ is attached to the first link of the manipulator, $\{\mathbf{B}_{21}\}$ to the second link, $\{\mathbf{B}_{22}\}$ to the third link, $\{\mathbf{B}_{12}\}$ to the fourth link, and $\{\mathbf{O}_1\}$ to the fifth link. Numbering of the manipulator links is defined in Fig. 2.

Remark 1: Links 4 and 5 are virtually cut from the same rigid body, using design principles of the VDC approach, which allows separate computations later.

The independent joint velocity coordinates are denoted as

$$\dot{\mathbf{q}}_m = [\dot{q}_2 \quad \dot{q}_3]^T \in \mathbb{R}^2. \tag{4}$$

The respective joint angles q_2 and q_3 are shown in Fig. 3. Then, velocities of all links of the master manipulator can be determined using the geometrical transformation matrices between each frame with the independent joint velocity coordinates as

$$\mathbf{V}_m = \Theta_m \dot{\mathbf{q}}_m \tag{5}$$

where $\mathbf{V}_m = \left[{}^{\mathbf{B}_{11}}V^T \;\; {}^{\mathbf{B}_{12}}V^T \;\; {}^{\mathbf{B}_{21}}V^T \;\; {}^{\mathbf{B}_{22}}V^T \;\; {}^{\mathbf{O}_1}V^T\right]^T \in \mathbb{R}^{30}$, and $\Theta_m \in \mathbb{R}^{30\times 2}$ is a mapping matrix defined as

$$\Theta_m = \begin{bmatrix} \mathbf{z} & \mathbf{0}_{6\times 1} \\ {}^{\mathbf{B}_{11}}\mathbf{U}_{\mathbf{B}_{12}}^T\mathbf{z} - \mathbf{z} & \mathbf{z} \\ \mathbf{0}_{6\times 1} & \mathbf{z} \\ \mathbf{z} & {}^{\mathbf{B}_{21}}\mathbf{U}_{\mathbf{B}_{22}}^T\mathbf{z} - \mathbf{z} \\ {}^{\mathbf{B}_{12}}\mathbf{U}_{\mathbf{O}_1}^T\left({}^{\mathbf{B}_{11}}\mathbf{U}_{\mathbf{B}_{12}}^T\mathbf{z} - \mathbf{z}\right) & {}^{\mathbf{B}_{12}}\mathbf{U}_{\mathbf{O}_1}^T\mathbf{z} \end{bmatrix} \tag{6}$$

where $\mathbf{z} = [0\ 0\ 0\ 0\ 0\ 1]^T \in \mathbb{R}^6$.

Let the independent velocity coordinates at master manipulator's handle be $\mathcal{V}_m \in \mathbb{R}^2$ subject to

$$\mathcal{V}_m = \mathbf{J}_m \dot{\mathbf{q}}_m \tag{7}$$

$$\mathbf{J}_m = [\boldsymbol{I}_{2\times 2} \quad \mathbf{0}_{2\times 4}]\,{}^{\mathbf{O}_1}\mathbf{U}_{\mathbf{S_{tcp}}}^T[\mathbf{0}_{6\times 24} \quad \boldsymbol{I}_{6\times 6}]\Theta_m \tag{8}$$

where $\mathbf{J}_m \in \mathbb{R}^{2\times 2}$ is the invertible Jacobian matrix of the master manipulator.

Then, another mapping matrix can be defined as

$$\Phi_m = \Theta_m \mathbf{J}_m^{-1}. \tag{9}$$

B. Dynamics

Dynamics of each rigid body of the master manipulator can be determined using (3) and (5). According to [29], and under Assumption 1, the dynamic model of the master manipulator can be expressed as

$$\Phi_m^T \mathcal{M}_m^* \frac{d}{dt}(\Phi_m \mathcal{V}_m) + \left(\Phi_m^T \mathcal{C}_m^* \Phi_m\right)\mathcal{V}_m + \Phi_m^T \mathcal{G}_m^* = \mathbf{J}_m^{-T}\boldsymbol{\tau}_m - \mathbf{f}_m \tag{10}$$

where $\mathbf{f}_m$ is the net reaction force from the master manipulator toward the human operator and will be defined later in more detail, $\boldsymbol{\tau}_m \in \mathbb{R}^2$ denotes the applied torques of the manipulator, and

$$\mathcal{M}_m^* = \mathrm{diag}\{\mathbf{M}_{\mathbf{B}_{11}},\ \mathbf{M}_{\mathbf{B}_{12}},\ \mathbf{M}_{\mathbf{B}_{21}},\ \mathbf{M}_{\mathbf{B}_{22}},\ \mathbf{M}_{\mathbf{O}_1}\} \tag{11}$$

$$\mathcal{C}_m^* = \mathrm{diag}\{\mathbf{C}_{\mathbf{B}_{11}},\ \mathbf{C}_{\mathbf{B}_{12}},\ \mathbf{C}_{\mathbf{B}_{21}},\ \mathbf{C}_{\mathbf{B}_{22}},\ \mathbf{C}_{\mathbf{O}_1}\} \tag{12}$$

$$\mathcal{G}_m^* = \left[\mathbf{G}_{\mathbf{B}_{11}}^T,\ \mathbf{G}_{\mathbf{B}_{12}}^T,\ \mathbf{G}_{\mathbf{B}_{21}}^T,\ \mathbf{G}_{\mathbf{B}_{22}}^T,\ \mathbf{G}_{\mathbf{O}_1}^T\right]^T. \tag{13}$$

Assumption 1: Bearing friction of all the revolute joints of the master manipulator is zero.

C. Human Operator

Based on literature [22], [30], and [31], sufficient accuracy for modeling the human operator can be achieved using a simple second-order linear time-invariant model. The following model is used here:

$$\mathbf{M}_h \ddot{\mathbf{x}}_h + \mathbf{D}_h \dot{\mathbf{x}}_h + \mathbf{K}_h \mathbf{x}_h = \mathbf{f}_m - \mathbf{f}_h^* \tag{14}$$

where $\mathbf{M}_h \in \mathbb{R}^{2\times 2}$, $\mathbf{D}_h \in \mathbb{R}^{2\times 2}$, and $\mathbf{K}_h \in \mathbb{R}^{2\times 2}$ are symmetric positive-definite matrices approximating the inertia, damping, and stiffness of the arm of the human operator, respectively, while $\mathbf{f}_m \in \mathbb{R}^2$, appeared first in (10), denotes the net force vector, exerted by the master manipulator toward the operator, and $\mathbf{f}_h^* \in \mathbb{R}^2$ denotes the exogenous force vector actively generated by the operator. The position of the arm of the operator is denoted by $\mathbf{x}_h \in \mathbb{R}^2$, while $\dot{\mathbf{x}}_h \in \mathbb{R}^2$ and $\ddot{\mathbf{x}}_h \in \mathbb{R}^2$

denote the first and second time-derivatives of the position vector, respectively, subject to $\dot{\mathbf{x}}_h = \mathcal{V}_m$.

In [16] and [32], it was suggested that the exogenous force of the operator could be estimated using a fast parameter adaptation function. This differs from the approach in [22], where a switching term with a constant force, instead of an estimate, was used to ensure stability. The precise expression of the exogenous force, denoted $\mathbf{f}_h^* \in \mathbb{R}^2$ in (14), would necessarily involve research on complex human motor neuron actions. In this article, we describe this exogenous force as a general linear-in-parameter form as

$$\mathbf{f}_h^* = \Psi(t)\mathbf{p} \tag{15}$$

where $\Psi(t)$ is a time-variant matrix and $\mathbf{p}$ is a parameter vector. We treat vector $\mathbf{p}$ as a constant by moving all time-variant properties into $\Psi(t)$.

Remark 2: Note that expression (15) is quite general. It covers the expressions used in [16] and [17], in which $\Psi(t) = 1$ are used. Most importantly, this expression takes the same form commonly used in neural networks, allowing flexible incorporation of basis radial functions into machine learning mechanisms. With more elegant design of $\Psi(t)$, for example, muscle activation measured by electromyography (EMG) could be used for the intent force modeling. A recent comprehensive attempt at human arm dynamics modeling has been proposed in [33]. By modeling the motion dynamics of the arm and using time-variant muscle activation measured by EMG as the time-variant part, the human arm can be modeled similar to any multibody series manipulator. The multibody dynamics of the human arm together with its numerous muscle groups, tendons, and other ligaments can be modeled in pursuit of higher precision for more critical applications, for example, teleoperated surgery.

D. Control of the Master Manipulator With a Human Operator

For accurate control of the master manipulator, dynamics of both the manipulator itself and the human operator need to be addressed together. The required control law must, therefore, define required contact force toward the human operator.

The estimated human operator exogenous force is written as

$$\hat{\mathbf{f}}_h^* = \Psi(t)\widehat{\mathbf{p}} \tag{16}$$

where $\widehat{\mathbf{p}}$ is an estimate of the parameter vector. The time-invariant parameters are estimated using the following parameter adaptation law as

$$\begin{aligned} \dot{\widehat{p_i}} &= \rho_i\, \kappa\, \Psi_i(t)(\mathcal{V}_{mr} - \mathcal{V}_m) \\ \kappa &= \begin{cases} 0, & \hat{p}_i \le \hat{p}_i^- \text{ and s} \le 0 \\ 0, & \hat{p}_i \ge \hat{p}_i^+ \text{ and s} \ge 0 \\ 1, & \text{otherwise} \end{cases} \end{aligned} \tag{17}$$

where $\widehat{p_i}$, $\widehat{p_i^+}$, and $\widehat{p_i^-}$ are the estimate of the ith element of the real time-invariant parameter vector $\mathbf{p} = [p_1,\ p_2, \ldots,\ p_i, \ldots]^T$ as well as its upper and lower bounds, respectively, ρ_i is the adaptation gain of the ith element of $\widehat{\mathbf{p}} = [\widehat{p}_1,\ \widehat{p}_2,\ \ldots,\ \widehat{p}_i,\ \ldots]^T$, $\Psi_i(t)$ denotes the ith column of the time-variant matrix $\Psi(t)$, and $\mathcal{V}_{mr} \in \mathbb{R}^2$ denotes the required velocity at the tip of the master manipulator, expressed in frame $\{\mathbf{S_{tcp}}\}$. The designed bounds of $\widehat{p}$ define the maximum operator forces and it is defined to match the application requirements.

In Section III-B, dynamics were calculated using the measured independent joint velocity vector $\dot{\mathbf{q}}_m$. However, since the proposed control method is velocity-based, we need to define the required velocities in Cartesian space. Let $\mathcal{V}_{md} \in \mathbb{R}^2$ be the desired velocity of the tip of the master manipulator, to be defined later in Section V. Then, the required velocity vector, $\mathcal{V}_{mr} \in \mathbb{R}^2$, is designed as

$$\mathcal{V}_{mr} = \mathcal{V}_{md} - \mathbf{A}\tilde{\hat{\mathbf{f}}}_m \tag{18}$$

where $\mathbf{A} \in \mathbb{R}^{2\times2}$ is a diagonal positive-definite gain matrix, and $\tilde{\hat{\mathbf{f}}}_m$ denotes a filtered estimate of the net reaction force of the master manipulator obtained using

$$\dot{\tilde{\hat{\mathbf{f}}}}_m + \mathbf{C}\tilde{\hat{\mathbf{f}}}_m = \mathbf{C}\hat{\mathbf{f}}_m \tag{19}$$

where $\mathbf{C} \in \mathbb{R}^{2\times2}$ is a diagonal positive-definite matrix, and $\hat{\mathbf{f}}_m \in \mathbb{R}^2$ is an estimate of $\mathbf{f}_m$. The specific form of $\hat{\mathbf{f}}_m$ is discussed in detail in Section III-E.

Compute

$$\dot{\mathbf{q}}_{mr} = \mathbf{J}_m^{-1}\mathcal{V}_{mr} \tag{20}$$

$$\mathbf{V}_{mr} = \Theta_m\dot{\mathbf{q}}_{mr} \tag{21}$$

where $\dot{\mathbf{q}}_{mr} \in \mathbb{R}^2$ denotes the required counterpart of $\dot{\mathbf{q}}_m$, and $\mathbf{V}_{mr} \in \mathbb{R}^{30}$ denotes the required counterpart of $\mathbf{V}_m$.

Remark 3: The second term on the right-hand side of (18) acts as a local force feedback term within the control design.

The linear parametrization of the required rigid body dynamics can be written according to [26] as

$$\mathbf{Y_A}\theta_\mathbf{A} \equiv \mathbf{M_A}\frac{d}{dt}({}^{\mathbf{A}}V_{\mathrm{r}}) + \mathbf{C_A}({}^{\mathbf{A}}\omega){}^{\mathbf{A}}V_{\mathrm{r}} + \mathbf{G_A}. \tag{22}$$

Interested reader is referred to the formulation of the regressor matrix $\mathbf{Y_A} \in \mathbb{R}^{6\times13}$ and the parameter vector $\boldsymbol{\theta}_\mathbf{A} \in \mathbb{R}^{13}$ in [26]. Using $\mathbf{A} \in \{\mathbf{B_{11}}, \mathbf{B_{12}}, \mathbf{B_{21}}, \mathbf{B_{22}}, \mathbf{O_1}\}$, dynamics of each rigid body can be calculated with (22) as

$$\begin{aligned} \mathbf{Y}_m\boldsymbol{\theta}_m = [&(\mathbf{Y_{B_{11}}}\theta_\mathbf{B_{11}})^T,\ (\mathbf{Y_{B_{12}}}\theta_\mathbf{B_{12}})^T,\ (\mathbf{Y_{B_{21}}}\theta_\mathbf{B_{21}})^T, \\ &(\mathbf{Y_{B_{22}}}\theta_\mathbf{B_{22}})^T,\ (\mathbf{Y_{O_1}}\theta_\mathbf{O_1})^T]^T \in \mathbb{R}^{30} \end{aligned} \tag{23}$$

Furthermore, dynamics of the human operator are calculated with a similar linear parametrization form as

$$\mathbf{Y}_h\boldsymbol{\theta}_h = \mathbf{M}_h\dot{\mathcal{V}}_{mr} + \mathbf{D}_h\dot{\mathbf{x}}_h + \mathbf{K}_h\mathbf{x}_h. \tag{24}$$

Then, control equations for the master manipulator can be defined as

$$\mathbf{J}_m^{-T}\boldsymbol{\tau}_m = \Phi_m^T\mathbf{Y}_m\boldsymbol{\theta}_m + \mathbf{Y}_h\boldsymbol{\theta}_h + \hat{\mathbf{f}}_h^* + K_m(\mathcal{V}_{mr} - \mathcal{V}_m) \tag{25}$$

where $K_m \in \mathbb{R}^{2\times2}$ is a positive-definite gain matrix. The last term in (25) is a velocity feedback term used to ensure the control stability.

E. Force Estimation

The net reaction force from the master manipulator toward the operator can be estimated using the known dynamics of the master manipulator as a base. This method is similar to the inverse dynamics-based estimation methods, described in [34]. The main difference here is that the estimated actuator torque and applied torque are calculated based on the inverse dynamics, yielding that the external force can be estimated in addition to the mere collision detection, possible with the simpler method. The force estimate can be expressed as

$$\hat{\mathbf{f}}_m = \mathbf{J}_m^{-T}(\boldsymbol{\tau}_m - \boldsymbol{\tau}_{mm}) \tag{26}$$

where $\boldsymbol{\tau}_m$ is the master robot control input defined in (25), and $\boldsymbol{\tau}_{mm}$ is the estimated master robot dynamics, defined as

$$\begin{aligned}\boldsymbol{\tau}_{mm} = \big(\Theta_m^T \mathcal{M}_m^* \Theta_m\big)\hat{\ddot{\mathbf{q}}}_m + \big(\Theta_m^T \mathcal{C}_m^* \Theta_m + \Theta_m^T \mathcal{M}_m^* \dot{\Theta}_m\big)\hat{\dot{\mathbf{q}}}_m \\ + \Theta_m^T \mathcal{G}_m^* \end{aligned}\tag{27}$$

where $\hat{\ddot{\mathbf{q}}}_m$ and $\hat{\dot{\mathbf{q}}}_m$ are estimates of $\ddot{\mathbf{q}}_m$ and $\dot{\mathbf{q}}_m$, respectively, obtained by differentiation from the measured joint angles $\mathbf{q}_m$.

F. Algebraic Loop and Computation Algorithms

The force estimate in the control law in (25) results in an algebraic loop that has to be addressed to ensure stability of the control system. This section defines required conditions to ensure stability of the algebraic loop.

Differentiating (18) and expressing $\dot{\mathcal{V}}_{mr}$ as an affine function of $\dot{\tilde{\mathbf{f}}}_m$ yields

$$\dot{\mathcal{V}}_{mr} = \mathbf{A}_1(t)\dot{\tilde{\hat{\mathbf{f}}}}_m + \mathbf{B}_1(t) \tag{28}$$

where $\mathbf{A}_1(t) \in \mathbb{R}^{2\times 2}$ is a known matrix and $\mathbf{B}_1(t) = \dot{\mathcal{V}}_{md} \in \mathbb{R}^2$ is a known vector (which will be given in Section V), and $\dot{\tilde{\mathbf{f}}}_m \in \mathbb{R}^2$ is a vector to be specified later in this section.

Using (20) and (21), it follows from (22)–(26) that

$$\hat{\mathbf{f}}_m = \mathbf{J}_m^{-T}(\boldsymbol{\tau}_m - \boldsymbol{\tau}_{mm}) = \mathbf{A}_2(t)\mathbf{A}\dot{\tilde{\hat{\mathbf{f}}}}_m + \mathbf{B}_2(t) \tag{29}$$

where $\mathbf{A}_2(t) \in \mathbb{R}^{2\times 2}$ is a known matrix and $\mathbf{B}_2(t) \in \mathbb{R}^2$ is a known vector. Then, it follows from (19) that

$$\dot{\tilde{\hat{\mathbf{f}}}}_m = (\mathbf{C}\mathbf{A}_2(t)\mathbf{A})\dot{\tilde{\hat{\mathbf{f}}}}_m + \mathbf{B}_3(t) \tag{30}$$

where $\mathbf{B}_3(t) \in \mathbb{R}^2$ is a known vector. The existence of a computational algebraic loop can be clearly seen in (30).

To ensure numerical stability, we must have

$$\underset{\max}{\sigma}(\mathbf{C}\mathbf{A}_2(t)\mathbf{A}) < 1. \tag{31}$$

This means that both $\mathbf{C}$ and $\mathbf{A}$ must be restricted.

Finally, $\dot{\tilde{\hat{\mathbf{f}}}}_m$ can be computed from (30) as

$$\dot{\tilde{\hat{\mathbf{f}}}}_m = [\mathbf{I}_{2\times 2} - (\mathbf{C}\mathbf{A}_2(t)\mathbf{A})]^{-1}\mathbf{B}_3(t). \tag{32}$$

Once $\dot{\tilde{\hat{\mathbf{f}}}}_m$ is obtained, $\tilde{\hat{\mathbf{f}}}_m$ in (18) can be computed using integration with $\dot{\tilde{\hat{\mathbf{f}}}}_m(0) = 0$.

G. Stability

Substituting (25) and (14) into (10) yields

$$\begin{aligned}\Phi_m^T \mathcal{M}_m^* \frac{d}{dt}(\Phi_m(\mathcal{V}_m - \mathcal{V}_{mr})) + M_h(\dot{\mathcal{V}}_m - \dot{\mathcal{V}}_{mr}) \\ = \big(\Phi_m^T \mathcal{C}_m^* + K_m\big)(\mathcal{V}_{mr} - \mathcal{V}_m) + \Psi(t)(\hat{\mathbf{p}} - \mathbf{p}). \end{aligned}\tag{33}$$

Next, the non-negative function for the master manipulator is chosen as

$$\begin{aligned}\nu_m = \frac{1}{2}(\mathcal{V}_{mr} - \mathcal{V}_m)^T \big(\Phi_m^T \mathcal{M}_m^* \Phi_m + M_h\big)(\mathcal{V}_{mr} - \mathcal{V}_m) \\ + \frac{1}{2}\sum_i \frac{p_i - \hat{p}_i}{\rho_i}. \end{aligned}\tag{34}$$

The time-derivative of the non-negative function in (34) is obtained using (33), (17), and the skew-symmetric properties of $\mathcal{C}_m^*$ as

$$\dot{\nu}_m \leq -(\mathcal{V}_{mr} - \mathcal{V}_m)^T K_m (\mathcal{V}_{mr} - \mathcal{V}_m). \tag{35}$$

Theorem 1: Analyzing the master manipulator (10) with the human operator (14) subject to control (25) with estimated exogenous operator force using adaptation law (17), it yields

$$\xi_m \equiv \mathcal{V}_{md} - \mathcal{V}_m - \mathbf{A}\tilde{\hat{\mathbf{f}}}_m \in L_2 \bigcap L_\infty. \tag{36}$$

The proof directly follows (34) and (35). For the concept of *L_2 and L_∞ stability* (having similarities to *Lyapunov functions method*), see Appendix A.

IV. SLAVE MANIPULATOR

A commercial HIAB-031 hydraulic manipulator is chosen to act as the slave manipulator of the teleoperation system. The manipulator is retrofitted with fast hydraulic servo valves, pressure transducers to measure cylinder chamber pressures, and high accuracy incremental encoders to measure joint angles. Although the manipulator is heavily retrofitted, it does not have force/torque sensor at the TCP. Consequently, a force-sensor-less control method with external force estimation is used for the slave manipulator as was the case with the master manipulator.

In the experiments, manipulation and force perception are considered within the same 2-DOF plane as with the master manipulator. The extension cylinder and rotation of the boom were mechanically locked. Fig. 4(a) illustrates the slave manipulator and shows several important frames of the manipulator. Frame $\{\mathbf{B_s}\}$ is fixed to the base of the slave manipulator, frame $\{\mathbf{O}_2\}$ is attached to the last link of the slave manipulator, and frame $\{\mathbf{G}\}$ is attached to the tip of the slave manipulator and has the same orientation as frame $\{\mathbf{O}_2\}$. Frame $\{\mathbf{C}\}$ has the same origin as frame $\{\mathbf{G}\}$, but is aligned with frame $\{\mathbf{B}_s\}$.

As discussed in Section I-B, *VDC enables modularity in the control design*. Consequently, the slave manipulator can be considered as a subsystem (with its own local subsystems) of the overall system. Stability-guaranteed constrained motion control of the slave manipulator has been demonstrated in [6]. Thus, taking advantage of the modular control design, only the control equations of the environment interacting object (see Object 2 in Figs. 4 and 5) need to be redesigned, while *rest*

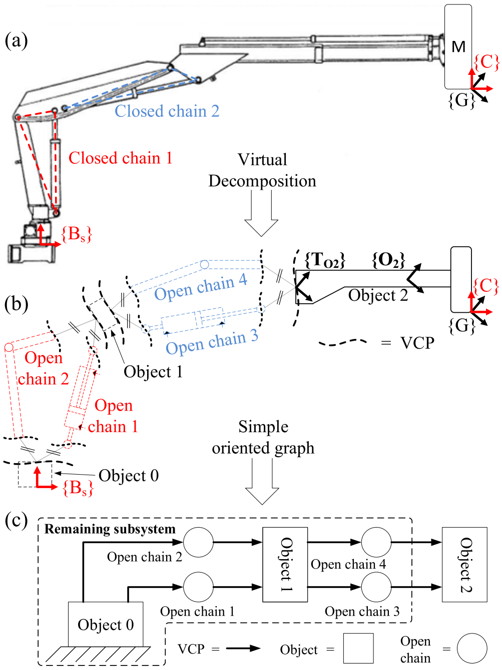

Fig. 4. (a) Slave manipulator. (b) Virtual decomposition of the slave manipulator. (c) Simple oriented graph (SOG) of the slave manipulator. The circled area in the SOG represents subsystem of the slave manipulator, for which the control has been designed in [6].

of the control system is kept identical to that of [6]. Fig. 4 presents the decomposed structure of the slave manipulator, with the reused control design circled by a dashed line.

A. Object 2—Kinematics and Dynamics

Let the linear/angular velocity vector ${}^{\mathrm{T_{O2}}}V \in \mathbb{R}^6$ at the driven VCP of Object 2 be known from the kinematic chain through the previous subsystems (see [6]). Then, kinematic transformations among the frames in Object 2 (see Fig. 5) can be written as

$$\begin{aligned} {}^{\mathrm{G}}V &= {}^{\mathrm{T_{O2}}}\mathbf{U}_{\mathrm{G}}^{T}\,{}^{\mathrm{T_{O2}}}V \\ &= {}^{\mathrm{O_2}}\mathbf{U}_{\mathrm{G}}^{T}\,{}^{\mathrm{O_2}}V \qquad (37) \\ {}^{\mathrm{C}}V &= \mathrm{diag}({}^{\mathrm{G}}\mathbf{R}_{\mathrm{C}}, {}^{\mathrm{G}}\mathbf{R}_{\mathrm{C}})\,{}^{\mathrm{G}}V. \qquad (38) \end{aligned}$$

Next, dynamics of the environment are defined. In this work, we assume flexible environment with dynamics described by second-order linear time-invariant model [22] as

$$\mathbf{f}_s = \mathbf{M}_e\ddot{\mathbf{x}}_s + \mathbf{D}_e\dot{\mathbf{x}}_s + \mathbf{K}_e\mathbf{x}_s \qquad (39)$$

where $\mathbf{M}_e \in \mathbb{R}^{2\times 2}$, $\mathbf{D}_e \in \mathbb{R}^{2\times 2}$, and $\mathbf{K}_e \in \mathbb{R}^{2\times 2}$ are symmetric positive-definite matrices approximating the inertia, damping, and stiffness of the environment, respectively, and $\mathbf{x}_s \in \mathbb{R}^2$ denotes the tip position of the slave manipulator, expressed in frame $\{\mathbf{B_s}\}$, subject to $\dot{\mathbf{x}}_s = \mathcal{V}_s$ with

$$\mathcal{V}_s = [\mathbf{I}_{2\times 2} \quad \mathbf{0}_{2\times 4}]\,{}^{\mathrm{C}}V. \qquad (40)$$

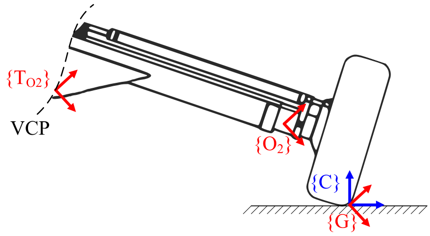

Fig. 5. Object 2 and its contact point with the environment.

Then, dynamics of the environment can be included on the slave manipulator as

$${}^{\mathrm{G}}F = \mathrm{diag}({}^{\mathrm{G}}\mathbf{R}_{\mathrm{C}}, {}^{\mathrm{G}}\mathbf{R}_{\mathrm{C}})[\mathbf{I}_{2\times 2} \quad \mathbf{0}_{2\times 4}]^T \sigma_f \mathbf{f}_s \qquad (41)$$

where

$$\sigma_f = \begin{cases} 0, & \text{approach motion} \\ 1, & \text{constrained motion.} \end{cases}$$

The net force/moment vector (rigid body dynamics) ${}^{\mathrm{O_2}}F^*$ of Object 2 can be written in view of (3) as

$$\mathbf{M}_{\mathrm{O_2}}\frac{d}{dt}({}^{\mathrm{O_2}}V) + \mathbf{C}_{\mathrm{O_2}}({}^{\mathrm{O_2}}\omega){}^{\mathrm{O_2}}V + \mathbf{G}_{\mathrm{O_2}} = {}^{\mathrm{O_2}}F^* \qquad (42)$$

and, eventually, the force balance (i.e. force resultant) equation of Object 2 can be written as

$${}^{\mathrm{O_2}}F^* = {}^{\mathrm{O_2}}\mathbf{U}_{\mathrm{T_{O2}}}\,{}^{\mathrm{T_{O2}}}F - \sigma_f\,{}^{\mathrm{O_2}}\mathbf{U}_{\mathrm{G}}\,{}^{\mathrm{G}}F. \qquad (43)$$

Remark 4: Disturbances in (14) and (39) are neglected in this manuscript, but they may affect the performance in practical applications. Approximation of operator dynamics and environmental parameters can be applied to mitigate this problem. Such an approach is proposed in [19], where a fuzzy logic system is deployed to approximate these parameters.

B. Object 2—Control

Let the required velocity of the slave manipulator be designed as

$$\mathcal{V}_{sr} = \mathcal{V}_{sd} - \mathbf{A}\tilde{\hat{\mathbf{f}}}_s \qquad (44)$$

where $\mathcal{V}_{sd} \in \mathbb{R}^2$ is to be defined in Section V, and $\tilde{\hat{\mathbf{f}}}_s \in \mathbb{R}^2$ is obtained from $\hat{\mathbf{f}}_s \in \mathbb{R}^2$ using a first-order filter as

$$\dot{\tilde{\hat{\mathbf{f}}}}_s + \mathbf{C}\tilde{\hat{\mathbf{f}}}_s = \mathbf{C}\hat{\mathbf{f}}_s \qquad (45)$$

and $\hat{\mathbf{f}}_s$ is obtained using (15) in [6].

Required piston velocities of the slave manipulator are then redesigned from (87) in [6] into

$$\begin{bmatrix} \dot{x}_{1\mathrm{r}} \\ \dot{x}_{3\mathrm{r}} \end{bmatrix} = \mathbf{J}_x^{-1}\mathcal{V}_{sr} \qquad (46)$$

where $\mathbf{J}_x^{-1} \in \mathbb{R}^{2\times 2}$ is the invertible Jacobian matrix of the slave manipulator, defined in [6].

Then, in view of (37), (38), and (40), the required linear/angular velocity vectors in Object 2 can be written as

$$\begin{aligned} {}^{\mathbf{G}}V_r &= {}^{\mathbf{T}_{\mathrm{O2}}}\mathbf{U}_{\mathbf{G}}^{T}\,{}^{\mathbf{T}_{\mathrm{O2}}}V_r \\ &= {}^{\mathbf{O}_2}\mathbf{U}_{\mathbf{G}}^{T}\,{}^{\mathbf{O}_2}V_r && (47) \\ {}^{\mathbf{C}}V_r &= \mathrm{diag}({}^{\mathbf{G}}\mathbf{R}_{\mathbf{C}}, {}^{\mathbf{G}}\mathbf{R}_{\mathbf{C}})\,{}^{\mathbf{G}}V_r && (48) \\ \mathcal{V}_{sr} &= [\mathbf{I}_{2\times 2} \quad \mathbf{0}_{2\times 4}]\,{}^{\mathbf{C}}V_r. && (49) \end{aligned}$$

The required contact force of the slave manipulator is designed as

$$\mathbf{f}_{sr} = \mathbf{M}_e\dot{\mathcal{V}}_{sr} + \mathbf{D}_e\dot{\mathbf{x}}_s + \mathbf{K}_e\mathbf{x}_s. \tag{50}$$

Finally, using (22) and (41)–(43), the required control laws for Object 2 dynamics can be written as

$$\begin{aligned} {}^{\mathbf{G}}F_r &= \mathrm{diag}({}^{\mathbf{G}}\mathbf{R}_{\mathbf{C}}, {}^{\mathbf{G}}\mathbf{R}_{\mathbf{C}})[\mathbf{I}_{2\times 2} \quad \mathbf{0}_{2\times 4}]^T\sigma_f\mathbf{f}_{sr} && (51) \\ {}^{\mathbf{O}_2}F_r^{*} &= \mathbf{Y}_{\mathbf{O}_2}\widehat{\boldsymbol{\theta}}_{\mathbf{O}_2} + \mathbf{K}_{\mathbf{O}_2}({}^{\mathbf{O}_2}V_{\mathrm{r}} - {}^{\mathbf{O}_2}V) && (52) \\ {}^{\mathbf{O}_2}F_r^{*} &= {}^{\mathbf{O}_2}\mathbf{U}_{\mathbf{T}_{\mathrm{o2}}}\,{}^{\mathbf{T}_{\mathrm{o2}}}F_r - \sigma_f\,{}^{\mathbf{O}_2}\mathbf{U}_{\mathbf{G}}\,{}^{\mathbf{G}}F_r. && (53) \end{aligned}$$

In line with (22), $\mathbf{Y}_{\mathbf{O}_2}\widehat{\boldsymbol{\theta}} \in \mathbb{R}^6$ in (52) is the model-based feedforward compensation term for the rigid body dynamics and $\mathbf{K}_{\mathbf{O}_2} \in \mathbb{R}^{6\times 6}$ is a positive-definite velocity feedback matrix to ensure the control stability. By defining

$$\mathbf{s}_{\mathbf{O}_2} = \mathbf{Y}_{\mathbf{O}_2}^T({}^{\mathbf{O}_2}V_{\mathrm{r}} - {}^{\mathbf{O}_2}V) \tag{54}$$

the estimated parameter vector $\widehat{\boldsymbol{\theta}}_{\mathbf{O}_2} \in \mathbb{R}^{13}$ in (52) is updated as

$$\begin{aligned} \dot{\widehat{\theta}}_{\mathbf{O}_2 i} &= \rho_i s_{\mathbf{O}_2 i}\kappa_i \quad \forall i \in \{1, 2, \dots, 13\} \\ \kappa_i &= \begin{cases} 0, & \widehat{\theta}_{\mathbf{O}_2 i} \le \theta_{\mathbf{O}_2 i}^{-} \text{ and } s_{\mathbf{O}_2 i} \le 0 \\ 0, & \widehat{\theta}_{\mathbf{O}_2 i} \ge \theta_{\mathbf{O}_2 i}^{+} \text{ and } s_{\mathbf{O}_2 i} \ge 0 \\ 1, & \text{otherwise} \end{cases} && (55) \end{aligned}$$

where $\widehat{\theta}_{\mathbf{O}_2 i}$ is the ith element of $\widehat{\boldsymbol{\theta}}_{\mathbf{O}_2}$, $s_{\mathbf{O}_2 i}$ is the ith element of $\mathbf{s}_{\mathbf{O}_2}$, $\rho_i > 0$ is the update gain, $\theta_{\mathbf{O}_2 i}^{-}$ is the lower bound of $\widehat{\theta}_{\mathbf{O}_2 i}$, and $\theta_{\mathbf{O}_2 i}^{+}$ is the upper bound of $\widehat{\theta}_{\mathbf{O}_2 i}$.

C. Stability

The remaining system, for which the control was designed first in [6], qualifies as virtually stable according to Theorem 2.

Theorem 2: Consider the system encircled by a dashed line in Fig. 4. The subsystem qualifies virtually stable with its affiliated vector $({}^{\mathbf{A}}V_r - {}^{\mathbf{A}}V), \forall \mathbf{A} \in \Psi_r$ and its affiliated scalar variables $(f_{\mathrm{p}i\mathrm{r}} - f_{\mathrm{p}i})$ for the hydraulic cylinder i, $\forall i \in 1, 2$, where Ψ_r contains the rigid body frames of each rigid link and object of the remaining subsystem. A non-negative accompanying function for this system can be found as

$$\nu_{\mathbf{R}} \ge \frac{1}{2}\sum_{\boldsymbol{A}\in\Psi_{\mathrm{r}}}({}^{\mathbf{A}}V_{\mathrm{r}} - {}^{\mathbf{A}}V)^T\mathbf{M}_{\mathbf{A}}({}^{\mathbf{A}}V_{\mathrm{r}} - {}^{\mathbf{A}}V) + \frac{1}{2}\sum_{i=1}^{2}\left[\frac{1}{\beta k_{\mathrm{x}i}}(f_{\mathrm{p}i\mathrm{r}} - f_{\mathrm{p}i})^2\right] \tag{56}$$

such that

$$\dot{\nu}_{\mathbf{R}} \leqslant -\sum_{\boldsymbol{A}\in\Psi_{\mathrm{r}}}({}^{\mathbf{A}}V_{\mathrm{r}} - {}^{\mathbf{A}}V)^T\mathbf{K}_{\mathbf{A}}({}^{\mathbf{A}}V_{\mathrm{r}} - {}^{\mathbf{A}}V) - p_{\mathbf{T}_{\mathrm{O2}}} - \frac{k_f}{k_x}\sum_{i=1}^{2}(f_{\mathrm{p}i\mathrm{r}} - f_{\mathrm{p}i}). \tag{57}$$

Proof: The proof for Theorem 2 can be obtained from the results of [6]. □

Theorem 3: Consider Object 2 described by (37)–(43), combined with the control equations (44)–(53) and with the parameter adaptation (54)–(55). This subsystem is virtually stable with its affiliated vector ${}^{\mathbf{O}_2}V_r - {}^{\mathbf{O}_2}V$ being a virtual function in both L_2 and L_∞ in the sense of Definition 3. This is because a non-negative accompanying function

$$\nu_{\mathbf{O}_2} = \frac{1}{2}({}^{\mathbf{O}_2}V_{\mathrm{r}} - {}^{\mathbf{O}_2}V)^T\mathbf{M}_{\mathbf{O}_2}({}^{\mathbf{O}_2}V_{\mathrm{r}} - {}^{\mathbf{O}_2}V) + \frac{1}{2}\sum_{i=1}^{13}\frac{(\theta_{\mathbf{O}_2 i} - \widehat{\theta}_{\mathbf{O}_2 i})^2}{\rho_{\mathbf{O}_2 i}} \tag{58}$$

can be found such that

$$\dot{\nu}_{\mathbf{O}_2} \leqslant -({}^{\mathbf{O}_2}V_{\mathrm{r}} - {}^{\mathbf{O}_2}V)^T\mathbf{K}_{\mathbf{O}_2}({}^{\mathbf{O}_2}V_{\mathrm{r}} - {}^{\mathbf{O}_2}V) + p_{\mathbf{T}_{\mathrm{O2}}} - p_{\mathbf{G}} \tag{59}$$

holds, where

$$\int_0^{\infty} p_{\mathbf{G}}(t)dt \geqslant -\gamma_s \tag{60}$$

holds with $0 \leqslant \gamma_s < \infty$. Note that $p_{\mathbf{T}_{\mathrm{O2}}}$ is the VPF by Definition 2 in the driven VCP of Object 2, and $p_{\mathbf{G}}$ characterizes the VPF between the end-effector and the environment while in constrained motion (i.e., $\sigma_f = 1$).

Proof: See Appendix C. □

Theorem 4: Considering (87) and Definition 3, the contact with the environment qualifies virtually stable. The non-negative accompanying function for the entire slave manipulator can be obtained by summing the individual functions from (56) and (58).

Stability analysis for the remaining subsystems follows exactly as shown in [6], ultimately yielding stability of the entire slave robot, as it follows:

$$\xi_s \equiv \mathcal{V}_{sd} - \mathcal{V}_s - \mathbf{A}\tilde{\hat{\mathbf{f}}}_s \in L_2 \bigcap L_\infty. \tag{61}$$

V. TELEOPERATION

After individual velocity-based controllers for both master and slave manipulators (see (25) and [6]) of the teleoperation system have been designed, a scheme for connecting the manipulators can be designed. Connection between the two manipulators is made with a *communication channel* that virtually connects the manipulators together. This section designs bilateral teleoperation and specifies two design vectors $\mathcal{V}_{md}$ and $\mathcal{V}_{sd}$, used in (18) and (44), respectively. Using position control $\delta = 1$ in [22], $\mathcal{V}_{md}$ and $\mathcal{V}_{sd}$ can be designed as

$$\begin{aligned} \mathcal{V}_{md} &= \frac{1}{\kappa_p}[\tilde{\mathcal{V}}_s + \Lambda(\tilde{\mathcal{P}}_s - \kappa_p\mathcal{P}_m) \\ &\qquad - \mathbf{A}(\tilde{\hat{\mathbf{f}}}_s + (\kappa_f - \kappa_p)\tilde{\hat{\mathbf{f}}}_m)] && (62) \\ \mathcal{V}_{sd} &= \kappa_p\tilde{\mathcal{V}}_m - \Lambda(\mathcal{P}_s - \kappa_p\tilde{\mathcal{P}}_m) - \mathbf{A}\kappa_f\tilde{\hat{\mathbf{f}}}_m && (63) \end{aligned}$$

where $\kappa_p > 0$ and $\kappa_f > 0$ are position and force scaling factors *for arbitrary motion/force scaling between the manipulators*, $\Lambda \in \mathbb{R}^{2\times 2}$ is a diagonal positive-definite matrix, and $\mathcal{P}_m \in \mathbb{R}^2$ and $\mathcal{P}_s \in \mathbb{R}^2$ denote the position/orientation of the master and slave manipulator, respectively, subject to $\dot{\mathcal{P}}_m = \mathcal{V}_m$ and

$\dot{\mathcal{P}}_s = \mathcal{V}_s$. Furthermore, $\tilde{\mathcal{V}}_m$, $\tilde{\mathcal{V}}_s$, $\tilde{\mathcal{P}}_m$, and $\tilde{\mathcal{P}}_s$ are filtered values of $\mathcal{V}_m$, $\mathcal{V}_s$, $\mathcal{P}_m$, and $\mathcal{P}_s$, respectively, obtained using the following first-order filter:

$$\dot{\tilde{\mathcal{X}}} + \mathbf{C}\tilde{\mathcal{X}} = \mathbf{C}\mathcal{X} \tag{64}$$

where $\mathcal{X} \in \mathbb{R}^2$ is the input signal and $\tilde{\mathcal{X}} \in \mathbb{R}^2$ is the filtered signal. The use of filtered variables in the two design vectors, (63) and (62), makes the required accelerations $\dot{\mathcal{V}}_{sd}$ and $\dot{\mathcal{V}}_{md}$ functions of $\mathcal{V}_m$, $\mathcal{V}_s$, $\mathbf{f}_m$, and $\mathbf{f}_s$.

A. Tracking

Substituting (62) and (63) into (36) and (61) and then subtracting the resulting error terms from each other yields

$$\begin{aligned}\kappa_p\xi_m - \xi_s = {} & (\mathcal{V}_s - \kappa_p\mathcal{V}_m) + \Lambda(\mathcal{P}_s - \kappa_p\mathcal{P}_m)\\ & + (\tilde{\mathcal{V}}_s - \kappa_p\tilde{\mathcal{V}}_m) + \Lambda(\tilde{\mathcal{P}}_s - \kappa_p\tilde{\mathcal{P}}_m).\end{aligned} \tag{65}$$

It can be easily seen that (65) can be further written as

$$\kappa_p\xi_m - \xi_s = \tilde{\mathcal{Z}} + \mathcal{Z} \tag{66}$$

where

$$\mathcal{Z} \equiv (\mathcal{V}_s - \kappa_p\mathcal{V}_m) + \Lambda(\mathcal{P}_s - \kappa_p\mathcal{P}_m) \tag{67}$$

and $\tilde{\mathcal{Z}}$ is obtained from $\mathcal{Z}$ using (64).

Following Lemma 2.4 in [22] yields

$$\mathcal{Z} \in L_2 \bigcap L_\infty. \tag{68}$$

Eventually, it follows from (67), (68) and Lemma 1 in [22] that

$$\xi_v = \kappa_p\mathcal{V}_m - \mathcal{V}_s \in L_2 \bigcap L_\infty \tag{69}$$

$$\xi_p = \kappa_p\mathcal{P}_m - \mathcal{P}_s \in L_2 \bigcap L_\infty \tag{70}$$

hold, which guarantees the L_2 and L_∞ stability of the velocity and position tracking of the teleoperation system.

B. Transparency

Transparency of the teleoperation system can be analyzed by substituting (62) and (63) into (36) and (61), then summing the resulting error terms together results in

$$\begin{aligned}\kappa_p\xi_m + \xi_s(\tilde{\mathcal{V}}_s - \mathcal{V}_s) + \kappa_p(\tilde{\mathcal{V}}_m - \mathcal{V}_m) + \Lambda(\tilde{\mathcal{P}}_s - \mathcal{P}_s)&\\ + \Lambda\kappa_p(\tilde{\mathcal{P}}_m - \mathcal{P}_m) - 2\mathbf{A}(\tilde{\hat{\mathbf{f}}}_s + \kappa_f\tilde{\mathbf{f}}_m).&\end{aligned} \tag{71}$$

Substituting (64) with $-\mathbf{C}^{-1}\dot{\tilde{\mathcal{X}}} = (\tilde{\mathcal{X}} - \mathcal{X})$ into (71) yields

$$\begin{aligned}\kappa_p\xi_m + \xi_s = -\mathbf{C}^{-1}[\dot{\tilde{\mathcal{V}}}_s + \kappa_p\dot{\tilde{\mathcal{V}}}_m + \Lambda\tilde{\mathcal{V}}_s + \Lambda\kappa_p\tilde{\mathcal{V}}_m]&\\ - 2\mathbf{A}(\tilde{\hat{\mathbf{f}}}_s + \kappa_f\tilde{\mathbf{f}}_m).&\end{aligned} \tag{72}$$

According to [22], we can rewrite (72), using (69)–(70), as

$$-\tilde{\mathbf{f}}_m = \kappa_f^{-1}\tilde{\mathbf{f}}_s + \kappa_f^{-1}\kappa_p\mathbf{A}^{-1}\mathbf{C}^{-1}(s + \Lambda)\tilde{\mathcal{V}}_m + \frac{\xi}{2\kappa_f} \tag{73}$$

where s denotes the Laplace operator, and

$$\xi \equiv \mathbf{A}^{-1}[-\mathbf{C}^{-1}(s + \Lambda)\tilde{\xi}_v + (\xi_s + \kappa_p\xi_m)] \tag{74}$$

where $\tilde{\xi}_v$ is obtained from ξ_v using (64). In view of Lemma 1 in [22], the following holds true:

$$\xi \in L_2 \bigcap L_\infty.$$

Transparency of the teleoperation system can be seen from (73). Within a limited frequency range, the filtered signals can be assumed to be approximately equal to their nonfiltered counterparts. The last term on the right-hand side of (73) is bounded to converge to zero. Then, the transparency error can be described by the second term on the right-hand side of (73). It comprises of velocity- and acceleration-dependent terms. The acceleration-related term $\kappa_f^{-1}\kappa_p\mathbf{A}^{-1}\mathbf{C}^{-1}$ acts as a *virtual mass* on the teleoperation system, while the velocity-dependent term $\kappa_f^{-1}\kappa_p\mathbf{A}^{-1}\mathbf{C}^{-1}\Lambda$ determines the *damping* of the teleoperation system.

C. Stability Under Time Delay

Time delay under teleoperation is a much investigated issue especially in space teleoperation. Although the focus of this study is in terrestrial applications, robustness against arbitrary time delay of the proposed method is discussed briefly. In [13], similar approach was used for longer and varying delays.

Without loss of generality, we consider a 1-D system in the stability analysis. The extension to multiple-dimensional systems can be proceeded accordingly. Due to the fact that both master and slave manipulators have independent stability-guaranteed controllers linked only by the communication channel, the stability under time delay can be analyzed by modifying (62) and (63) as

$$\begin{aligned}\mathcal{V}_{md} = {} & \kappa_p^{-1}[e^{-sT}(\tilde{\mathcal{V}}_s + \Lambda\tilde{\mathcal{P}}_s) - \kappa_p\Lambda\mathcal{P}_m\\ & - \mathbf{A}(e^{-sT}\tilde{\hat{\mathbf{f}}}_s + (\kappa_f - \kappa_p)\tilde{\hat{\mathbf{f}}}_m)]\end{aligned} \tag{75}$$

$$\mathcal{V}_{sd} = e^{-sT}\kappa_p(\tilde{\mathcal{V}}_m - \Lambda\tilde{\mathcal{P}}_m) - \Lambda\mathcal{P}_s - e^{-sT}\mathbf{A}\kappa_f\tilde{\hat{\mathbf{f}}}_m \tag{76}$$

where the communication channel is represented as pure time delay of T (see Fig. 6). The stability under arbitrary time delay can be analyzed similar to the method presented in [22].

Fig. 6 represents the teleoperation system under arbitrary time delay based on (75) and (76). In the figure, Z_h is the operator dynamics defined in (14) (now considered 1-D) and Z_e is environment dynamics, which is approximated with second-order linear dynamics. Sufficient condition for stability under time delay can then be summarized as

$$\mathbf{b} + 4C\sqrt{\Lambda AK(2ACM + 1)} \geq 0 \tag{77}$$

where

$$\mathbf{b} = \Lambda^2 + 2AC(2ACD - K - 2\Lambda ACM).$$

The detailed steps leading to (77) are shown in Appendix D.

VI. EXPERIMENTS

This section evaluates the performance of the proposed teleoperation system. First, Section VI-A addresses the system implementation issues. Then, Section VI-B provides the experiments without time delay, followed by the experiment with time delay in Section VI-C.

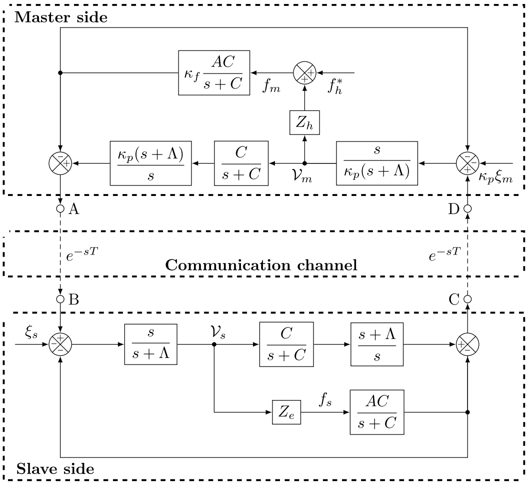

Fig. 6. 1-D block diagram representation of the teleoperation system under arbitrary time delay of T.

TABLE I

USED COMMUNICATION CHANNEL PARAMETERS

	κ_p	κ_f	Λ	**A**	**C**
Experiment 1:	1	300	2.0	60×10^{-6}	35
Experiment 2:	4	800	2.0	100×10^{-6}	35
Experiment 3:	1.5	500	1.5	40×10^{-6}	35

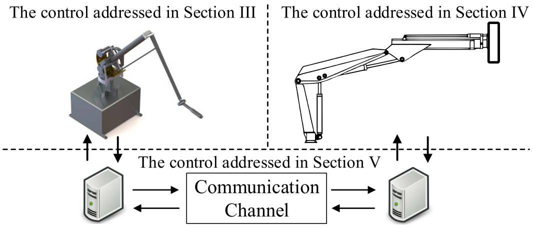

Fig. 7. High-level overview of the experimental implementation.

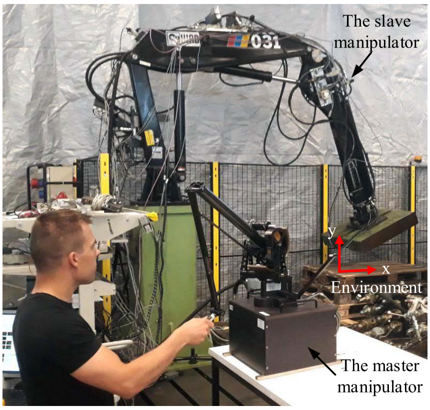

Fig. 8. Experimental implementation and setup.

A. Experiment Description

The experimental implementation comprises four main components, visualized in Fig. 7, which are the electric master manipulator (Phantom Premium 6DOF/3.0L haptic device), the host computer for the master manipulator, the real-time computer, and the hydraulic slave manipulator (HIAB-031 manipulator). The 2-DOF hydraulic manipulator (in Fig. 8) has a maximum reach of approximately 3.2 m, and a payload of 475 kg is attached to its tip. For the real-time control system, the following components were used: a DS1005 processor board, a DS3001 incremental encoder board, a DS2103 DAC board, a DS2003 ADC board, and a DS4504 100 Mb/s Ethernet interface. The remaining hardware implementations can be found in [6], [11] or [23]. Control computations have been run with 500-Hz frequency. The communication channel parameters of each experiment are shown in Table I.

Teleoperation control between the master and slave manipulators was engaged by pressing a pushbutton and disengaged by releasing the button. At first, the slave manipulator was driven from free space to contact with the environment along the Cartesian y-axis (see Fig. 8 for the directions of the Cartesian coordinate system). After contact with the environment was established, the slave manipulator was driven along the surface of the pallets, while maintaining constant force against the environment. Finally, the slave manipulator was driven back to free space after approximately 0.5 m of sliding against the wooden pallets. The above described task was repeated *without any time delay* with two different sets of motion/force scaling parameters (κ_p and κ_f) of the communication system (see Fig. 9). Then, an experiment *with 80-ms one-way time delay* in the communication channel was performed (see Fig. 10). In Figs. 9 and 10, the master manipulator data is shown in blue, and the slave manipulator data in red.

B. Experiments Without Time Delay

In the *first experiment* [Fig. 9(a)], 1:1 position mapping was used between the manipulators ($\kappa_p = 1$), while forces of the master manipulator were scaled up by a factor of $\kappa_f = 300$ (see Table I). In the *second experiment* [Fig. 9(b)], 4:1 position scaling between the master and slave manipulators was used ($\kappa_p = 4$), yielding four times larger movement of the slave manipulator compared to the movement of the master manipulator, along with force scaling by a factor of $\kappa_f = 800$ (see Table I).

As Fig. 9 shows, accurate position (see the *first* and *second rows*) and force tracking (the *third* and *fourth rows*) between the master and slave manipulators is achieved with different scaling parameters, as predicted by the theory, despite the inherent challenges of force control of hydraulic manipulator in the teleoperation system (see the discussion in

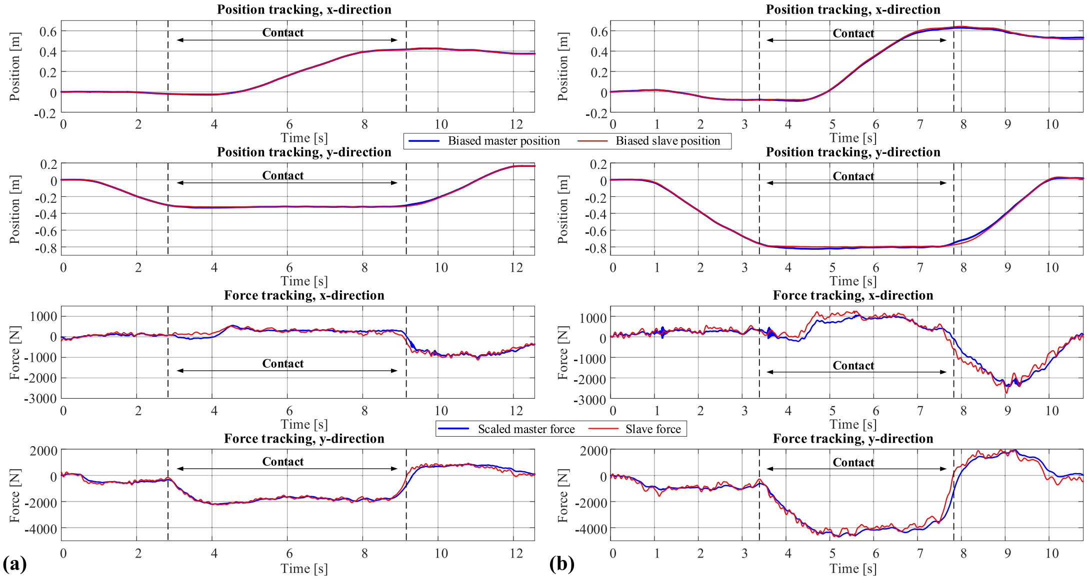

Fig. 9. Results from experimental implementation with bilateral force-reflected teleoperation. In the experiments, two different set of scaling parameters in the communication system were used as: (a) $\kappa_p = 1.0$ and $\kappa_f = 300$, and (b) $\kappa_p = 4.0$ and $\kappa_f = 800$. Scaling of the axes of the figures is kept the same between the two experiments to elaborate the effect of the scaling parameters to the behavior of the system.

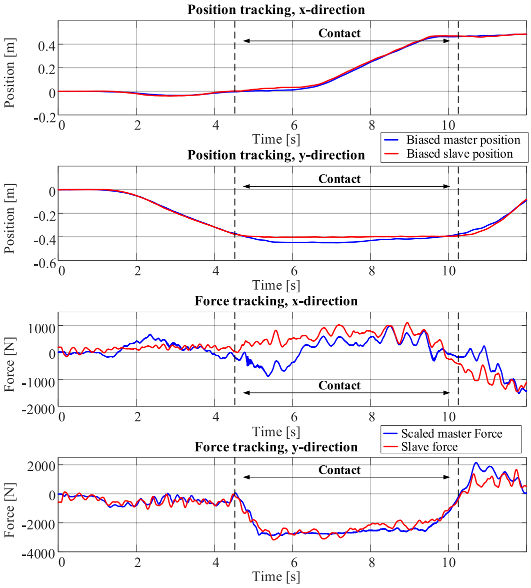

Fig. 10. Teleoperation task under one-way time delay of 80 ms. Parameters of the communication channel were set as: $\kappa_p = 1.5$ and $\kappa_f = 500$, $\Lambda = 1.5$, $\mathbf{C} = 35$, and $\mathbf{A} = 40 \times 10^{-6}$.

Section I). The forces in the third and fourth rows presents the *estimated* contact forces of the slave and master manipulators along the x- and y-axes, respectively. In the results, the master manipulator forces are scaled up by the respective scaling factor.

Table II shows the maximum and mean Cartesian tracking errors for each individual experiment. For objective motion tracking performance evaluation and to set a benchmark for future developments, a normalizing performance indicator $\rho = \max(\|\kappa_p X_m - X_s\|_2)/\max(\|\dot{X}_s\|_2)$ values are also reported in Table II (see [5] and [28] for more details on ρ). Comparative results from our preliminary study in [23] with the same system are also reported in Table II. The results from that study are mostly relevant compared to experiment 1 of this study due to similar scaling values. Improved motion and force tracking can be noticed as well as the improved performance indicator value.

Note that the slave manipulator contact forces are estimated from chamber pressures of the cylinder. Thus, some inaccuracies can exist in the measured contact forces (see [11] for more details). However, the operator is still able to effectively sense the contact forces between the slave and the environment, and excessive contact forces can be prevented. It is valid to mention that the proposed force sensorless approach provides a practical solution for teleoperation of extremely powerful hydraulic manipulators, as conventional 6-DOF force/torque sensors are fragile and prone to overloading [6].

Remark 5: Note that in the second experiment, the transition from free space motion to contact motion was done rapidly with a velocity of approximately 0.2 m/s. This is to demonstrate the stable behavior of the control system even with high velocity and rapid changes of system states.

C. Experiment With One-Way Time Delay of 80 ms

Fig. 10 shows respective results as in Fig. 9 with one-way time delay of 80 ms. To demonstrate the versatility, in the experiment, the scaling factors were selected as $\kappa_p = 1.5$

TABLE II
CARTESIAN TRACKING ERRORS DURING EXPERIMENTS

	Position error [mm]		Force error [N]		Perf. index
	mean	max	mean	max	ρ [s]
Experiment 1:	3.60	14.9	141	801	0.060
Experiment 2:	12.6	37.7	307	1476	0.074
Experiment 3:	19.4	50.4	467	1632	0.158
Exp. in [23]:	13.8	31.2	406	1111	0.147

and $\kappa_f = 500$. As the results indicate, the proposed method: 1) is robust against time delays and communication noises (as predicted by the theory in Section V-C) and 2) is capable of handling the delay without significant loss of performance.

VII. CONCLUSION

This study presented force-reflected bilateral teleoperation using asymmetric electrical master and hydraulic slave manipulators. The control design takes advantage of the VDC approach, which allows us to design local subsystem-dynamics-based controllers for the master and slave manipulators independently. Then, the teleoperation system was completed by designing the communication channel between the master and slave controllers as motivated by Zhu and Salcudean [22]. The teleoperation scheme provided unique features, such as arbitrary motion/force scaling between the manipulators, effectively enabling both micro- and macro-manipulations with appropriate force levels, which is an essential feature for asymmetric teleoperation systems.

The experimental results demonstrated the performance of the proposed method and showed excellent motion and force tracking between the manipulators. Furthermore, robustness against an arbitrary time delay was demonstrated theoretically and experimentally. Similar to our previous studies [6], [11], and [35], tracking performance improvements can be expected after rigorous application of a full parameter adaptation implementation and with tuning of the system parameters.

The aim of our research is to enable the use of LfD approaches on heavy-duty manipulators. Teleoperation is seen as a key enabling technology for the use of LfD-type methods safely on large-scale manipulators that cannot be taught by kinesthetic teaching. Our vision is that in the future, large manipulators can be taught to perform various tasks with the same ease as programming of lightweight arms. Alternatively, teleoperation can be used as such, as an intuitive and precise control method for large work machines. The proposed approach is demonstrated on commercially available hardware, and the fact that no force/torque sensor is required makes this approach very appealing for commercial use. Our interests lie in terrestrial low-latency force-reflecting teleoperation over the emerging cellular 5G networks. This article lays down experimentally verified control theoretic foundation, advancing force-reflected bilateral teleoperation control one more step toward practical applications in a wide variety of industrial applications of controlling heavy-duty machinery. The theoretical and experimental studies in this article concluded that the use of a force-sensor-less design for bilateral teleoperation is feasible.

Future work will focus on maximizing the system performances of position tracking and transparency, as well as forming basis functions for human operator exogenous forces through machine learning. Moreover, we intend to focus on expanding the experimental system to possess more DOFs with the goal of achieving a 6-DOF manipulation.

APPENDIX A
L_2 AND L_∞ STABILITY

Definition 1 provides a definition for the Lebesgue space.

Definition 1 [26]: The Lebesgue space, denoted as L_p with p being a positive integer, contains all Lebesgue measurable and integrable functions $f(t)$ subject to

$$\|f\|_p = \lim_{T\to\infty} \left[\int_0^T |f(t)|^p d\tau \right]^{\frac{1}{p}} < +\infty. \tag{78}$$

Two particular cases are considered:

1) A Lebesgue measurable function $f(t)$ belongs to L_2 if and only if $\lim_{T\to\infty} \int_0^T |f(t)|^2 d\tau < +\infty$.
2) A Lebesgue measurable function $f(t)$ belongs to L_∞ if and only if $\max_{t\in[0,\infty)} |f(t)| < +\infty$.

Lemma 1 (a simplified version of Lemma 2.3 in [26]) provides that a system is L_2 and L_∞ stable with its affiliated vector $\mathbf{x}(t)$, being a function in L_∞ and its affiliated vector $\mathbf{y}(t)$, being a function in L_2.

Lemma 1 [26]: Consider a non-negative differentiable function $\xi(t)$ defined as

$$\xi(t) \geqslant \frac{1}{2}\mathbf{x}(t)^T \mathbf{P}\mathbf{x}(t) \tag{79}$$

with $\mathbf{x}(t) \in \mathbb{R}^n$, $n \geqslant 1$, and $\mathbf{P} \in \mathbb{R}^{n\times n}$ being a symmetric positive-definite matrix. If the time-derivative of $\xi(t)$ is Lebesgue integrable and governed by

$$\dot{\xi}(t) \leqslant -\mathbf{y}(t)^T \mathbf{Q}\mathbf{y}(t) - s(t) \tag{80}$$

where $\mathbf{y}(t) \in \mathbb{R}^m$, $m \geqslant 1$, and $\mathbf{Q} \in \mathbb{R}^{m\times m}$ being a symmetric positive-definite matrix, and $s(t)$ is subject to

$$\int_0^\infty s(t)dt \geqslant -\gamma_0 \tag{81}$$

with $0 \leqslant \gamma_0 < \infty$, then, it follows that $\xi(t) \in L_\infty$, $\mathbf{x}(t) \in L_\infty$, and $\mathbf{y}(t) \in L_2$ hold.

Lemma 2 provides an alternative to Barbalat's lemma.

Lemma 2 [36]: If $e(t) \in L_2$ and $\dot{e}(t) \in L_\infty$, then $\lim_{t\to\infty} e(t) = 0$.

Remark 6: As a distinction to Lyapunov approaches, Lemma 1 allows different appearances of variables in the non-negative function itself and in its time-derivative. When all error signals are proved to belong to L_2 and L_∞ in the sense of Lemma 1, then asymptotic stability can be proved with Lemma 2, if the time-derivatives of all error signals belong to L_∞. Note that $s(t) = 0$ is a special case that satisfies (81) in Lemma 1.

APPENDIX B
VIRTUAL STABILITY

The unique feature of the VDC approach is the introduction of a scalar term, namely the VPF [26] (see Definition 2). The VPFs uniquely define the dynamic interactions among the subsystems and play an important role in the definition of *virtual stability* [26], which is defined in a simplified form in Definition 3.

Definition 2 [26]: The VPF with respect to frame $\{\mathbf{A}\}$ is the inner product of the linear/angular velocity vector error and the force/moment vector error as

$$p_{\mathbf{A}} = ({}^{\mathbf{A}}V_{\mathrm{r}} - {}^{\mathbf{A}}V)^T({}^{\mathbf{A}}F_{\mathrm{r}} - {}^{\mathbf{A}}F) \tag{82}$$

where ${}^{\mathbf{A}}V_{\mathrm{r}} \in \mathbb{R}^6$ and ${}^{\mathbf{A}}F_{\mathrm{r}} \in \mathbb{R}^6$ represent the required vectors of ${}^{\mathbf{A}}V \in \mathbb{R}^6$ and ${}^{\mathbf{A}}F \in \mathbb{R}^6$, respectively.

Definition 3 [26]: A subsystem with a *driven* VCP to which frame $\{\mathbf{A}\}$ is attached and a *driving* VCP to which frame $\{\mathbf{C}\}$ is attached is said to be virtually stable with its affiliated vector $\mathbf{x}(t)$ being a virtual function in L_∞ and its affiliated vector $\mathbf{y}(t)$ being a virtual function in L_2, if and only if there exists a non-negative accompanying function

$$\nu(t) \geqslant \frac{1}{2}\mathbf{x}(t)^T\mathbf{P}\mathbf{x}(t) \tag{83}$$

such that

$$\dot{\nu}(t) \leqslant -\mathbf{y}(t)^T\mathbf{Q}\mathbf{y}(t) - s(t) + p_{\mathbf{A}} - p_{\mathbf{C}} \tag{84}$$

holds,

$$\int_0^\infty s(t)d\tau \geqslant -\gamma_s \tag{85}$$

where $0 \leqslant \gamma_0 < \infty$, $\mathbf{P}$, and $\mathbf{Q}$ are two block-diagonal positive-definite matrices, and $p_{\mathbf{A}}$ and $p_{\mathbf{C}}$ denote the VPFs (by Definition 2) at frames $\{\mathbf{A}\}$ and $\{\mathbf{C}\}$, respectively.

Remark 7: In view of Theorem 2.1 in [26], when all subsystems qualify as *virtually stable* (in the sense of Definition 3), the L_2 and L_∞ stability of the entire system can be guaranteed in the sense Lemma 1.

APPENDIX C
PROOF OF THEOREM 3

According to Definition 2 and (39), (38), (41), (50), (48), and (51), it follows that

$$\begin{aligned} p_{\mathbf{G}} &= ({}^{\mathbf{G}}V_{\mathrm{r}} - {}^{\mathbf{G}}V)^T({}^{\mathbf{G}}F_{\mathrm{r}} - {}^{\mathbf{G}}F) \\ &= ({}^{\mathbf{G}}V_{\mathrm{r}} - {}^{\mathbf{G}}V)^T\mathrm{diag}({}^{\mathbf{G}}\mathbf{R}_{\mathbf{C}}, {}^{\mathbf{G}}\mathbf{R}_{\mathbf{C}}) \\ &\quad \times [\mathbf{I}_{2\times 2} \quad \mathbf{0}_{2\times 4}]^T\sigma_f(\mathbf{f}_{sr} - \mathbf{f}_s) \\ &= ({}^{\mathbf{G}}V_{\mathrm{r}} - {}^{\mathbf{G}}V)^T\mathrm{diag}({}^{\mathbf{G}}\mathbf{R}_{\mathbf{C}}, {}^{\mathbf{G}}\mathbf{R}_{\mathbf{C}}) \\ &\quad \times [\mathbf{I}_{2\times 2} \quad \mathbf{0}_{2\times 4}]^T\sigma_f\mathbf{M}_e(\dot{\mathcal{V}}_{sr} - \dot{\mathcal{V}}_s) \\ &= \left({}^{\mathbf{C}}V_{\mathrm{r}} - {}^{\mathbf{C}}V\right)^T[\mathbf{I}_{2\times 2} \quad \mathbf{0}_{2\times 4}]^T\sigma_f\mathbf{M}_e(\dot{\mathcal{V}}_{sr} - \dot{\mathcal{V}}_s) \\ &= \sigma_f(\mathcal{V}_{sr} - \mathcal{V}_s)^T\mathbf{M}_e(\dot{\mathcal{V}}_{sr} - \dot{\mathcal{V}}_s). \end{aligned} \tag{86}$$

For a constant value of σ_f, the following holds true:

$$\begin{aligned} \int_0^\infty p_{\mathbf{G}}dt &= \int_0^\infty \sigma_f(\mathcal{V}_{sr} - \mathcal{V}_s)^T\mathbf{M}_e(\dot{\mathcal{V}}_{sr} - \dot{\mathcal{V}}_s)dt \\ &\geq -\frac{1}{2}\sigma_f(\mathcal{V}_{sr}(0) - \mathcal{V}_s(0))^T\mathbf{M}_e(\mathcal{V}_{sr}(0) - \mathcal{V}_s(0)) \end{aligned} \tag{87}$$

APPENDIX D
STABILITY UNDER TIME DELAY

To analyze the effect of time delay on the system stability, transfer functions on both sides of the communication channel need to be defined. The transfer function for the master side, from input D to output A (see Fig. 6), can be formed as

$$\begin{aligned} G_m &= \frac{\frac{C}{s+C} - \frac{sAC\frac{\kappa_f}{\kappa_p}Z_h}{(s+\Lambda)(s+C)}}{1 + \frac{sAC\frac{\kappa_f}{\kappa_p}Z_h}{(s+\Lambda)(s+C)}} \\ &= \frac{-ACM_h^*s^2 + \left(C - ACD_h^*\right)s + \left(C\Lambda - ACK_h^*\right)}{\left(1 + ACM_h^*\right)s^2 + \left(\Lambda + C + ACD_h^*\right)s + \left(\Lambda C + ACK_h^*\right)} \end{aligned} \tag{88}$$

where $M_h^* = (\kappa_f/\kappa_p)M_h$, $D_h^* = (\kappa_f/\kappa_p)D_h$, and $K_h^* = (\kappa_f/\kappa_p)K_h$.

Following the same procedure, the transfer function from the input B of the slave side to output C can be formed as

$$G_s = \frac{\frac{C}{s+C} - \frac{sACZ_e}{(s+\Lambda)(s+C)}}{1 + \frac{sACZ_e}{(s+\Lambda)(s+C)}}. \tag{89}$$

Assume flexible environment with dynamics as

$$Z_e = M_e s + D_e + \frac{K_e}{s} \tag{90}$$

where M_e, D_e, and K_e define the inertia, damping, and stiffness of the environment, respectively.

Then, the transfer function from B to C can be written as

$$G_s = \frac{-ACM_e s^2 + (C - ACD_e)s + (C\Lambda - ACK_e)}{(1 + ACM_e)s^2 + (\Lambda + C + ACD_e)s + (\Lambda C + ACK_e)}. \tag{91}$$

To guarantee stability under arbitrary time delay, the gain of each manipulator together with their respective local controllers must remain equal to or smaller than the one across the entire frequency spectrum. Thus, to ensure stability of the entire teleoperation system with arbitrary time delay (see Fig. 6), the following conditions need to be satisfied:

$$\left\| \frac{-ACM_h^*(j\omega)^2 + \left(C - ACD_h^*\right)(j\omega) + \left(C\Lambda - ACK_h^*\right)}{\left(1 + ACM_h^*\right)(j\omega)^2 + \left(\Lambda + C + ACD_h^*\right)(j\omega) + \left(\Lambda C + ACK_h^*\right)} \right\|_\infty \leq 1 \tag{92}$$

$$\left\| \frac{-ACM_e(j\omega)^2 + (C - ACD_e)(j\omega) + (C\Lambda - ACK_e)}{\left(1 + ACM_e\right)(j\omega)^2 + (\Lambda + C + ACD_e)(j\omega) + (\Lambda C + ACK_e)} \right\|_\infty \leq 1. \tag{93}$$

To satisfy the stability conditions in (92) and (93), the following relation must be satisfied:

$$\begin{aligned} &[(\Lambda C + ACK) - (1 + ACM)\omega^2]^2 \\ &\quad + [(\Lambda + C + ACD)\omega]^2 - [(C - ACD)\omega]^2 \\ &\quad - [(\Lambda C - ACK) + ACM\omega^2]^2 \geq 0 \end{aligned} \tag{94}$$

for both the slave and master manipulators by substituting M, D, and K with M_e, D_e, and K_e (the slave side), or M_h^*, D_h^*, and K_h^* (the master side), respectively. Furthermore, to satisfy (94),

$$\mathbf{a}\omega^4 + \mathbf{b}\omega^2 + \mathbf{c} \geq 0 \tag{95}$$

must hold, where

$$\begin{cases}\mathbf{a} = 1 + 2ACM \\ \mathbf{b} = \Lambda^2 + 2AC(2ACD - K - 2\Lambda ACM) \\ \mathbf{c} = 4\Lambda AC^2 K.\end{cases} \tag{96}$$

It follows directly from the positive-definite properties of M, D, K, C, and Λ that $\mathbf{a} \geq 0$ and $\mathbf{c} > 0$ hold indefinitely. Consequently, it follows from (94)–(96) that

$$\mathbf{b} + 4C\sqrt{\Lambda AK(2ACM + 1)} \geq 0 \tag{97}$$

must hold to fulfill the stability conditions in (92) and (93).

REFERENCES

[1] B. D. Argall, S. Chernova, M. Veloso, and B. Browning, "A survey of robot learning from demonstration," *Robot. Auto. Syst.*, vol. 57, no. 5, pp. 469–483, May 2009.

[2] M. Suomalainen, J. Koivumaki, S. Lampinen, V. Kyrki, and J. Mattila, "Learning from demonstration for hydraulic manipulators," in *Proc. IEEE/RSJ Int. Conf. Intell. Robots Syst. (IROS)*, Oct. 2018, pp. 3579–3586.

[3] A. Pervez, A. Ali, J.-H. Ryu, and D. Lee, "Novel learning from demonstration approach for repetitive teleoperation tasks," in *Proc. IEEE World Haptics Conf. (WHC)*, Jun. 2017, pp. 60–65.

[4] I. Havoutis and S. Calinon, "Learning from demonstration for semi-autonomous teleoperation," *Auto. Robots*, vol. 43, no. 3, pp. 713–726, Mar. 2019.

[5] J. Mattila, J. Koivumäki, D. G. Caldwell, and C. Semini, "A survey on control of hydraulic robotic manipulators with projection to future trends," *IEEE/ASME Trans. Mechatronics*, vol. 22, no. 2, pp. 669–680, Apr. 2017.

[6] J. Koivumaki and J. Mattila, "Stability-guaranteed force-sensorless contact force/motion control of heavy-duty hydraulic manipulators," *IEEE Trans. Robot.*, vol. 31, no. 4, pp. 918–935, Aug. 2015.

[7] P. F. Hokayem and M. W. Spong, "Bilateral teleoperation: An historical survey," *Automatica*, vol. 42, no. 12, pp. 2035–2057, Dec. 2006.

[8] M. Ostoja-Starzewski and M. Skibniewski, "A master-slave manipulator for excavation and construction tasks," *Robot. Auto. Syst.*, vol. 4, no. 4, pp. 333–337, Apr. 1989.

[9] S. Salcudean, K. Hashtrudi-Zaad, S. Tafazoli, S. P. DiMaio, and C. Reboulet, "Bilateral matched-impedance teleoperation with application to excavator control," *IEEE Control Syst.*, vol. 19, no. 6, pp. 29–37, Dec. 1999.

[10] S. Tafazoli, S. E. Salcudean, K. Hashtrudi-Zaad, and P. D. Lawrence, "Impedance control of a teleoperated excavator," *IEEE Trans. Control Syst. Technol.*, vol. 10, no. 3, pp. 355–367, May 2002.

[11] J. Koivumaki and J. Mattila, "Stability-guaranteed impedance control of hydraulic robotic manipulators," *IEEE/ASME Trans. Mechatronics*, vol. 22, no. 2, pp. 601–612, Apr. 2017.

[12] J. Koivumäki, W.-H. Zhu, and J. Mattila, "Energy-efficient and high-precision control of hydraulic robots," *Control Eng. Pract.*, vol. 85, pp. 176–193, Apr. 2019.

[13] D.-H. Zhai and Y. Xia, "A novel switching-based control framework for improved task performance in teleoperation system with asymmetric time-varying delays," *IEEE Trans. Cybern.*, vol. 48, no. 2, pp. 625–638, Feb. 2018.

[14] A. Aijaz, M. Dohler, A. H. Aghvami, V. Friderikos, and M. Frodigh, "Realizing the tactile Internet: Haptic communications over next generation 5G cellular networks," *IEEE Wireless Commun.*, vol. 24, no. 2, pp. 82–89, Apr. 2017.

[15] J. Guo, C. Liu, and P. Poignet, "A scaled bilateral teleoperation system for robotic-assisted surgery with time delay," *J. Intell. Robotic Syst.*, vol. 95, no. 1, pp. 165–192, Aug. 2018.

[16] P. Malysz and S. Sirouspour, "A kinematic control framework for single-slave asymmetric teleoperation systems," *IEEE Trans. Robot.*, vol. 27, no. 5, pp. 901–917, Oct. 2011.

[17] A. Shahdi and S. Sirouspour, "Adaptive/robust control for time-delay teleoperation," *IEEE Trans. Robot.*, vol. 25, no. 1, pp. 196–205, Feb. 2009.

[18] S. Sirouspour, "Modeling and control of cooperative teleoperation systems," *IEEE Trans. Robot.*, vol. 21, no. 6, pp. 1220–1225, Dec. 2005.

[19] Z. Chen, F. Huang, C. Yang, and B. Yao, "Adaptive fuzzy backstepping control for stable nonlinear bilateral teleoperation manipulators with enhanced transparency performance," *IEEE Trans. Ind. Electron.*, vol. 67, no. 1, pp. 746–756, Jan. 2020.

[20] D. Sun and Q. Liao, "Asymmetric bilateral telerobotic system with shared autonomy control," *IEEE Trans. Control Syst. Technol.*, early access, Sep. 23, 2020, doi: 10.1109/TCST.2020.3018426.

[21] A. Muhammad *et al.*, "Development of water hydraulic remote handling system for divertor maintenance of ITER," in *Proc. IEEE 22nd Symp. Fusion Eng.*, Jun. 2007, pp. 1–4.

[22] S. E. Salcudean and W.-H. Zhu, "Stability guaranteed teleoperation: An adaptive motion/force control approach," *IEEE Trans. Autom. Control*, vol. 45, no. 11, pp. 1951–1969, Nov. 2000.

[23] S. Lampinen, J. Koivumäki, and J. Mattila, "Full-dynamics-based bilateral teleoperation of hydraulic robotic manipulators," in *Proc. IEEE 14th Int. Conf. Autom. Sci. Eng. (CASE)*, Aug. 2018, pp. 1343–1350.

[24] S. Lampinen, J. Koivumäki, and J. Mattila, "Bilateral teleoperation of a hydraulic robotic manipulator in contact with physical and virtual constraints," in *Proc. BATH/ASME Symp. Fluid Power Motion Control*, Sep. 2018, Art. no. V001T01A021.

[25] S. Mastellone and A. van Delft, "The impact of control research on industrial innovation: What would it take to make it happen?" *Control Eng. Pract.*, vol. 111, Jun. 2021, Art. no. 104737.

[26] W.-H. Zhu, *Virtual Decomposition Control: Toward Hyper Degrees of Freedom Robots*, vol. 60. Berlin, Germany: Springer-Verlag, 2010.

[27] W.-H. Zhu, Y.-G. Xi, Z.-J. Zhang, Z. Bien, and J. De Schutter, "Virtual decomposition based control for generalized high dimensional robotic systems with complicated structure," *IEEE Trans. Robot. Autom.*, vol. 13, no. 3, pp. 411–436, Jun. 1997.

[28] W.-H. Zhu, T. Lamarche, E. Dupuis, D. Jameux, P. Barnard, and G. Liu, "Precision control of modular robot manipulators: The VDC approach with embedded FPGA," *IEEE Trans. Robot.*, vol. 29, no. 5, pp. 1162–1179, Oct. 2013.

[29] W.-H. Zhu, "Dynamics of general constrained robots derived from rigid bodies," *J. Appl. Mech.*, vol. 75, no. 3, pp. 031005-1–031005-11, May 2008.

[30] H. Kazerooni and M.-G. Her, "The dynamics and control of a haptic interface device," *IEEE Trans. Robot. Autom.*, vol. 10, no. 4, pp. 453–464, Aug. 1994.

[31] J. D. Cooke, "Dependence of human arm movements on limb mechanical properties," *Brain Res.*, vol. 165, no. 2, pp. 366–369, Apr. 1979.

[32] P. Malysz and S. Sirouspour, "Nonlinear and filtered force/position mappings in bilateral teleoperation with application to enhanced stiffness discrimination," *IEEE Trans. Robot.*, vol. 25, no. 5, pp. 1134–1149, Oct. 2009.

[33] T. Hu, J. Kühn, and S. Haddadin, "Forward and inverse dynamics modeling of human shoulder-arm musculoskeletal system with scapulothoracic constraint," *Comput. Methods Biomech. Biomed. Eng.*, vol. 23, no. 11, pp. 785–803, Aug. 2020.

[34] S. Haddadin, A. De Luca, and A. Albu-Schaffer, "Robot collisions: A survey on detection, isolation, and identification," *IEEE Trans. Robot.*, vol. 33, no. 6, pp. 1292–1312, Dec. 2017.

[35] J. Koivumäki and J. Mattila, "Adaptive and nonlinear control of discharge pressure for variable displacement axial piston pumps," *J. Dyn. Syst., Meas., Control*, vol. 139, no. 10, Oct. 2017.

[36] G. Tao, "A simple alternative to the Barbalat lemma," *IEEE Trans. Autom. Control*, vol. 42, no. 5, p. 698, May 1997.

Santeri Lampinen received the bachelor's and M.Sc. degrees (Hons.) in machine automation from the Tampere University of Technology, Tampere, Finland, in 2017 and 2018, respectively.

He has been working with the Tampere University of Technology since 2017 and since 2018 he has been pursuing doctoral degree in machine automation. His research interests include mining automation, control of teleoperation systems, control of hydraulic systems, and nonlinear-model-based control.

Janne Koivumäki (Member, IEEE) received the M.Sc. degree in automation engineering and the Dr.Tech. degree in automation science and engineering from the Tampere University of Technology, Tampere, Finland, in 2012 and 2016, respectively.

From 2011 to 2019, he worked with the Department of Intelligent Hydraulics and Automation, Tampere University of Technology. In 2019, he joined the Novatron Oy, Pirkkala, Finland, where he currently works as a Robotics and Control Systems Scientist. His research interests include an earth-moving automation, hydraulic robotic manipulators, constrained motion control, and energy efficiency.

Wen-Hong Zhu (Senior Member, IEEE) received the bachelor's and M.S. degrees from Northwestern Polytechnical University, Xi'an, China, in 1984 and 1987, respectively, and the Ph.D. degree from Xi'an Jiaotong University, Xi'an, in 1991.

He was a Post-Doctoral Fellow with Shanghai Jiao Tong University, Shanghai, China, during 1991–1993; the Korea Advanced Institute of Science and Technology, Daejeon, Korea, in 1995; Katholieke Universiteit Leuven, Leuven, Belgium, during 1996–1997; and the University of British Columbia, Vancouver, BC, Canada, during 1997–1999. He was with the University of British Columbia as a Scientific Engineer from 1999 to 2001 until he joined the Canadian Space Agency (CSA), Saint-Hubert, QC, Canada, as an engineering employee. He is the initiator of Virtual Decomposition Control.

Jouni Mattila (Member, IEEE) received the M.Sc. and Ph.D. degrees in automation engineering, both from the Tampere University of Technology, Tampere, Finland, in 1995 and 2000, respectively.

He is currently a Professor of machine automation with the unit of Automation Technology and Mechanical Engineering, Tampere University. His research interests include machine automation, nonlinear model-based control of robotic manipulators, and energy-efficient control of heavy-duty robotic systems.